Synchrotron FTIR Spectroscopy of Interstellar and Atmospherically Relevant Molecules

Andy Wong, B. Sc (Honours)

School of Chemistry, Monash University

January 2016

Abstract

A recurring theme throughout this thesis is the analysis of Fourier transform infrared (FTIR) spectra of molecules that exist in planetary atmospheres and interstellar media. FTIR spectroscopy enables the accurate characterisation and identification of molecules based on the shapes and positions of vibrational bands. Unless stated otherwise, all of the experimental work has been performed at the Australian Synchrotron THz/far-IR beamline utilising a synchrotron source which is several magnitudes brighter than conventional thermal sources. This is crucial for the far-IR region, as there are no efficient thermal emitters of far-IR radiation. Furthermore, spectroscopy within this region is most applicable to monitoring atmospheric and interstellar molecules.

Chapter 1 introduces some of the key concepts associated with FTIR spectroscopy as well as the instrumentation used for the experiments. Quantum theory is also introduced where needed as part of the concepts that are discussed.

Chapter 2 focuses on the spectra of molecules recorded using high resolution FTIR spectroscopy and the fundamental theory is introduced in **Chapter 2.1** as it is a prerequisite to understanding the rotational Hamiltonian, transition assignment and fitting processes used throughout **Chapters 2.2 - 2.5**.

Chapter 2.2 describes an ongoing analysis of the first high resolution FTIR spectrum of propynethial which is predicted to exist in interstellar media. The ν_5 band near 1100 cm^{-1} is the focus of this work as it was predicted to be the most intense band based on B3LYP/cc-pVTZ calculations. Due to inaccurate ground state rotational and centrifugal distortion constants, it was not possible to accurately assign the ro-vibrational transitions of the ν_5 band. Thus, it was necessary to record millimetre-wave spectra in order to assign transitions with a wider range of J'' and K_a'' quantum number so that more accurate ground state constants could be determined before re-assigning the ν_5 infrared transitions. This work will hopefully lead to the identification of propynethial in the interstellar media.

Chapter 2.3 contains the first published paper on the analysis of the far-IR bands of 1,1-difluoroethane. This molecule is relevant to atmospheric applications due to its high global warming potential and will help facilitate the analysis of higher energy vibrational bands that are present within the greenhouse window.

Chapter 2.4 contains a publication on one of the far-IR bands of 1,1,1,2-tetrafluoroethane. Also known as R134a, this molecule is commonly used in industry and needs to be continuously monitored due to its high global warming potential and long atmospheric lifetime.

Chapter 2.5 is a submitted paper on the analysis of the four lowest IR-active fundamental bands of *trans*-d_2-ethylene. The work completed here is part of a chemical-education collaboration between Dr. C. Thompson (Monash University) and Prof. T. L. Tan (Nanyang Technological University).

Chapter 3 progresses into the analysis of low resolution particulate ices that were formed in a collisional cooling cell that has been installed onto the Australian Synchrotron THz/far-IR beamline. These molecular ices are important to interstellar chemistry, as they can provide reaction sites for building more complex molecules from smaller molecules; and atmospheric chemistry by having a large influence on the radiative forcing of planetary atmospheres. Some key aspects of condensed phase spectroscopy are introduced in **Chapter 3.1**

Chapter 3.2 is an accepted paper detailing the analysis of the mid-IR spectra of isotope mixed H_2O crystalline ice particles. The effect of isotopic mixing using D_2O is explored over a range of temperatures and concentrations, giving new insights to the behaviour of inter- and intramolecular bonding.

Chapter 3.3 contains a manuscript that reports the mid- and far-IR spectra of particulate crystalline ethylene. Ethylene is one of the most abundant species found in Titan's atmosphere (largest moon orbiting Saturn) and is formed from the photodissociation of methane. An accurate characterisation of these ethylene particles *in situ* will provide a more direct relationship with what is observed from passing satellites and help profile the temperature of Titan's atmosphere at different altitudes.

Chapter 4 describes the application of a chemometric technique: band target entropy minimisation (BTEM) to gas phase Fourier transform microwave (FTMW) and FTIR spectra. Chemometrics is a widely used technique to help extract additional information from chemical, physical and biological systems that may not be readily discernible through conventional methods. The preliminary results from the analysis of FTMW and FTIR spectra, using BTEM, highlights both the potential application of chemometrics to gas phase spectroscopy as well as its shortcomings.

Chapter 5 introduces preliminary data on the application of the EFC cell to transient spectroscopy. Many of the gaseous molecules that are found in interstellar media often exist as short-lived species under laboratory conditions. This work is aimed at increasing the lifetime of transient molecules so that some of the experimental burdens can be reduced when performing high resolution spectroscopy.

Declaration

This thesis contains no material which has been accepted for the award of any other degree or diploma at any university or equivalent institution and that, to the best of my knowledge and belief, this thesis contains no material previously published or written by another person, except where due reference is made in the text of the thesis.

General Declaration

In accordance with Monash University Doctorate Regulation 17.2 Doctor of Philosophy and Research Master's regulations the following declarations are made:

I hereby declare that this thesis contains no material which has been accepted for the award of any other degree or diploma at any university or equivalent institution and that, to the best of my knowledge and belief, this thesis contains no material previously published or written by another person, except where due reference is made in the text of the thesis.
The data used in Chapter 2.3 was obtained during my undergraduate degree, however the analysis and writing of the paper was done during this degree.

This thesis includes 2 original papers published in peer reviewed journals, 1 accepted and 2 unpublished publications. The core theme of the thesis is the analysis of infrared spectra of interstellar and atmospherically relevant molecules. The ideas, development and writing up of all the papers in the thesis were the principal responsibility of myself, the candidate, working within the School of Chemistry under the supervision of Prof. Don McNaughton.

The inclusion of co-authors reflects the fact that the work came from active collaboration between researchers and acknowledges input into team-based research.

In the case of chapters 2 and 3 my contribution to the work involved the following:

Thesis chapter	Publication title	Publication status*	Nature and extent of candidate's contribution
2.1	Synchrotron far-infrared spectroscopy of the two lowest fundamental modes of 1,1-difluoroethane	Published	Initiation, key ideas, experimental, development and writing up (80%)
2.2	High resolution far-infrared spectroscopy of HFC-134a using a collisional cooling cell adapted to a synchrotron source	Published	Initiation, key ideas, experimental, development and writing up (80%)
2.3	High resolution FTIR spectral analysis of the tetrad system (ν_4, ν_7, ν_{10} and ν_{12}) of *Trans-*d_2-ethylene.	Submitted	Initiation, key ideas, experimental, development and writing up (80%)
3.1	Heavy Snow: IR spectroscopy of isotope mixed crystalline water ice	Accepted	Initiation, key ideas, experimental, development and writing up (80%)
3.2	Far and mid-IR spectroscopy of ethylene aerosols at astrophysical temperatures	To be submitted	Initiation, key ideas, experimental, development and writing up (80%)

I have renumbered sections of submitted or published papers in order to generate a consistent presentation within the thesis.

Signed:…… **Date:……..……**

Acknowledgements

First and foremost, I would like to thank the Faculty of Science for awarding me a Faculty of Science Dean's scholarship which has allowed me to pursue the art of FTIR spectroscopy.

This project would not have been possible without the unwavering support of my supervisors. Don, your almost unlimited knowledge has shown me that I have much to learn and your guidance has always pushed me in the right direction. Evan, thank you for having the patience to teach me new things about condensed phase spectroscopy and that I should always look beyond what is in front of me. Dom, your expertise in dealing with the most intricate problems that pop up due to instrument failures (natural or otherwise) has always saved the day. Chris, I have enjoyed the many philosophical discussions about high resolution spectroscopy and very much appreciate your attention to my work (especially with R134a) throughout the years even with your busy schedule.

I would like to thank the members of the Monash Biospectroscopy group, most of which have moved on from Monash. Especially to Chris, Mot, David and Michael, thank you for the moral and intellectual support since the beginning of my research career and for putting up with me; and Donna, thank you for sharing good banter with me every now and then whenever we bumped into each other in the School of Chemistry corridors.

Finally, I would like to thank my family for their emotional and financial support. It most certainly would not have been possible for me to pursue my PhD without them. Likewise to my extended family of friends from high school - thank you for the weekly Friday night dinners and the meaningless conversations had after having a bit too much to drink.

Table of Contents

If you can’t explain it to a six year old, you don’t understand it yourself.

-Albert Einstein

Chapter 1.0

Infrared Spectroscopy and Instrumentation

1.1 Infrared (IR) spectroscopy

Photons within the infrared region of the electromagnetic spectrum cover a range of wavelengths ranging from 100,000 - 800 nm, or 100 - 12,500 cm^{-1}. In general, infrared radiation can be divided into three regions commonly known as: far-IR (100 - 700 cm^{-1}), mid-IR (700 - 5,000 cm^{-1}) and near-IR (5,000 - 12,500 cm^{-1}). The window between 0 - 100 cm^{-1} is often referred to the THz or millimetre-wave region. The boundaries for each region may differ between commentators, however in the context of this thesis the definitions given above are used throughout.

Infrared photons are considered low in energy as molecules are generally limited to vibrational excitations when absorbed. The wavenumber at which an IR photon is absorbed is proportional to the strength of the bond (force constant *k*) and the mass of the atoms involved in the vibration, and is related to Hooke's law via **equation 1.1**,

$$\bar{\nu} = \frac{1}{2\pi c}\left[k/\left(\frac{m_1+m_2}{m_1 m_2}\right)\right]^{1/2} \qquad \textbf{(1.1)}$$

where $\bar{\nu}$ is the vibrational frequency (cm^{-1}), *c* is the speed of light (cm s^{-1}), *k* is the force constant (*N* m^{-1}), and m_1 and m_2 are the masses of atoms 1 and 2 (kg mol^{-1}), respectively. $\frac{m_1+m_2}{m_1 m_2}$ is also known as the reduced mass, μ.

1.1.1 Vibrational transitions

A molecule in the gas phase will have a certain number of unique fundamental vibrations which is determined by the number of atoms, *N*, as well as its molecular geometry. Linear molecules will have 3*N* - 5 fundamentals whereas non-linear molecules will have 3*N* - 6. It is also possible to observe other types of vibrational transitions such as overtones; which consist of multiple quanta of a fundamental vibration, and combinations; the combination of two or more different vibrations, as illustrated in **figure 1.1**.

Although overtone and combination levels are not accounted for in harmonic theory, their energies are often approximated using a harmonic potential (**equation 1.2**) by assuming a proportional increase in energy with vibrational quantum number. This is shown as the red trace in **figure 1.2**,

$$E_v = \hbar\omega\left(v + \frac{1}{2}\right) \qquad \textbf{(1.2)}$$

where v = 0, 1, 2, 3… is the vibrational quantum number, $\hbar$ is Planck's reduced constant (m^2 kg s^{-1}) and ω is the angular vibrational frequency (cm^{-1}).

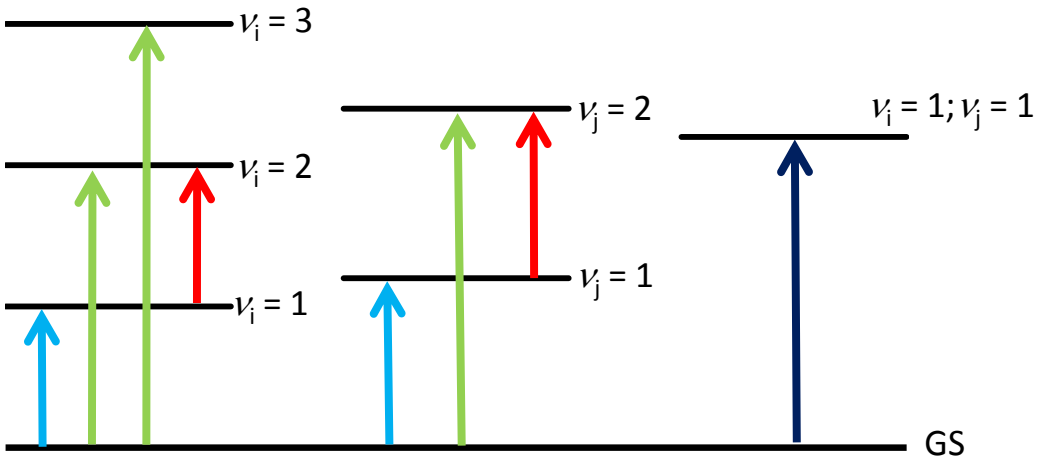

Figure 1.1: An illustration of possible vibrational excitations from the ground vibrational state (GS). Fundamental, overtone, hot band and combination transitions are denoted by light blue, light green, red and dark blue arrows respectively.

This potential is effective for low energy vibrational levels however it becomes insufficient for describing more complex effects such as anharmonicity and bond dissociation. A more appropriate anharmonic, or Morse potential, is therefore used (blue trace in **figure 1.2**) and the vibrational energies are now described using **equation 1.3**,

$$E_v = \omega_e \left(v + \frac{1}{2}\right) - \omega_e x_e \left(v + \frac{1}{2}\right)^2 + \omega_e y_e \left(v + \frac{1}{2}\right)^3 + \cdots \qquad \textbf{(1.3)}$$

where $\omega_e x_e$ and $\omega_e y_e$ are the anharmonic correction terms.

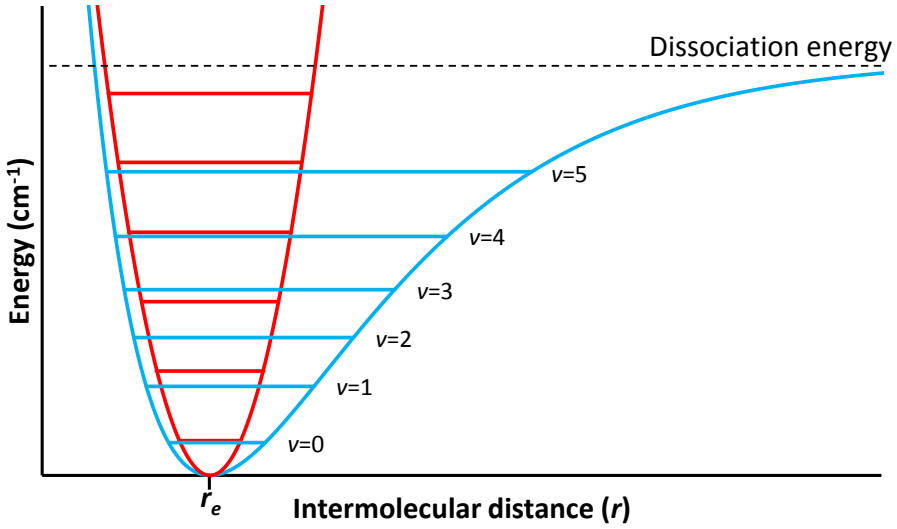

Figure 1.2: A 2-dimensional plot of the harmonic (red) and anharmonic (blue) potential wells.

Molecules within the condensed phases (i.e. liquids and solids) will also have the same fundamental, overtone and combination vibrations. However, they may exhibit additional vibrations that are purely due to intermolecular coupling (e.g. ν_L librational mode in water). Intermolecular coupling will often weaken the strength of intramolecular bonds, thus reducing the vibrational energy level and red-shifting the wavenumber value of a vibrational band.

1.1.2 Transition dipole

For a molecular vibration to be observed in an IR spectrum there must be an oscillation of the permanent dipole moment as a molecule vibrates. Quantum mechanically, this is described as the transition probability (**equation 1.2**) [1], where the intrinsic intensity of an infrared band, *I*, is proportional to the square of the transition probability, $[\hat{\mu}_F]$,

$$I = [\hat{\mu}_F]^2 = \langle \Psi_m^* | \hat{\mu}_F | \Psi_n \rangle^2 \qquad \textbf{(1.2)}$$

where $\hat{\mu}$ is the electric dipole moment of the molecule and *F* represents the *x*, *y*, *z* matrix elements. Ψ_m and Ψ_n are the wave functions for vibrational states *m* and *n* respectively.

In practice, the intensity of an IR band is not presented simply by the pure transition probability, rather a summation of intensity contributions from several processes such as: temperature; concentration; intramolecular; and intermolecular coupling. Contributions from each of these effects are systematically discussed below and the latter two are introduced in **Chapters 2** and **3** respectively.

1.1.2.1 Temperature

The temperature of a molecular system will determine the populations of molecules occupying different excited vibrational levels and can be estimated using Boltzmann's distribution (**equation 1.3**),

$$\frac{N_i}{N_0} = \frac{e_i}{e_0} exp^{\left(\frac{-\Delta E}{k_B T}\right)} \qquad \textbf{(1.3)}$$

where N_i and N_0 are the populations of molecules in the excited and ground states respectively. $\frac{e_i}{e_0}$ is the degeneracy factor, ΔE is the energy of an excited state (cm^{-1}), k_B is Boltzmann's constant (1.38×10^{23} J K^{-1}) and *T* is the temperature in (Kelvin).

At colder temperatures, more molecules will occupy the ground vibrational state and therefore the number of transitions to fundamental, overtone or combination levels will increase, thus increasing the intensities of these bands. The Boltzmann distribution is also useful for estimating the relative intensities of hot bands (red arrows in **figure 1.1**) which can have significant intensity contributions in

gas phase spectra. **Figure 1.3** illustrates the percentage of molecules of 1,1,1,2-tetrafluoroethane that are occupying the four lowest energy fundamental levels as a function of temperature.

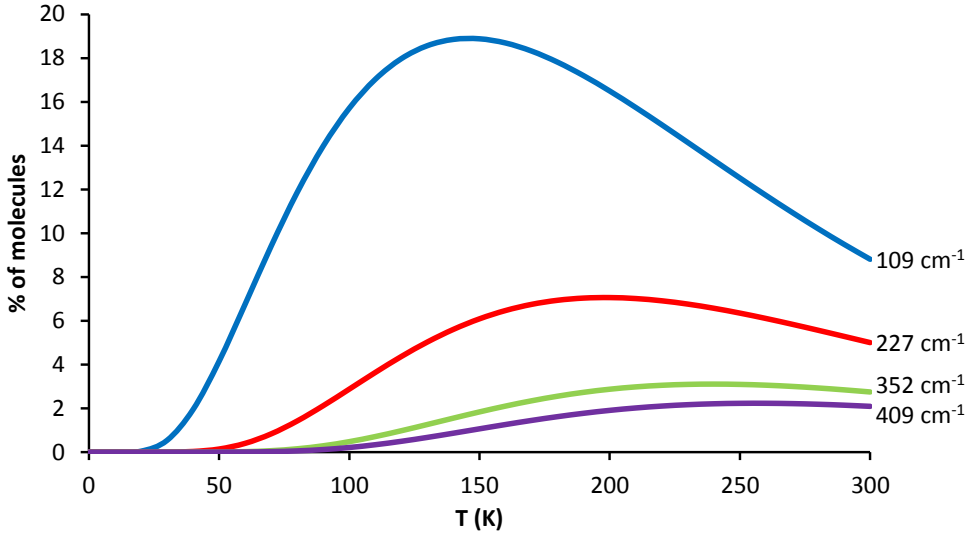

Figure 1.3: The percentage of molecules in the four lowest fundamental levels in 1,1,1,2-tetrafluoroethane as a function of temperature.

1.1.2.2 Concentration and pathlength

The absorbance of a material is related to the transmittance of light through it (**equation 1.4**) and is linearly proportional to both the concentration of a sample *c*, and optical path *l*, via the Beer-Lambert law (**equation 1.5**) within a certain concentration range,

$$T = \frac{P}{P_0}; A = \log_{10}\frac{P}{P_0} \qquad \textbf{(1.4)}$$

where $\frac{P}{P_0}$ is the transmittance (T) of photons before (P_o) and after (P) passing through a material respectively,

$$A = \varepsilon c l \qquad \textbf{(1.5)}$$

where ε is the extinction coefficient (mol L^{-1} cm^{-1}), c is the concentration (mol L^{-1}) and l is the pathlength (cm).

As concentration increases, the number of molecules found within a given volume increases which subsequently increases the probability of a photon being absorbed. In most cases (e.g. low resolution spectroscopy), it is more convenient to increase the sample concentration rather than the optical path length, however it becomes necessary to increase l when sample availability is limited or when it is impractical to increase concentration. This is particularly true for high resolution spectroscopy as increasing sample concentration often leads to undesired pressure broadening (**Chapter 1.2.4)**.

1.2 Instrumentation

Early infrared spectrometers were limited to either grating or dispersive type optics where the spectrum was recorded at discrete wavenumber values. These methods were not very time efficient and sources often had weak intensities which impacted on acquisition time and signal-to-noise (S/N) quality. However, since the development of the Michelson interferometer [2], **figure 1.4**, most of these issues have been alleviated. The addition of the interferometer allows one to take advantage of broadband radiation from an IR source, known as the multiplex or Fellgett's advantage [3]. A direct result of this is Jacquinot's advantage [4], where the source throughput is greatly enhanced because there is no need to exclude radiation by introducing slits.

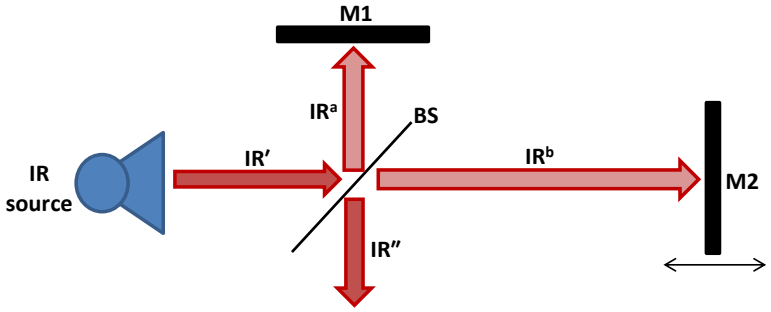

Figure 1.4: A basic schematic of the Michelson interferometer.

The interferometer is designed such that an incoming light source (IR′) is split by a beamsplitter (BS) into two beams of almost equal energy (IR^a and IR^b). IR^a is directed onto a stationary (M1) and IR^b onto a moving mirror (M2) before recombining into IR″. The interference pattern is recorded by a detector as an interferogram (**figure 1.5**) and is plotted as a function of intensity (*I*) versus optical displacement (*l*).

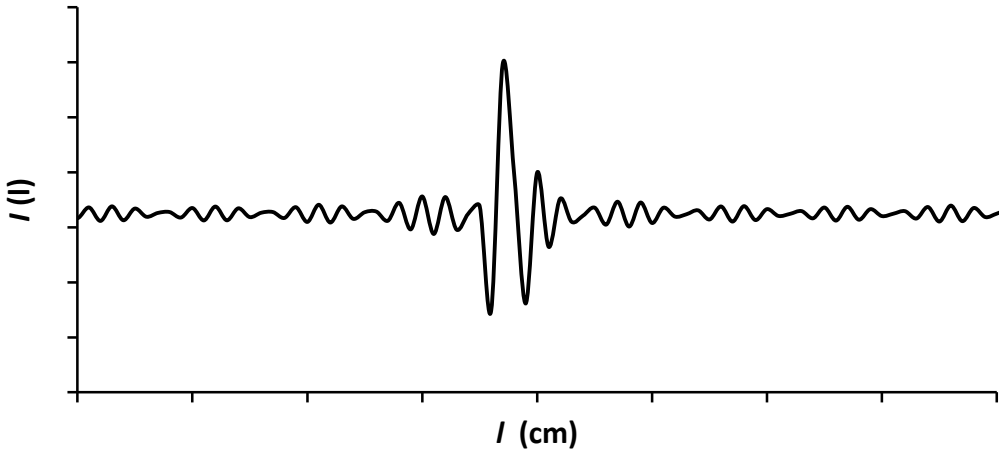

Figure 1.5: An illustration of a simulated interferogram.

The interferogram can be described using **equation 1.5**, where the Fourier transform (**equation 1.6**) is then applied in order to obtain a spectrum (intensity versus wavenumber),

$$I(l) = S_0(1 + cos2\pi\tilde{\nu}l) \qquad \textbf{(1.5)}$$

where S_0 is the intensity of a wavenumber $\tilde{\nu}$ and l is the optical displacement in cm.

$$S(\tilde{\nu}) = \int_{-\infty}^{\infty} \left[I(l) - \frac{I(0)}{2}\right] cos2\pi\tilde{\nu}l \; dl \qquad \textbf{(1.6)}$$

where $I(0)$ is the intensity of the interferogram at zero optical path difference.

1.2.1 Bruker IFS 125HR spectrometer

A Bruker IFS 125HR spectrometer has been installed onto the Australian Synchrotron THz/far-IR beamline and is used throughout the experiments described in **Chapters 2 - 5**. This model is the instrument of choice as it is able to achieve a nominal resolution of 0.00096 cm^{-1} as a result of the long interferometer arm (5.2 m), where spectral resolution is inversely proportional to the optical path difference (OPD) (**equation 1.7**). This a prerequisite for gas phase studies due to intrinsically narrow ro-vibrational lines, as well as the high level of accuracy that is required when reporting line positions In order to maintain a high level of accuracy, the instrument is calibrated via precise tracking of the moving mirror using a HeNe laser (Connes advantage [5]).

$$resolution = \frac{1}{OPD\ (cm)} \qquad \textbf{(1.7)}$$

Although the instrument is designed for high resolution studies, it is also capable of recording spectra at lower resolutions which are more applicable to the condensed phase experiments discussed in **Chapter 3**, as well as lifetime studies in **Chapter 5**.

The spectrometer can house up to six different detectors depending on the region of interest, with detectors available at the Australian Synchrotron THz/far-IR beamline covering: the far-IR region (deuterated triglycine sulfate (DTGS); boron-doped Si-B photodetector and Si bolometer); and mid- and near-IR regions (mercury cadmium telluride (MCT)). There are also three internal sources which can be used depending on the region of interest: mercury-arc lamp (far-IR); silicon carbide globar (mid-IR); or a tungsten lamp (near-IR) and one external synchrotron source. Before choosing a source, an informed decision should be made after considering the brightness and S/N level of each.

Figure 1.6: The Bruker IFS125 HR Spectrometer at the Australian Synchrotron THz/far-IR beamline. Pictured is the interferometer arm, with the enclosive flow cooling (EFC) cell manifold in the background

1.2.2 Sources

The brightness of an IR source is important for samples that are weak IR absorbers, or have limited availability. For a thermal source, the brightness can be determined using Planck's law (**equation 1.8**) [9], which is often used to calculate the brightness of blackbody emitters (solid line in **figure 1.9**).

$$B_{bb}(\omega) = \frac{\hbar\omega^3}{(2\pi)^2 c^2} \frac{d\omega}{e^{\hbar\omega/kT}-1} \qquad \textbf{(1.8)}$$

where $\hbar$ is the reduced Planck constant (J s), c is the speed of light (m s^{-1}), k is Boltzmann's constant (m^2 kg s^{-2}), T is temperature (K) and ω is the wavelength (μm).

For low resolution spectroscopy, there are numerous sources available which can produce a bright source of radiation with a high S/N within the mid- and near-IR regions. Unfortunately this is not the case for far-IR spectroscopy. Aside from mercury-arc lamps, there are currently no other available thermal sources which can efficiently emit far-IR radiation which is critical for monitoring interstellar and atmospheric molecules [10, 11]. This lack of available sources therefore creates a need for a new type of far-IR source such as a Synchrotron.

In principle Synchrotrons are able to emit photons which cover wavelengths ranging from millimetre-waves to X-rays. The brightness of Synchrotron IR radiation (B_{sr}) will be dependent on the types of magnets used (e.g. bending magnets or undulators) as well as the current of the stored beam. Since IR radiation at the Australian Synchrotron is generated from a bending magnet, the brightness can be estimated using **equation 1.9** [9] and is expected to be at least three orders of magnitude brighter than a 2000 K thermal source (dashed line **figure 1.9**). For example, at 10 μm (1000 cm^{-1}) the expected brightness (photons s^{-1} per 0.1 % bandwidth mm^{-1} sr^{-1}) of a Synchrotron source is on the order of 4.0×10^{18} in comparison to 9.3×10^{15} for a 2000 K blackbody emitter.

$$B_{sr}(\tilde{\nu}) \approx 10^{-8} I \tilde{\nu}^2 \qquad \textbf{(1.9)}$$

where I is the stored beam current (amperes) and $\tilde{\nu}$ is the frequency (cm^{-1}).

The Australian synchrotron is a 3rd generation synchrotron facility which currently operates using a "top-up" mode where the beam current is constantly maintained at 200 mA by periodically injecting electron bunches. The IR beamline receives radiation from a bending magnet and is split in half via a beamsplitter box where the incoming bending radiation is directed toward the low resolution microscopy branch and the edge radiation toward the THz/far-IR branch. Edge radiation from the bending magnet allows access to photons with wavelengths as long as 1,000 μm (10 cm^{-1}).

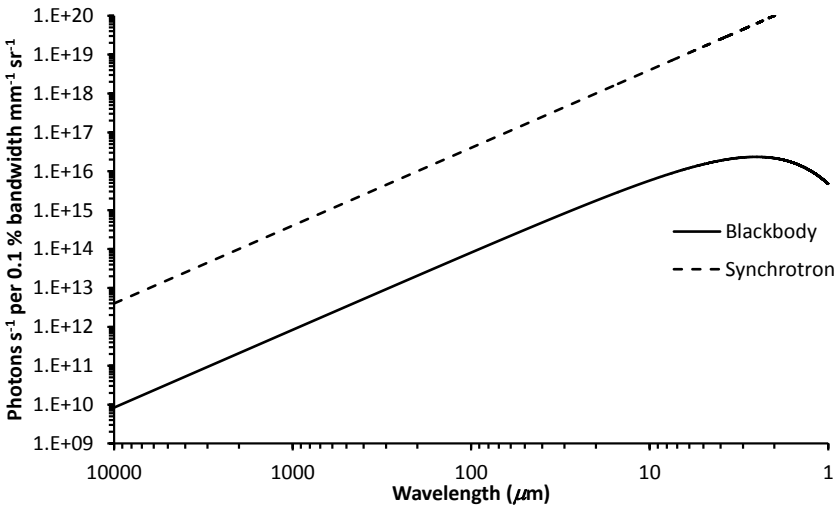

Figure 1.9: The brightness of a blackbody source (2000 K) and simulated brightness for a synchrotron source.

The highly collimate nature of a synchrotron source provides a beam that is ≈ 300 μm in diameter at the full-width half-max (FWHM) in comparison to a thermal source which emits radiation in all directions. The narrow beam removes the need for a physical aperture (**equation 1.10**) to filter out stray radiation and subsequently increases both the brightness and S/N level of the beam (**equation 1.11**),

$$d_{max} = 2\sqrt{2}F\sqrt{\frac{\Delta\tilde{\nu}}{\tilde{\nu}}} \qquad \textbf{(1.10)}$$

where d is the diameter of the aperture (mm), F is the focal length of the collimating mirror (cm). $\Delta\tilde{\nu}$ and $\tilde{\nu}$ are the resolution (cm^{-1}) and maximum recorded wavenumber (cm^{-1}) respectively.

This is crucial for high resolution spectroscopy due to the intrinsically noisy spectra, making synchrotron radiation superior to thermal sources in the far-IR region and up to *ca*. 2000 cm^{-1} in the mid-IR region,

$$S/N = \frac{B(\bar{\nu})(\delta\bar{\nu})\Theta\xi D^*}{(\Delta f)^{1/2}A^{1/2}} \qquad \textbf{(1.11)}$$

where $B(\bar{\nu})$ is the source brightness, $\delta\bar{\nu}$ is the resolution, Θ is the limiting etendue (or the product of the area × solid angle), ξ is the optical efficiency (amount of light passing through the system) and D^* is the detectivity (in Hz$^{1/2}$ W^{-1}) as defined by **equation 1.12** [12]. Δf and A are the electronic bandwidth and area of the detector respectively,

$$D^* = (A\Delta f)^{1/2}D \qquad \textbf{(1.12)}$$

where Δf here is the noise equivalent bandwidth.

1.2.3 Apodization functions and zero filling

Equation 1.5 represents an ideal case where the optical displacement is recorded continuously over infinitely long distance *l*. In practice, data is actually recorded over discrete intervals using a fast Fourier transform (FFT) [6] and a finite total distance, *l*. The latter causes the intensity of the sample signal to abruptly decrease to zero at *l*. The effect of this is that the interferogram is multiplied by a boxcar function (left panel in **figure 1.7**) which causes undesirable side lobes in the lineshape (sinc function shown on the right of **figure 1.7**).

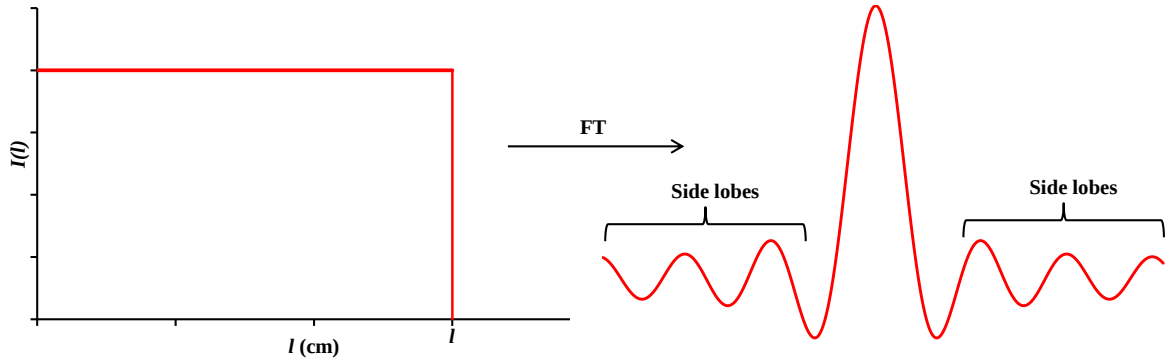

Figure 1.7: The Fourier transform (right) of a boxcar function (left).

In order to minimise these lobes, different apodization functions [7] can be applied to smoothly reduce the intensity to zero which comes at the cost of reducing the resolution of the spectrum. For the high resolution spectroscopic studies in **Chapters 2** and **4**, where the narrowest lineshapes are required, a four point apodization function is used, that is the last 4 points in the boxcar are linearly reduced to zero. This function sufficniently reduces the intensities of the side lobes without having a large effect on the resolution. A 3-term Blackman-Harris function is adequate for low resolution spectroscopy (**Chapters 3** and **5**).

A direct consequence of recording and transforming the interferogram using a FFT results in a picket fence effect causing spectral lines to appear jagged (bottom trace in **figure 1.8**). In order to smooth spectral lines, zero filling is used to interpolate between each of the recorded data points so that an absorption feature has a more accurate position and shape that is closer to the expected mixed Gaussian-Lorentzian profile [8] (top trace of **figure 1.8**). A zero fill factor of 2 is conventionally used during the Fourier transformation with an additional post-zero fill factor (pzff) being applied before spectral analysis. High resolution spectra typically require a pzff of at least 8, compared to 4 for low resolution spectra.

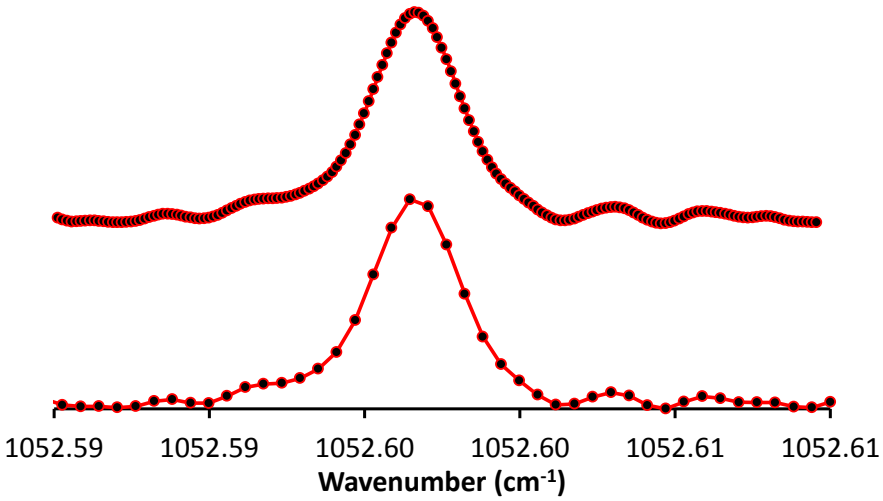

Figure 1.8: The top trace shows a spectral line with a zero-fill factor of 8 that is applied during the Fourier transformation. The bottom trace is the same line with a pzff of 2.

1.2.4 Pressure broadening

Although pressure broadening does not have a big influence on low resolution spectroscopy, this is not the case for high resolution spectroscopy as increased sample pressures often leads to undesired broadening of ro-vibrational lines. If we assume that the average time between collisions is described by τ, then the frequency of a broadened line can be estimated via **equation 1.13**,

$$\Delta\nu = (2\pi\tau)^{-1} \quad \textbf{(1.13)}$$

where $\Delta\nu$ is the frequency of the broadened line (Hz).

Although this equation doesn't explicitly describe pressure broadening, it is useful to be able to estimate line broadening. In practice, it is quite difficult to accurately calculate line broadening as a function of pressure, as it is dependent on the molecular mass, temperature and frequency of collisions. However, as a general rule of thumb, ro-vibrational linewidths for high resolution FTIR spectra increase at a rate of approximately 0.001 cm^{-1} $Torr^{-1}$ (or 0.001 cm^{-1} 0.013 kPa^{-1} [13]).

1.2.5 White-type cells

To overcome the issue of pressure broadening, White-type [14] cells can be used to increase the optical path through a sample without inducing pressure broadening, A longer optical path subsequently increases the sample absorbance, as described by **equation 1.4**, and is particularly advantageous for samples that have limited quantities or are weak IR absorbers.

The optics for a White cell are designed such that incoming radiation is repeatedly reflected off spherical mirrors to create multiple passes before exiting the cell (**figure 1.9a**). On one end of the cell, two spherical "D" shaped mirrors are used whilst one spherical "T" shaped mirror is placed on the opposite end. The distance between the D and T mirrors is dependent on the focal point of the mirrors which dictates the base path length of the cell with a minimum of 4 passes (**figure 1.9b**).

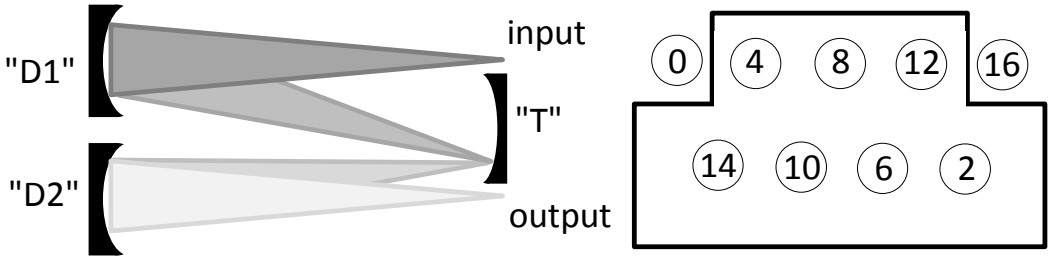

Figure 1.9: (**a**) Placement of the spherical "D" and "T" mirrors to allow for multiple passes in a White cell. (**b**) An illustration of where the reflections bounce on the "T" mirror.

1.2.5.1 Enclosive flow cooling (EFC) cell

Situated at the Australian Synchrotron far-IR beamline is an EFC cell [15] which is capable of producing a cold environment for both gas and condensed phase studies (schematic shown in **figure 1.10**) and is briefly described below.

The cell consists of White-type optics which is installed onto the ends of a metal cylinder with large holes resembling a colander. This is attached onto the cell base, forming the internal skeleton, with a second cylinder placed around the outside of this central cylinder. The second cylinder is sealed to the cell base via an indium gasket. The whole ensemble sits inside a glass Dewar which can be filled with a cooling agent depending on the desired temperature. Buffer gas can then be introduced into the cell and is cooled when the molecules collide with the cold outer cylinder. The buffer gas molecules then diffuse through the central cylinder which in turn cools down sample molecules via collisional cooling.

The temperature of the cell is read by *k*-type thermocouples that are placed near the mirrors and on the metal colander for temperatures between 298 - 30 K, as well as one central iron-rhodium thermistor which is sensitive to 1.4 K. Heaters are attached to the top and bottom mirrors, as well as on the metal colander and are monitored by a controller box (**figure 1.11**).

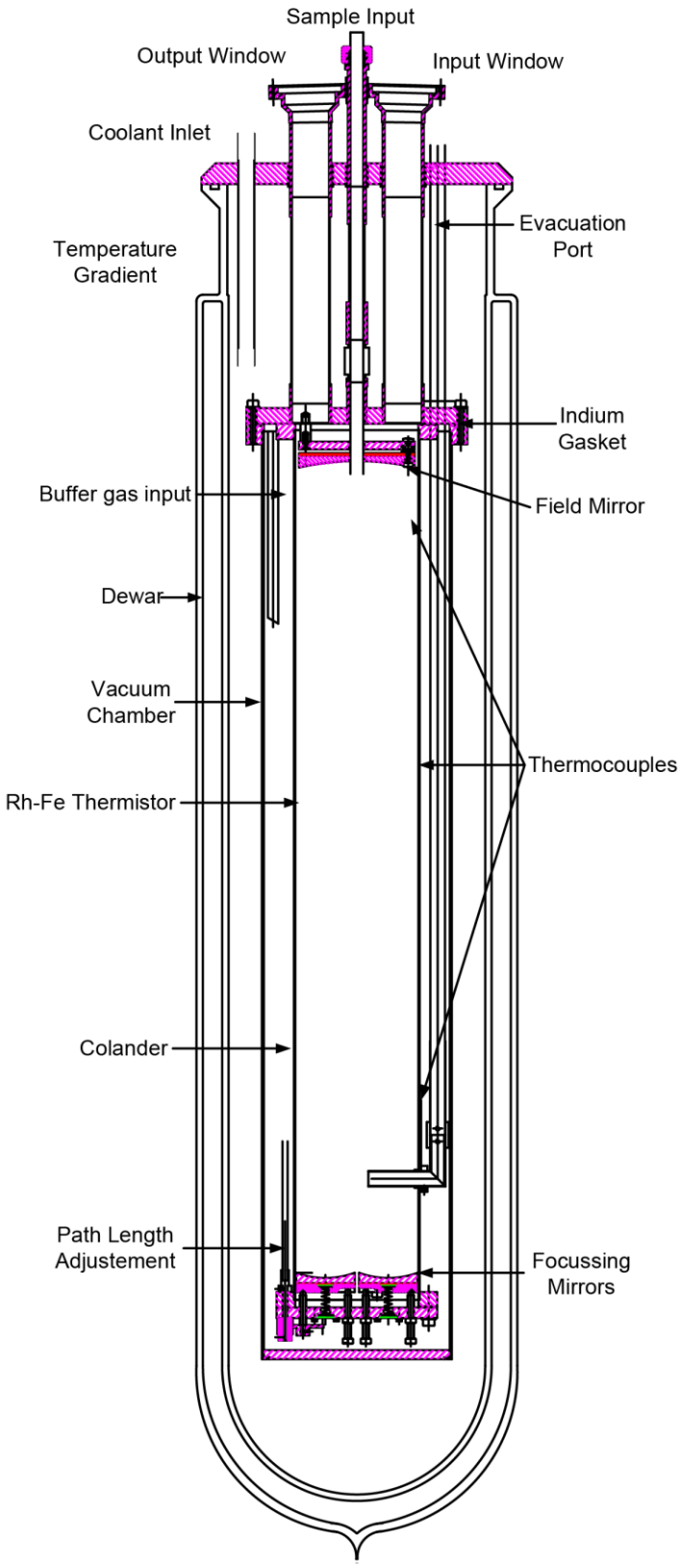

Figure 1.10: Schematic of the EFC cell at the Australian Synchrotron THz/far-IR beamline adapted from [16].

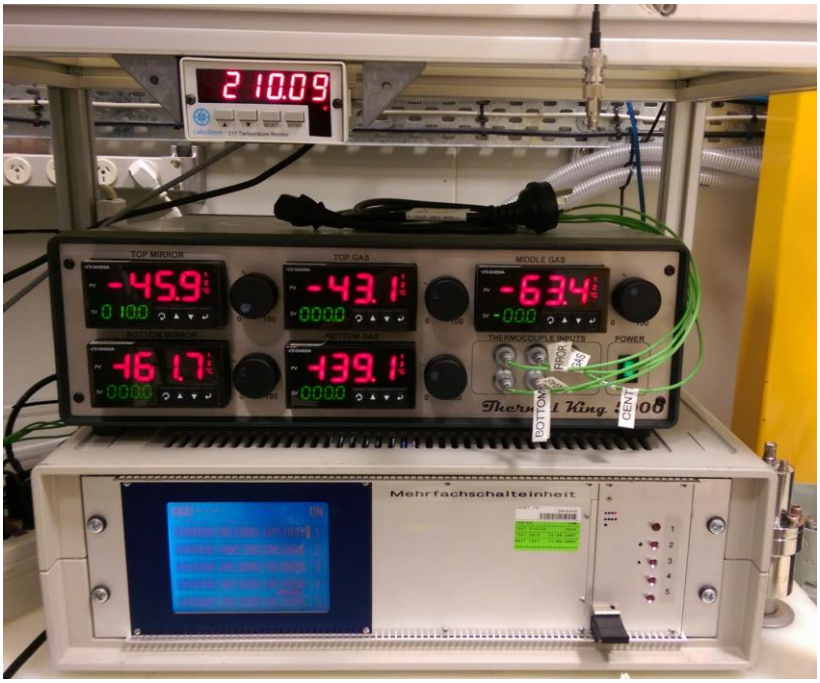

Figure 1.11: Picture of the temperature controller box (black) showing temperatures for the EFC cell under non-equilibrium conditions. The display above the temperature controller box is for the iron-rhodium thermistor and the white box on the bottom is the controller for the pulsing solenoid gate valves.

Cooling of molecules is important for gas phase spectroscopy and provides two major benefits to help simplify the analysis of ro-vibrational spectra. First, the population of molecules occupying high energy ro-vibrational states is reduced with colder temperatures. This decreases spectral congestion and is governed by the Boltzmann distribution (introduced in **Chapter 1.1.2.1**). The intensity of ro-vibrational lines with high rotational quantum number (refer to **Chapter 2.1.3**), as well as those from low energy hot bands, will decrease whereas the intensity of ro-vibrational lines with low quantum number will increase.

Second, the width of a ro-vibrational line will decrease with temperature as the translational temperature is reduced. Referred to as the Doppler width of a line, this value can be calculated using **equation 1.14** [17, 18] and is dependent on the molecular mass of a molecule, temperature, concentration and wavenumber value of the ro-vibrational line,

$$\Delta f_{FWHM} = \frac{\tilde{\nu}}{c}\sqrt{\frac{8NkT\ln 2}{M}} \qquad \textbf{(1.14)}$$

where $\tilde{\nu}$ is the frequency (cm^{-1}) and c is the speed of light ($cm\ s^{-1}$). T is the temperature (Kelvin) and M is the molecular mass of the molecule ($g\ mol^{-1}$).

This ensures that the maximum resolution of the instrument can be utilised which will yield the most accurate results when reporting line positions in high resolution spectra. In the case of polyatomic molecules where M > 30 g mol^{-1} the Doppler width of ro-vibrational lines in the far-IR region will be smaller than the resolution (0.00096 cm^{-1}) of the instrument at 298 K.

The cell has been used in a cold static mode for several gas phase studies for molecules such as C_2F_4 [19] and 1,1,1,2-tetrafluroethane [20], and the theory associated with the analysis of high resolution gas phase spectra is given in **Chapter 2**. We have also demonstrated the application of the EFC cell to condensed phase low resolution spectroscopy [21, 22]. The work described in **Chapter 3** utilises the EFC cell to generate molecular ices in cold environments which are analogous to those found in interstellar media. Being able to accurately characterize the physical and chemical properties of such ices under controlled conditions is a necessary step toward understanding data that is observed from natural systems.

1.2.5.2 Pyrolysis Cell

The pyrolysis cell (M24V) is a room temperature White-cell which is capable of achieving path lengths of up to 24 m (1.6 m base pathlength) which can be heated to warm temperatures. The cell is primarily used in a flow through mode for flash pyrolysis experiments (**figure 1.12**) to generate transient species from a precursor molecule. This is made possible by having entry and exit ports installed onto the side of the cell.

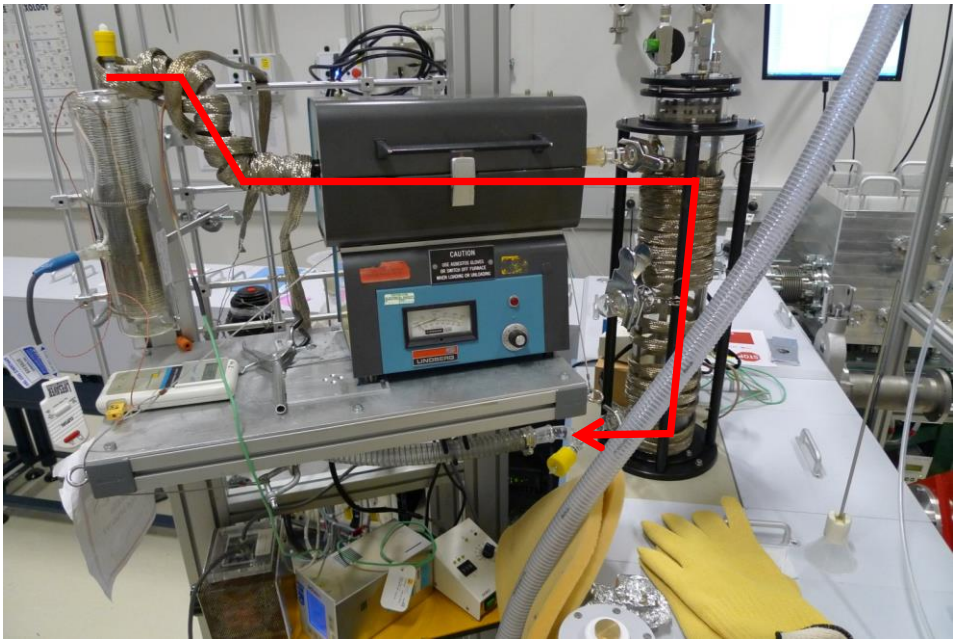

Figure 1.12: A typical instrumental setup of a pyrolysis experiment adapted from [23]. The red arrow indicates the direction of flow starting from the precursor molecule, through the furnace, and then to the exhaust port on the multipass cell.

The temperature of the furnace often affects the dynamics of a pyrolysis reaction and needs to be adjusted in order to generate as much of a transient species as possible. Variation of the furnace temperature also makes it possible to investigate the dynamics of the reaction and hence deduce different thermal breakdown pathways for the observed products.

1.3 Computational Chemistry

Although not extensively used throughout this project, computational chemistry often provides useful information about molecular systems that may otherwise be difficult to understand. In the context of this thesis, density functional theory (DFT) methods were used to aid the analysis of high resolution gas phase spectra. Calculations were performed on the Monash Sun Grid cluster using Gaussian09 (Revision D.01) [24] with the "anharm" and "vibrot" keywords in order to calculate anharmonic band centre values, rotational and centrifugal distortion constants, Coriolis and Fermi coupling constants using the three different DFT methods described below.

The Becke 3-parameter Lee-Yang-Parr (B3LYP) [25, 26] is a hybrid method involving a linear combination of Becke's exchange energy functional with the Lee-Yang-Parr (LYP) correlation energy functional. These are hybrid functionals as they are based on the exact Hartree-Fock (HF) [27, 28] functional which describes the electron density distributions within molecules.

Møller-Plesset perturbation theory (MP) [29] is a slightly more advanced DFT method in comparison to B3LYP. This method also calculates the effect of electron correlation, however it uses a different approach by employing Rayleigh-Schrödinger perturbation theory. Second order MP theory (MP2) is used because of its accuracy and relatively cheap computational cost.

Coupled cluster single and double substitutions (CCSD) [30] utilises the molecular orbitals generated from HF theory in order to calculate multi-electron wavefunctions by re-expressing the Schrödinger equation using the exponential cluster operation.

Along with each method used, basis sets must be chosen to calculate the molecular orbital space for each atom. The basis sets used here follow either the Pople type [31] (e.g. 6-31G) which uses two (*s* and *p*) functionals to calculate each atomic valence orbital, or Dunning correlation consistent type [32] (e.g. cc-pVTZ) which includes the contracted Gaussian functionals (pnTZ) derived by Ahlrichs *et al*. [33].

References

[1] *Vibrational Spectroscopy in Life Science: Chapter 2*, Friedrich Siebert and Peter Hildebrandt Copyright © 2008 WILEY-VCH Verlag GmbH & Co. KGaA, Weinheim.

[2] A. A. Michelson and E. W. Mobley, *Am. J. Sci.*, **XXXIV**, 333 (1887).

[3] P. Fellgett, *J. Phys.-Paris*, **19**, 237 (1958).

[4] P. Jacquinot, *J. Opt. Soc. Am.*, **44**, 761 (1954).

[5] W. Herres and J. Gronholz, *Comput. Appl. Lab.*, **2**, 216 (1984).

[6] J. W. Cooley and J. W. Tukey, *Math. Comput.*, **19**, 297 (1965).

[7] J. Kauppinen, T. Kärkkäinen and E. Kyrö, *Appl. Opt.*, **17**, 1587 (1978).

[8] G. K. Wertheim, M. A. Butler, K. W. West and D. N. E. Buchanan, *Rev. Sci. Instrum.*, **45**, 1369 (1974).

[9] G. P. Williams in *Handbook of Vibrational Spectroscopy*, Volume 1, John Wiley & Sons (2006).

[10] L. Palchetti, Contribution to the CLARREO Science Definition Team Meeting, (2011).

[11] M. G. Mlynczak, R. P. Cageao, H .Latvakoski, D. Kratz, D. Johnson, J. Mast, Earth-Zine, (2013).

[12] R. C. Jones, *J. Opt. Soc. Am.*, **50**, 1058 (1960).

[13] P. W. Anderson, *Phys. Rev.*, **76**, 647 (1949).

[14] J. U. White, *J. Opt. Soc. Am.*, **32**, 285 (1942).

[15] S. Bauerecker, M. Taraschewski, C. Weitkamp, H. K. Cammenga, *Rev. Sci. Instrum.*, **72**, 3946 (2001).

[16] C. Medcraft, *Infrared Spectroscopy of Cold Molecules*, PhD Thesis, Monash University (2012).

[17] J. M. Hollas, *High Resolution Spectroscopy*, 2nd ed., Chichester, John Wiley & Sons (1998).

[18] D. McNaughton, in *Handbook of Vibrational Spectroscopy*, Vol. 1, John Wiley & Sons (2002)

[19] C. Medcraft, W. Fuss, D. R. T. Appadoo, D. McNaughton, C. D. Thompson and E. G. Robertson, *J. Chem. Phys.*, **137**, 1 (2012).

[20] A. Wong, C. Medcraft, C. D. Thompson, E. G. Robertson, D. Appadoo and D. McNaughton, *Chem. Phys. Lett.*, **634**, 225 (2015).

[21] C. Medcraft, D. McNaughton, C. D. Thompson, D. Appadoo, S. Bauerecker and E. G. Robertson, *ApJ*, **758**, 1 (2012).

[22] C. Medcraft, D. McNaughton, C. D. Thompson, D. R. T. Appadoo, S. Bauerecker and E. G. Robertson, *Phys. Chem. Chem. Phys.*, **15**, 3630 (2015).

[23] M. K. Bane, *Far-infrared ro-vibrational spectroscopy of Coriolis coupled molecules of interstellar importance*, PhD Thesis, Monash University, Monash University, (2012).

[24] Gaussian 09, Revision D.01, M. J. Frisch, G. W. Trucks, H. B. Schlegel, G. E. Scuseria, M. A. Robb, J. R. Cheeseman, G. Scalmani, V. Barone, B. Mennucci, G. A. Petersson, H. Nakatsuji, M. Caricato, X. Li, H. P. Hratchian, A. F. Izmaylov, J. Bloino, G. Zheng, J. L. Sonnenberg, M. Hada, M. Ehara, K. Toyota, R. Fukuda, J. Hasegawa, M. Ishida, T. Nakajima, Y. Honda, O. Kitao, H. Nakai, T. Vreven, J. A. Montgomery, Jr., J. E. Peralta, F. Ogliaro, M. Bearpark, J. J. Heyd, E. Brothers, K. N. Kudin, V. N. Staroverov, T. Keith, R. Kobayashi, J. Normand, K. Raghavachari, A. Rendell, J. C. Burant, S. S. Iyengar, J. Tomasi, M. Cossi, N. Rega, J. M. Millam, M. Klene, J. E. Knox, J. B. Cross, V. Bakken, C. Adamo, J. Jaramillo, R. Gomperts, R. E. Stratmann, O Yazyev, A. J. Austin, R. Cammi, C. Pomelli, J. W. Ochterski, R. L. Martin, K. Morokuma, V. G. Zakrzewski, G. A. Voth, P. Salvador, J. J. Dannenberg, S. Dapprich, A. D. Daniels, O Farkas, J. B. Foresman, J. V. Ortiz, J. Cioslowski and D. J. Fox, Gaussian, Inc., Wallingford CT, 2013.

[25] A. D. Becke, *J. Chem. Phys.*, **88**, 1053 (1988)

[26] C. Lee, W. Yang and R. G. Parr, *Phys. Rev. B*, **37**, 785 (1988)

[27] V. Fock, *Z. Physik*, **61**, 126 (1951).

[28] D. R. Hartree and W. Hartree, *P. Roy. Soc. Lond. A Mat.*, **150**, 9 (1935).

[29] C. Møller and M. S. Plesset, *Phys. Rev.*, **46**, 618 (1934).

[30] G. D. Purvis III and R. J. Bartlett, *J. Chem. Phys.*, **76**, 1910 (1982).

[31] R. Krishnan, J. S. Rinkley, R. Seeger and J. A. Pople, *J. Chem. Phys.*, **72**, 650 (1980).

[32] T. H. Dunning Jr., *J. Chem. Phys.*, **90**, 1007 (1989).

[33] A. Schäfer, H. Horn and R. Alrichs, *J. Chem. Phys.*, **97**, 2571 (1992).

Chapter 2.0

High Resolution Gas Phase Spectroscopy

2.1 Theory

It is useful that the total wave function for a molecule (Ψ_{total}) can be factorised into its electronic, *e*, and nuclear, *n*, wave functions (**equation 2.1**) according to the Born-Oppenheimer approximation [1].

$$\Psi_{total} = \Psi_e \Psi_n \qquad \textbf{(2.1)}$$

For molecular spectroscopy we assume a further approximation that the nuclear part is separable into vibrational and rotational wave functions (**equation 2.2**) which can be treated independently such that they satisfy Schrödinger's equation [2],

$$H_x \Psi_x = E_x \Psi_x \qquad \textbf{(2.2)}$$

where H_x is the Hamiltonian which operates on Ψ_x to give $E_x\Psi_x$. *x* represents the electronic, vibrational and rotational wave functions.

Given that the scope of the research detailed throughout this thesis does not include electronic excitations, it is therefore only necessary to consider effects from the vibrational and rotational wave functions. Contributions from the vibrational wave function have already been covered in **Chapter 1** thus only the rotational wave function is considered here.

2.1.1 Rotational Hamiltonian

In its simplest form, the rotational Hamiltonian for a linear molecule can be described using the term **equation 2.3**, where the moments of inertia are such that $I_c = I_b > I_a = 0$ and only *J* (total angular momentum) and *B* (rotational constant) are required to accurately calculate the energies of rotational levels,

$$E_J = BJ(J+1) - DJ^2(J+1)^2 + HJ^3(J+1)^3 \ldots \qquad \textbf{(2.3)}$$

where *D* and *H* are the quartic and sextic centrifugal distortion terms respectively.

For a symmetric molecule, an additional quantum number *K* is required in order to account for the projection (or vector component) of *J* about the symmetry axis, where $K \leq J$. The *A* rotational constant is also introduced due to inequalities in the moments of inertia ($I_c = I_b > I_a$ for a prolate symmetric top, or $I_c > I_b = I_a$ for an oblate symmetric top) and **equation 2.3** is now expressed as:

$$E_{J,K} = BJ(J+1) + (A-B)K^2 - D_J[J(J+1)]^2 - D_{JK}[J(J+1)]K^2 - D_K K^4 + H_{JJJ}[J(J+1)]^3 + H_{JJK}[J(J+1)]K^2 + H_{JKK}[J(J+1)]K^4 + H_{KKK}K^6 \ldots \qquad \textbf{(2.4)}$$

In the case of an asymmetric molecule, where $I_c \neq I_b \neq I_a$, the quantum number K is no longer a "good" label and therefore K_a and K_c are introduced in order to better approximate K. Given the complexity of the Hamiltonian, it is not practical to calculate the energies of rotational energies using term equations such as those in **equations 2.3** and **2.4**. Instead, the matrix representation of the Hamiltonian is solved. It is possible to reduce the number of terms that are used in the Hamiltonian by taking into account their symmetries such as those derived by Watson [3]. Two common forms of the vibration-rotation Hamiltonian are the *S*-reduced (symmetrically) and *A*-reduced (asymmetrically) Hamiltonians. The former is given below as an example (**equation 2.5**),

$$\widehat{\boldsymbol{H}} = \frac{1}{2}(B_x + B_y)\hat{J}^2 + \left[B_z - \frac{1}{2}(B_x + B_y)\right]\hat{J}_z^2 + \frac{1}{4}(B_x - B_y)(\hat{J}_+^2 + \hat{J}_-^2) - D_J\hat{J}^4 - D_{JK}\hat{J}^2\hat{J}_z^2 - D_k\hat{J}_z^4 + d_1\hat{J}^2(\hat{J}_+^2 + \hat{J}_-^2) + d_2(\hat{J}_+^4 + \hat{J}_-^4) + H_{JJJ}\hat{J}^6 + H_{JJK}\hat{J}^4\hat{J}_z^2 + H_{JKK}\hat{J}^2\hat{J}_z^4 + H_{KKK}\hat{J}^6 + h_1\hat{J}^4(\hat{J}_+^2 + \hat{J}_-^2) + h_2\hat{J}^2(\hat{J}_+^4 + \hat{J}_-^4) + h_3(\hat{J}_+^6 + \hat{J}_-^6) - L_{JJJJ}\hat{J}^8 - L_{JJJK}\hat{J}^6\hat{J}_z^2 - L_{JJKK}\hat{J}^4\hat{J}_z^4 - L_{JKKK}\hat{J}^2\hat{J}_z^6 - L_K\hat{J}_z^8 + l_1\hat{J}^6(\hat{J}_+^2 + \hat{J}_-^2) + l_2\hat{J}^4(\hat{J}_+^4 + \hat{J}_-^4) + l_3\hat{J}^6(\hat{J}_+^6 + \hat{J}_-^6) + l_4(\hat{J}_+^8 + \hat{J}_-^8) \ldots \quad \textbf{(2.5)}$$

where $\hat{J}$ is the total angular momentum vector and $\hat{J}_x$, $\hat{J}_y$, $\hat{J}_z$ are the angular momentum vectors along the *x*, *y*, *z* molecular axes. $\hat{J}^2$ and $\hat{J}_\pm^2$ are defined as:

$$\hat{J}^2 = \hat{J}_x^2 + \hat{J}_y^2 + \hat{J}_z^2 \qquad \textbf{(2.6)}$$

$$\hat{J}_\pm^2 = \hat{J}_x \pm i\hat{J}_y \qquad \textbf{(2.7)}$$

Similar to symmetric molecules, asymmetric molecules can also be classed as either near prolate or near oblate where $I_c \cong I_b > I_a$ or $I_c > I_b \cong I_a$ respectively. The extent of asymmetry is calculated via Ray's asymmetry parameter [4],

$$\kappa = \frac{2B - A - C}{A - C} \qquad \textbf{(2.8)}$$

where κ approaches -1 or 1 for the limiting prolate and oblate symmetric tops respectively.

From here, it is possible to calculate the rotational constants of a molecule using the inverse relationship between the moments of inertia and rotational constants using **equation 2.9**,

$$A = \frac{h}{8\pi^2 I_a}; B = \frac{h}{8\pi^2 I_b}; C = \frac{h}{8\pi^2 I_b} \qquad \textbf{(2.9)}$$

where h is Planck's constant (m^2 kg s^{-1}). I_a, I_b and I_c are the moments of inertia about the *a*, *b* and *c* molecular axes respectively.

By convention, the moments of inertia are labelled such that $I_c > I_b > I_a$ (**equation 2.10**). A more rigorous treatment and derivation can be found within textbooks by Hollas [5] and Gordy & Cook [6].

$$I_x = \sum_i m_i\left(y_i^2 + z_i^2\right);\ I_y = \sum_i m_i\left(x_i^2 + z_i^2\right);\ I_z = \sum_i m_i\left(x_i^2 + y_i^2\right) \qquad \textbf{(2.10)}$$

where m_i is the mass of the molecule.

As there are three moments of inertia about the molecular axes, there must also be three components of the angular momentum *J* which are projected onto the *a*, *b* and *c* molecular axes (i.e. J_a, J_b and J_c). Permutation of (J_a, J_b, J_c) leads to 3! possibilities in which (J_a, J_b, J_c) can be identified with (J_x, J_y, J_z), giving the six representations in **table 2.2**, where *r* and *l* refer to right- and left-handed representations of the Hamiltonian [7].

Table 2.2: Designation of the molecular axes with respect to the Cartesian axes

	Representation					
	***I*^{r}**	***II*^{r}**	***III*^{r}**	***I*^{l}**	***II*^{l}**	***III*^{l}**
x	*b*	*c*	*a*	*c*	*a*	*b*
y	*c*	*a*	*b*	*b*	*c*	*a*
z	*a*	*b*	*c*	*a*	*b*	*c*

2.1.2 Molecular symmetry

As discussed in **Chapter 1.1.1**, a molecule in the gas phase will have either 3*N* - 6 or 3*N* - 5 fundamental vibrations depending on its molecular structure. Further to this point, the number of vibrations (fundamentals, overtones and combinations) that will be IR active is dependent on the irreducible representation (symmetry) of the vibration, which is in turn determined by the point group of the molecule. The point group of a molecule describes all of the possible symmetry elements that are found within a molecule through a point of reference. For a vibration to be IR active, the irreducible representation must have either *x*, *y* and/or *z* linear translations in the point group table. The point group table for a molecule with C_s symmetry is given below as an example.

Table 2.1: Point group table for a molecule with C_s symmetry

C_s	E	σ_h	linear, rotations	quadratic
A′	1	1	*x*, *y*, R_z	x^2, y^2, z^2, *xy*
A″	1	-1	*z*, R_x, R_y	*yz*, *xz*

A similar rule is applied for vibrations where the vibrational quantum number is greater than 1 (overtone levels) or consists of multiple different vibrations (combination levels). The symmetry of these types of bands is determined simply by the cross-product of the irreducible representations for each vibrational state. For example, the ν_8 band of 1,1,1,2-tetrafluoroethane has an *A*″ symmetry; therefore the symmetry of $\nu_8 = 4$ would be *A*′ (i.e. *A*″ × *A*″ × *A*″ × *A*″).

2.1.3 Selection rules

The band type of a ro-vibrational transition is governed by the direction of the change in dipole as a molecule vibrates. For a change in dipole along the *a*- molecular axis, an *a*-type ro-vibrational band will be observed. Similarly, changes in the dipole along the *b*- or *c*- molecular axes will yield *b*- or *c*-type bands respectively (**figure 2.1**). It is also possible to observe hybrid bands where the dipole changes along multiple axes (e.g. the *a*- and *b*-axes) which gives rise to an *a*/*b*-hybrid band. In general, *a*- and *c*-type ro-vibrational bands will look similar at low resolution and are difficult to differentiate, whereas *b*-type bands typically lack the characteristic central sharp *Q*-branch structure.

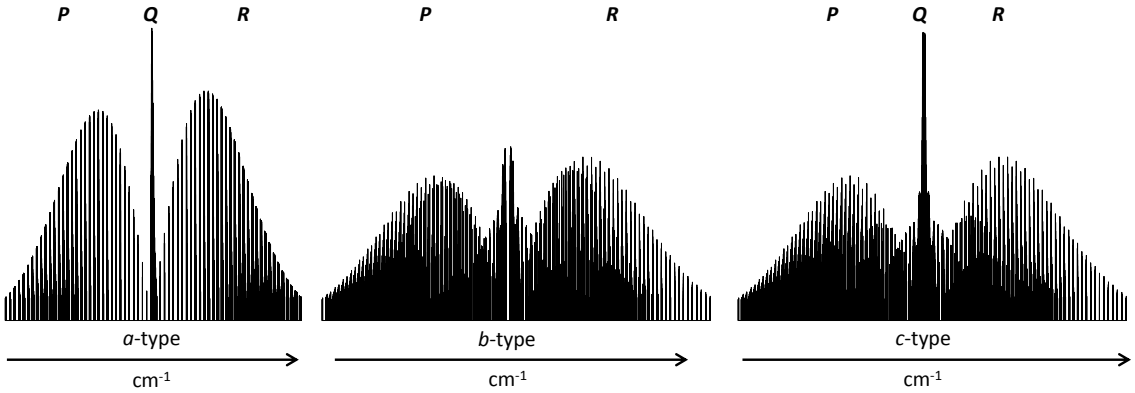

Figure 2.1: Simulated *a*-, *b*- and *c*-type bands at 40 K for 1,1,1,2-tetrafluoroethane.

For each band type, ro-vibrational transitions must obey selection rules in order to be infrared allowed. In the case of *P*-, *Q*- and *R*-branch transitions, ΔJ is often -1, 0 or +1 respectively, for a transition being excited from v'' to v' (**figure 2.2**) where ΔJ is the difference in the J value for a transition between the two states. v'' and v' represent the lower (often ground state) and upper states respectively.

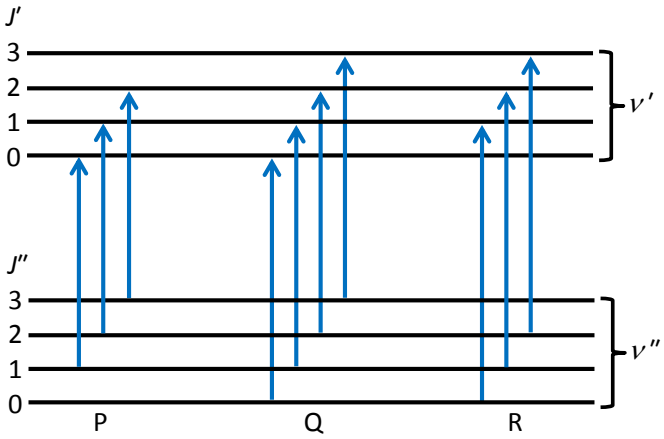

Figure 2.2: Examples of *P*, *Q* and *R* ro-vibrational transitions.

It is also possible to observe ro-vibrational transitions with $\Delta J \pm 2$, however these transitions are often much weaker in intensity. Since the quantum numbers K_a and K_c are introduced for an asymmetric top molecule, the selection rules will differ slightly for either: *a*-, *b*- or *c*-type ro-vibrational transitions and are summarised in **table 2.3**. Furthermore, it is possible to observe asymmetry splitting which causes a degenerate rotational level in the excited state to become non-degenerate, giving two rotational levels which follow either $K_a' + K_c' - J' = 0$ or $K_a' + K_c' - J' = 1$.

Table 2.3: Selection rules for *a*-, *b*- and *c*-type ro-vibrational transitions.

transition type	ΔK_a	ΔK_c
a	0, ±2, ±4 …	±1, ±3, ±5 …
b	±1, ±3, ±5 …	±1, ±3, ±5 …
c	±1, ±3, ±5 …	0, ±2, ±4 …

2.1.4 Transition assignment

In order to make sense of the observed ro-vibrational lines, two different techniques are used to aid transition assignment. The first is an interactive program called MacLoomis which was written by the Monash spectroscopy group [8]. The program utilises a Loomis-Wood plot [9] which slices the spectrum into strips with widths of *ca.* $\frac{(B+C)}{2}$ before stacking them vertically onto each other (**figure 2.3**).

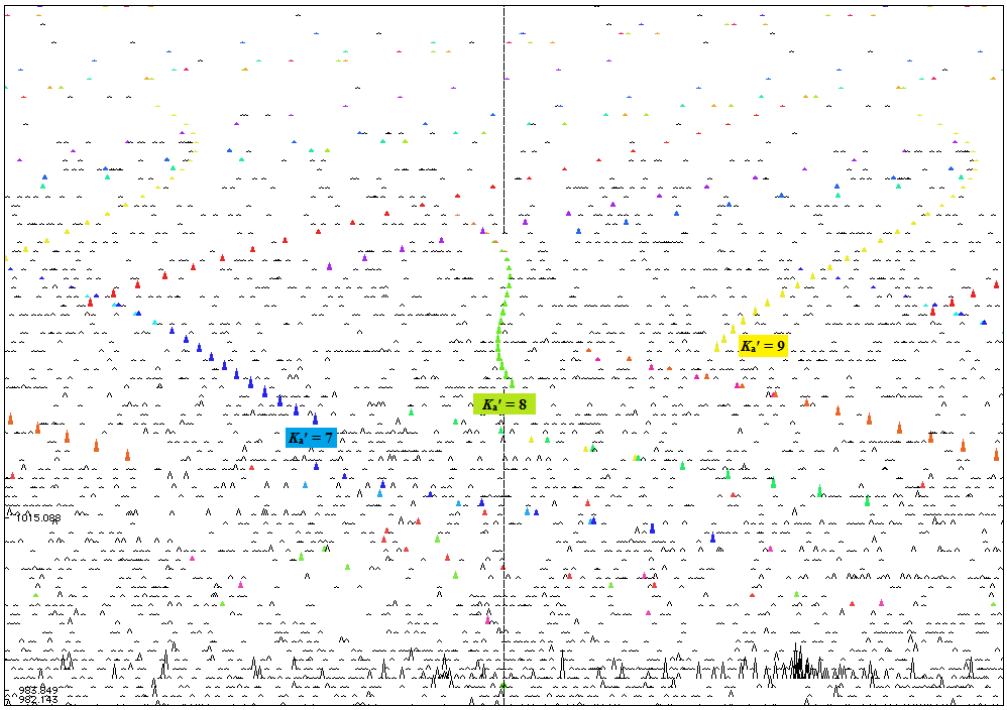

Figure 2.3: A Loomis-Wood plot of the *R*-branch of the ν_4 band of *trans*-d_2-ethylene. The $K_a' = 8$ series is displayed as the green triangles in MacLoomis where the *x*-axis is in cm^{-1} and the *y*-axis is *J'*.

Ro-vibrational transitions with the same K_a' are grouped together and are aligned down the centre of the screen with increasing J' when fitted to a polynomial expansion of the type shown in **equation 2.3**. Although the program was originally written for linear molecules, it still works well for symmetric and asymmetric molecules [10 - 14] and provides a more convenient means of viewing a high resolution spectrum in comparison to traditional methods as shown in **figure 2.4**.

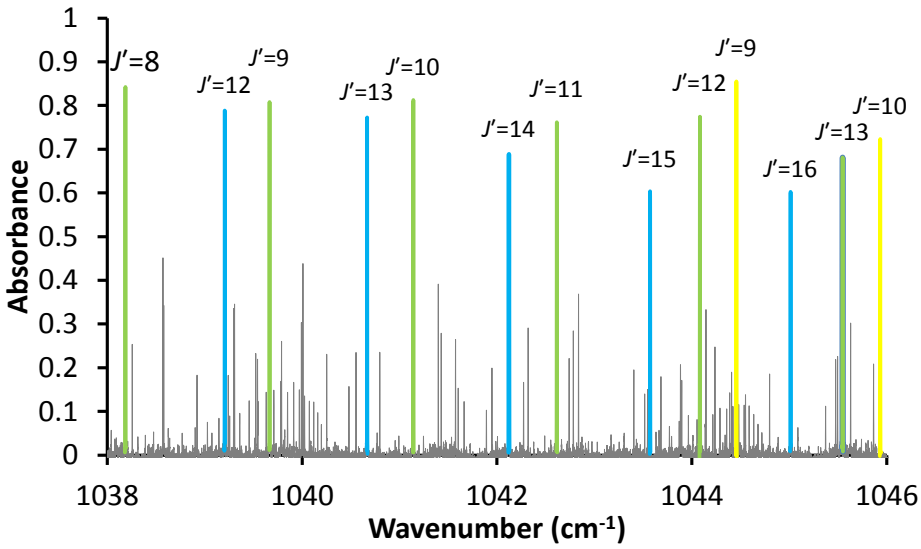

Figure 2.4: Inset of the ν_4 band of *trans*-d_2-ethylene with transitions from K_a' = 7 (blue), K_a' = 8 (green) and K_a' = 9 (yellow).

Confirmations of transition assignment are then required and this is done via calculation of experimental ground state combination differences (GSCDs) and comparing these with values calculated from known ground state constants often determined from microwave or millimetre-wave studies. GSCDs can be calculated using analytical programs such as SPFIT by Pickett [15] which is used throughout the analyses described in **Chapters 2.2.1 - 2.2.4**. For molecules which either a) do not have a permanent dipole or b) have not been studied before, ground state rotational and centrifugal distortion constants from *ab initio* or density functional theory (DFT) calculations can be used as an initial approximation.

As shown in **figure 2.2**, two different transitions (e.g. *P*- and *R*-branch) that are excited to the same rotational level in the upper state will originate from different rotational levels in the ground state. The energy difference between these two ro-vibrational states therefore form the experimental GSCD (**figure 2.5**). Transitions recorded at high resolution which are assigned correctly will typically have an error (observed – calculated) of < 0.0005 cm^{-1}.

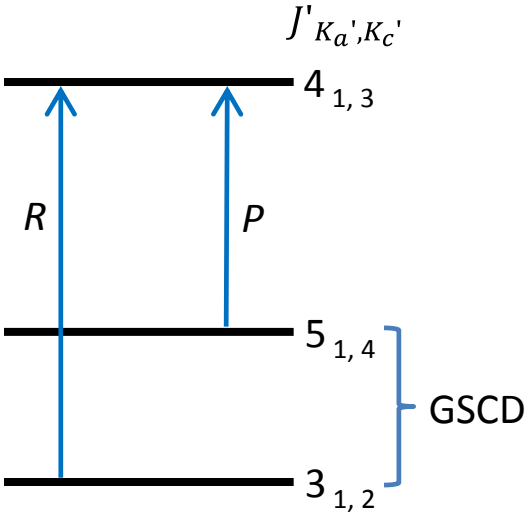

Figure 2.5: Example of a GSCD using selection rules for an *a*-type transition, where $\Delta K_a'' = 0$, $\Delta J'' = 2$ and $\Delta K_c'' = 2$.

2.1.5 SPFIT and SPCAT

The SPFIT and SPCAT program suite was written by Pickett [15] and are the predominant programs used when fitting and simulating high resolution FTIR spectra.

The first of the two programs, SPFIT, utilises a line list file (.lin) and a parameter file (.par) to fit rotational and centrifugal distortion constants to the assigned ro-vibrational transitions. The program diagonalizes the Hamiltonian (**equation 2.5**) for each fitted vibrational state in order to determine the rotational and centrifugal distortion constants (ground state included if fitted). Although **equation 2.5** represents only the *S*-reduced Hamiltonian [3], it is also possible use the *A*-reduced Hamiltonian as well as any of the six representations given in **table 2.2**. The number of states fitted (and their parameters) can be selected using parameter identifiers in the .par file, as shown below in **table 2.4**.

SPFIT then uses the fitted constants to predict the theoretical wavenumber values for the assigned transitions and compares these values to their experimental values in the .fit output file. A residual error (observed – calculated) is determined and is used as a measure of the goodness of the fit. SPFIT repeats the diagonalization process using a non-linear regression until the residuals are minimised to their smallest values.

Table 2.4: An excerpt of the parameters used in the .par file for *trans*-$C_2H_2D_2$.

Identifier	Constant	Value (MHz)	Uncertainty**
10000	*A*	1.0451337E+05	1.00E-19
20000	*B*	2.4971466E+04	1.00E-19
30000	*C*	2.0105276E+04	1.00E-19
11	v_1*	2.9612003E+07	1.00E+21
10011	*A*	1.0431698E+05	1.00E+21
20011	*B*	2.4945461E+04	1.00E+21
30011	*C*	2.0117815E+04	1.00E+21

* v_1 is the band origin for the first excited state.

** A "-" or "+" sign denotes whether the value for a parameter is either fixed or fitted, respectively..

SPCAT is the second part of the Pickett [15] software suite which uses the fitted rotational and centrifugal distortion constants in order to predict the rotational energy levels in each vibrational state as well as the wavenumber values for each transition. The program can also calculate the intensity of a transition using the dipole moment of a molecule and the q^{rot} partition function (**equation 2.11**) in the .int file.

$$q^{rot} = \frac{\pi^{1/2}}{\sigma}\left(\frac{8\pi^2 I_A kT}{h^2}\right)^{1/2}\left(\frac{8\pi^2 I_B kT}{h^2}\right)^{1/2}\left(\frac{8\pi^2 I_C kT}{h^2}\right)^{1/2} \qquad (\mathbf{2.11})$$

where σ is a symmetry factor, k is the Boltzmann constant (1.38×10^{23} J K^{-1}), I_X is the moment of inertia about the *a*, *b* and *c* molecular axes, h is Planck's constant (m^2 kg s^{-1}) and T is the temperature (Kelvin).

2.1.6 Intramolecular coupling

Coupling between two vibrational states occurs when the vibrational and rotational wave functions cannot be treated independently. This is due to molecules not being rigid rotors and experiencing centrifugal distortion when rotating and the motion of one vibration influences a second (or more) vibrations through Coriolis and/or Fermi resonances. Ro-vibrational transitions (hence rotational levels) within each of the interacting states can become perturbed, leading to differences between their observed values and expected values.

These couplings generally manifest in the forms of either Coriolis coupling or Fermi resonance and have their own unique selection rules as summarised by the Wang sub-blocks in **table 2.5**. Here, E and O represents an even or odd value for the *K* level, and + ($K_a' + K_c' - J' = 0$) or - ($K_a' + K_c' - J' = 1$) denote the parity.

Table 2.5: Interacting Wang sub-blocks for the Coriolis and Fermi resonances

Interaction	Linked sub-blocks	
a-axis Coriolis	$E^+ \leftrightarrow E^-$	$O^+ \leftrightarrow O^-$
b-axis Coriolis	$E^+ \leftrightarrow O^-$	$E^- \leftrightarrow O^+$
c-axis Coriolis	$E^+ \leftrightarrow O^+$	$E^- \leftrightarrow O^-$
Fermi resonance	$E^+ \leftrightarrow E^+$	$E^- \leftrightarrow E^-$
	$O^+ \leftrightarrow O^+$	$O^- \leftrightarrow O^-$

For two vibrational bands to be Coriolis coupled, the cross-product of the irreducible representations for the two interacting states must contain a rotational component in the point group table (i.e. R_x, R_y and/or R_z). Tanaka & Morino [16] have derived the matrix elements for the coupling terms, which are given below (**equations 2.12** and **2.13**) for reference.

$$1^{st}\ order: \langle v_s, v_{s'} | \hat{\boldsymbol{H}} | v_s + 1, v_{s'} - 1 \rangle = i\zeta^a_{vv'}\hat{J}_\alpha \qquad \textbf{(2.12)}$$

$$2^{nd}\ order: \langle v_s, v_{s'} | \hat{\boldsymbol{H}} | v_s + 1, v_{s'} - 1 \rangle = \eta^{\beta\gamma}_{vv'}\{\hat{J}_\beta, \hat{J}_\gamma\}_+ \qquad \textbf{(2.13)}$$

where ζ and η are the Coriolis coupling constants linking two states v_s and $v_{s'}$.

The latter Fermi resonance, **equations 2.14** and **2.15**, only occurs between two vibrational states if they have the same irreducible representation, causing the band origins of the lower energy and higher energy interacting states to be red- and blue-shifted, respectively. Furthermore, if one of the vibrational states has zero intrinsic intensity, then Fermi resonance will not be observed.

$$1^{st}\ order: \langle v; J, K | \hat{\boldsymbol{H}} | v'; J, K \rangle = F_{vv'} + F^J_{vv'}J(J+1) + F^K_{vv'}K^2 \qquad \textbf{(2.14)}$$

$$2^{nd}\ order: \langle v; J, K | \hat{\boldsymbol{H}} | v'; J, K \pm 2 \rangle = \pm F^\alpha_{vv'}F_\pm(J, K)F_\pm(J, K \pm 1) \qquad \textbf{(2.15)}$$

Both Coriolis and Fermi resonances can be fitted within SPFIT [15] by introducing new parameter identifiers into the .par file which correspond to either a Coriolis or Fermi resonance. For example, a first order *a*-axis Coriolis interaction between v_1 and v_2 can be designated by the identifier 200012 in the .par file. The fitted value of the Coriolis term ($G^a_{v_1,v_2}$) is related to the *z* Coriolis coupling constant via **equation 2.16**,

$$G^a_{v_1,v_2} = 2\,\Omega\,\zeta^{1,2} \qquad \textbf{(2.16)}$$

where $\Omega \approx \sqrt{2}$ and ζ is the *a*-axis Coriolis coupling constant connecting states v_1 and v_2.

2.2 Projects on high resolution spectroscopy

The following sections details the experimental and analytical work on various gaseous molecules using high resolution FTIR spectroscopy. A major theme of the molecules studied here are that they are pertinent to both atmospheric and interstellar chemistry. **Chapters 2.2.2** and **2.2.3** are published papers, however they have been inserted as word documents to maintain consistency with the formatting used throughout the thesis. Supplementary data for **Chapters 2.2.2 – 2.2.3** can be accessed via the online version of the papers, whereas data for **Chapters 2.2.1** and **2.2.4** can be provided upon request.

Chapter 2.2.1 covers the experimental and analytical details for the transient species propynethial (C_3H_2S).

Chapter 2.2.2 is a publication on the ν_{18} and ν_{17} far-IR bands of 1,1-difluoroethane.

Chapter 2.2.3 is a publication on the ν_8 far-IR band of 1,1,1,2-tetrafluoroethane.

Chapter 2.2.4 is a submitted paper on the far-IR (ν_{10}) and mid-IR (ν_7, ν_4 and ν_{12}) bands of *trans*-d_2-ethylene.

2.2.1 Propynethial

Propynethial is a molecule that is predicted to exist in interstellar media and is a transient species when generated via flash pyrolysis of dipropargyl sulfide under laboratory conditions. To date, only a few spectroscopic studies have been performed on propynethial using microwave spectroscopy [17], matrix isolation [18] and photoelectron spectroscopy [19]. The limited amount of available data makes it difficult to accurately assign rotational transitions from propynethial if it is indeed found in interstellar media. This experiment was performed in order to help rectify this problem by improving the ground state rotational and centrifugal distortion constants by analysing spectra recorded using coherent synchrotron radiation (CSR) and millimetre-wave spectroscopy, as well as to provide the first high resolution FTIR study on the ν_5 band of propynethial.

Propynethial (**figure 2.6**) is a planar molecule with C_s symmetry and 12 fundamental vibrations which have either *a*/*b*-hybrid or *c*-type ro-vibrational band structure. The ν_5 band (**figure 2.7**) is located near 1100 cm^{-1} and is predicted to be the most intense band (70.47 km mol^{-1}) based on B3LYP/cc-pVTZ calculations which were performed by our group using Gaussian09 (Revision D.01) [20] on the Monash Sun Grid cluster. The intensities of these bands differ in comparison to MP2/cc-pVTZ and CCSD/cc-pVTZ calculations which shows that the most intense band using this method is the ν_9 band (**table 2.6**).

Analyses of the other bands of propynethial were not possible due to their low intensities as well as the presence of vibrational bands from by-products overlapping in similar areas as shown in **figure 2.7** where bands of allene and thioformaldehyde are easily apparent.

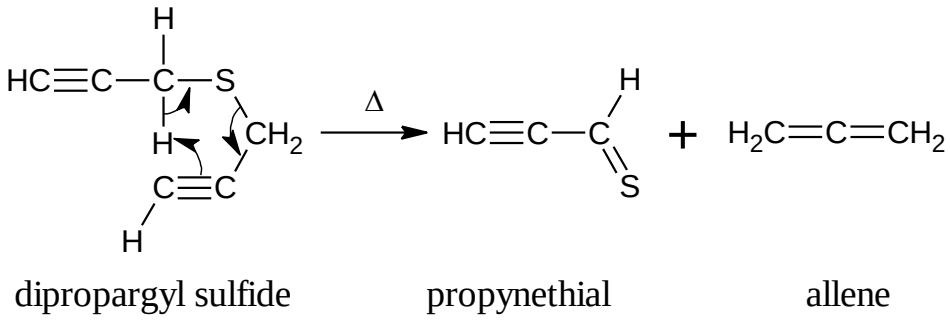

Figure 2.6: Proposed reaction mechanism of the breakdown of dipropargyl sulfide to yield propynethial and allene [17].

Table 2.6: Comparison of the band positions and intensities for propynethial from harmonic *ab initio* and density functional theory methods using a cc-vPVTZ basis set.

		B3LYP	MP2	CCSD	B3LYP	MP2	CCSD
Symmetry	Assignment		Position (cm^{-1})			Intensity (km mol^{-1})	
A'	ν_1	197.64	186.39	194.81	2.85	2.41	2.42
A'	ν_2	516.38	498.03	509.42	3.40	2.60	3.06
A'	ν_3	654.89	644.02	656.89	46.34	40.40	41.68
A'	ν_4	913.94	914.15	915.13	6.34	11.15	11.75
A'	ν_5	1126.88	1146.06	1147.30	70.39	26.28	49.29
A'	ν_6	1351.89	1351.56	1378.16	39.13	22.67	38.54
A'	ν_7	2180.23	2124.76	2193.17	47.03	26.02	41.80
A'	ν_8	3081.98	3136.34	3150.75	7.56	5.13	4.04
A'	ν_9	3464.51	3489.27	3486.49	66.43	72.61	57.21
A''	ν_{10}	328.47	320.20	319.86	11.24	8.55	10.61
A''	ν_{11}	715.33	638.63	696.10	33.59	39.69	35.70
A''	ν_{12}	865.61	855.72	863.67	11.89	11.84	10.46

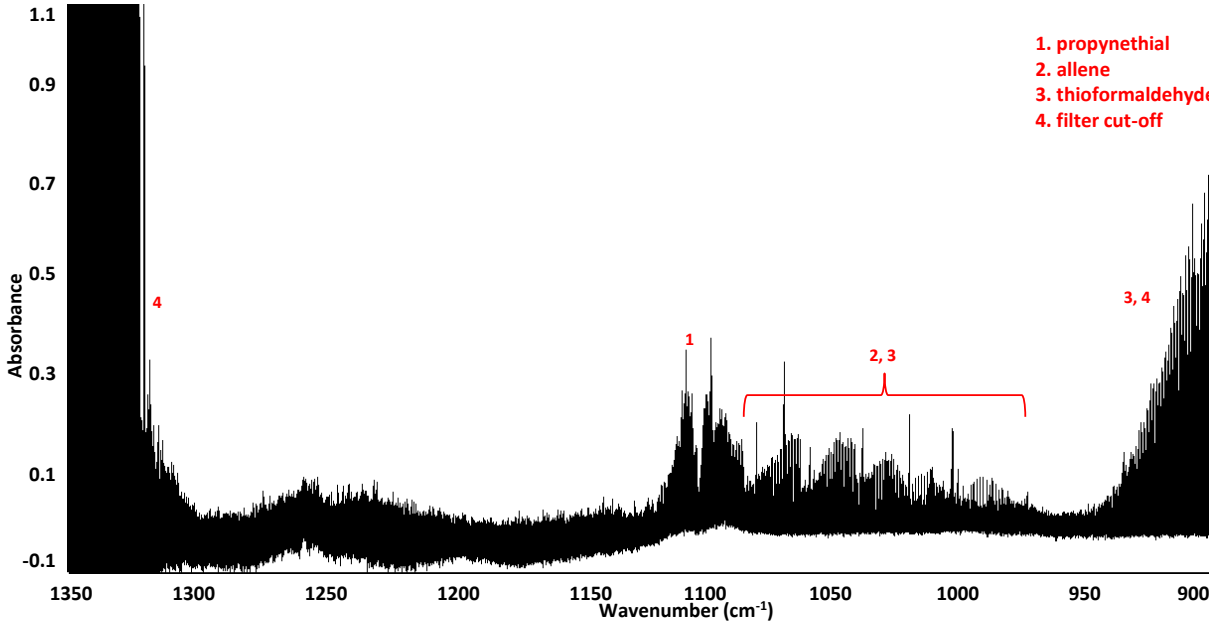

Figure 2.7: Survey spectrum of the pyrolysis products at 500 °C.

2.2.1.1 Experimental

The high resolution FTIR experiments were performed at the Australian Synchrotron THz/far-IR beamline using a flow through pyrolysis setup similar to **figure 1.12**.

Spectra were recorded at 0.00096 cm^{-1} within the mid-IR region using a Bruker IFS125 HR spectrometer. KBr windows were installed onto an ambient temperature cell with White optics and set to 16 passes (6.4 m) which was then placed onto the front channel sample chamber. The spectrometer itself was equipped with the synchrotron source, a KBr beamsplitter and MCTm detector for optimum throughput and sensitivity with a 1350 cm^{-1} high wavenumber cut-off optical filter to reduce the size of data files. Background spectra of the cell under vacuum conditions were recorded prior to introducing the sample vapour and were used to calculate absorbance spectra.

Dipropargyl sulfide was prepared by an undergraduate student Mr. Andrew Wright following the method prescribed by Gal & Choi [21] and its structure and purity were confirmed with ^{1}H-NMR spectroscopy and low resolution FTIR spectroscopy. Sample vapour was flowed through a furnace set to 500 °C and into the multipass cell. A total of 64 scans (32 files with 2 scans each) were recorded before the source throughput was reduced to *ca*. 50 % due to the mirrors being coated with solid by-products from the pyrolysis. Spectra were treated with a zero fill factor of 2 and a four point apodization function during the Fourier transformation before being averaged together. A post zero-fill factor of 8 was applied prior to any spectral analysis.

2.2.1.2 Analysis

The general methods used for transition assignment that were discussed in **Chapter 2.1.4** are also employed in this study. GSCDs following *a*-type selection rules ($\Delta J'' = 2$, $\Delta K_a'' = 0$ and $\Delta K_c = 2$) were calculated using Pickett's SPFIT software [15] and compared to the experimental combination differences. It was found that for some transitions, assignment to multiple K_a' series was possible where the errors (observed – calculated) for the GSCDs were generally < 0.001 cm^{-1} (**figure 2.8**), making it difficult to difficult to confidently assign the transitions. In this situation, K_a' assignment was made based on the average magnitude of the error, and in the example given in **figure 2.8**, the ro-vibrational transitions were assigned to $K_a' = 14$ (black dots in **figure 2.8**).

Overall, a total of 794 *a*-type transitions were assigned and subsequently fitted to Watson's *S*-reduced Hamiltonian [3] yielding the effective rotational and centrifugal distortion constants given in **column 3** of **table 2.7**. These effective constants are a result of an incomplete analysis which may not have much physical significance, and in principle, can be fitted to more than one value which gives the same result. A residual plot can then be made (**figure 2.9**) to graphically represent the errors (observed - calculated wavenumber values) for each transition, where the label $[K_a' + (J' / 100)]$ is used to organise the transitions into groups of constant K_a' and increasing J'. The value of the A rotational constant from this initial fit differs greatly in comparison to the ground state value [17] and could be due to possible interactions at low K_a' values with vibrational levels that are close in energy to the ν_5 level such as ν_4 (914 cm^{-1}) or ν_6 (1351 cm^{-1}). Furthermore, the large A value makes it possible to have interactions with vibrational levels that are further away in energy, such as the ground state or ν_7 (2125 cm^{-1}), although these interactions typically occur at high values of K_a'. This unsatisfactory fit prompted a re-analysis of the ground state by attempting to record pure rotational lines within the THz/millimetre-wave region using coherent synchrotron radiation (CSR). This would allow for the determination of the higher order sextic (H_J, H_{JK} and H_K centrifugal distortion constants in order to improve the ground state constants before re-fitting the ν_5 excited state constants.

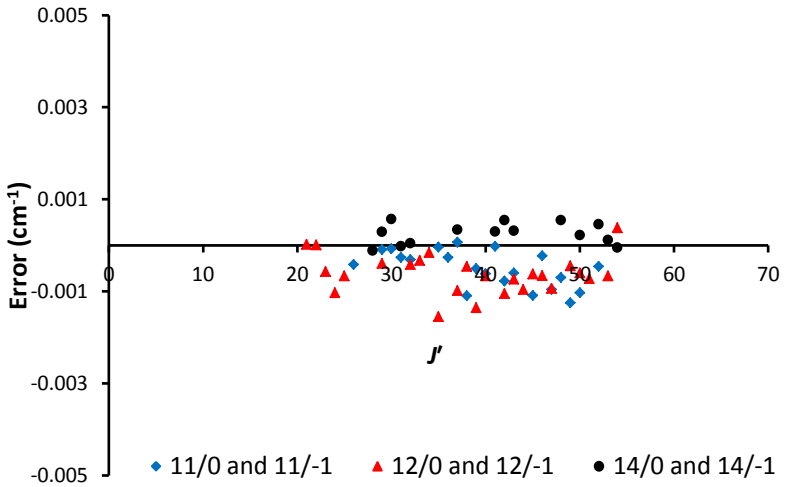

Figure 2.8: Possible ro-vibrational transition assignments for a set of *P*- and *R*-branch transitions, where 11, 12 and 14 refer to the value of K_a'. ($K_a' + K_c' - J' = 0$) and ($K_a' + K_c' - J' = 1$) are denoted by 0 and -1 respectively.

Table 2.7: The effective rotational and centrifugal distortion constants for the ground state and ν_5 band of propynethial fitted to Watson's *S*-reduced Hamiltonian in the I^r representation.

Constant	Brown *et al.* [17]	G.S. effective	ν_5 effective
Centre/cm^{-1}	-	-	1101.4217 (1)
A	42652.0263	42652.03040 (541)	42036.1560 (650)
B	3109.38231	3109.3824630 (618)	3094.8598 (140)
C	2894.26571	2894.2656810 (584)	2912.7160 (149)
D_J	0.0011278	0.0011297990 (269)	0.001010459 (279)
D_{JK}	-0.104774	-0.10482080 (103)	-0.0914847 (225)
D_K	4.16771	4.16920 (114)	3.947370 (400)
d_1x10^4	-2.1021	-2.110060 (154)	[b]
d_2x10^6	-6.03	-5.38340 (306)	[b]
H_Jx10^9	-	2.48700 (495)	-
H_{JK}x10^7	-	-1.40380 (151)	-
H_{KJ}x10^5	-1.84	-2.06100 (114)	[b]
h_1x10^{10}	-	8.4140(355)	-
J' max		56	56
K_a' max		13	13
number trans.		729	786
r.m.s deviation / cm^{-1}		0.3[a]	0.09
σ_{dev}		0.3[a]	67.13

Figures in brackets are one standard deviation according to the least squares fit in units of the least significant figure quoted

[a] Units in MHz

[b] Constants constrained to their respective ground state values.

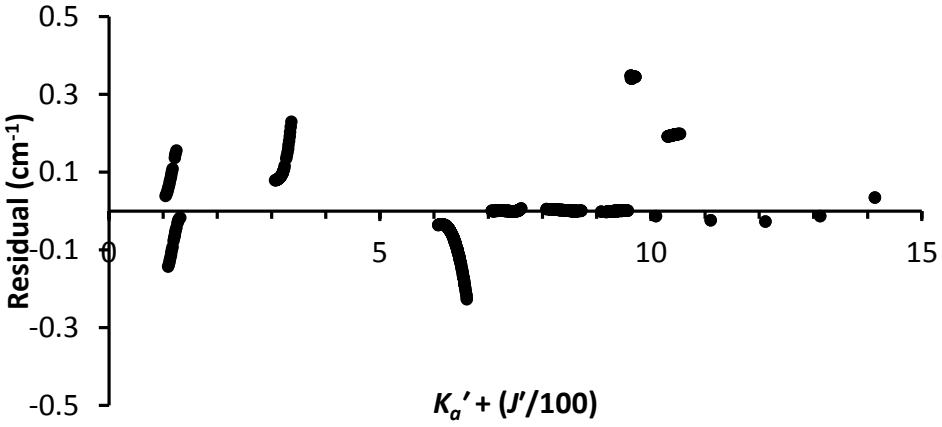

Figure 2.9: A residual plot of the assigned *a*-type transitions for the ν_5 band.

2.2.1.3 Coherent synchrotron radiation (CSR)

Operating under standard beam current conditions (top-up mode maintained at 200 mA), the Australian Synchrotron is able to emit IR radiation to *ca.* 10 cm^{-1} in the THz/millimetre-wave region. At these wavenumbers, it is possible to observe pure rotational transitions from the ground vibrational state of propynethial because it has a large *A* rotational constant which spreads the energy of K_a'' stacks, whilst the spacing between rotational levels will be dependent on $B + C$. Rotational transitions will often have high J'', K_a'' and K_c'' quantum numbers and spectra can be congested with rotational lines from molecules occupying low energy vibrational levels (or satellites). To further complicate this issue, the low flux of radiation in the THz/millimetre-wave region often produces a beam with low S/N and requires a long acquisition time in order increase the S/N to a reasonable level.

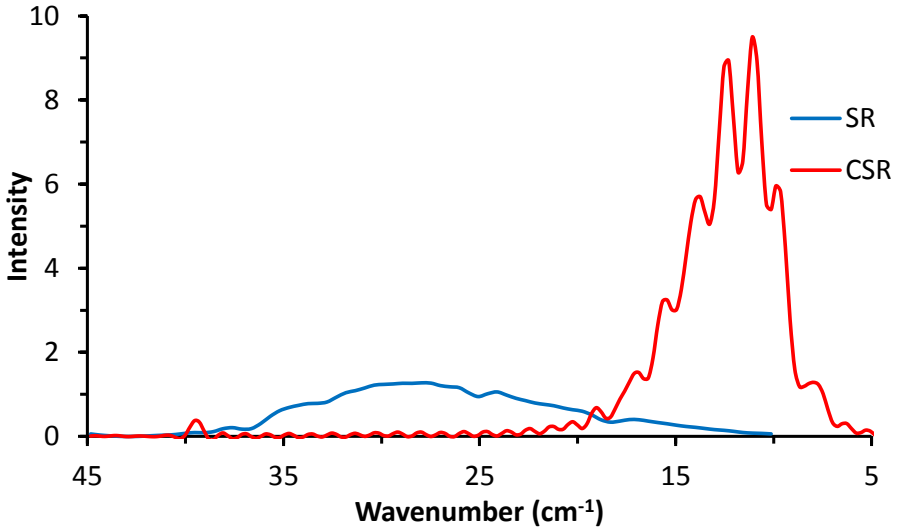

Figure 2.10: Low resolution profile (1 cm^{-1}) of the single channel beam using a stored synchrotron beam (SR) and coherent synchrotron radiation (CSR) at the Australian Synchrotron THz/far-IR beamline.

CSR overcomes the former issue by utilising a single bunch of electrons in the stored beam, rather than multiple bunches. By reducing the longitudinal distribution of electrons (length of an electron bunch), it is possible to observe coherent emission of radiation up to wavelengths $\lambda \approx \sigma$, where λ is the wavelength and σ is the bunch length, both in μm. As illustrated in **figure 2.10**, CSR at the Australian Synchrotron facility is several orders of magnitude brighter than the stored beam, and under the most stable conditions produces radiation from *ca*. 5 – 20 cm^{-1}.

A noticeable effect of using CSR are the oscillations in the single channel profile of the beam which are caused by the acquisition speed of the detector being slower than the revolution speed of the electron bunch around the storage ring. The observed oscillations are typically very intense and have an additive effect to the intrinsic noise of the beam which complicates both the detection and assignment of molecular lines, further inhibiting the assignment of rotational lines to even the ground state of propynethial.

As a result of these large oscillations, it was not possible to extract any information on the pure rotational transitions from the CSR measurements, and therefore millimetre-wave spectroscopy was used as it is more sensitive within the THz/millimetre-wave region and provides a higher resolution in comparison to FTIR techniques.

2.2.1.4 Millimetre-wave spectroscopy

The fundamental theory and instrumentation associated with millimetre-wave spectroscopy will not be discussed in detail although the theory is the same as microwave spectroscopy (**Chapter 4**). However, it should be noted that the range of microwaves and millimetre-waves generally range from 10 – 100 GHz and100 – 600 GHz respectively.

Millimetre-wave experiments were performed by Prof. Laurent Margules at Université de Lille 1. Spectra were recorded between 150 – 650 GHz using solid state millimetre-wave sources (< 550 GHz [22]) and a backward wave oscillator (580 – 660 GHz [23]) before being sent to the McNaughton group for analysis. A full assignment of the millimetre-wave spectra is outside the scope of this project and thus ground state perturbations have not been treated. Perturbations between the ground state and low energy vibrational levels are possible due to a large value for the *A* rotational constant resulting in the ground state energy levels essentially "catching up" with the lowest vibrational states. Given the right symmetry of the vibrational satellite, perturbations can occur, and have been observed in several other molecules with large *A* rotational constants such as ketenimine [24], thioketene [25] and propynal [26].

Rotational transitions emanating from vibrational satellites, as well as the ^{34}S isotopologue species, were not assigned and will be completed by collaborators at a later date. Thus, the resulting ground

state rotational and centrifugal distortion constants in this preliminary fit are in essence effective constants derived from a set of assigned rotational transitions which have a range quantum numbers equal to those observed in the IR spectrum.

A total of 734 *a*-type rotational transitions in the millimetre-wave were assigned with J'' and K_a'' max values of 53 and 13 respectively. Transitions were fitted by introducing three sextic centrifugal distortion terms (H_J, H_{JK} and H_K) to the fit, in addition to fitting the rotational constants (A, B and C) and the quartic centrifugal distortion constants (D_J, D_{JK}, D_K, d_1 and d_2), and are given in **column 2** of **table 2.7**. The fitted effective constants were then used to calculate more accurate GSCDs and in principle will allow for a unique assignment of the ro-vibrational transitions for the ν_5 band. A re-assignment of the ν_5 transitions is currently being performed however it is not presented here due to an incomplete analysis.

2.2.1.5 Conclusions

A re-assessment of the ground state rotational and centrifugal distortion constants has been performed following the measurement of the high resolution FTIR band of propynethial in the ν_5 region. The ground state constants derived from microwave spectroscopy proved to be inadequate for calculating accurate GSCDs that are conventionally used when confirming the assignment ro-vibrational lines from high resolution FTIR spectra. This highlights the need for a large range of transitions with differing quantum numbers to ensure that accurate rotational and centrifugal distortion constants can be calculated. Millimetre-wave spectroscopy is an ideal technique in this situation as it is able to record spectra over a wide range of frequencies which gives a) rotational lines with high J'' and K_a'' quantum number and b) the ability to derive rotational and centrifugal distortion constants for low energy vibrational satellites. The improved ground state rotational and centrifugal distortion constants can then be used to more accurately simulate the rotational spectrum of propynethial, hence increasing the probability of finding this molecule in interstellar media. Ground state perturbations also need to be taken into consideration for molecules with large A rotational constants, as rotational energies in the ground state can overlap with those in low energy vibrational satellites.

References

[1] M. Born and R. Oppenheimer, *Annalen der Physik*, **74**, 30 (1924).

[2] E. Nelson, *Phys. Rev.*, **150**, 1079 (1966).

[3] J. K. G. Watson, in *Vibrational Spectra and Structure*, 1977, Vol 6, ed. J. R. Duric, Elsevier, Amsterdam.

[4] B. S. Ray, *Z. Phys.*, **78**, 74 (1932).

[5] J. M. Hollas, *High resolution spectroscopy*, 4th edition, Butterworth-Heinemann (2013).

[6] W. Gordy and R. L. Cook, *Microwave Molecular Spectra*, Wiley (1989).

[7] G. W. King, R. M. Hainer and P. C. Cross, *J. Chem. Phys.*, **11**, 27 (1943).

[8] D. McNaughton, D. McGilvery and F. Shanks, *J. Mol. Spectrosc.*, **149**, 458 (1991).

[9] F. W. Loomis and R. W. Wood, *Phys. Rev.*, **32**, 223 (1928).

[10] M. K. Bane, E. G. Robertson, C. D. Thompson, C. Medcraft, D. R. T. Appadoo and D. McNaughton, *J. Chem. Phys.*, **134**, 234306 (2011).

[11] M. K. Bane, E. G. Robertson, C. D. Thompson, C. Medcraft, D. R. T. Appadoo and D. McNaughton, *J. Chem. Phys.*, **135**, 224306 (2011).

[12] M. K. Bane, C. D. Thompson, E. G. Robertson, D. R. T. Appadoo and D. McNaughton, *Phys. Chem. Chem. Phys.*, **13**, 6793 (2011).

[13] C. Medcraft, C. D. Thompson, E. G> Robertson, D. R. T. Appadoo and D. McNaughton, *Astrophys. J.*, **753**, 18 (2012).

[14] C. Medcraft, W. Fuss, D. R. T. Appadoo, D. McNaughton, C. D. Thompson and E. G. Robertson, *J. Chem. Phys.*, **137**, 214301 (2012).

[15] H. M. Pickett, *J. Mol. Spectrosc.*, **148**, 371 (1991).

[16] T. Nakagawa and Y. Morino, *J. Mol. Spectrosc.*, **38**, 84 (1971).

[17] R. D. Brown, P. D. Godfrey, R. Champion and M. Woodruff, *Aust. J. Chem.*, **35**, 1747 (1982).

[18] N. D. Kargamanov, V. A. Korolev and A. K. Mal'tsev, *B. Acad. Sci. U.S.S.R. Ch+.*, **36**, 2152 (1987).

[19] O. M. Nefedov, V. A. Korolev, L. Zanathy, B. Solouki and H. Bock, *Mendeleev Commun.*, **2**, 67 (1992).

[20] Gaussian 09, Revision D.01, M. J. Frisch, G. W. Trucks, H. B. Schlegel, G. E. Scuseria, M. A. Robb, J. R. Cheeseman, G. Scalmani, V. Barone, B. Mennucci, G. A. Petersson, H. Nakatsuji, M. Caricato, X. Li, H. P. Hratchian, A. F. Izmaylov, J. Bloino, G. Zheng, J. L. Sonnenberg, M. Hada, M. Ehara, K. Toyota, R. Fukuda, J. Hasegawa, M. Ishida, T. Nakajima, Y. Honda, O. Kitao, H. Nakai, T. Vreven, J. A. Montgomery, Jr., J. E. Peralta, F. Ogliaro, M. Bearpark, J. J. Heyd, E. Brothers, K. N. Kudin, V. N. Staroverov, T. Keith, R. Kobayashi, J. Normand, K. Raghavachari, A. Rendell, J. C. Burant, S. S. Iyengar, J. Tomasi, M. Cossi, N. Rega, J. M. Millam, M. Klene, J. E. Knox, J. B. Cross, V. Bakken, C. Adamo, J. Jaramillo, R. Gomperts, R. E. Stratmann, O Yazyev, A. J. Austin, R. Cammi, C. Pomelli, J. W. Ochterski, R. L. Martin, K. Morokuma, V. G. Zakrzewski, G. A. Voth, P.

Salvador, J. J. Dannenberg, S. Dapprich, A. D. Daniels, O Farkas, J. B. Foresman, J. V. Ortiz, J. Cioslowski and D. J. Fox, Gaussian, Inc., Wallingford CT, 2013.

[21] Y. S. Gal and S. K. Choi, *J. Polym. Sci. Pol. Lett.*, **26**, 115 (1988).

[22] B. Tercero, L. Margulès, M. Carvajal, R. A. Motiyenko, T. R. Huet, E. A. Alekseev, I. Kleiner, J. C. Guillemin, H. Møllendal and J. Cernicharo, *Astron. Astrophys.*, **538**, A119 (2012).

[23] R. A. Montiyenko, L. Margulès, E. A. Alekseev, J. –C. Guillemin and J. Demaison, *J. Mol. Spectrosc.*, **264**, 94 (2010).

[24] M. K. Bane, E. G. Robertson, C. D. Thompson, C. Medcraft, D. R. T. Appadoo and D. McNaughton, *J. Chem. Phys.*, **134**, 234306 (2011).

[25] D. McNaughton, E. G. Robertson and L. D. Hatherley, *J. Mol. Spectrosc.*, **175**, 377 (1996).

[26] Private communication with Dr. E. G. Robertson.

Declaration for Thesis Chapter 2.2.2

Declaration by candidate

In the case of Chapter 2.2.2, the nature and extent of my contribution to the work was the following:

Nature of contribution	**Extent of contribution (%)**
Initiation, key ideas, development and writing up	80

The following co-authors contributed to the work. If co-authors are students at Monash University, the extent of their contribution in percentage terms must be stated:

Name	**Nature of contribution**	**Extent of contribution (%) for student co-authors only**
C. D. Thompson	Initiation and key ideas	
D. R. T. Appadoo	Experimental assistance	
R. Plathe	Experimental assistance	
P. Roy	Initiation and key ideas	
L. Manceron	Initiation and key ideas	
J. Barros	Experimental assistance	5 %
D. McNaughton	Initiation and key ideas	

The undersigned hereby certify that the above declaration correctly reflects the nature and extent of the candidate's and co-authors' contributions to this work*.

Candidate's Signature		**Date**
Main Supervisor's Signature		**Date**

*Note: Where the responsible author is not the candidate's main supervisor, the main supervisor should consult with the responsible author to agree on the respective contributions of the authors.

Synchrotron far infrared spectroscopy of the two lowest fundamental modes of 1,1-difluoroethane

Andy Wong[1], Christopher D. Thompson[1], Dominique. R. T. Appadoo[2], Ruth Plathe[2], Pascale Roy[3], Laurent Manceron[3, 4], Joanna Barros[3] and Don McNaughton[1]*

1. School of Chemistry, Monash University, Wellington Rd., Clayton, Victoria 3800, Australia.
2. Australian Synchrotron, 800 Blackburn Rd, Clayton, Victoria 3168, Australia.
3. Synchrotron SOLEIL, l'Orme des Merisiers. Saint-Aubin, BP 48, 91192 Gif-sur-Yvette, France.

4 LADIR, CNRS-UMPC, UMR 7075, Case 49, 4 Place Jussieu, 75252 Paris Cedex

* Corresponding author. Email: [redacted]

Abstract

The far-infrared (FIR) spectrum (50 – 600 cm^{-1} of 1,1-difluoroethane was recorded using the high resolution infrared AILES beamline at the Soleil Synchrotron. A ro-vibrational assignment was performed on the lowest wavenumber, low intensity 18_0^1 and 17_0^1 modes, yielding band centres of 224.241903 (10) cm^{-1} and 384.252538 (13) cm^{-1} respectively. A total of 965 and 2013 FIR transitions were assigned to the 18_0^1 and 17_0^1 fundamentals respectively. Previously measured pure rotational transitions from the upper states were included into the respective fits to yield improved rotational and centrifugal distortion constants. The 18_1^2 hot band was observed within the fundamental band, with 369 FIR transitions assigned and co-fitted with the fundamental to give a band centre of 431.956502 (39) cm^{-1} for v_{18} = 2. The 18_0^2 overtone was observed with 586 transitions assigned and fitted to give a band centre of 431.952763 (23) cm^{-1} in the v_{18} = 2 state. Two hot bands originating from the v_{18} = 1 and v_{17} = 1 states were observed within the 17_0^1 fundamental.

Keywords

Synchrotron, 1,1-difluoroethane, far-infrared (FIR), ro-vibrational

Citation: A. Wong, C. D. Thompson, D. R. T. Appadoo, R. Plathe, P. Roy, L. Manceron, J. Barros and D. McNaughton, *Mol. Phys.*, **111**, 2198 (2013).

1. Introduction

Since the signing of the Montreal Protocol[1] some 25 years ago, hydrofluorocarbons (HFCs) have become the predominant replacement molecules for the ozone depleting chlorofluorocarbon (CFC) species and their temporary replacements the hydrochlorofluorocarbons (HCFCs), in applications such as foam blowing agents, propellants and refrigerants. However due to their large global warming potentials (GWP), these molecules need to be understood in detail and constantly monitored. One suitable method to do so is through high resolution Fourier transform infrared spectroscopy (FTIR) - which has been used to understand and characterize many different CFCs, HCFCs and HFCs[2].

R152a, or 1,1-difluoroethane, has a stratospheric lifetime of 1.4 years and a GWP of 122[3]. The first infrared and Raman measurements of R152a were performed by Smith et al[4]. These were later re-measured by Durig[5], followed by Guirgis and Crowder[6] in 1984. A vibrational reassignment was later performed by McNaughton and Evans[7] in 1996, and then by Tai et al[8] in 1999.

Solimene and Dailey[9], 1951, were the first to measure R152a in the microwave region followed by Villamañan et al[10], in 1995, who established the most recent set of ground state rotational and centrifugal distortion constants using Fourier transform microwave spectroscopy and millimetre wave spectroscopy. Over four decades, several papers analysing the torsional frequencies[11, 12] and rotational barriers[13-15] of vibrational satellites in the microwave and millimetre wave regions were published.

To date, only 6 of the 18 fundamental modes have been analysed via high resolution FTIR spectroscopy: 4_0^1 [16], 5_0^1 [7], 9_0^1 [7, 17] and 16_0^1 [17], 10_0^1 and 11_0^1 [18] – these being the strongest intensity modes contributing to the very high GWP value for this molecule. Given that hot bands from low wavenumber modes of R152a contribute significantly to the overall intensity of these bands it is important to also fully characterize these modes, specifically 18_0^1 and 17_0^1, which like many low wavenumber modes are extremely low in intensity. These modes are predicted from ab initio calculations at the MP2/6-311(d,p) level to have intensities of 0.09 and 0.03 km mol^{-1} respectively[7].

The FIR or terahertz region (30 cm^{-1} to 500 cm^{-1}) is difficult to measure because of a lack of practical tunable lasers and the low brightness of ordinary thermal or arc sources. Synchrotron radiation (SR) provides intrinsic advantages (brightness, stability, small beam divergence) which improve the S/N allowing the observation of weak ro-vibrational bands at high resolution. Pioneering gas-phase FIR spectroscopy at Max-lab[19, 20] and LURE[21] illustrated both the great potential of SR, and some of the challenges (the main challenge being minimizing noise). These results have prompted the development of a FIR beamline at the Soleil, Paris and Australian synchrotron light source, Melbourne as well as at the ALS, Berkeley and the Swiss light source, Zurich[22-26]. The AILES beamline at Synchrotron Soleil, France, makes use of infrared synchrotron radiation from both edge emission and constant field emission of a bending magnet, with optics optimized for extracting a large

solid angle (20 x 78 mrad) and permits a significantly higher S/N in the FIR region for high-resolution (0.001 cm^{-1}) than conventional thermal sources[27].

We present here a ro-vibrational analysis of the weak 18_0^1 , 17_0^1 and 18_0^2 modes of 1,1-difluoroethane recorded on the AILES beamline at the Soleil synchrotron using a long path length cell to attain sufficient S/N for analysis.

1,1-difluoroethane is an asymmetric rotor belonging to the C_s point group, with an asymmetry parameter, κ, equal to 0.75. It has 18 normal vibrational modes – 11 with A' symmetry and 7 with A'' symmetry, exhibiting either *a/c*-type or *b*-type band profiles respectively. The fundamental modes of interest in this report are: 18_0^1 (torsion) and 17_0^1 (CF_2 rock), both having A'' symmetry. An initial analysis of these two fundamentals revealed that both bands were heavily congested with hot band structure - at room temperature hot bands originating from the $\nu_{18} = 1$ and $\nu_{17} = 1$ states are approximately 34 % and 16 % the intensity of the fundamentals.

2. Experimental

The spectra were recorded using the AILES Bruker IFS 125HR Fourier transform spectrometer, fitted with a 6 μm Mylar/Si multilayer beam splitter and a liquid-helium cooled Si bolometer detector, and operated at the full spectral resolution (0.001 cm^{-1}) given by the 882 cm maximum optical path difference (MOPD). The average storage beam electron beam current for the present results was 400 mA.

The Fourier transform spectrometer (FTS) was evacuated down to 5.10^{-5} mbar pressure with turbo molecular pumps[27] (to minimize residual H_2O and CO_2 absorption in the spectrometer) and all spectra were recorded at room temperature. Two White-type multipass absorption cells were used for these experiments: a 20 cm base length cell, for optical path lengths up to 8 m and a 250 cm base length one, for optical path lengths up to 151.8 m. The sample of 1,1-difluoroethane was obtained from Sigma Aldrich. The chemical purity was specified better than 98 % and was used without further purification. The absorption cells were evacuated and filled with 0.2 or 1.2 mbar of 1,1-difluoroethane. The sample pressure in the cells was measured using calibrated Pfeiffer capacitive gauges, with full scale readings of 1 or 10 mbars.

Three high resolution spectra have been used in this work: the first obtained with an 8 m optical path length and a 0.25 mbar sample pressure is an average of 140 interferograms recorded with an optical scan velocity of 5.06 cm/s in a total time of 7 hours. For this spectrum, the detector was fitted with a 200 - 600 cm^{-1} cold optical filter and the spectrometer with a 12.5 mm entrance aperture, but the SR effective source diameter results in a beam diameter that fulfils the resolution criterion. The Synchrotron was operating in the equal filling mode with 416 approximately equally filled and spaced

electron bunches. The second and third spectra were taken with a 151.8 m optical path length, 0.2 and 1.2 mbar sample pressures with 200 - 600 cm^{-1} and 30 - 300 cm^{-1}, cold optical filter, respectively. For these spectra, the Synchrotron was operating in the so-called hybrid mode with a large electron bunch (about 10 mA) and 415 equally small bunches. The specific instabilities observed in the FIR range when using large bunch currents[28] caused a decrease of the S/N ratio. To alleviate this difficulty, small interferometer entrance apertures of 1.7 or 2.5 mm were used to filter out the noisier part of the incoming radiation, emitted in the lower end of the spectrum over a larger solid angle. To make up for the increase in noise, about 400 scans were collected for each spectrum.

The spectra were calibrated with residual H_2O lines observed in the spectra between 100 cm^{-1} and 500 cm^{-1}, with their wavenumber values taken from HITRAN08[29]. The spectral calibration is accurate to better than 0.0001 cm^{-1} (RMS).

3. Results and Discussion

The high resolution infrared spectrum in the region of 170 – 530 cm^{-1} is shown in **Figure 1** (top), alongside simulations of the 18_0^1, 18_1^2, 18_0^2 and 17_0^1 bands (bottom). The sharp saturated lines dominating the spectrum are due to trace water vapour which built up in the large volume of the cell over the several days of spectral acquisition. Spectra were first post zero filled with a factor of 8 in OPUS 6.0 to generate peak lists for importation into MacLoomis[30], and subsequent line assignment aided by Loomis-Wood[31] plots.

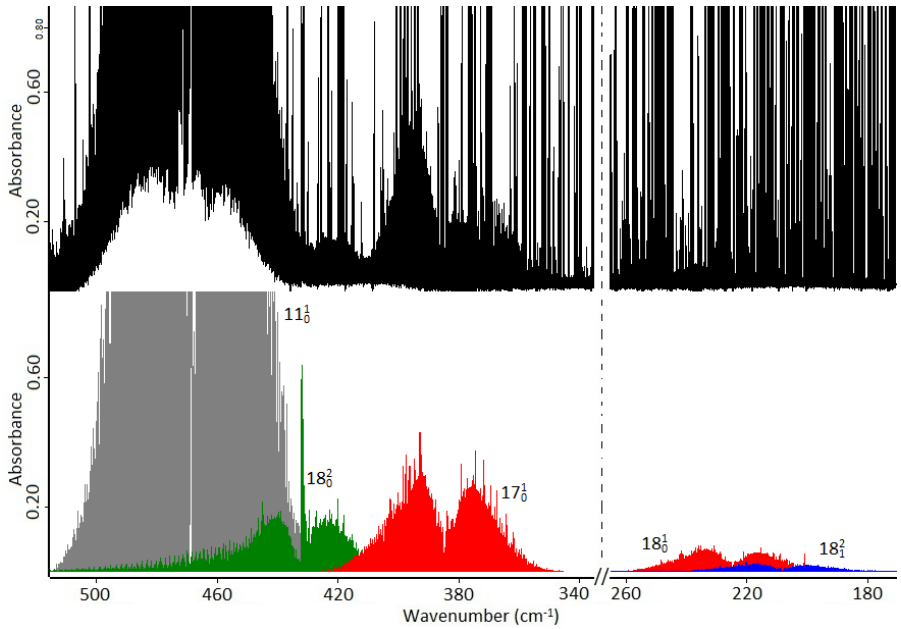

Figure 1: A comparison between experimental (black) and simulated spectra: red (18_0^1 and 17_0^1), blue (18_1^2) and green (18_0^2). A simulation of the 11_0^1 band (grey) is included for reference.

The fitting procedure and subsequent simulations of spectra were performed using the Pickett[32] software packages SPFIT and SPCAT. The Pickett output from which the constants were obtained are available as supplementary tables, **S1-S4**. Line shapes in simulated spectra were constructed using a Gaussian profile with a full-width half height of 0.0008 cm^{-1}, and Watson's[33] *A*-reduced rotational Hamiltonian in the I^r representation was used in all fits. Ground state combination differences were used to confirm the quantum number assignments of fundamental and overtone transitions, and lower state combination differences (LSCD) were used to confirm hot band assignments. Summaries of the selection rules for transitions observed, and an energy diagram showing the major transitions, are given in **Table 1** and **Figure 2** respectively.

Table 1: Quantum number selection rules for observed transitions: **1a** (18_0^1, 18_1^2 and 18_0^2) and **1b** (17_0^1, $17_0^1 18_1^1$ and 17_1^2).

	18_0^1		18_1^2		18_0^2	
1a	P	R	P	R	P	R
ΔJ	-1	1	-1	1	-1	1
ΔK_a	1	1	1	1	0	0
ΔK_c	-1	1	-1	1	-1	1

	17_0^1			$17_0^1 18_1^1$	17_1^2
1b	P	Q	R	R	R
ΔJ	-1	0	1	1	1
ΔK_a	1	-1	1	1	1
ΔK_c	-1	1	1	1	1

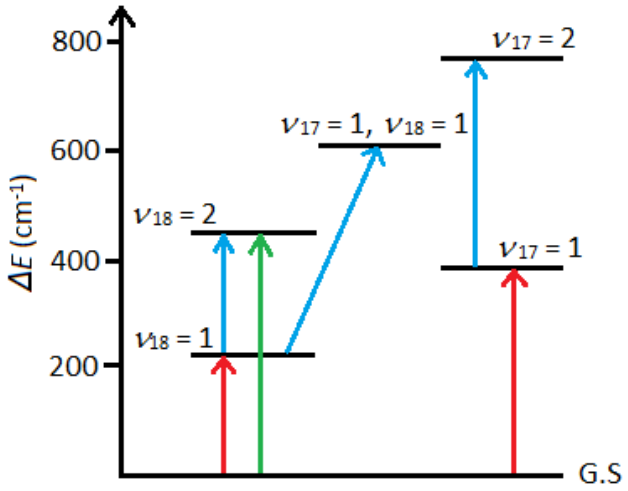

Figure 2: Energy diagram for the lowest vibrational modes of 1,1-difluoroethane.

FIR transitions were all weighted to an uncertainty of 0.0002 cm^{-1}, whereas microwave transitions that were used in co-fits were weighted to an uncertainty of 20kHz, 50 kHz, 300 kHz for the ground state based on the line widths expected from the experiments of Villamañan et al[10]; and 50 kHz for the $v_{18} = 1$ and $v_{17} = 1$ excited states.

3.1 18_0^1 & 18_1^2 – The torsion modes

A very weak band was observed in the 200 – 250 cm^{-1} region, corresponding to the earlier 18_0^1 band assignment at low resolution by McNaughton and Evans[7]. Using ground state combination differences as a guide, a total of 965 *b*-type transitions were assigned to the 18_0^1 mode, with J' max = 74 and K_a' max = 19 and fitted to give a band centre of 224.24 cm^{-1}. These FIR transitions were fitted together with the appropriately weighted microwave transitions recorded by Villamañan et al[10], yielding the molecular constants in **Table 2**. The microwave transitions fit well with the infrared data and the constants compare well with those tentatively labelled as the torsion by Villamañan et al but with the rotational constants better determined.

Due to the internal rotation from the methyl rotor in 1,1-difluoroethane, the A'' symmetry of the v_{18} torsional modes are split into two sublevels – a non-degenerate *A* species, and a degenerate *E* species[11].No torsional splitting between the *A* and the *E* species was observed from either the ground state or $v_{18} = 1$, which given the observed splitting in the microwave work of up to 13 MHz for $v_{18} = 1$ and up to 0.2 MHz in the ground state[10] is expected.

With an intensity of approximately one-third of the fundamental band, the 18_1^2 hot band was also observed. Using the ro-vibrational constants from the 18_0^1 fit above, 369 line assignments were confirmed using LSCD, with J' max = 53 and K_a' max = 13. These transitions were fitted to produce the constants in the 4th column of **Table 2** for $v_{18} = 2$.

From the selection rules[34], which allow *E*-*E* transitions only these should be for the *E* state. The rotational constants match approximately with the effective constants derived for the *A* state by Ageno et al. from a limited number of measured microwave transitions and without considering centrifugal distortion[12]. The discrepancy between our constants (**Table 2**, 4th column) and those reported by Ageno et al[12] can be attributed to the splitting between the *A* and the *E* species of the $v_{18} = 2$ level being large enough to be observed.

Table 2. Fitted rotational and centrifugal distortion constants in Watson's *A*-reduced I^r Hamiltonian for the ground state, 18_0^1, 18_0^2 and 18_1^2 of CHF_2CH_3 (MHz).

constant	ground state	ν_{18} = 1 (MW)	ν_{18} = 1 (IR+MW)	ν_{18} = 2 (E hot band)	ν_{18} = 2 (A overtone)
band centre /cm^{-1}	-	-	224.241903 (10)	431.956502 (39)	431.952763 (23)
A	9419.98158 (23)	9492.30789 (72)	9492.31026 (52)	9497.42 (20)	9497.08 (12)
B	8962.73275 (22)	8934.26974 (70)	8934.26974 (37)	8909.80 (16)	8910.201 (98)
C	5170.45413 (25)	5163.83760 (89)	5163.83750 (40)	5158.6974 (22)	5158.7028 (14)
Δ_J	0.00475183 (42)	0.0046573 (18)	0.00465634 (19)	0.00467321 (96)	0.00476275 (46)
Δ_{JK}	0.00180884 (39)	0.0019115 (13)	0.0019097 (16)	0.002848 (12)	0.0029680 (61)
Δ_K	0.00291225 (41)	0.0027477 (13)	0.0027677 (24)	0.004002 (32)	0.003302 (19)
δ_J	0.001728155 (69)	0.00168493 (34)	0.00168583 (14)	0.00168583[d]	0.001728155[c]
δ_k	0.004647730 (112)	0.00445195 (44)	0.00445231 (74)	0.00445231[d]	0.004647730[c]
$\Phi_J \times 10^{-8}$	0.7607 (92)	0.7607[c]	0.7607[c]	0.7607[c]	0.7607[c]
$\Phi_{JK} \times 10^{-8}$	-0.9686 (179)	-3.284 (52)	-2.486 (40)	-2.486[d]	-0.9686[c]
$\Phi_{KJ} \times 10^{-7}$	0.1559 (26)	0.1559[c]	0.1559[c]	0.1559[c]	0.1559[c]
$\phi_J \times 10^{-8}$	0.3611 (22)	0.259 (17)	0.3723 (31)	0.3723[d]	0.3611[c]
$\phi_K \times 10^{-7}$	0.55481 (141)	0.4424 (87)	0.3985 (71)	0.3985[d]	0.55481[c]
J max	69	45	45/74[e]	53	58
K_a max	43	27	27/19[e]	13	13
number trans	592	206	203/965[e]	369	586
r.m.s deviation / cm^{-1}			0.084250[f]/0.00027	0.00026	0.00024
σ_{dev}		0.026[f]	1.39870	1.28011	1.20560

[a] Figure in brackets are one standard deviation according to the least squares fit in units of the least significant figure quoted
[b] Constants reported by Villamañan et al[10] for the ground state and the ν_{18} = 1 (MW) state.
[c] Constrained to ground state constants from Villamañan et al[10].
[d] Constrained to constants from the ν_{18} = 1 (IR+MW) fit.
[e] The two numbers refer to microwave and infrared transitions respectively.
[f] Value given in units of MHz.

3.1.1 18_0^2 torsion mode

Serendipitously, the 18_0^2 overtone was also observed with sufficient intensity to assign ro-vibrational lines, thus providing additional information about this upper state. The 18_0^2 overtone has an *A*' symmetry and exhibits ro-vibrational transitions that follow *a*-type selection rules. While the *R*-branch of this band was initially unassignable due to overlap with the neighbouring and much stronger 11_0^1 fundamental band, 432 lines were assigned to the *P*-branch of the overtone band using transitions from a simulated spectrum based on the $v_{18} = 2$ hot band constants in **Table 2**. Once having an adequate fit, individual *R*-branch lines could be assigned and 154 such lines were added to the fit These transitions were initially co-fitted with transitions assigned within the 18_1^2 hot band but a successful fit could not be obtained. These transitions were thus fitted independently of the observed hot band transitions to give the constants in the 5th column of **Table 2**. Given that the band centre is lower than that derived from the hot band fit it would appear that these lines are due to the A_1–A_1 transition of the overtone. The rotational constants are also outside two standard deviations of those derived above but much better determined than those tentatively assigned to the *E* state. Given that the *A* state would be expected to be better handled by the Pickett[32] program this is consistent with the lines belonging to the *A* state. The energy difference of 0.003740 (45) cm^{-1} or 112.1 (13) MHz is most likely attributable to the torsional splitting in the $v_{18} = 2$ state. Given the magnitudes of the ground and first excited state splitting observed in the microwave[10], this is a plausible number.

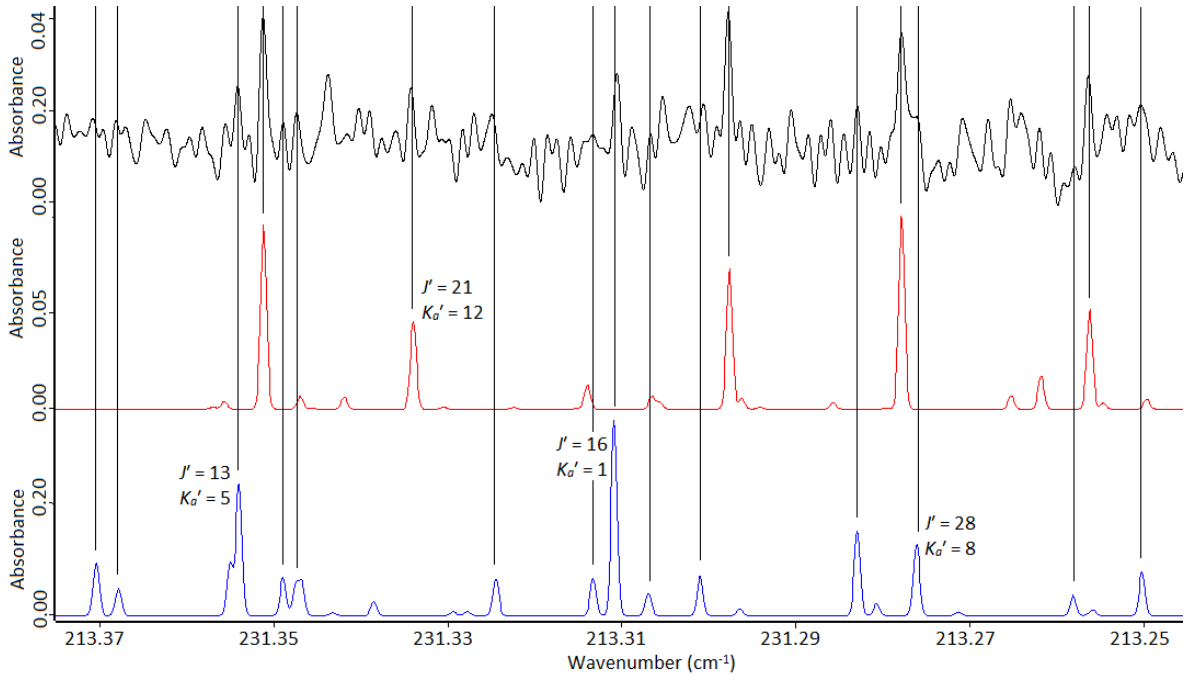

Figure 3: An expansion of the experimental (black), 18_0^1 fundamental (red) and 18_1^2 hot band (blue) spectra. Only the labelled lines were considered to be of sufficient S/N for assignment.

The band centre for the overtone fitted to 431.95 cm^{-1} also revealed a shift due to anharmonicity of ~16.53 cm^{-1}. A simulated spectrum predicted using the constants of **Table 2** is shown in **Figure 1**.

It is apparent from **Figure 1** that the relative intensities of the experimental *R*- and *P*-branches are not consistent with the prediction , most likely due to a Herman-Wallis[35] effect, however this has not been further pursued in this work. Using the rotational and centrifugal distortion constants derived from the fundamental and hot band given in **Table 2**, **Figure 3** shows a small section of the predicted spectrum of the 18_0^1 band and an excellent correlation between the experimental and simulated spectra can be seen. It should be noted that the weaker lines in this figure were not used in the fitting procedure. A simulation of the overtone spectrum using the constants in the 5th column of **Table 2** produces a spectrum that is offset by *ca*. 0.003 cm^{-1} compared with the experimental.

3.2 17_0^1 – CF_2 twist

Three vibrational bands were observed within the region of the 17_0^1 fundamental mode – the fundamental itself and two hot bands originating from the $v_{18} = 1$ and $v_{17} = 1$ states. A fitted band centre of 384.25 cm^{-1} for the 17_0^1 fundamental mode was calculated from the assignment of 2031 transitions with a J' max = 91 and a K_a' max = 23. For the fundamental the assignment and fit was straightforward and the results of a co-fit using both the FIR transitions and the microwave transitions recorded by Villamañan et al[10] are presented in **Table 3**.

A further 477 and 211 ro-vibrational lines were assigned to the $17_0^1 18_1^1$ and 17_1^2 hot bands. Unfortunately, line assignments for the *P*-branch of both bands were not straightforward due to poor S/N in this region and strong overlap with these weak bands with water lines, subsequently hampering confirmation of the assignment via LSCD. As a result, fitted constants are not provided for these two modes in this work.

The 17_0^1 fundamental mode also exhibits a discrepancy between the intensities of the *P*- and *R*-branches, which could most likely be due to a Herman-Wallis[35] effect. In addition, ro-vibrational structure with spacings that are not immediately apparent as belonging to R152a occur within the *P*-branch of the fundamental; making it difficult to model the Herman-Wallis effect.

Table 3. Fitted rotational and centrifugal distortion constants in Watson's *A*-reduced I^r Hamiltonian for 17_0^1 of CHF_2CH_3 (MHz)

Constant	ν_{17} = 1 (MW)	ν_{17} = 1 (IR+MW)
band centre / cm^{-1}	-	384.252538 (13)
A	9510.2016 (25)	9510.20185 (87)
B	8970.1761 (25)	8970.17672 (82)
C	5145.8160 (25)	5145.81777 (63)
Δ_J	0.004689 (24)	0.00472730 (35)
Δ_{JK}	0.0019640 (75)	0.0019380 (26)
Δ_K	0.0028947 (55)	0.0029233 (50)
δ_J	0.0017810 (12)	0.00177944 (15)
δ_K	0.0048254 (112)	0.0048354 (14)
$\Phi_J \times 10^{-8}$	0.7607[c]	0.7607[c]
$\Phi_{JK} \times 10^{-8}$	-0.9686[c]	-0.9686[c]
$\Phi_{KJ} \times 10^{-7}$	0.1559[c]	0.1559[c]
$\phi_J \times 10^{-8}$	0.3611[c]	0.4265 (16)
$\phi_K \times 10^{-7}$	0.55481[c]	0.6968 (84)
J max	40	40/91[e]
K_a max	31	31/23[e]
number trans.	85	85/2031[e]
rms deviation/cm^{-1}	-	0.033935[d]/0.00015
σ_{dev}	0.011[d]	0.76474

[a] Figures in brackets are one standard deviation according to the least squares fit in units of the least significant figure quoted.

[b] Constants reported by Villamañan et al[10] for the ν_{17} = 1 (MW) state.

[c] Constrained to ground state constants from Villamañan et al[10].

[d] Values given in units of MHz.

[e] The two numbers refer to microwave and infrared transitions respectively.

4. Conclusion

By exploiting FIR radiation from a synchrotron source and a long path length cell, the inherently weak 18_0^1, 17_0^1 and 18_0^2 modes of R152a were observed and assigned. Ro-vibrational analysis of these two bands gave reliable molecular constants, which are shown to satisfactorily reproduce the experimental spectral positions and for the excited vibrational states confirm the tentative assignments of Villamañan et al[10]. In addition a complete ro-vibrational analysis was performed on one hot band and one overtone band, yielding rotational constants for the $v_{18} = 2$ state. The effects of anharmonicity were clearly observed, redshifting the band centre of the 18_0^2 overtone and 18_1^2 hot band by ~16.53 cm^{-1}. A difference in the energy of the $v_{18} = 2$ state is tentatively attributed to a torsional splitting of 0.00360 (5) cm^{-1}. A discrepancy between the predicted relative intensities of the *P*- and *R*-branches for both fundamental modes, and hot bands were also observed.

5. Acknowledgements

We thank the Australian synchrotron and the Soleil synchrotron for the collaboration and the Australian government for funding through the International Science Linkages (ISL), French-Australian science and technology (FAST) program. AW would also like to thank the Monash Faculty of Science for a Deans Scholarship.

6. References

1. Technology and Economic Assessment Panel, Montreal Protocol on Substances that Deplete the Ozone Layer, UNEP, 2006.
2. D. McNaughton, Robertson, E. G., Thompson, C. D., Chimdi, T., Bane, M. K., Appadoo, D., Anal. Chem. 82, 7958-7964 (2010).
3. World Meteorological Organization, Scientific Assessment of Ozone Depletion, Report No.47, Global Ozone Research and Monitoring Project, 2002.
4. D. C. Smith, Saunders, R. A., Nielsen, J. R., Ferguson, E. E., J. Chem. Phys. 20, 847-859 (1952).
5. J. R. Durig, Craven, S. M., Hawley, C. W., Bragin, J., J. Chem. Phys. 57 (1), 131-143 (1972).
6. G. A. Guirgis, Crowder, G. A., J. Fluorine Chem. 25, 405-418 (1984).
7. D. McNaughton, Evans, C., J. Phys. Chem. 100, 8660-8664 (1996).
8. S. Tai, Papasavva, S., Kenny, J. E., Gilbert, B. D., Janni, J. A., Steinfeld, J. I., Taylor, J. D., Weinstein, R. D., Spectrochim. Acta, Part A 55, 9-24 (1999).
9. N. Solimene, Dailey, B. P., J. Chem. Phys. 22, 2042-2044 (1954).
10. R. M. Villamañan, Chen, W. D., Wlodarczak, G., Demaison, J., Lesarri, A. G., Lopez, J. C., Alonso, J. L., J. Mol. Spectrosc. 171, 223-247 (1995).
11. W. G. Fateley, Miller, F. A., Spectrochim. Acta 17, 857-868 (1961).
12. H. Y. Ageno, Raley, J. M., Wollrab, J. E., J. Mol. Spectrosc. (52), 163-165 (1974).
13. D. R. Herschbach, J. Chem. Phys. 25, 358-359 (1956).
14. R. D. Parra, Zeng, X. C., J. Phys. Chem. A 102, 654-658 (1998).
15. B. Velino, Melandri, S., Favero, P. G., Dell'Erba, A., Caminati, W., Chem. Phys. Lett. 316, 75-80 (2000).
16. D. R. T. Appadoo, Robertson, E. G., McNaughton, D., J. Mol. Spectrosc. 217, 96-104 (2003).
17. T. Chimdi, Robertson, E. G., Puskar, L., Thompson, C. D., Tobin, M. J., McNaughton, D., J. Mol. Spectrosc. 251, 256-260 (2008).
18. T. Chimdi, Robertson, E. G., Puskar, L., Thompson, C. D., Tobin, M. J., McNaughton, D., Chem. Phys. Lett. (465), 203-206 (2008).
19. B. Nelander, Vib. Spectrosc. 9, 29-41 (1995).
20. R. Wugt Larsen, Hegelund, F., Nelander, B., Mol. Phys. 102, 1743-1747 (2004).
21. P. Roy, Brubach, J.-B., Calvani, P., deMarzi, G., Filabozzi, A., Gerschel, A., Lupi, S., Marcouillé, O., Mermet, A., Nucara, A., Orphal, J., Paolone, A., Vervolet, M., Nucl. Instrum. Methods. Phys. Res. A 467-468, 423-436 (2001).
22. A. R. W. McKellar, Tokaryk, D. W., Li-Hong Xu., Appadoo, D. R. T., May, T., J. Mol. Spectrosc. 242, 31-38 (2007).
23. A. R. W. McKellar, Tokaryk, D. W., Li-Hong Xu., Appadoo, D. R. T., J. Mol. Spectrosc. 244, 146-152 (2007).
24. A. R. W. McKellar, Appadoo, D. R. T., J. Mol. Spectrosc. 250, 146-152 (2008).
25. R. J. S. G. L. Carr, L. Mihaly, H. Zhang, D. H. Reitze, D. B. Tanner, Infrared Phys. Technol. 51, 404-406 (2008).
26. K. K. A. S. Albert, P. Lerch, M. Quack, Faraday Discuss. 150, 71-99 (2011).

27. J. B. Brubach, Manceron, L., Rouzières, M., Pirali, O., Balcon, D., Kwabia Tchana, F., Boudon, V., Tudorie, M., Huet, T., Cuisset, A., Roy, P., Infrared Phys. Technol. 223 (2009).

28. J. Barros, Manceron, L., Brubach, J. B., Creff, G., Evain, C., Couprie, M. E., Loulergue, A., Nadolski, L., Tordeux, M. A., Roy, P., Europhys. Lett. 98, 40006 (2012).

29. L. S. Rothman, Gordon, I. E., Barbe, A., Benner, D. C., Bernath, P. F., Birk, M., Boudon, V., Brown, L. R., Campargue, A., Champion, J.-P., Chance, K., Coudert, L. H., Dana, V., Devi, V. M., Fally, S., Flaud, J.-M., Gamache, R. R., Goldman, A., Jacquemart, D., Kleiner, I., Lacome, N., Lafferty, W., J., Mandin, J.-Y., Massi, S. T., Mikhailenko, S. N., Miller, C. E., Moazzen-Ahmadi, N., Naumenko, O. V., Nikitin, A. V., Orphal, J., Perevalove, V. I., Perrin, A., Predoi-Cross, A., Rinsland, C. P., Rotger, M., Simečková, M., Smith, M. A. H., Sung, K., Tashkun, S. S., Tennyson, J., Toth, R. A., Vandaele, A. C., Auwera, J. V., J. Quant. Spectrosc. Radiat. Transfer 110, 533-572 (2008).

30. D. McNaughton, McGilvery, D., Shanks, F., J. Mol. Spectrosc. 149, 458-473 (1991).

31. F. W. Loomis, Wood, R. D., Phys. Rev. 32, 223-237 (1928).

32. H. M. Pickett, J. Mol. Spectrosc. 148, 371-377 (1991).

33. J. K. G. Watson, Vibrational Spectra and Structure 6 (ed. Duric, J. R., Elsevier, Amsterdam) (1877).

34. M. V. F. J. M. M. L. Senent, R. Domínguez-Gómez, ApJ 627, 567-576 (2005).

35. J. K. G. Watson, J. Mol. Spectrosc. 153, 211-224 (1992).

Declaration for Thesis Chapter 2.2.3

Declaration by candidate

In the case of Chapter 2.2.3, the nature and extent of my contribution to the work was the following:

Nature of contribution	**Extent of contribution (%)**
Initiation, key ideas, development and writing up	80

The following co-authors contributed to the work. If co-authors are students at Monash University, the extent of their contribution in percentage terms must be stated:

Name	**Nature of contribution**	**Extent of contribution (%) for student co-authors only**
C. D. Thompson	Initiation and key ideas	
D. R. T. Appadoo	Experimental assistance	
E. G. Robertson	Initiation and key ideas	
C. Medcraft	Experimental assistance	5 %
D. McNaughton	Initiation and key ideas	

The undersigned hereby certify that the above declaration correctly reflects the nature and extent of the candidate's and co-authors' contributions to this work*.

Candidate's Signature		**Date**
Main Supervisor's Signature		**Date**

*Note: Where the responsible author is not the candidate's main supervisor, the main supervisor should consult with the responsible author to agree on the respective contributions of the authors.

High resolution far infrared spectroscopy of HFC-134a using a collisional cooling cell adapted to a synchrotron source.

Andy Wong[1], Chris Medcraft[1,2], Christopher D. Thompson[1], Evan G. Robertson[3], Dominique Appadoo[4] and Don McNaughton[1]*

1. School of Chemistry, Monash University, Wellington Road, Clayton, Victoria, 3800, Australia.
2. Current address: Max-Planck-Institut für Struktur und Dynamik der Materie, 22761, Hamburg Germany
3. Department of Chemistry & Physics, La Trobe Institute of Molecular Sciences, La Trobe University, Victoria 3086, Australia
4. Australian Synchrotron, 800 Blackburn Road, Clayton, Victoria, 3168, Australia

* Corresponding author [redacted] fax 61399054597

Abstract

A low temperature (176 K), high resolution far-IR spectrum of 1,1,1,2-tetrafluoroethane (HFC-134a) has been recorded at the Australian Synchrotron Far-IR beamline. The ν_8 band, located at 665.62 cm^{-1}, has been analysed and 4635 ro-vibrational transitions were assigned and confirmed using ground state combination differences. Local perturbations emanating from two interacting dark states were identified, and subsequently treated using two *c*-axis Coriolis coupling terms. The necessary modifications of a collisional cooling/enclosive flow cooling cell for synchrotron far-IR spectroscopy are outlined.

Keywords

R134a, Synchrotron far-IR, collisional cooling, greenhouse gas, high resolution spectroscopy, hydrofluorocarbons

Citation: A. Wong, C. Medcraft, C. D. Thompson, E. G. Robertson, D. Appadoo and D. McNaughton, *Chem. Phys. Lett.*, **634**, 225 (2015).

Introduction

Since the signing of the Montreal protocol, uses of chloro-fluoro-carbons (CFC's) and other molecules containing halogens such as iodine and bromine have been forbidden due to their significant ozone depleting properties. As a result, hydro-fluoro-carbons (HFC's) have been synthesized for industrial use as foam blowing agents and refrigerants. Although these molecules do not cause ozone depletion, they can have long atmospheric lifetimes and also strong absorptions in the greenhouse window. This leads to large atmospheric global warming potentials, therefore creating a need for these molecules to be continually monitored. By 2011, the atmospheric concentration of HFC-134a had risen to 63 ppt, an increase of 28 ppt from 2005 levels [1]. HFC-134a has an atmospheric lifetime of 13 years with a 100-year global warming potential of 1300 relative to CO_2 [2]. Because of this relatively high GWP, its use is being phased out in Europe. High resolution Fourier transform infrared (FTIR) techniques are suitable for this application because once fully assigned to obtain accurate ro-vibrational constants, spectra can be simulated at any temperature and pressure relevant to different parts of the Earth's atmosphere. This paper seeks to contribute to the vast amount of literature data for a large number of atmospherically important molecules [3].

R134a was first studied spectroscopically at low resolution in the far-IR region by Danti et al [4]. Later, Nielsen and Halley [5] recorded the mid-IR spectrum up to 6000 cm^{-1} and a liquid Raman spectrum. The Raman spectroscopy was re-examined by Lopata and Durig in 1977 [6] using gas phase measurements, and a subsequent study combining jet-cooled mid-IR spectra, room temperature far-IR spectra and *ab initio* calculations updated the assignment of fundamental bands [7]. The first rotational study in the microwave region was performed by Ogata and Miki later [8], followed by Xu et al [9] and then Ilyushin et al [10]. To date, only three of the 18 normal vibrational modes, and one other band, have been analysed using high resolution FTIR techniques: ν_6 [11]; ν_{14}, ν_{15} and [7]; ν_{14} has also been analysed using diode laser jet spectroscopy [12]. Another band near ν_{15}, first assigned as the hot band $\nu_{15} = 1;\nu_{18} = 1 \leftarrow \nu_{18} = 1$ [7], was subsequently shown to be $\nu_8 = 1;\nu_{18} = 3 \leftarrow \nu_{18} = 1$ from Fourier transform microwave spectroscopy [9]. Assignment and fitting of such complex ro-vibrational bands, even at high resolution is often precluded by a plethora of highly populated rotational and vibrational states at room temperature because of spectral congestion. With a number of low wavenumber modes, HFC-134a suffers from such a problem, thus previous IR work was carried out at low temperatures [10] or in a jet expansion [7]. In the far-IR region, spectral band intensities are usually extremely low further complicating spectral assignment. Hence in this work we describe how we have coupled an enclosive flow cooling cell to the synchrotron source at the Australian synchrotron Far-IR beamline to provide increased source brightness and higher signal to noise ratio as a result of a highly collimated beam. We also present the resultant analysis of the low temperature high resolution FTIR spectrum for the ν_8 band of HFC-134a located at 665.52 cm^{-1}.

Instrumental and experimental

Collisional and enclosive flow cooling

For these low temperature gas phase experiments we have coupled a collisional cooling cell to the far-IR beamline at the Australian synchrotron. The cell itself can be used in an enclosive flow cooling mode and has been described thoroughly elsewhere [13]; in brief it consists of an inner invar steel cylinder enclosing White cell optics capable of up to 20 M in optical path length, multiple heaters and thermocouples. This cylinder is similar to a colander with a large number of small holes that allow for a flow of buffer gas to enter from an outer cylinder which seals the vacuum via an indium gasket. The whole assembly sits inside a large glass Dewar that can be filled, or part filled, with coolant (liquid helium, liquid nitrogen or cold gas) to achieve temperatures between 10 - 350 K. The infrared windows are located outside of this Dewar and are kept at ambient temperature thus preventing thermal stress or water condensation issues. In this work the mode utilized is a flow of cold nitrogen gas through the volume between the outer cylinder and the Dewar which can be controlled to achieve stable equilibrium temperatures from ≈ 100 K to 250 K. This mode of operation is particularly useful for high resolution studies where spectra are often recorded over a number of days and temperature stability is crucial. In this mode of operation the temperature of the sample can be maintained at ± 0.5 K for days.

In its original optical configuration for mid-IR spectroscopy, the collisional cooling cell was coupled to the Bruker IFS125 spectrometer (Bruker Optics, Karlsruhe, Germany) via the parallel exit port of the IFS125, and the IR beam was then steered through the cell onto a liquid nitrogen cooled MCT or InSb detector mounted in the evacuated optical chamber of the cooling system. The detector mount was not capable of handling the large liquid helium cooled bolometers which are conventionally used in the far-IR, thus limiting studies to the mid-IR region (> 700 cm^{-1}).

The infrared flux advantage of the synchrotron output is maximized in the far-IR. In order to take advantage of this the optics for the beam exiting the cooling cell were replaced with a system to direct the beam back into the spectrometer and directly onto the far-IR (as well as mid-IR) detectors mounted in the vacuum chamber of the IFS125. The new optical setup is illustrated in **figure 1** where the expanding beam at the exit of the cell is directed to an off axis parabolic mirror (F); the resultant collimated beam is steered into the sample compartment of the spectrometer (top view panel in **figure 1**) and focussed with a second off axis parabolic mirror (J). The two flat mirrors (K, M) can be translated to bring the beam to a focal point coincidental with the spectrometers focus (N).

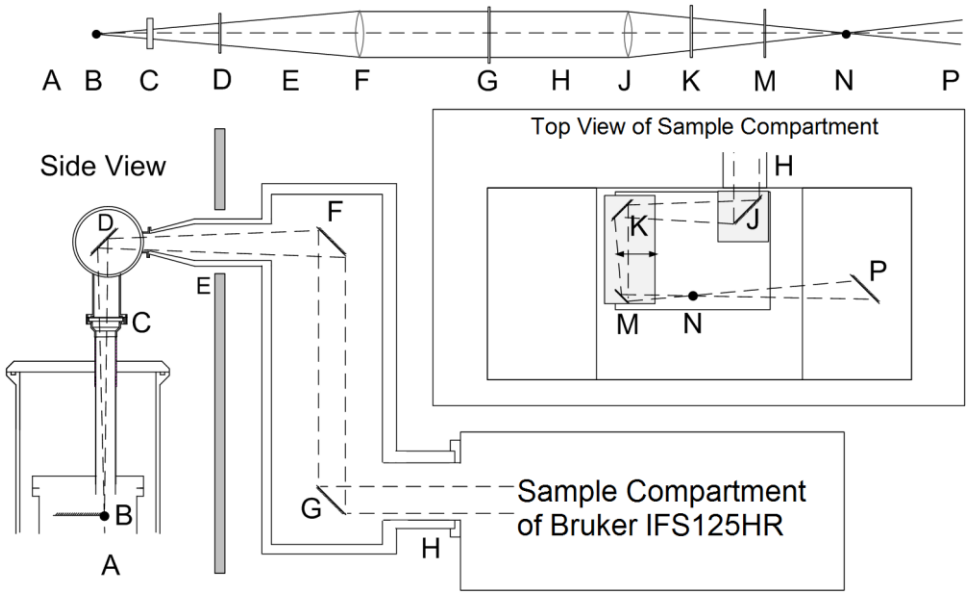

Figure 1: Optical schematic of cooling cell transfer optics, not to scale. A: cooling cell optics, B: Focal point of white cell optics, f/16, C: cooling cell window, D: plane mirror, E: supporting plate for cooling cell, F: collimating mirror (off axis parabolic mirror, f/16), G: plane mirror, H: entrance into spectrometer, J: focussing mirror (off axis parabolic mirror, f/6.5), K & M: plane mirrors on translation state, N: spectrometer focus location, P: spectrometer optics (beam goes onward to detector compartment).

The beam then passes into the detector compartment of the spectrometer where any one of the five IR detectors can be selected. The resultant apparatus provides us with a unique system for spectroscopy of cold gases and aerosols in the far-IR and we have recently demonstrated the application of the cold collisional cell within the far-IR region for ice nanoparticles [14], as well as for spectra of cold C_2F_4 [15].

HFC-134a experimental conditions

At the time of recording the far-IR spectra the synchrotron was operating in a decay mode where the beam current decreased from 200 to 150 mA over several hours before electron bunch injections. The spectrometer was equipped with a KBr beamsplitter, a numerical aperture of 3.15 mm and an external liquid helium cooled, boron-doped silicon photodetector set to a pregain of 4000. Sample spectra were recorded at 0.00096 cm^{-1} and treated with a four point apodization function during the Fourier transform and a zero fill factor of two. The collisional cooling cell was pre-cooled to 176 K using cold gas and set to 4 passes (optical path length = 2.5 m) before recording a background reference spectrum under vacuum conditions. 38 kPa of HFC-134a sample gas (BOC, 99 % purity) was then introduced into the cell and a total of 400 scans (recorded in batches of 20 × 2 co-additions) were added and weighted by the number of scans.

Results and discussion

Prior to any analysis, the final spectrum was treated with a post zero fill factor of eight and then calibrated to the HITRAN08 database [16] using residual CO_2 lines near 685 cm^{-1}. A peak list was generated using the peak pick function in OPUS 6.0 [17] for importation into MacLoomis [18]. MacLoomis presents the IR spectrum in a Loomis-Wood format [19] so that regularly spaced sets of ro-vibrational transitions, such as those with the same K_a', are grouped together. Transitions with increasing values of J' quantum number are then lined up vertically down the centre of the screen when fitted to a polynomial expansion. The MacLoomis software provides advantages such as colour coding and pattern recognition which aid transition assignment and although the program is based on the Hamiltonian for a linear molecule, even highly asymmetric molecules are successfully treated for assignment [20-23].

HFC-134a is a near prolate asymmetric top molecule, κ = -0.989, with C_s symmetry and 18 normal vibrational modes, all of which are IR and Raman active. The ν_8 band is assigned as the CF_3 symmetric deformation with *a*/*b*-hybrid band structure (A' symmetry). A total of 4344 (2509 *a*-type and 1835 *b*-type) ro-vibrational transitions have been assigned and confirmed using ground state combination differences, with K_a' max and J' max of 26 and 66 respectively. Confirmed transitions with $K_a' < 20$ were subsequently fitted to Watson's *S*-reduced Hamiltonian in the I^r representation [24] using Pickett's SPFIT and SPCAT software packages [25].

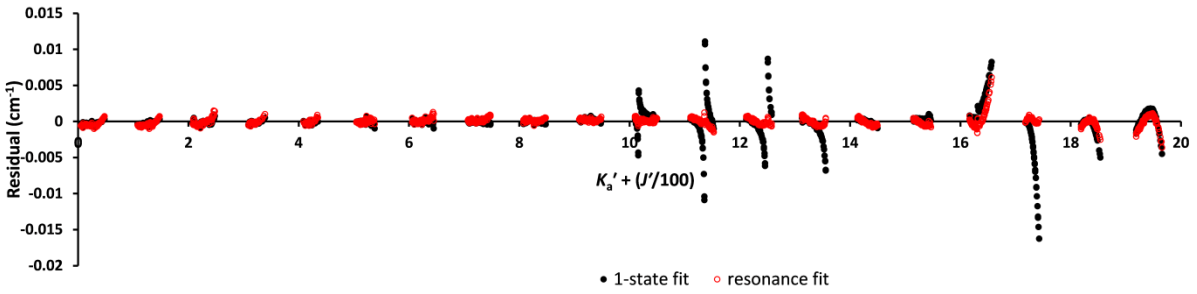

Figure 2: A residual plot of the ν_8 band. The black and red data points indicate the fit before and after the inclusion of the interacting states.

With so many ro-vibrational transitions being fitted, it can be difficult to efficiently interpret the SPFIT output file. However, a residual plot overcomes this problem by visually displaying any ro-vibrational transitions that may either be incorrectly assigned or perturbed. The residual (observed – calculated) wavenumber values for the fit of this ν_8 band without the inclusion of any interacting states is shown as the black symbols in **figure 2**. It is quite clear from the plot that there are interacting states perturbing the ν_8 band: namely the avoided level crossings affecting K_a' 10 – 13 and the perturbed series ranging from K_a' 15 – 19. Additionally, the transitions with $K_a' \geq 20$ are heavily perturbed, however they were not included in the fit (outlined below) and thus are not shown

here. The energy levels associated with the other fundamentals are too far away to interact with ν_8 at 665.5 cm^{-1}, the nearest being ν_9 at 549.4 cm^{-1} [7], and therefore combination and overtone levels must be considered. From the harmonic approximation, a total of five possible combination and overtones are possible with wavenumber values of $\pm$ 25 cm^{-1} from $\nu_8 = 1$, **figure 3**, making it difficult to pinpoint which level or levels are interacting with $\nu_8 = 1$. Wavenumber values for the fundamental levels, specifically $\nu_{11} = 1$, are taken from [7], whereas $\nu_{18} = 2$ and $\nu_{18} = 3$ overtone values are taken from [6]. Also, due to symmetry considerations, all vibrational modes can in principle interact with one another since their cross-products (A' x A', A'' x A'' or A' x A'') all contain a rotational component in the C_s point group table, further complicating the issue.

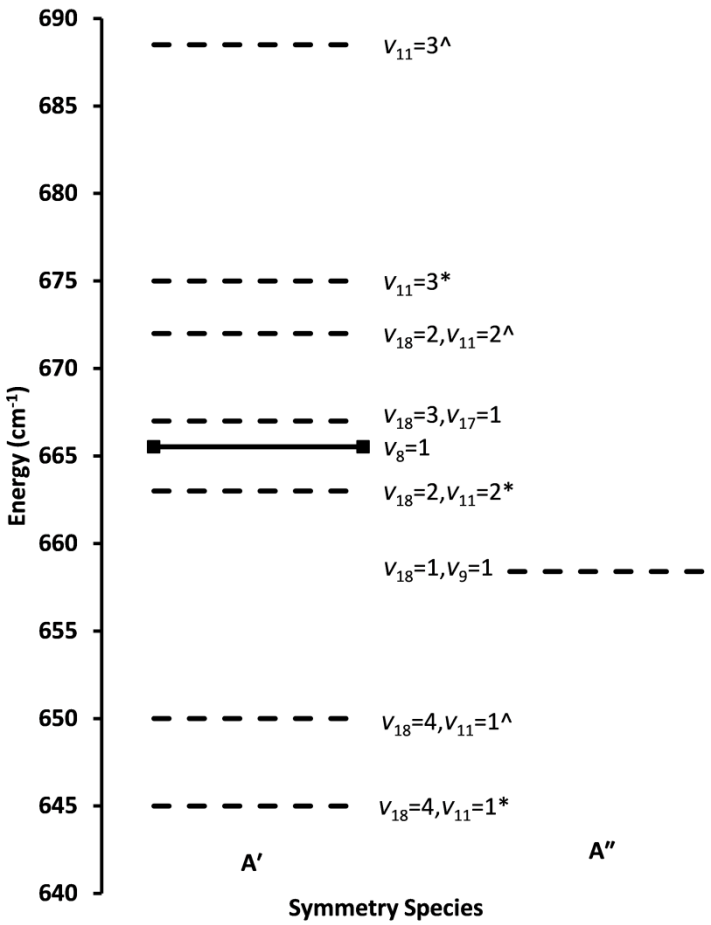

Figure 3: Possible combinations near the $\nu_8 = 1$ vibrational level. Those with * and ^ denote a wavenumber value for $\nu_{11} = 1$ of either 225 cm^{-1} or 229.5 cm^{-1} respectively.

Transitions with $K_a < 20$ can be fitted using only the band centre value, rotational constants (A, B, C) and the quartic centrifugal distortion constants (D_J, D_{JK}, D_K and d_2). The higher order sextic (H_J, H_{JK}, H_{KJ}, H_K, h_1, h_2 and h_3) and octic (L_{JK}, L_{KKJ}) terms were constrained to their respective ground state values. Although the rms deviations could be slightly improved by fitting the sextic and octic centrifugal distortion constants, their values deviated greatly from their respective ground state values, resulting in a purely effective fit that would not be useful for spectral prediction at different temperatures. The standard deviation of the fit for transitions with $K_a' < 20$ is significantly improved with the inclusion of two first order c-axis Coriolis coupling terms for two interacting dark states with A' symmetry. Dark states 1 and 2 treat the perturbations at K_a' 10 – 13 and K_a' 15 – 19, respectively. It is possible to fit transitions with $K_a' \geq 20$, however it would require at least a third interacting state to achieve a satisfactory fit. Thus, transitions with $K_a' \geq 20$ were not included in the final fit.

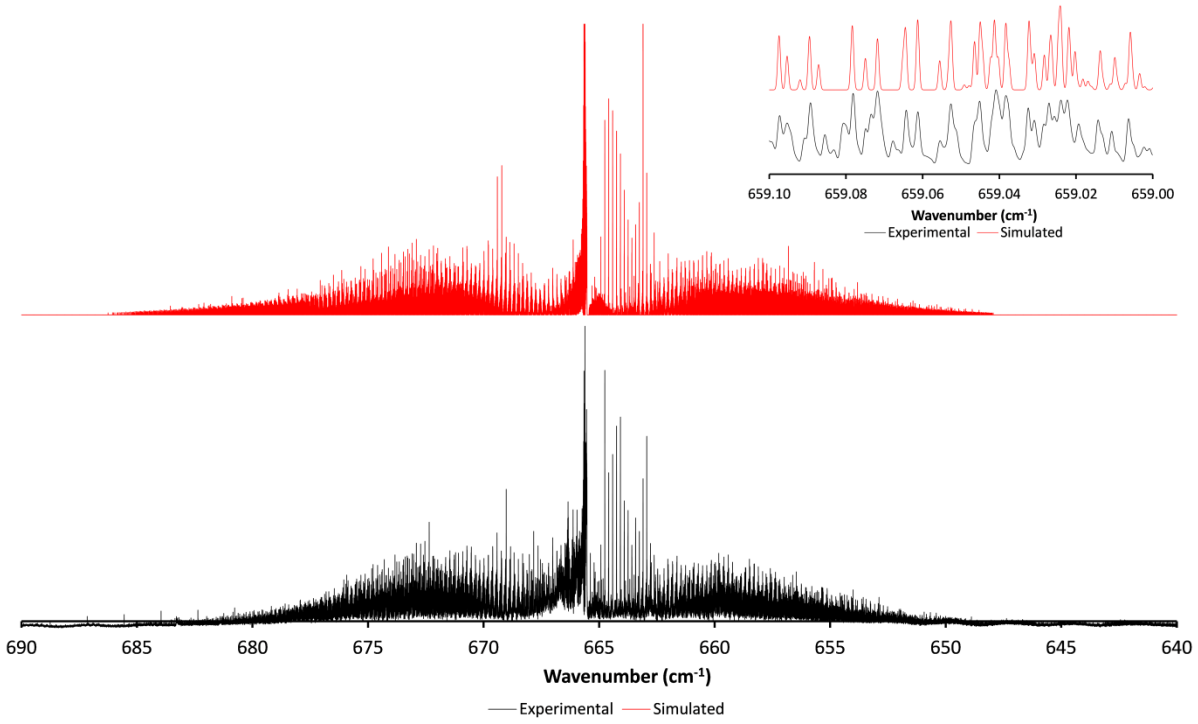

Figure 4: Experimental and simulated spectra of the ν_8 band at 176 K. Spectra have been vertically offset for easy of comparison.

Considering the above, a global fit of the ν_8 band with two interacting states results in a satisfactory fit for the ro-vibrational transitions with $K_a' < 20$. The residuals are shown as the red data points in **figure 2**. Only the band centre, A, $\frac{(B+C)}{2}$ and $\frac{(B-C)}{4}$ have been fitted for the interacting states with all centrifugal distortion constants constrained to their respective ground state values, given in **table 1**. The final fit to the data is included in a supplementary file [26] and contains all assigned transitions along with their associated residuals from the SPFIT output. From the fitted constants of the ν_8 band, and two interacting states, a simulated spectrum can then be produced to compare with the experimental (**figure 4**). Discrepancies between the simulated and experimental spectrum are accounted for by a) errors propagating from the fit, where residuals for assigned transitions are greater than 0.005 cm^{-1} (see inset of **figure 4**) and b) intensity contributions from hot bands originating from low energy vibrational states which have not been accounted for in this simulation. Although the spectra were recorded at 176 K, only 44 % of molecules are in the ground vibrational state, with 18 % and 7 % of molecules occupying the $v_{18} = 1$ and $v_{11} = 1$ vibrational states respectively and 7.4 % in $v_{18} = 2$. The presence of these hot bands is most apparent in the intense Q-bands near 667 cm^{-1} in the experimental spectrum.

Table 1. Fitted rotational and centrifugal distortion constants in Watson's *S*-reduced I^r Hamiltonian for the ground state and $v_8 = 1$ of R134a (MHz)

Constant	Ground state[i]	$v_8 = 1$	DS 1	DS 2
Band centre / cm^{-1}	-	665.5240016 (3)	663.55945 (1)	662.86046 (1)
A	5355.617460	5365.4457010 (463)	5411.88196 (204)	5339.81642 (121)
B	2799.217245	2799.2419521 (143)	-	-
C	2759.436637	2758.4937970 (136)	-	-
$\frac{(B+C)}{2}$	2779.326941	-	2773.076429 (248)	2777.819761 (211)
$\frac{(B-C)}{4}$	9.9451518	--	12.38729 (325)	[ii]
D_J	0.0005121585	0.00051713217 (311)	[ii]	[ii]
D_{JK}	0.004330557	0.0028352304 (311)	[ii]	[ii]
D_K	-0.003399581	-0.004749226 (164)	[ii]	[ii]
$d_1 \times 10^{-6}$	0.6551	[ii]	[ii]	[ii]
$d_2 \times 10^{-6}$	-2.78768	-4.1591 (160)	[ii]	[ii]
$H_J \times 10^{-10}$	0.6244	[ii]	[ii]	[ii]
$H_{JK} \times 10^{-8}$	0.22642	[ii]	[ii]	[ii]
$H_{KJ} \times 10^{-8}$	0.3860	[ii]	[ii]	[ii]
$H_K \times 10^{-8}$	-0.5037	[ii]	[ii]	[ii]
$h_1 \times 10^{-12}$	-0.633	[ii]	[ii]	[ii]
$h_2 \times 10^{-11}$	0.8816	[ii]	[ii]	[ii]
$h_3 \times 10^{-11}$	-0.283	[ii]	[ii]	[ii]
$L_{JK} \times 10^{-13}$	0.1007	[ii]	[ii]	[ii]
$L_{KKJ} \times 10^{-13}$	-0.2998	[ii]	[ii]	[ii]
$G^c_{(8,DS1)}$[iii]	-	-	26.40100 (344)[iv]	-
$G^c_{(8,DS2)}$[iii]	-	-	-	25.56040 (402)[iv]
J' max	-	66	-	-
K_a' max	-	20	-	-
number trans.		4344	-	-
r.m.s deviation / cm^{-1}		0.005	-	-
σ_{dev}	-	1.438	-	-

Figures in brackets are one standard deviation according to the least squares fit in units of the least significant figure quoted.

[i] Ground state constants and uncertainties from Ilyushin et al 1999 [9].

[ii] Constants constrained to their respective ground state values.

[iii] Denotes first order *c*-axis Coriolis terms G^c (is equivalent to ζ) is defined in the fit as $\langle v_i|\Psi_{first\ order}|v_j\rangle = iG^c_{i,j}P_b$ and is given in units of MHz.

Conclusion

The application of a collisional cooling cell in high resolution FTIR spectroscopy significantly reduces the complexity of ro-vibrational spectra if recorded at cold temperatures. By modifying the optics of the collisional cooling cell to redirect the beam back into the IFS125 it is also possible to take advantage of the synchrotron far-IR source which provides superior data quality in the far-IR region. This combination is likely to prove beneficial considering the increasing interest in atmospheric studies that are centred on the far-IR region, illustrated by programs such as the FORUM explorer [27] (The Far-Infrared Outgoing-Radiation-Understanding and Monitoring explorer) and the FIRST instrument [28] (The Far-Infrared Spectroscopy of the Troposphere Instrument).

Acknowledgements

We thank the staff at the Australian synchrotron Far-IR beamline for helping record the spectra, as well as the synchrotron facility. AW would also like to thank the Monash University Faculty of Science for a Dean's post graduate scholarship.

References

[1] L. V. Alexander, S. Brönnimann, Y. A. –R. Charabi, F. J. Dentener, E. J. Dlugokencky, D. R. Easterling, A. Kaplan, B. J. Soden, P. W. Thorne, M. Wild, P. Zhai, IPCC, Climate Change 2013: The Physical Science Basis, Chapter 2

[2] F. –M. Bréon, W. Collins, J. Fuglestvedt, J. Huang, D. Koch, J. –F. Lamarque, D. Lee, B. Mendoza, T. Nakajima, A. Robock, G. Stephens, T. Takemura, H. Zhang, IPCC, Climate Change 2013: The Physical Science Basis, Chapter 2

[3] D. McNaughton, E. G. Robertson, C. D. Thompson, T. Chimdi, M. K. Bane and D. Appadoo, *Anal. Chem.* **82**, 7958 (2010)

[4] A. Danti and J. L. Wood, *J. Chem. Phys.* **30**, 582 (1959)

[5] J. R. Nielsen and C. J. Halley, *J. Mol. Spectrosc.* **17**, 341 (1965)

[6] A. D. Lopata and J. R. Durig, *J. Raman Spectrosc.* **6**, 61 (1977)

[7] D. McNaughton, C. Evans and E. G. Robertson, *J. Chem. Soc. Faraday. Trans.* **91**, 1723 (1995)

[8] T. Ogata and Y. Miki, *J. Mol. Struc.* **140**, 49 (1986)

[9] L. -H. Xu, A. M. Andrews, R. R. Cavanagh, G. T. Fraser, K. K. Irikura, F. J. Lovas, J. -U. Grabow, W. Stahl, M. K. Crawford and R. J. Smalley, *J. Phys. Chem. A* **101**, 2288 (1997)

[10] V. V. Ilyushin, E. A. Alekseev, S. F. Dyubko and O. I. Baskakov, *J. Mol. Spectrosc.* **195**, 246 (1999)

[11] C. D. Thompson, E. G. Robertson, C. J. Evans and D. McNaughton, *J. Mol. Spec.* **218**, 48 (2003)

[12] M. Snels and G. D'Amico, *J. Mol. Spectrosc.* **221**, 156 (2003)

[13] S. Bauerecker, M. Taraschewski, C. Weitkamp, H. K. Cammenga, *Rev. Sci. Instrum.* **72**, 3946 (2001)

[14] C. Medcraft, D. McNaughton, C. D. Thompson, D. R. T. Appadoo, S. Bauerecker, E. G. Robertson, *ApJ* **758**, 1 (2012)

[15] C. Medcraft, W. Fuss, D. R. T. Appadoo, D. McNaughton, C. D. Thompson and E. G. Robertson, *J. Chem. Phys.* **137**, 214301 (2012)

[16] L. S. Rothman, I. E. Gordon, A. Barbe, D. C. Benner, P. F. Bernath, M. Birk, V. Boudon, L. R. Brown, A. Campargue, J. -P. Champion, K. Chance, L. H. Coudert, V. Dana, V. M. Devi, S. Fally, J. –M. Flaud, R. R. Gamache, A. Goldman, D. Jacquemart, I. Kleiner, N. Lacome, W. J. Lafferty, J. –Y. Mandin, S. T. Massie, S. N. Mikhailenko, C. E. Miller, N. M. –Ahmadi, O. V. Naumenko, A. V. Nikitin, J. Orphal, V. I. Perevalov, A. Perrin, A. P. –Cross, C. P. Rinsland, M. Rotger, M. Šimečková, M. A. H. Smith, K. Sung, S. A. Tashkun, J. Tennyson, R. A. Toth, A. C. Vandaele, J. Vander Auwera, *J. Quant. Spectrosc. Radiat. Transfer* **110**, 533 (2009)

[17] OPUS Version 6.0, *Build: 6, 0, 72 (20060822) Copyright © Bruker Optik GmbH*.

[18] D. McNaughton, D. McGilvery and F. Shanks, *J. Mol. Spectrosc.* **149**, 458 (1991)

[19] F. W. Loomis and R. W. Wood, *Phys. Rev.* **32**, 223 (1928)

[20] M. K. Bane, E. G. Robertson, C. D. Thompson, C. Medcraft, D. R. T. Appadoo and D. McNaughton, *J. Chem. Phys.* **134**, 234306 (2011)

[21] C. Medcraft, C. D. Thompson, E. G. Robertson, D. R. T. Appadoo and D. McNaughton, *ApJ* **753**, 1 (2012)

[22] M. K. Bane, E. G. Robertson, C. D. Thompson, D. R. T. Appadoo and D. McNaughton, *J. Chem. Phys.* **135**, 224306 (2011)

[23] M. K. Bane, C. D. Thompson, D. R. T. Appadoo and D. McNaughton, *J. Chem. Phys.* **137**, 084306 (2012)

[24] J. K. G. Watson, *in Vibrational Spectra and Structure*, edited by J. R. Durig (Elsevier, Amsterdam, 1977), **vol 6**.

[25] H. M. Pickett, *J. Mol. Spectrosc.* **148**, 371 (1991)

[26] The SPFIT output file converted to a readable format using PIFORM

[27] L. Palchetti, Contribution to the CLARREO Science Definition Team Meeting (2011)

[28] M. G. Mlynczak, R. P. Cageao, H. Latvakoski, D. Kratz, D. Johnson and J. Mast, *Earthzine* (2013)

Declaration for Thesis Chapter 2.2.4

Declaration by candidate

In the case of Chapter 2.2.4, the nature and extent of my contribution to the work was the following:

Nature of contribution	**Extent of contribution (%)**
Initiation, key ideas, development and writing up	80

The following co-authors contributed to the work. If co-authors are students at Monash University, the extent of their contribution in percentage terms must be stated:

Name	**Nature of contribution**	**Extent of contribution (%) for student co-authors only**
C. D. Thompson	Initiation and key ideas	
D. R. T. Appadoo	Experimental assistance	
M. Gabona	Analysis assistance	5 %
D. McNaughton	Initiation and key ideas	
A. T. T. Lee	Initiation and key ideas	

The undersigned hereby certify that the above declaration correctly reflects the nature and extent of the candidate's and co-authors' contributions to this work*.

Candidate's Signature		**Date**
Main Supervisor's Signature		**Date**

*Note: Where the responsible author is not the candidate's main supervisor, the main supervisor should consult with the responsible author to agree on the respective contributions of the authors.

High resolution FTIR spectral analysis of the tetrad system (ν_4, ν_7, ν_{10} and ν_{12}) of *Trans*-d_2-ethylene

Andy Wong[a], T. L. Tan[b], M. G. Gabona[b], Dominique Appadoo[c] and Don McNaughton[a]*.

[a] *School of Chemistry, Monash University, Wellington Rd., Clayton, Victoria, 3800, Australia.*

[b] *Natural Sciences and Science Education, National Institute of Education, Nanyang Technological University, 1 Nanyang Walk, Singapore 637616, Singapore.*

[c] *Australian Synchrotron, 800 Blackburn Rd., Clayton, Victoria 3168.*

Running head: High resolution FTIR spectral analysis of *Trans*-d_2-ethylene

***Corresponding author:**

Prof. Don McNaughton

School of Chemistry, Monash University
Wellington Rd., Clayton, Victoria 3800
Australia

[redacted]

Keywords:

Trans-$C_2H_2D_2$; ethylene isotopologue, rovibrational structure of ethylene, high-resolution FTIR spectroscopy; rovibrational constants; Coriolis coupling

Submitted: Journal of Molecular Spectroscopy

Abstract

The rotational and centrifugal distortion constants for both the ground state, and the tetrad system below 1300 cm^{-1}, have been re-assessed using ro-vibrational transitions from two high resolution spectra recorded at 0.00096 (ν_7, ν_4, and ν_{12}) and 0.0063 cm^{-1} (ν_{10}) resolution. The number of centrifugal distortion constants required to fit the ground state are reduced from 11 to 9 and compared to anharmonic values from MP2/cc-pVTZ calculations. Molecular constants for the tetrad system (ν_{10}, ν_7, ν_4 and ν_{12}) have also been determined in a global analysis and Coriolis coupling terms linking the four states together have been fitted with uncertainties < 4 %.

Introduction

Trans-d_2-ethylene is a near prolate asymmetric top molecule with C_{2h} symmetry, $\kappa \approx 0.88$, and 12 normal fundamental vibrations (six infrared (IR) active and six Raman active). Of the IR active bands, four are located below 1300 cm^{-1} forming a tetrad system (ν_{10}, ν_7, ν_4 and ν_{12}) and have been previously studied using Fourier transform infrared (FTIR) techniques at various resolutions. The ν_7 band was first analysed by Lauro [1] at a resolution of 1 cm^{-1} with Hegelund *et al.* [2] publishing the first global fit of the tetrad system later. In a following paper [3], the tetrad system was reanalysed at 0.03 cm^{-1} and two second order *a*-axis Coriolis coupling terms were determined for the ν_7 and ν_{10} interacting states. Two combination bands ($\nu_7 = 1;\nu_8 = 1$) and ($\nu_4 = 1;\nu_8 = 1$) have also been analysed by the same group [4]. Recently, the effective molecular constants for the ($\nu_4 = 1;\nu_8 = 1$) [5] and ν_4 [6] bands have been reported by Tan *et al*. using spectra recorded at an unapodized resolution of 0.0063 cm^{-1}; the ν_{12} [7] band was analysed at 0.0024 cm^{-1} and then at 0.0063 cm^{-1} [8] by the same group. In this work a high resolution spectrum (0.00096 cm^{-1}) of *trans*-d_2-ethylene has been recorded at the Australian synchrotron between 650 - 1300 cm^{-1} and a subsequent global analysis of the tetrad system has been performed. Ground state rotational and centrifugal distortion constants are re-fitted using new ground state combination differences and the molecular constants for the perturbed tetrad system have been refined. Furthermore, first and second order Coriolis coupling terms were determined in order to treat resonances linking the four bands together.

Experimental

Trans-d_2-ethylene was obtained from Cambridge Isotope Laboratories (99 % purity) and used without further purification. 1.7×10^{-2} kPa of sample gas was introduced into an ambient temperature cell housing White type optics and set to a path length of 8.8 m (16 passes). The cell, equipped with KBr windows, was coupled to a Bruker IFS125 HR spectrometer situated on the far-IR beamline of the Australian Synchrotron. Synchrotron mid-IR radiation was used for optimum throughput and the spectrometer equipped with a KBr beamsplitter and MCTm detector (recording rate of 80 kHz with preamplifier gain A) between 650 - 1300 cm^{-1}. Spectra were treated with a four point apodization function and a zero fill factor of 2 during the Fourier transformation. A total of 88 sample scans were recorded at 0.00096 cm^{-1} and converted to an absorption spectrum using a background spectrum that was recorded prior to introducing the sample gas

The ν_{10} band was recorded on a Bruker IFS125 at the Spectroscopy Laboratory of the National Institute of Education (NIE), Nanyang Technological University, Singapore. A 20 cm multipass cell was set to a path length of 80 cm and 1.2 kPa of sample gas was introduced into the cell. The internal globar was used as a source with a liquid N_2 cooled MCT detector. A total of 1080 scans were recorded and averaged together before being treated with a four point apodization function and zero fill factor of 2.

Results

Transition assignment

Prior to spectral analysis, a post zero fill factor of 8 was applied to the synchrotron spectrum which was subsequently calibrated to the HITRAN08 database [9] using residual CO_2 lines near 2300 cm^{-1}. The spectrum for the ν_{10} band was also treated with a post zero fill factor of 8 and calibrated to H_2O lines near 1450 cm^{-1}. A survey spectrum of the ν_7, ν_{10} and ν_4 bands is given in **figure 1** and peak lists of for these three bands were generated using the peak pick function in Bruker's OPUS 6.0 software. Transitions for the ν_{10} band were not observed in this experiment because the band origin at 673 cm^{-1} is located near the detector low wavenumber cut-off and is also very weak in intensity. Transition centre wavenumber values were therefore taken from a spectrum recorded at NIE (0.0063 cm^{-1}) and used in the following global fit. Transitions for all four bands were given an uncertainty of approximately 10 % of the experimental full-width half-height (i.e. 0.0002 cm^{-1} for ν_7, 0.00025 cm^{-1} for ν_4, 0.00035 cm^{-1} for ν_{12} and 0.0005 cm^{-1} for ν_{10}). Linewidths for the ν_{10} band are somewhat broadened due to the increased sample pressure required to observe *P*- and *Q*-branch transitions, hence an experimental uncertainty of 0.0005 cm^{-1}.

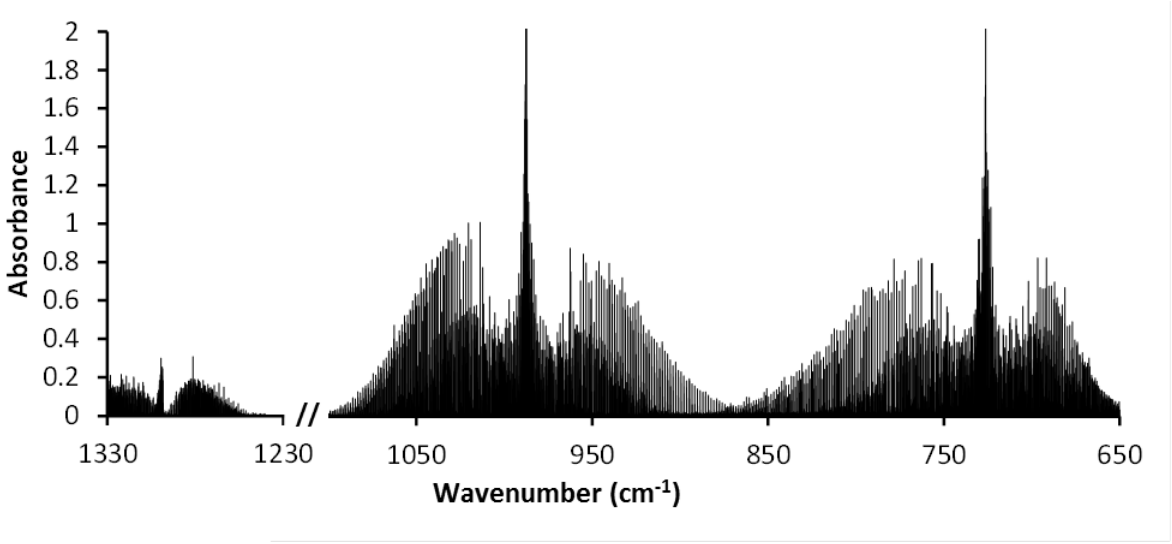

Figure 1: A high resolution survey spectrum of the ν_{12} (1298 cm^{-1}), ν_4 (988 cm^{-1}) and ν_7 (725 cm^{-1}) of *trans*-d_2-ethylene recorded at the Australian Synchrotron at ambient temperature.

Peak lists for all four bands were then imported into MacLoomis [10], where the spectrum is displayed in a Loomis-Wood format [11]. Transitions with a constant K_a' are grouped together with increasing J' quantum number and are aligned vertically down the centre of the screen when fitted to a polynomial expansion. An example Loomis-Wood plot of the *R*-branch for the ν_4 band is given in **figure 2** and can be compared to a traditional high resolution spectrum (**figure 3**) where the series are seen as almost equally spaced sets of lines.

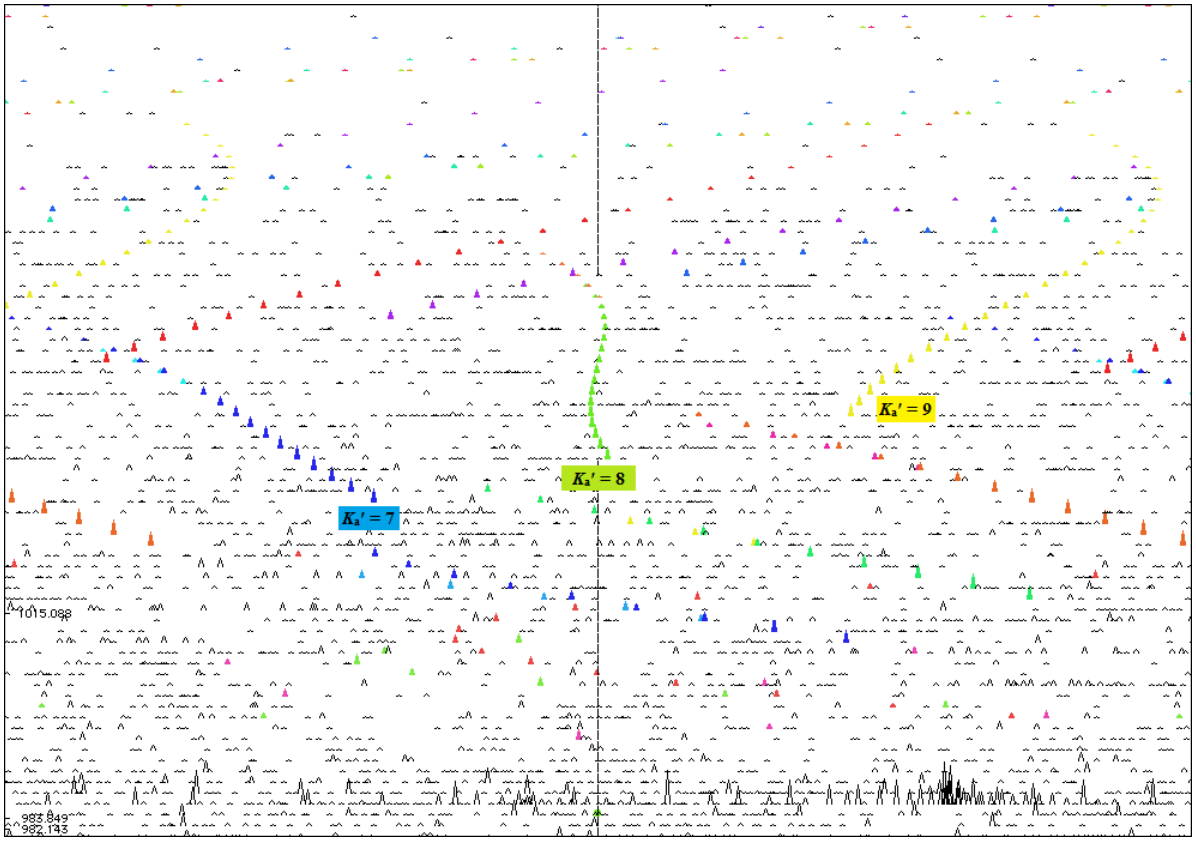

Figure 2: A Loomis-Wood plot of the *R*-branch of the ν_4 band. The $K_a' = 8$ series is displayed as the green triangle in MacLoomis where the *x*-axis is cm^{-1} and the *y*-axis is *J*′.

The four fundamental bands have ro-vibrational transitions which follow *c*-type (ν_7 and ν_4) and *a*- or *b*-type (ν_{10} and ν_{12}) selection rules, although the ν_{10} and ν_{12} are dominated by *b*- and *a*-type transitions respectively. A total of 3138 ro-vibrational transitions have been assigned and fitted to Watson's *A*-reduced rotational Hamiltonian in the I^r representation [12] using Pickett's SPFIT and SPCAT software packages [13]. All spectral assignments were confirmed by ground state combination differences.

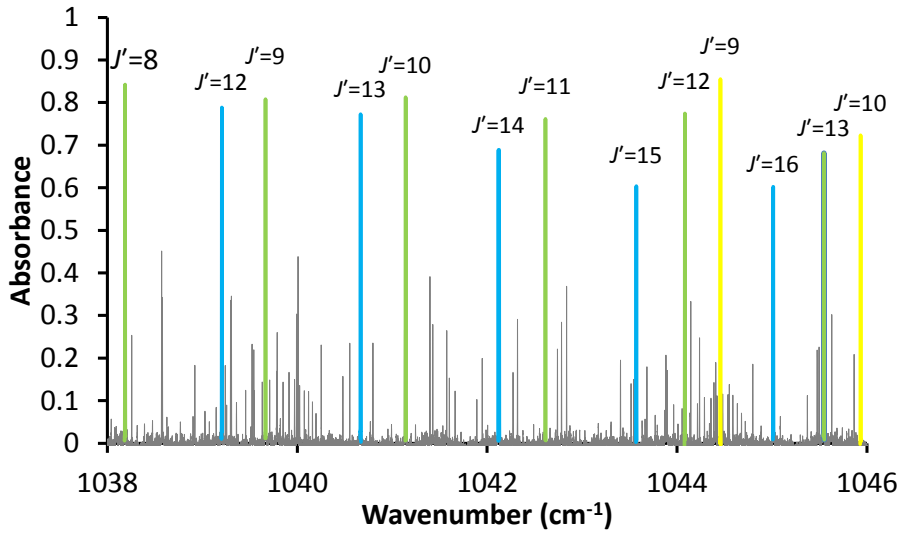

Figure 3: Inset of the ν_4 band showing transitions with K_a' = 7 (blue), K_a' = 8 (green) and K_a' = 9 (yellow).

Ground state fit

1561 ground state combination differences were calculated using *P*- and *R*-branch transitions from the ν_7, ν_4 and ν_{12} bands and were used in the following ground state re-fit. In a recent analysis by Tan *et al*. [8], all of the quartic (Δ_J, Δ_{JK}, Δ_K, δ_J and δ_K) and sextic (Φ_{JK}, Φ_{KJ} and Φ_K) centrifugal distortion constants for the ground state had been fitted using 4597 individual GSCD's from their $\nu_4 = 1;\nu_8 = 1$ [5] fit, data from their previously fitted ν_4 band [6] and the most recently fitted ν_{12} band [8].

The set of ground state combination differences used would have most likely contained duplicate transitions, which were not taken into account, and would have resulted in smaller standard deviations for the fitted constants. This however would not improve the accuracy of the ground state constants as the range of transitions with K_a' and J' would still be quite limited. This is reflected in the relatively large uncertainties for the Φ_{JK} (14 %) and Φ_{KJ} (21 %) constants, as well as their discrepancies with *ab initio* values (**table 1**).

In this study, we have found that it is not essential to fit all three sextic centrifugal distortion constants to achieve a satisfactory fit, as shown in the residual plot in **figure 4**. Residual plots (observed-calculated wavenumber values) are used to visually show the errors associated with fitted transitions and allows for efficient analysis and identification of incorrectly assigned or perturbed transitions. The red data points represent the residuals from the fit excluding all of the sextic centrifugal distortion constants. As (K_a' + J' / 100) increases, the oscillating residuals indicate that it is still necessary to include a higher order term.

All three sextic centrifugal distortion constants (Φ_{JK}, Φ_{KJ} and Φ_K) were initially fitted, however Φ_K was the most precisely determined constant and therefore kept in the ground state fit (black data points in **figure 4**).

Harmonic and anharmonic calculations, in Gaussian09 (Revision D.01) [14], have also been performed by our group using three levels of theory: B3LYP, MP2 and CCSD with a triple zeta (cc-pVTZ) basis set. The resulting rotational and centrifugal distortion constants are provided in columns 1 to 3 (harmonic) and column 4 (MP2 anharmonic) in **table 1**. The calculated values for the quartic centrifugal distortion terms are consistent across all three methods for the harmonic calculations, and match up nicely with the experimental ground state constants with the exception of Δ_{JK}, which has an error of *ca*. 40 %. The experimental values, for Φ_{JK} and Φ_{KJ} from the study by Tan *et al*. [8], are roughly 3.8 and 2.4 times smaller than the predicted values from the MP2/cc-pVTZ anharmonic calculation and are evidence that the fit is indeed an effective fit. The fitted value of Φ_K in this work is closer to the prediction, compared to Tan's value [8], and has an uncertainty of less than 1 %.

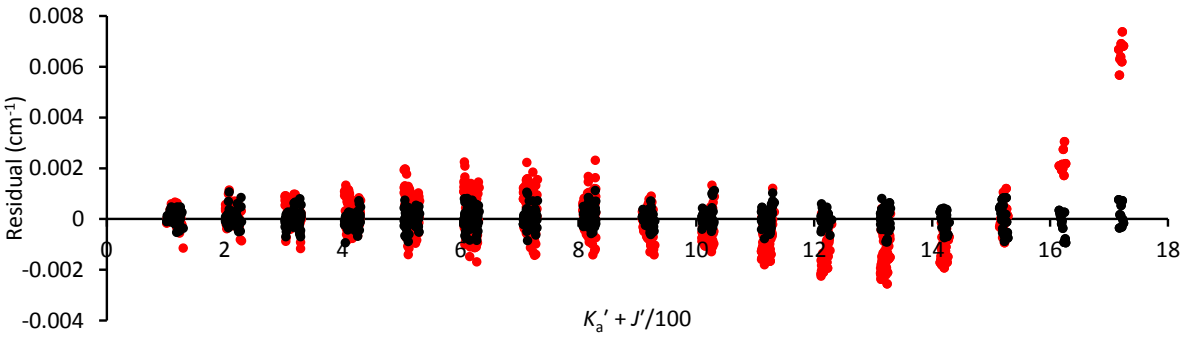

Figure 4: The ground state residual plots with (black) and without (red) the inclusion of the sextic centrifugal distortion term Φ_K.

Table 1: Fitted rotational and centrifugal distortion constants in Watson's *A*-reduced I^r Hamiltonian for the ground state of trans-$C_2H_2D_2$ (MHz)

	Calculations					
	Harmonic			Anharmonic	Tan *et al.* [8][b]	this work
Constant	B3LYP/cc-pVTZ	MP2/cc-pVTZ	CCSD/cc-pVTZ	MP2/cc-pVTZ		
A	105884.28	105374.71	105554.17	105374.71	104513.158 (5)	104513.329 (36)
B	25223.129	25125.680	25088.658	25125.680	24971.5247 (90)	24971.3762 (138)
C	20370.572	20288.148	20270.630	20288.148	20105.2755 (90)	20105.1399 (210)
Δ_J	0.03053	0.03050	0.03012	0.03050	0.0320868 (90)	0.0318473 (160)
Δ_{JK}	0.14488	0.14810	0.14342	0.14810	0.090717 (180)	0.091025 (69)
Δ_K	1.48101	1.41060	1.42443	1.41060	1.68513 (30)	1.68623 (32)
δ_J	0.00687	0.00682	0.00673	0.00682	0.0074289 (30)	0.0074358 (63)
δ_K	0.18030	0.17937	0.17673	0.17937	0.172351 (210)	0.171102 (214)
$\Phi_{JK} \times 10^6$	-	-	-	2.91011	0.77 (11)	-
$\Phi_{KJ} \times 10^6$	-	-	-	-8.41974	-3.57 (75)	-
$\Phi_K \times 10^6$	-	-	-	79.56672	97.10 (144)	95.690 (720)
J' max	-	-	-	-	-	33
K_a' max	-	-	-	-	-	17
Number of trans.	-	-	-	-	4597[c]	1561[c]
r.m.s deviation / cm^{-1}	-	-	-	-	0.0004	0.0003
σ_{dev}	-	-	-	-	-	0.8753

[a] Figures in brackets are one standard deviation according to the least squares fit in units of the least significant figure quoted.
[b] Ground state constants reported by Tan *et al.* 2015 [8].
[c] The number of GSCD's used.

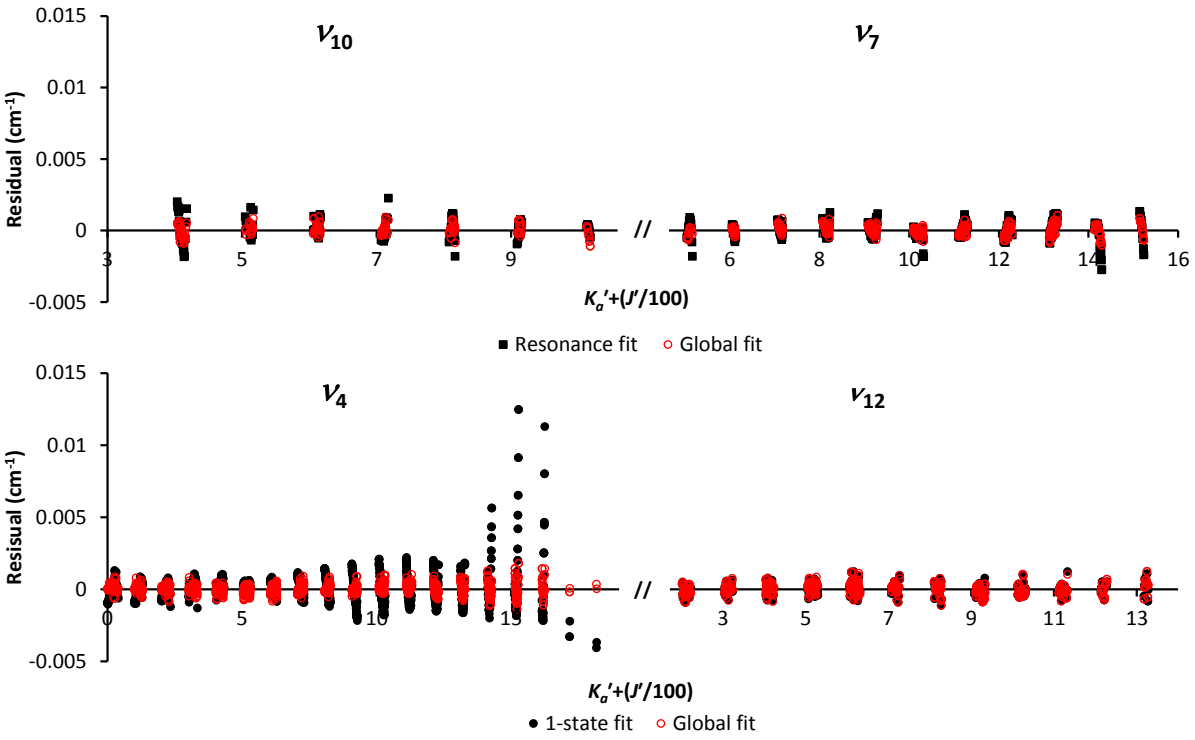

Figure 5: Residual plots for each band within the tetrad system. The top two panels show residuals for the $\nu_7 \leftrightarrow \nu_{10}$ resonance fit (black squares) and global fit (red circles). The bottom two panels show residuals for the 1-state ν_4 and ν_{12} (black circles) as well as the global fit (red circles).

The ν_4 and ν_{12} bands are not greatly influenced by resonance effects, as seen by the black data points in the bottom two panels in **figure 5**, and can be fitted independently prior to their inclusion into the global fit. Transitions with $K_a' = 14 - 16$ for the ν_4 band are somewhat perturbed and in principle, it is possible for both *a*- and *b*-axis Coriolis couplings to occur between $\nu_4 \leftrightarrow \nu_{10}$ as well as $\nu_4 \leftrightarrow \nu_{12}$. The *a*-axis terms ($G^a_{10,4}$ and $G^a_{4,12}$) are excluded from the global fit since a) they do not improve the residuals and b) cannot be fitted with reasonable uncertainty. Thus, *b*-axis (two first order $G^b_{4,10}$, $G^b_{4,12}$ and one second order $F^{ac}_{4,10}$) Coriolis coupling terms were fitted to treat the perturbation.

Coriolis coupling constants

Based on a general harmonic force field used for ethylene [15], Hegelund *et al*. [3] had predicted nine non-zero first order Coriolis terms and fall within 5 % of the calculated values from the MP2/cc-pVTZ calculations (**table 3**). Comparison of the theoretical results to our fitted Coriolis terms shows that only two are similar to theory ($G^a_{10,7}$ and $G^b_{10,7}$); which are within 3 % of the calculated value, whereas $G^b_{4,10}$ and $G^b_{4,12}$ are roughly 30 % times larger than theory. This is mainly attributed to the number of Coriolis terms used in the fit. Hegelund *et al*. [3] had included all nine first order Coriolis terms into the fit which were fixed to their predicted values, compared to only four that are used here. This also affects the fitted values for the second order terms and is reflected in the

difference between the fitted $F_{4,10}^{bc}$ terms where our fitted value is six times larger than what Hegelund *et al*. [3] determined. Inclusion of the additional terms would be analogous to using more centrifugal distortion constants to produce an effective fit. By limiting the number of terms used, this gives large correlations between some of the fitted Coriolis terms and rotational constants which are also influenced by the limited types of transitions fitted (i.e. only *c*-type transitions fitted for ν_7 and ν_4, *b*-type transitions for ν_{10} and *a*-type transitions for ν_{12}). A list of all transitions for the ground state and excited states are given in supplementary files **S1** and **S2** respectively. We also note that the signs of the $G_{10,7}^{a}$ and $G_{10,7}^{b}$ terms in the previous study [3] are the opposite to those predicted by theory as well as the fitted values in this work. In principle this does not affect the Coriolis interaction, given that $G_{10,7}^{a} = -G_{7,10}^{a}$, where the sign of the zeta (ζ) constant is described as either a positive or negative perturbation by Mills [16]. Upon inspection of the spectra, we find that the *P*-branch of the low wavenumber band and the *R*-branch of the high wavenumber band are enhanced and corresponds to a negative perturbation, hence the negative values used for $G_{10,7}^{a}$ and $G_{10,7}^{b}$.

Table 3: Comparison of the fitted and predicted values for the Coriolis coupling terms.

	Coriolis	$\nu_i \leftrightarrow \nu_j$	Fitted	Hegelund *et al*. [3]	MP2/cc-pVTZ
1st order	*a*-axis	$\nu_{10} \leftrightarrow \nu_7$	-108980.0 (591)	110833.2717	-106118.2395
	b-axis	$\nu_{10} \leftrightarrow \nu_7$	-32558.7 (360)	32977.17038	-33676.44774
		$\nu_{10} \leftrightarrow \nu_4$	34914 (214)	26441.6948	26834.68898
		$\nu_4 \leftrightarrow \nu_{12}$	48853 (745)	38823.12331	36841.59116
2nd order	*a*-axis	$\nu_{10} \leftrightarrow \nu_7$	37.97 (135)	6 (1)	n/a
	b-axis	$\nu_{10} \leftrightarrow \nu_7$	266.00 (304)	203 (4)	
		$\nu_{10} \leftrightarrow \nu_4$	369.20 (603)	--	

Table 2: Fitted rotational and centrifugal distortion constants in Watson's *A*-reduced I^r Hamiltonian for the $\nu_{10} = 1$, $\nu_7 = 1$, $\nu_4 = 1$ and $\nu_{12} = 1$ bands of trans-$C_2H_2D_2$ (MHz).

Constant	ν_{10}	ν_7	ν_4	ν_{12}
Centre / cm^{-1}	673.53039 (29)	724.75596 (17)	987.75328 (2)	1298.03782 (6)
A	104220.30 (858)	104790.30 (835)	103326.6540 (522)	105345.3370 (870)
B	25034.77 (232)	24906.23 (152)	25003.90 (638)	24917.40 (789)
C	20074.480 (417)	20137.950 (371)	20120.6520 (371)	20074.2070 (824)
Δ_J	0.029951 (229)	0.0332830 (557)	0.0313500 (696)	0.0328050 (800)
Δ_{JK}	[b]	0.08295 (189)	[b]	0.097555 (365)
Δ_K	0.79120 (580)	2.64990 (176)	1.429280 (275)	1.910830 (580)
δ_J	0.006115 (133)	[b]	0.0071230 (362)	0.0082230 (522)
δ_K	[b]	[b]	0.169000 (638)	0.17667 (243)
$\Phi_K \times 10^6$	[b]	[b]	69.910 (638)	[b]
$G^a_{10,7} = -108980.0\ (591);\ G^b_{10,7} = -32558.7\ (360);\ F^{bc}_{10,7} = 37.97\ (135);\ F^{ac}_{10,7} = 266.00\ (304)$[c]				
$G^b_{10,4} = 34914\ (214);\ G^b_{4,12} = 48853\ (745);\ F^{ac}_{10,4} = 369.20\ (603)$				
J' max	18	33	41	34
K_a' max	10	15	18	13
Number trans.	156	557	1902	523
r.m.s. deviation / cm^{-1}	0.0004	0.0003	0.0003	0.0004
σ_{dev}	0.8395	1.3635	1.1289	1.1587

[a] Figures in brackets are one standard deviation according to the least squares fit in units of the least significant figure quoted.
[b] Constrained to ground state value in column 6 of **table 1**.
[c] The Coriolis terms *G* (equivalent to ζ) and *F* (equivalent to η) are defined, for the *a*-axis in this case, as $\langle \nu_i | \Psi_{first\ order} | \nu_j \rangle = iG^a_{i,j}P_a$ for the first order and $\langle \nu_i | \Psi_{second\ order} | \nu_j \rangle = F^{bc}_{i,j}(P_bP_c + P_cP_b)$.

Conclusions

From the ground state and global fits, we find that it is not essential to fit all available centrifugal distortion constants. It is important to consider which constants are relevant for a fit, as well as how accurately they can be determined. Within the tetrad system of *trans*-d_2-ethylene (ν_{10}, ν_7, ν_4 and ν_{12}) numerous interactions are possible. The global fit in **table 2** indicates that it is also not necessary to include all possible resonance terms, as the inclusion of some terms may have either no effect on the dataset at all or result in high correlation. Synchrotron radiation in combination with a multipass White-type cell proves to be advantageous, over the internal globar source, for high resolution spectroscopy generally at wavenumber values below *ca*. 2000 cm^{-1}. The increased signal to noise ratio helps alleviate some of the difficulties when searching for weak transitions as well as reducing acquisition times.

References

[1] C. D. Lauro, *J. Mol. Spectrosc.*, **30**, 266-274 (1969)

[2] F. Hegelund and F. M. Nicolaisen, *Mol. Phys.*, **56**, 171-191 (1985)

[3] F. Hegelund and F. M. Nicolaisen, *J. Mol. Spectrosc.*, **116**, 214-227 (1986)

[4] F. Hegelund, *J. Mol. Spectrosc.*, **135**, 45-58 (1989)

[5] G. B. Lebron and T. L. Tan, *J. Mol. Spectrosc.*, **271**, 44-49 (2012)

[6] T. L. Tan and W. H. Tan, *Chem. Phys. Lett.*, **411**, 43-45 (2005)

[7] H. H. Teo, P. P. Ong, T. L. Tan and K. L. Goh, *J. Mol. Spectrosc.*, **204**, 145-147 (2000)

[8] T. L. Tan, L. L. Ng and M. G. Gabona, *J. Mol. Spectrosc.*, **312**, 6-12 (2015)

[9] L. S. Rothman, I. E. Gordon, A. Barbe, D. C. Benner, P. F. Bernath, M. Birk, V. Boudon, L. R. Brown, A. Campargue, J. –P. Champion, K. Chance, L. H. Coudert, V. Dana, V. M. Devi, S. Fally, J. –M. Flaud, R. R. Gamache, A. Goldman, D. Jacquemart, I. Kleiner, N. Lacome, W. J. Lafferty, J. –Y. Mandin, S. T. Massie, S. N. Mikhailenko, C. E. Miller, N. M. -Ahmadi, O. V. Naumenko, A. V. Nikitin, J. Orphal, V. I. Perevalov, A. Perrin, A. P. –Cross, C. P. Rinsland, M. Rotger, M. Šimečková, M. A. H. Smith, K. Sung, S. A. Tashkun, J. Tennyson, R. A. Toth, A. C. Vandaele and J. V. Auwera, *J. Quant. Spectrosc. Radiat. Transfer*, **110**, 533-572 (2009)

[10] D. McNaughton, D. McGilvery and F. Shanks, *J. Mol. Spectrosc.*, **149**, 458-473 (1991)

[11] F. W. Loomis and R. W. Wood, *Phys. Rev.*, **32**, 223-237 (1928)

[12] J. K. G. Watson in *Vibrational Spectra and Structure*, edited by J. R. Durig (Elsevier, Amsterdam, 1977) **vol 6**

[13] H. M. Pickett, *J. Mol. Spectrosc.*, **148**, 371-377 (1991)

[14] Gaussian 09, Revision D.01, M. J. Frisch, G. W. Trucks, H. B. Schlegel, G. E. Scuseria, M. A. Robb, J. R. Cheeseman, G. Scalmani, V. Barone, B. Mennucci, G. A. Petersson, H. Nakatsuji, M. Caricato, X. Li, H. P. Hratchian, A. F. Izmaylov, J. Bloino, G. Zheng, J. L. Sonnenberg, M. Hada, M. Ehara, K. Toyota, R. Fukuda, J. Hasegawa, M. Ishida, T. Nakajima, Y. Honda, O. Kitao, H. Nakai, T. Vreven, J. A. Montgomery, Jr., J. E. Peralta, F. Ogliaro, M. Bearpark, J. J. Heyd, E. Brothers, K. N. Kudin, V. N. Staroverov, T. Keith, R. Kobayashi, J. Normand, K. Raghavachari, A. Rendell, J. C. Burant, S. S. Iyengar, J. Tomasi, M. Cossi, N. Rega, J. M. Millam, M. Klene, J. E. Knox, J. B. Cross, V. Bakken, C. Adamo, J. Jaramillo, R. Gomperts, R. E. Stratmann, O Yazyev, A. J. Austin, R. Cammi, C. Pomelli, J. W. Ochterski, R. L. Martin, K. Morokuma, V. G. Zakrzewski, G. A. Voth, P. Salvador, J. J. Dannenberg, S. Dapprich, A. D. Daniels, O Farkas, J. B. Foresman, J. V. Ortiz, J. Cioslowski and D. J. Fox, Gaussian, Inc., Wallingford CT, 2013

[15] J. L. Duncan and E. Hamilton, *J. Mol. Struct.*, **76**, 65-80 (1981)

[16] I. M. Mills, *Pure Appl. Chem.*, **11**, 325-344 (1965).

[S1] The SPFIT ground state output re-formatted into a more readable form using PIFORM

[S1] The SPFIT global fit output re-formatted into a more readable form using PIFORM

Chapter 3.0

Low Resolution FTIR Spectroscopy of Nanoparticle Ices

3.1 Introduction

The majority of matter that is found in interstellar media exists as either gaseous molecules or condensed matter; the latter of which are comprised of molecular ice particles or thin ice coatings on silicate or carbonaceous dust grains. These icy surfaces often act as reaction sites by trapping small volatile organic compounds which undergo photolysis and are converted to larger molecules. Molecular ices are also of interest both scientifically and fundamentally because they can influence the radiative forcing in the atmospheres of planets [1], as well as contribute to atmospheric chemistry. By characterising molecular ices, it is possible to gain an understanding of these physical and chemical properties.

Owing to the diversity and complexity of natural systems (i.e. interstellar media and planetary atmospheres), it is often quite difficult to be able to accurately interpret IR emission or absorption data which is collected from passing satellites [2] or unmanned robotic probes [3]. This creates a need for molecular ices to be synthesized under laboratory conditions which enables easy control over physical conditions, and hence the possibility of fully characterising a molecular ice. Laboratory data can then be used to infer the physical and chemical conditions of natural systems, forming the major motivation behind the work described in **Chapters 3.2.1** and **3.2.2**.

Interpretation of IR spectra of molecular ices does not come without its own difficulties. Similar to gas phase spectroscopy, molecules in the condensed phases will also exhibit their own characteristics which need to be taken into consideration in order to deduce meaningful conclusions.

3.1.1 Intermolecular coupling

Depending on the molecular system being studied, the types of intermolecular bonding and its influence on vibrational bands will have differing effects. Of the numerous types of intermolecular bonding, the most relevant ones to this thesis are: hydrogen bonding (H-bonding) as seen in H_2O/D_2O and non-bonded atom repulsions/attractions in acetylene and ethylene. Since molecules are linked together in one way or another, the vibration of one molecule will influence neighbouring molecules causing “macro” vibrations known as phonon modes described by Sievers & Takeno [4]. This also enhances the effect of Fermi resonance in both intramolecular (e.g. $\nu_1 \leftrightarrow 2\nu_2$ of H_2O) and intermolecular (host-guest interactions) situations.

Phonon modes emanate from periodically arranged molecules which vibrate in phase with one another. The direction of a phonon mode can be described as either acoustic or optical, where the displacements of molecules are either in the same direction or alternating directions respectively. Also, the direction of propagation of the phonon mode can also move either parallel (longitudinal) or

perpendicular (transverse) to the direction of the phonon. For simplicity, the direction of propagation of a phonon mode is only shown for the in-plane directions in **figure 3.1**.

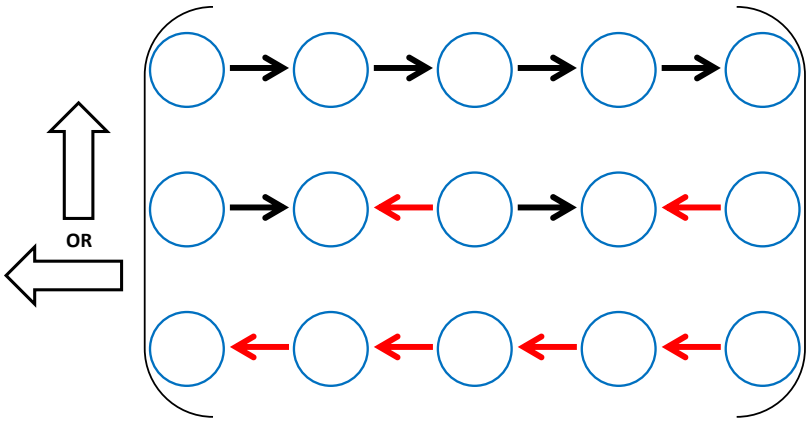

Figure 3.1: An illustration of possible phonon modes. The 1st and 3rd rows of atoms represent acoustic phonons and the 2nd row represents an optical phonon. The large arrows outside of the brackets indicate either a parallel (longitudinal) or perpendicular (transverse) propagation of the whole phonon.

3.1.2 Vibrations

The positions of vibrational bands for liquids and solids are often red-shifted, in comparison to gas-phase wavenumber values, where the extent of red-shift is largely dependent on a) the strength of intermolecular bonding as well as the phase of a material. In general, as the degree of crystallinity increases the position of a vibrational band will red-shift to a lower wavenumber value (**figure 3.2**) and the band shape may also become more structured.

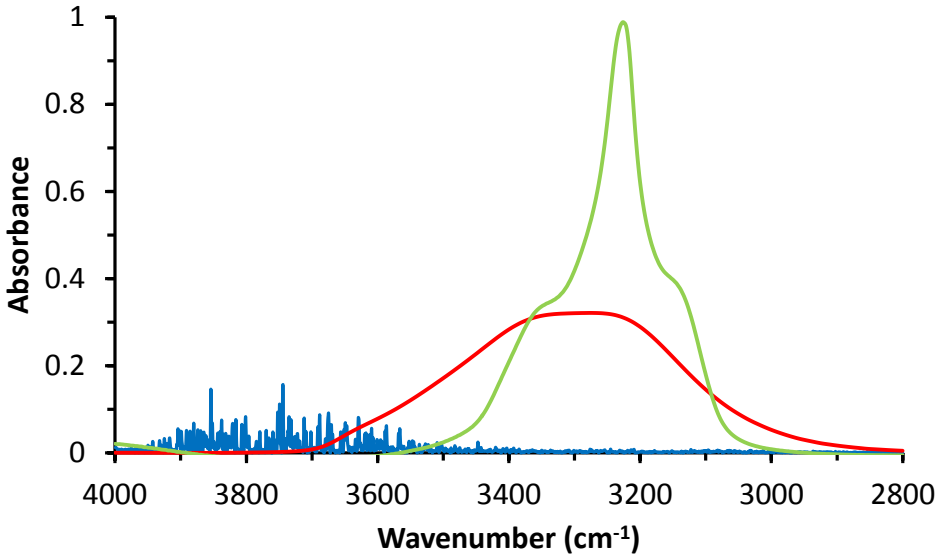

Figure 3.2: Spectra of the OH stretching region of H_2O in the gas (blue) and liquid (red) phases at 298 K. Cubic crystalline ice (I_c) at 78 K is shown in the green trace.

In the example used here, the OH stretch of H_2O is red-shifted as its phase changes from gas, to liquid, solid. Although water ice has 17 different polymorphs, cubic crystalline ice (I_c) is the most relevant to the research presented in **Chapter 3.2.1** of this thesis, and exists with oxygen atoms being arranged in a cubic lattice whilst the hydrogen atoms remain disordered.

Without exception the number of fundamental vibrational bands for molecular ices will also follow the rule of $3N - 5$ or $3N - 6$ (see **Chapter 1.1.1**). However there is also the possibility of new "macro" vibrations (or phonon modes (see **Chapter 3.1.1**)) being formed, such as low energy lattice translations and libration bands. These phonon modes will often have broad IR band profiles because the extent of intermolecular coupling will vary across the crystal lattice. The IR bands of these modes often appear to be weak in intensity because the dipole moment of each molecule within a phonon is randomly arranged, leading to incomplete cancellation of individual dipoles. Furthermore, vibrational bands which are not IR active in the gas phase may become active due to a higher symmetry of the crystal in comparison to a single molecule.

3.1.3 Thin films

Molecular ices are conventionally synthesized using thin film techniques where molecules are either: isolated within a host gas (matrix isolation [5]), or deposited onto a cold substrate (either an IR transparent window [6], or metal surface [7]). The stability of these systems allows for sensitive control over the growth rate of an ice sample, as well as allowing for long spectral acquisition times. Thin film techniques are also vital for characterising bulk properties of ices and provide insights into how a molecular ice may behave under varying experimental conditions.

In light of these advantages, thin film ices are often too thick (> 1 μm) and absorption features in an IR spectrum can become distorted due to the dependence of the refractive index on film thickness. Contributions from the scattering component of the refractive index (**equation 3.1**) become significant when the thickness of a film approaches $\lambda/2\pi$; where λ is the wavelength of an absorption feature [8].

$$\tilde{n} = n + ik \qquad \textbf{(3.1)}$$

where n is the real (scattering) component and k is the imaginary (absorptive) component of the refractive index.

In principle the IR spectrum for a material is equivalent to its refractive index ($\tilde{n}$) since the observed spectrum is a summation of contributions from both the scattering (n) and absorptive (k) components of the refractive index. For example, the OH stretch of H_2O crystalline ice near 3200 cm^{-1} will require a film thickness that is < 0.45 μm (given that the band extends to 3600 cm^{-1}) to have no contributions from scattering. This implies that the spectrum below 3600 cm^{-1} is therefore represented only by the

absorptive component (k) (since $n = 0$). By changing the thickness of a film, it is therefore possible to extract the n and k optical constants through a Kramers-Kronig transformation [9,10]. In practice, this can be quite difficult as the values of n and k are sensitive not only to film thickness, but also to temperature; frequency; purity and homogeneity of the film.

Derivation of the n and k optical constants is not sufficient to simulate thin film spectra. Knowledge of additional physical properties (film thickness, absorption coefficients and density) are also required. Spectra and be simulated either numerically [11] or through more complex methods such as discrete dipole approximation (DDA) [12] or quantum mechanically [13].Furthermore, thin film ices are not representative of molecular ices (in terms of size and shape) that are found in natural systems, and thus a different method of synthesizing molecular ices is required. One such method is collisional cooling, which is used throughout the experiments described in **Chapters 3.2.1 - 3.2.2**. Although particulate ices are more directly relatable to interstellar and planetary ices, interpretation of their spectra has its own intrinsic difficulties.

3.1.4 Particulate ices

There exist several different techniques of generating particulate ices such as: jet expansion [14], electrospray [15], acoustic levitation [16, 17], collisional cooling [18, 19], and many more described by Pruppacher [20]. From the available techniques, we find that collisional cooling provides the most stable conditions for particle formation, as well as the largest sample size per experiment in comparison to jet expansion (which gives very small clusters), and electrospray and acoustic levitation (where particles are too large and suffer from optical contributions). The dynamics of particle formation is an active area of research and the exact pathway of particle formation is still not well known. Since the theory is not covered in detail here, we can only infer that molecules are collisionally cooled with cold buffer gas when pulsed into a cold environment. The volume of gas becomes supersaturated before the onset of particle nucleation, and as particles diffuse through the cell, small particles aggregate toward one another where Ostwald ripening [21, 22] becomes the dominant mechanism for large particle formation.

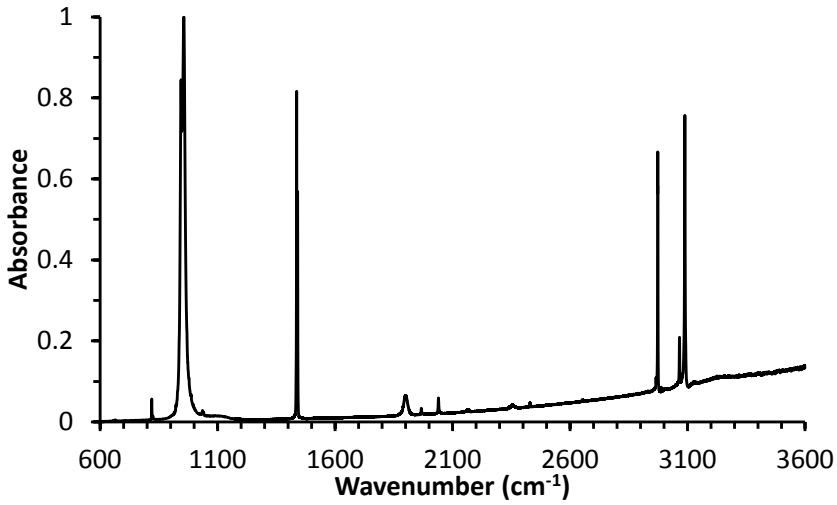

Figure 3.3: A survey spectrum of crystalline ethylene particles at 78 K using a mixture of 10 % ethylene to helium. The increase in the baseline beginning near 1300 cm^{-1} shows short-wave scattering, indicating the presence of large particles to be *ca*. 0.61 μm in diameter.

Similar to thin film ices, particles with diameters approaching $\lambda/2\pi$ will also exhibit short-wave scattering (**figure 3.3**), as seen by the increasing baseline. In order to be entirely free of scattering effects up to 3600 cm^{-1}, particle diameters (μm) should $\approx \lambda/4\pi$ (or 0.2 μm). In contrast to large particles, small particles also exhibit their own characteristics such as increased contributions to vibrational bands from surface molecules (e.g. ν_2 bending band of surface H_2O molecules). This is predominantly due to a decrease in ratio between molecules at the core to molecules on the surface, as well as increased molecular disorder throughout a small particle.

For any given experiment, the distribution of particle sizes is often quite difficult to measure and is responsible for particles that are both large and small. By convention particle size distributions are often characterised using a log-normal function (**equation 3.2**) in atmospheric applications [23], and is also adopted for these studies, leading to the probability distribution functions (PDF) of the type shown in **figure 3.4**.

$$\frac{\mathrm{d}n}{\mathrm{d}\ln d_\mathrm{p}} = \frac{F_{\mathrm{m}N}}{\sqrt{2\pi}\ln\sigma_\mathrm{g}} \times exp\left[-\frac{\left(\ln d_\mathrm{p} - \ln d_{\mathrm{g}N}\right)^2}{2\left(\ln\sigma_g\right)^2}\right] \qquad \textbf{(3.2)}$$

where d_p is the particle diameter (nm), σ_g is the geometric standard deviation, $d_{\mathrm{g}N}$ is the number-median diameter (nm) and $F_{\mathrm{m}N}$ is the concentration of particles with diameter $d_{\mathrm{g}N}$ [23].

If one assumes $F_{\mathrm{m}N}$ = 1 and $d_{\mathrm{g}N}$ = 100 nm, the PDFs shift to lower particle sizes with increasing σ_g values as larger and larger deviations from the mean value are allowed. This results in a decreased probability of finding a particle of a particular size, and in increase in the number of different particle sizes.

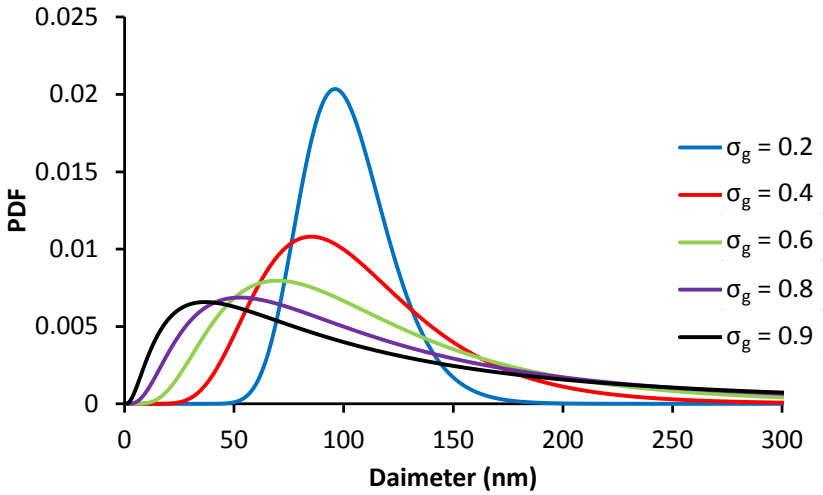

Figure 3.4: Log-normal PDFs for particle sizes with a mean size of 100 nm in diameter with differing σ_g.

Alongside size effects, particle shape is also an important factor to consider as different particle shapes can affect the structure of vibrational bands. Each molecular ice will behave differently and the particles that are formed may not be spherical (or uniform) in shape. In order to understand the effects of particle shape, spectra are often simulated using the *n* and *k* components of a particular ice in combination with theoretical methods [24, 25]. For simplicity, aerosol particles are assumed to be spherical in shape in the following works.

3.1.5 Experimental method

The size, shape and phase of particulate ices are also dependent on the physical conditions that are used in an experiment. At any given time, there can be up to five different factors which will influence the formation of particles: temperature; buffer gas pressure; sample concentration; sample pressure and pulse width, and need to be taken into consideration when performing experiments and analysing spectra. For a molecular ice that has not been studied before, it is often necessary to explore the influence of the above parameters by systematically varying one or more of the experimental conditions (**figure 3.5**). By doing so, it is possible to determine the optimum conditions for generating appropriately sized particles so that spectra are not affected by scattering contributions or surface effects. Differences in the refractive index, and phase, of particulate ices can also lead to large discrepancies when comparing to literature data from thin film techniques (e.g thin film H_2O ice deposited below 110 K will have an amorphous solid structure, whereas particulate ices at the same temperature will be crystalline in structure).

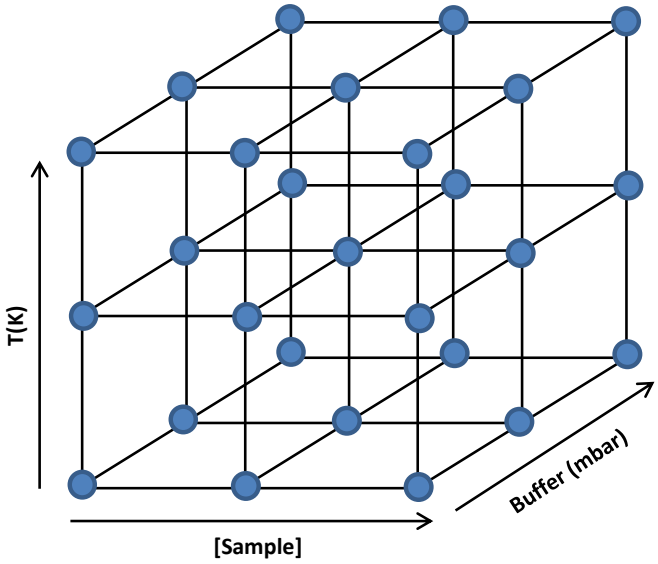

Figure 3.5: An illustration for three of the different experimental conditions that can be systematically varied.

Sample preparation will vary depending on whether the sample is a gas or liquid. Gaseous samples will often be mixed with a buffer gas (either N_2 or He) into a metal cylinder and pressurised up to 400 kPa. If particle sizes are too large, the concentration of the mixture can be adjusted to generate smaller particles. The opposite can be done if particles are too small. In general, mixture concentrations typically range between 1 - 10 % of sample gas to buffer gas. The metal cylinder is then connected to a manifold via 6 mm nylon tubing which is *ca*. 60 cm in length and is pressurised with 70 - 275 kPa of a gas mixture. The manifold holds four separate solenoid valves that are used to control the pulse length of gas that is directed into the collisional cooling cell introduced in **Chapter 1.2.4.1**.

In the case of liquids, samples can be prepared by either a) flowing buffer gas over a warm liquid and into a metal cylinder used for gases, or b) bubbling carrier gas through the liquid. The former method has been used previously [18, 19], and was found to produce particles that were small enough to have undesired spectral contributions from surface molecules. Consequently, the method was changed such that carrier gas was bubbled through a liquid, rather than flowed over the surface in order to overcome this issue. Due to the high pressures used for a carrier gas, it is not practical to employ glass bubblers as they have a risk of exploding. Instead, a steel bubbler (**figure 3.6**) was designed so to withstand the high carrier gas pressures.

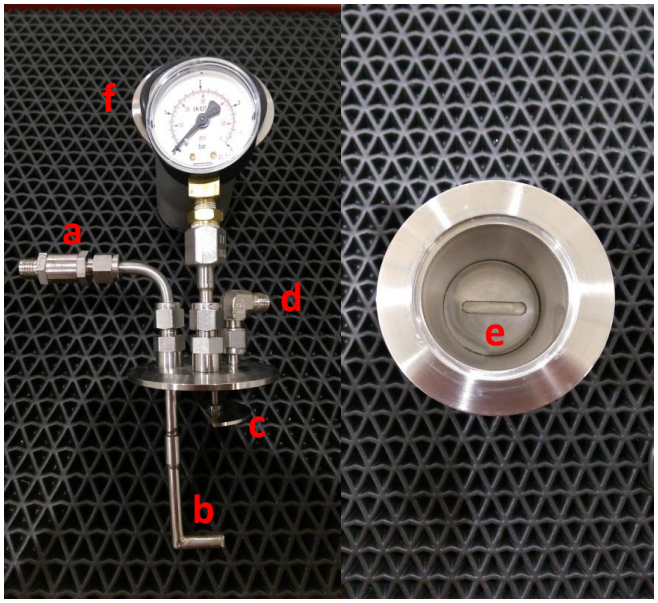

Figure 3.6: The steel bubbler designed for high pressure applications. On the left is the lid of the bubbler and the bottom half shown on the right. Carrier gas is flowed through a non-return valve (a) toward the bottom (b). An adjustable baffle (c) is used to stop liquid splashing through into the outlet port (d). The bottom of the tube rests in the groove (e) and pressure is read by an analogue gauge (f).

The steel bubbler is approximately 100 mL in volume and carrier gas is bubbled through a liquid up to pressures of 70 - 275 kPa forming a "wet" or saturated gas-sample mixture. 6 mm nylon tubing is then used to connect the bubbler to the solenoid vales before being pulsed into the collisional cooling cell.

Prior to introducing the sample-buffer gas mixture, the collisional cooling cell is cooled down by filling the outer jacket with a cryogen until the desired temperature is reached using heaters as described in **Chapter 1.2.3.1**. Buffer gas is then introduced into the cell (either He or N_2) with pressures ranging from 5 - 50 kPa. The cell is operated in a static mode and left to thermally equilibrate over one to two minutes. As the gas mixture is pulsed into the cell, spectra are recorded to monitor both particle formation and time taken for particles to diffuse through the optical beam. A front view of the EFC cell is given in **figure 3.7**.

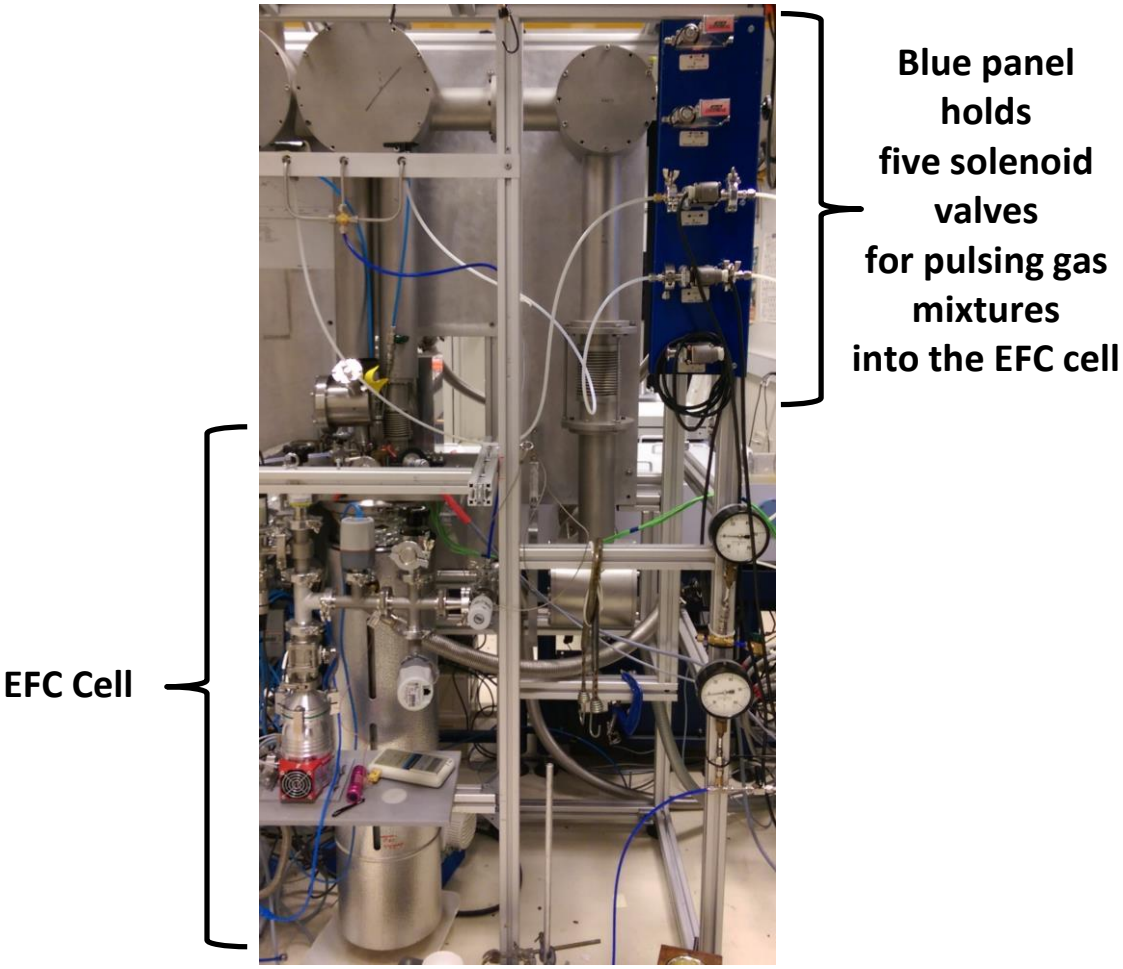

Figure 3.7: Front view of the EFC cell installed behind the Bruker IFS 125HR spectrometer.

References

[1] F. Montmessin, F. Forget, P. Rannou, M. Cabane and R. M. Haberle, *J. Geophys. Res.*, **109**, E10004 (2004).

[2] voyager.jpl.nasa.gov

[3] Saturn.jpl.nasa.gov

[4] A. J. Sievers and S. Takeno, *Phys. Rev. Lett.*, **61**, 970 (1988).

[5] M. V. Thiel, E. D. Becker and G. C. Pimentel, *J. Chem. Phys.*, **27**, 486 (1957).

[6] G. Ritzhaupt and J. P. Devlin, *J. Chem. Phys.*, **67**, 4779 (1977).

[7] S. B. Mohsin, M. Trenary and H. J. Robota, *J. Phys. Chem.*, **92**, 5229 (1988).

[8] D. M. Hudgins, S. A. Sandford, L. J. Allamandola and A. G. G. M. Tielens, *Astrophys. J. Suppl. S.*, **86**, 713 (1993).

[9] R. D. L. Kronig, *J. Opt. Soc. Am.*, **12**, 547 (1926).

[10] H. A. Kramers, *Atti Cong. Intern. Fisica, Como*, **2**, 545 (1927)

[11] R. L. Hudson, R. F. Ferrante and M. H. Moore, *Icarus*, **228**, 276 (2014).

[12] S. Bauerecker, A. Wargenau, M. Schultze, T. Kessler, R. Tuckermann and J. Reichardt, *J. Chem. Phys.*, **126**, 134711 (2007).

[13] T. C. Preston, G. Firanescu and R. Signorell, *Phys. Chem. Chem. Phys.*, **12**, 7924 (2010).

[14] J. Q. Searcy and J. B. Fenn, *J. Chem. Phys.*, **61**, 5282 (1974).

[15] D. –R. Chen, D. Y. H. Pui and S. L. Kaufman, *J. Aerosol Sci.*, **26**, 963 (1995).

[16] M. Seaver, A. Galloway and T. J. Manuccia, *Rev. Sci. Instrum.*, **60**, 3452 (1989)

[17] E. J. Davis, *Aerosol Sci. Tech.*, **26**, 212 (1997).

[18] C. Medcraft, D. McNaughton, C. D. Thompson, D. Appadoo, S. Bauerecker and E. G. Robertson, *Astrophys. J.*, **758**, 17 (2012).

[19] C. Medcraft, D. McNaughton, C. D. Thompson, D. R. T. Appadoo, S. Bauerecker and E. G. Robertson, *Phys. Chem. Chem. Phys.*, **15**, 3630 (2013).

[20] H. R. Pruppacher, J. D. Klett and P. K. Wang, *Aerosol Sci. Tech.*, **28**, 4 (1998).

[21] J. A. Marqusee and J. Ross, *J. Chem. Phys.*, **80**, 536 (1984)

[22] P. W. Vorhees, *J. Stat. Phys.*, **38**, 231 (1985).

[23] J. Heintzenberg, *Aerosol Sci. Tech.*, **21**, 46 (1994).

[24] S. Bauerecker, A. Wargenau, M. Schultze, T. Kessler, R. Tuckermann and J. Reichardt, *J. Chem. Phys.*, **126**, 134711 (2007).

[25] G. Firanescu, D. Hermsdorf, R. Ueberschaer and R. Signorell, *Phys. Chem. Chem. Phys.*, **8**, 4149 (2006).

Chapter 3.2 Projects on low resolution spectroscopy of nanoparticle ices

The following sections details the experimental and analytical work on various molecular ices studied using a collisional cooling cell. Numbering of references and pages within **Chapters 3.2.1** and **3.2.2** remain unchanged to maintain consistency within the manuscripts. Supplementary data for **Chapter 3.2.1** can be found with the online version of the paper.

Chapter 3.2.1 is an accepted paper on isotope mixed H_2O crystalline ices at various temperatures and concentrations.

Chapter 3.2.2 is a manuscript on ethylene ice particles

Declaration for Thesis Chapter 3.2.1

Declaration by candidate

In the case of Chapter 3.2.1, the nature and extent of my contribution to the work was the following:

Nature of contribution	**Extent of contribution (%)**
Initiation, key ideas, development and writing up	80 %

The following co-authors contributed to the work. If co-authors are students at Monash University, the extent of their contribution in percentage terms must be stated:

Name	**Nature of contribution**	**Extent of contribution (%) for student co-authors only**
D. R. T. Appadoo	Experimental assistance	
D. McNaughton	Initiation and key ideas	
E. G. Robertson	Initiation and key ideas	
R. Auchettl	Experimental assistance	5 %
L. Shi	Computational assistance	5 %

The undersigned hereby certify that the above declaration correctly reflects the nature and extent of the candidate's and co-authors' contributions to this work*.

Candidate's Signature		**Date**
Main Supervisor's Signature		**Date**

*Note: Where the responsible author is not the candidate's main supervisor, the main supervisor should consult with the responsible author to agree on the respective contributions of the authors.

Heavy Snow: IR spectroscopy of isotope mixed crystalline water ice

Authors

A. Wong[a], R. Auchettl[b], L. Shi[d†], D. R. T. Appadoo[c], D. McNaughton[a], E. G. Robertson[b]*

[a] School of Chemistry, Monash University, Wellington Road, Clayton, Victoria 3011, Australia.

[b] Department of Chemistry & Physics, La Trobe Institute for Molecular Science, La Trobe University, Victoria 3086, Australia.

[c] Australian Synchrotron, 800 Blackburn Road, Clayton, Victoria 3168, Australia

[d] Theoretical Chemistry Institute and Department of Chemistry, University of Wisconsin, Madison, Wisconsin 53706, USA.

[†] Currently at the Department of Chemistry, Massachusetts Institute of Chemistry, 77 Massachusetts avenue, Cambridge, Massachusetts 02139, USA.

*Corresponding author email: [redacted]

Accepted: Physical Chemistry Chemical Physics

Abstract

Mid-infrared spectra have been measured for crystalline water ice aerosols of widely varied H/D isotopic composition. Particles with diameters ranging from 10 – 200 nm were generated via rapid collisional cooling with a cold buffer gas over a range of temperatures from 7 – 200 K. In near isotopically pure ices, the ν_L band position is slightly red-shifted with increasing temperature whilst in the ν_2 region apparently anomalous shifts in peak maxima are explained by the contribution of broad $2\nu_L$ band of H_2O and $3\nu_L$ band of D_2O together with $\square_2$ intensity that is particularly weak in low temperature crystalline ice. The hydrogen bonded OH (or OD) oscillator bands of near pure H_2O (or D_2O) ices are blue-shifted with temperature, with a gradient very similar to that of the corresponding band in isotope diluted samples, HOD in D_2O (or H_2O). It implies that this observed temperature trend is predominantly due to the intrinsic change in local hydride stretch potential energy, rather than to changes in intermolecular coupling. However, it is also observed that the narrow hydride stretch bands of isotope diluted sample rapidly develops phonon structure as the oscillator concentration

increases, evidence of strong intermolecular coupling and a high degree of delocalisation. Anomalous blue-shifts in the OD stretch profile as D_2O concentration grows is attributable to Fermi resonance with $2\nu_2$ of D_2O, in much closer proximity than the corresponding H_2O levels. Theoretical results from a mixed quantum/classical approach are used to validate these findings in the hydride stretching region. Theory qualitatively reproduces the experimental trends as a function of temperature and isotopic variance.

Introduction

Water is a remarkable substance, with apparently simple molecular structure that gives rise to many unique properties in condensed phases. Intense scrutiny by spectroscopy, both experimental and theoretical, has not yet resolved all the questions and the vibrational spectroscopy of water ice is no exception. Studies over the past eight decades have revealed Infrared (IR) and Raman spectra of great complexity, largely due to the effects of intermolecular bonding. With the recent discovery of ice XVI [1] there are now 17 experimentally established crystalline phases together with three amorphous phases, each with its own characteristic vibrational spectrum with subtle differences. The focus of this paper will be crystalline ice I_c (cubic) which is the predominant phase of ice particles synthesized under the experimental conditions described below.

Water is a non-linear triatomic molecule with three normal vibrational modes in the gas phase: ν_1 3657 cm^{-1} (symmetric stretch), ν_2 1595 cm^{-1} (bend) and ν_3 3756 cm^{-1} (asymmetric stretch). As water is converted to the liquid phase, these modes are transformed and additional bands appear in the IR spectrum as a result of intermolecular bonding. The distinct ν_1 and ν_3 bands merge into a single, broad OH stretch band with a highly red-shifted wavenumber value. The new bands in the IR spectrum are associated with libration (labelled as ν_L and referring to a frustrated rotation) and lattice modes [2]. Progressing from liquid to solid, the stretching bands within ice are further red-shifted and shoulder features become more pronounced due to contributions from different phonon bands. Phonon modes are collective excitations of periodically arranged molecules and can be described as either acoustic (displaced in the same direction) or optical (alternating direction of displacement). Also, the direction of propagation of the phonon can either be longitudinal (parallel) or transverse (perpendicular) to the direction of the displacement of the phonon. Consequently, the two lattice bands in the far-IR spectrum of ice are labelled as follows: TO (transverse optic) and LA (longitudinal acoustic) [3-5], although there is still some uncertainty on the assignment of these bands [6]. Furthermore, molecules on the surface layers of ice particles that are not tetrahedrally co-ordinated produce dangling bands (dOH/dOD) [7]. Band assignments from the literature for each isotopologue in the gas, liquid and crystalline phases are summarised in **Tables 1a, b and c**. A more extensive list can be found in **Tables S1a - c** in the supplementary data.

In addition to the fundamental scientific motivation of understanding its complex spectra, ice is relevant to our atmosphere (ice particles in clouds) and plays a large role in atmospheric processes such as radiative forcing [8]. Ice is also abundant in interstellar media with sources of ice being found from large comets, to ice coatings on small interstellar dust grains [9]. However, the IR spectra of these natural ices are very difficult to interpret without experimental data and thus laboratory molecular ices are synthesized in order to emulate interstellar or atmospheric ices using methods to create ices such as thin films on cold surfaces or as particles.

Table 1a Literature wavenumber values for the vibrational bands of H_2O in the gas, liquid, amorphous solid and crystalline (I_h/I_c) phases. Aerosol particles are predominantly crystalline for diameters >5 nm.

Phase	Ref.	T (K)	ν_1 ,ν_3	ν_2	ν_L	dOH	TO	LA
Aerosol	[10]	80	3228	--	--	--	--	--
		110	3257	--	--	--	--	--
		170	3252	--	--	--	--	--
Aerosol (12 nm)	[11]	100	3255	--	--	3676	--	--
Aerosol (3 nm)		100	--	1658	842	--	--	--
Aerosol (in He)	[3]	5	--	--	--	--	233	166
	[12]	78	3223	1650	*ca.* 850	3690	--	--
Aerosol (in He)	[7]	80	--	--	--	3692	--	--
Aerosol (in N_2)		80	--	--	--	3677	--	--
Aerosol (in N_2)	[3]	200	--	--	--	--	225	157
	[12]	209	3253	1650	860	--	--	--
Amorph. Film	[7]	15	--	--	--	3720 2cs[b]	--	--
		60	--	--	--	3696 3cs[b]	--	--
	[11]	100	--	1671	770-810	--	--	--
	[13]	20	3210	1550	835	--	--	--
		120	3220	1555	828	--	--	--
Cryst. Film	[14]	12	--	--	842	--	--	--
	[15]	78	3240	1585	847	--	--	--
	[16]	78	--	--	--	--	233	230

Cryst. Film	[17]	218	3240	1650	820	--	--	--
		258	--	1650	800	--	--	--
	[13]	15	3295	1660	732	--	--	--
		120	3245	1645	785	--	--	--
Cryst. Film (H_2O in D_2O)	[18]	90	3224, 3270	1735	840	--	--	--
	[14]	90	--	--	817/735	--	--	--
Liquid	[19]	292	--	--	--	--	300[a]	80[a]
	[20]	298	--	1638	--	--	--	--
	[21]	300	3405	1651	698	--	--	--
		348	3437	1651	682	--	--	--
Vapour	[22]		3657, 3756	1595	--	--	--	--

[a] Determined using the imaginary component (*k*) of the refractive index from thin film data.

[b] 2cs and 3cs represent 2-co-ordinated and 3-co-ordinated surface molecules respectively.

Table 1b: Literature wavenumber values for the vibrational bands of HOD.

Phase	Ref.	T (K)	ν_1	ν_2	ν_3	ν_L	dOD
Aerosol (18 % HOD in H_2O 4, 6, 7, 8 nm)	[23]	100	2415 (sub-surf)	--	--	--	--
Aerosol (18 % HOD in H_2O 40 nm)			2419	--	--	--	--
Aerosol (18 % HOD in H_2O)	[11]	100	--	1455	--	--	--
Aerosol (50 % H to 50 %D 8 nm)			--	1215	--	--	--
Aerosol in He (HOD in D_2O 12 nm)	[14]	80	--	--	--	824/850	--
Aerosol in He (HOD in H_2O 12 nm)			--	--	--	506/515	--
Amorph. Film (0.5 % in D_2O)	[24]	70	--	--	3297	--	--
Cryst. Film (18 % HOD, 81 % H_2O)	[15]	78	2417	--	--	--	--
Cryst. Film (30 % HOD in D_2O)	[18]	90	2417	1510	--	--	--
Cryst. Film (30 % HOD in H_2O)			--	1490	3270	--	--
Cryst. Film (50 % HOD)	[15]	78	--	1450	--	--	--
Cryst. Film (50 % HOD, 25 % H_2O)			2388	1449	3192	--	--
Cryst. Film (52 % HOD, 49 % H_2O)			2381	1477	3192	819	--
Cryst. Film (9.5 % HOD, 90.25 % H_2O)			2415	--	--	--	--
Cryst. Film (HDO in D_2O)	[25]	100	--	--	3277	822	--
Cryst. Film (HDO in H_2O)			2421	--	--	515	--
Cryst. Film (HOD in D_2O)	[26]	80	2425	--	3272	--	--
Liquid	[27]	283	--	--	3393	--	--
Liquid	[20]	298	--	1469	--	--	--
Liquid (10 % H to 90 % D)	[21]	298	2471	1457	3390	--	--

Liquid (29.8 % D_2O and 25.6 % H_2O)	[20]	298	--	1446	--	--	--
Liquid (50 % H to 50 % D)	[21]	298	2493	1457	3391	--	--
Liquid (90 % H to 10 % D)			2499	1457	3377	--	--
Liquid ('pure' HOD)	[20]	298	2485	1439	3370	--	--
Nanocryst. (18 % HOD in H_2O)	[28]	136	--	--	--	--	2713
Vapour	[29]		2724	1403	3707	--	--

Table 1c: Literature wavenumber values for the vibrational bands of D_2O.

Phase	Ref.	T (K)	ν_1 , ν_3	ν_2	ν_L	dOD	TO	LA
Aerosol	[10]	80	2428	--	--	--	--	--
	[30]	100-145	2438[a]	--	--	--	--	--
Aerosol (12 nm isolated in H_2O)	[14]	90	--	--	453/504/525	--	--	--
Aerosol (12 nm)			--	--	628/663	--	--	--
Aerosol (16 nm)	[23]	100	2430	--	--	--	--	--
Aerosol (8 nm)	[11]	100	--	1211	--	--	--	--
Amorph. Film	[7]	15	--	--	--	2748 2cs[b]	--	--
			--	--	--	2727 3cs[b]	--	--
Amorph. Film	[23]	80	2459	--	--	--	--	--
Amorph. Film (HOD in D_2O)	[31]	80	--	--	--	--	--	--
Amorph. Film (in He)	[7]	15	--	--	--	2749 2cs[b]	--	--
			--	--	--	2729 3cs[b]	--	--
Amorph. Film (in N_2)		15	--	--	--	2725 2cs[b]	--	--
			--	--	--	2707 3cs[b]	--	--
Cryst. Film	[16]	78	--	--	--	--	227	--
	[14]	90	--	--	633/661	--	--	--
	[17]	103	2450	1210	630	--	--	--
	[25]	110	2425	1210	640-675	--	--	--
	[32]	110	2524	1214	--	2728	--	--
Cryst. Film (2 % D_2O in H_2O)	[18]	90	2366, 2444	1225	640	--	--	--

Cryst. Film (D_2O on H_2O)	[33]	145	2425	--	--	--	--	--
Low Density Amorph. Film	[24]	70	2435[c]	--	--	--	--	--
Liquid	[34]	278	2475	1217	--	--	--	--
	[17]	283	--	--	530	--	--	--
	[35]	298	2500	1210	--	--	--	--
Liquid ('pure' D_2O)	[20]	298	2484	1214	--	--	--	--
Vapour	[36]		2672, 2788	1178	--	--	--	--

[a] The sub-surface position determined by subtracting a spectrum at 145 K from 100 K.

[b] 2cs and 3cs represents 2-co-ordinated and 3-co-ordinated surface molecules respectively.

[c] Determined using the imaginary component of the dielectric constant ε (=2nk) from thin film data.

Thin films and particles

Thin film studies present certain advantages such as: the availability of many instruments that are capable of performing vapour depositions; generation of samples that are representative of the bulk material; stable conditions in which to grow and maintain the ices and hence more time to gather data; the ability to control thickness and whether multiple samples are deposited separately or simultaneously. It should be noted that slow deposition of water vapour onto a cold substrate below 110 K leads to a more disordered phase known as low density amorphous ice. It has band positions and shapes that differ from those in I_c, however a transition to the crystalline phase is possible by annealing to temperatures above 135 K where the glass transition occurs. Spectra of molecular ices synthesized using these techniques suffer from optical effects that depend on the thickness of the film because of the wavelength dependence of the refractive index. Sample-substrate interactions are also possible which may further distort and shift spectral lines.

An alternative technique, collisional cooling [12, 37-39], is employed in the present study to produce nanoscale ice particles ranging from 20 – 500 nm in diameter. This is advantageous as it avoids generating particles that are either too small (e.g. supersonic jet expansion [40]) where vibrational features from disordered surface molecules dominate the IR spectra; or too large (e.g. electrospray [41-43] and acoustic levitation [44, 45]) where scattering contributions from the real (n) component of the refractive index becomes significant. Furthermore, particulate ices are more representative (in terms of size and shape) of particles found naturally in clouds and interstellar media when compared to vapour deposited flat samples and thus their spectra are more directly comparable. Furthermore, parameters extracted from such spectra yield more accurate prediction models. Naturally, size effects must be accounted for, and for spectra of large particles (with diameters $\geq \lambda / 10$, or *ca*. 0.5 μm in diameter for full mid-IR spectra) contributions from short-wave scattering become increasingly substantial and require meticulous data processing in order to remove this contribution. At the small end of the scale, particles of less than ≈ 20 nm show a significant spectral contribution from strained surface molecules and a disordered core occurs for diameters less than 4 nm [46]. In the size regime of 20 - 200 nm [12], ice nanoparticle spectra are relatively unaffected by such spectral and optical distortions, but still present spectra from which bulk ice spectra can be derived [47].

Temperature effects

It is known that the wavenumber values of the IR bands of ice shift with size and temperature [26]. As temperature decreases: thermal population of excited vibrational levels is reduced; the ice volume is decreased and intermolecular H-bonds are strengthened. This results in blue-shifted wavenumber values for the ν_L libration and ν_2 bending bands due to their vibrational motion becoming more restricted, and a red shift in the OH stretch band as the intramolecular O-H bond weakens. The

thermally induced shift in the OH stretch band is particularly marked, ≈ 0.2 cm^{-1} K^{-1} [12] such that it could be used as a proxy for temperature. A question that arises however, is just how much of that temperature gradient is due to the intrinsic change in the force constants due to the weakening of the H-bonds with increasing temperature, and how much is due to the associated changes in mode coupling between molecules. This provides part of the motivation for our reassessment of the temperature dependant wavenumber values for all vibrational bands, and consideration of the effects of Fermi resonance and phonon coupling using isotopic dilution.

Theoretical studies

Computational studies can provide valuable insights to help interpret such spectroscopic behaviour as a valuable complement to experiments. Molecular dynamics (MD) is often the method of choice for ice because it is capable of computing large arrays of molecules which is important for modelling bulk properties of ice. Some applications of MD include, but are not limited to investigating: proton tunnelling in I_h [48]; the length and elongation of phonon modes [49]; approximating wavenumber shifts due to temperature [50] and isotopic dilution [51]; intensity differences due to phase changes [52] and the anomalous behaviour of water ice under mechanical compression and thermal excitation [53, 54]. Recently, Skinner *et al*. developed a mixed quantum/classical approach for modelling the OH (OD) stretch vibrational spectroscopy of water in its condensed phases [55-60]. Specifically for ice, the model has been vigorously tested and compared with experimental IR, Raman, 2D-IR, pump-probe, and inelastic incoherent neutron scattering data of pure of mixed hexagonal ices [58-63]. Some results for cubic ice from this model are compared to our nanoparticle experimental data in the work presented below.

Isotopic dilution

In order to assist the interpretation of the complex spectra of pure ices, one can manipulate the molecular ice by distributing small amounts of H_2O in an inert gas matrix [64] or by depositing isolated H_2O molecules on D_2O [32]. The former method simplifies the spectrum by removing the intermolecular bonds entirely, although ro-vibrational transitions can still be observed in some spectra [65]; the latter approach which consists of H_2O deposition onto pre-deposited D_2O [32] can be an effective method for isolating H_2O molecules while still maintaining the H-bonding interactions. If a sample is deposited at temperatures below 145 K, proton exchange is not observed on the surface layers between H_2O and D_2O [33]. In earlier works by Devlin and co-workers [18, 66], spectra for intact isolated D_2O [18] and H_2O [66] were reported showing clearly resolved peaks for the ν_1 and ν_3 OD/OH stretches. Separate deposition of the samples proves advantageous if one wants to avoid making HOD (**Equation 1**), which is formed as a result of the equilibrium between H_2O and D_2O [20].

$$H_2O_{(l)} + D_2O_{(l)} \rightleftharpoons 2HOD_{(l)} \qquad K_e \approx 3.76 \text{ to } 3.94 \text{ at } 25\ ℃ \qquad (1)$$

Formation of HOD by pre-mixing solutions or co-deposition also has its own benefits, in particular for measuring the dynamics of intermolecular bonding in solutions [67, 68]. However, the main advantage of producing HOD diluted in either D_2O (or H_2O) is its effectiveness in isolating and therefore vibrationally decoupling the OH (or OD) oscillator of HOD [18]. The resulting localised excitation greatly simplifies that part of the IR spectrum and can therefore help with interpretation of the underlying physics, a strategy that has been applied to conventional IR spectroscopy [18, 21, 69] and with 2D and 3D techniques [26, 31]. Advantageously, the ν_3 band of HOD should be located approximately in between the ν_1 and ν_3 bands of decoupled H_2O and similarly for the ν_1 of HOD and D_2O.

While pure D_2O and mixed molecular ices of dilute HOD have been subject to spectroscopic studies, most of these have concerned thin films with a limited number focussing on particulate ices. Devlin [10] reported the first spectra of both crystalline and amorphous micro-particle ices of H_2O, D_2O and mixtures in the hydride stretch region with the amorphous ice bands blue-shifted from the crystalline bands by some 10 - 30 cm^{-1}, see **Tables 1a-c**. The dangling band of amorphous ice is also blue-shifted due to the highly disordered surface layers and transitions to a doublet band [70] which is assigned to the 2 (2748 cm^{-1}) and 3 co-ordinated (2727 cm^{-1}) surface D_2O molecules [7]. However, in the presence of adsorbate molecules such as H_2, Ar or N_2, the dangling band can be red-shifted up to 20 cm^{-1}. For nanoparticles ≤ 16 nm in diameter, surface and subsurface molecules contribute strongly to the overall intensities and band shapes, along with the core. Even in 16 nm diameter D_2O particles, it is estimated that more than 25 % of the OD stretching band comes from surface and subsurface molecules [23]. The surface contribution is also clearly evident in the sharp band feature near 1650 cm^{-1} associated with the bending mode of surface H_2O molecules which is superimposed over the broad $\nu_2/2\nu_L$ absorption [11]. Serendipitously, the ν_L band is influenced only in small particles [14].

The present study explores the IR spectroscopy of nanoscale particulate ice in the stretch, bend and libration regions. We systematically examine the effects of both temperature, and of varying isotopic concentration, where some intriguing differences emerge between the OH and OD stretching regions. Complementary molecular dynamics calculations explore the temperature and isotope effects in this region of the spectrum.

Experimental

The instrumental setup is described in detail elsewhere [3, 12]. Briefly, spectra were recorded at the Australian Synchrotron THz/Far-IR beamline using a Bruker IFS125/HR spectrometer coupled to an enclosive flow cooling (EFC) cell [72]. The internal globar was used as the light source and the spectrometer was fitted with a KBr beamsplitter; KBr windows were also used on the EFC cell. Spectra covering the full bandwidth (550 - 5000 cm^{-1}) were recorded using a MCTm (mercury cadmium telluride mid band) detector at a resolution of 1 cm^{-1}. A Blackman-Harris 3-Term apodization function with a zero fill factor of 2 was used in the Fourier transformation of the data.

Distilled H_2O and D_2O (99.9 % Merck) were used without further purification to make the H_2O-D_2O mixtures. Aliquots of either H_2O or D_2O were portioned into a steel cylinder (*ca*. 100 mL) using either a 5 mL or 10 mL disposable syringe. Helium gas was flowed through the bubbler to minimise contamination from atmospheric CO_2, N_2 and H_2O whilst the liquids were being added. The container was then gently swirled once the top had been placed on. For each mixture, helium was slowly bubbled through the system toward the pump for *ca*. one minute (bypassing the EFC) to establish an equilibrium between the adsorption and desorption of H_2O/HOD/D_2O molecules onto the nylon tubing and bubbler walls.

For an experiment at 180 K, the EFC cell was filled with 20 kPa He buffer gas and left to thermally equilibrate for *ca*. two minutes. During this time, the steel bubbler was pressurised with 275 kPa He carrier gas. The helium gas flow was then isolated and the He-H_2O/HOD/D_2O gas mixture was left to equilibrate for *ca*. one to two minutes. A control background spectrum was recorded once the temperature of the EFC cell had stabilised and a set of 400 scans (200 files with 2 scans per file) was initiated using Bruker's OPUS 6.0 software to record the spectra resulting from a single pulse (1000 ms) of the equilibrated He-H_2O/HOD/D_2O gas mixture that was introduced into the EFC cell. Spectra of nanoparticle formation was recorded over a time period of approximately six minutes as particles were formed and diffused through the optical beam, with the final averaged spectrum consisting of spectra taken after a short delay (< two seconds) to allow for the complete formation of nanoparticles. Upon completion of the 400 scans, the EFC cell was evacuated to remove the sample and a second control background spectrum was recorded to monitor any ice that had adsorbed onto the surface of the bottom mirrors. Spectral contributions emanating from ice adsorbed onto the mirrors were removed via spectral subtraction of the adsorbed ice from the final averaged spectrum.

The central temperature of the cell was monitored using an iron-rhodium thermistor, whereas k-type thermocouples were used for the colander (top, middle and bottom positions) as well as the top and bottom mirrors. The heater temperatures for the mirrors were maintained approximately 10 K above the colander temperatures in order to minimise ice adsorption and the central cell temperature was recorded before and after each experiment. This process was repeated for each measured temperature

in the temperature series down to 7 K. Three different coolants were used in the outer jacket of the EFC cell for the different temperature ranges: liquid helium for temperatures below 78 K, liquid nitrogen for temperatures between 78 – 150 K and cold nitrogen gas for 130 - 190 K.

For the dilution series, the experimental conditions used are as given above, except that the detector was changed to a MCTn (narrow band) which has a more restricted low wavenumber cut off of 700 cm^{-1}.

Computational

The OH (OD) stretch IR spectra were modelled using a mixed quantum/classical approach developed by Skinner and co-workers [73]. In this method, the OH (OD) stretches are treated quantum mechanically, while the translational and rotational degrees of freedom are described by classical molecular dynamics (MD) simulations using rigid water models and the intra-molecular bends are ignored. The detail of this method, including the *ab initio*-based spectroscopic maps used in this work, is discussed in ref. [58]. One noteworthy point about this method is that the intramolecular and intermolecular OH (OD) vibrational couplings are explicitly considered when there are multiple OH (OD) chromophores in the systems (e.g. neat H_2O ice).

The MD simulations were performed for bulk cubic ice instead of cubic ice nanoparticles in that their experimental IR spectra are very similar (except for the dangling OH or OD peak) provided that the diameter of the ice nanoparticle is greater than 8 nm [12]. The initial proton-disordered configuration for cubic ice is a 216-molecule configuration from ref. [74]. It is known that at 88 K the density of cubic ice is almost identical to that of hexagonal ice [75], but only the temperature dependence of the latter is well documented [76]. Therefore, the cubic simulation box was scaled to match the experimental density of hexagonal ice at a given temperature (e.g. 10, 80 and 200 K). The system then was simulated in a substance, volume temperature (NVT) ensemble using the explicit three-body (E3B) water model recently developed by Skinner and co-workers [77]. All simulations were performed with a modified GROMACS package 4.5.5 [78]. Other simulation details are identical to those in Ref. [58] except that in this work the MD trajectories were saved every 5 fs in the production runs for the spectral calculations.

For the spectral calculations of the H_2O/HOD/D_2O mixtures with % OD < 50 %, after running the MD simulations for H_2O, we assigned the H atoms to be D atoms at random based on % OD (this is equivalent to the assumption of the equilibrium constant in **Equation 1** to be 4.00, which is close to the experimental value for liquid water [20]). Likewise, for the H_2O/HOD/D_2O mixtures with % OH < 50 %, the D atoms from the D_2O simulations were randomly assigned to be H atoms. For each mixture, an average over 400 different random realizations was performed to guarantee the spectral convergence.

Results and discussion

Peak maxima vs centre of gravity (COG)

Unless stated otherwise, the wavenumber values given herein are obtained using a method for estimating the COG position (**Equation 2**), rather than the conventional peak max method due to the broad, asymmetric nature of the vibrational bands.

$$\text{Peak position}_{\text{COG}} = \frac{\int \bar{\omega} A(\bar{\omega})\, d\bar{\omega}}{\int A(\bar{\omega}) d\bar{\omega}} \qquad (2)$$

where $\bar{\omega}$ is in cm^{-1}

The (default 90 %) COG wavenumber value is calculated using the peak picking procedure in Bruker's OPUS 6.0 software with upper and lower integration limits for $\bar{\omega}$ such that $A(\bar{\omega}) = 0.1A_{max}$. Spectra were re-transformed at 4 cm^{-1} resolution in order to minimise noise which affected the COG and peak max wavenumber values of the ν_L libration and OH/OD stretching bands. Plots shown below do not include data points for temperature between 58 - 78 K because it was difficult to maintain stable temperatures within this range. Some data points do not have error bars as they are too small to be included.

Particle size

The average particle diameter observed throughout the experiments ranges from 10 nm at 7 K to 40 nm at 150 K. Beyond that, they are larger still. Average particle sizes, **Figure 1**, are determined by comparing the integrated intensity of the dangling OH or OD bands (dOH or dOD) with their respective hydrogen-bonded stretch bands, and accounting for the N_2 adsorption observed at temperatures less than 60 K [46]. Short-wave scattering is also observed in some of our experiments, and although conventionally used for thin film ices [79] it can also be used to estimate particle sizes as diameters approach $\lambda / 4\pi$ at warmer temperatures, where λ is the wavelength in nm. Although not shown on the scale in **Figure 1**, particles can reach diameters of *ca*. 300 nm diameter at 200 K. The scattering is measured at *ca*. 4000 cm^{-1} and then compared to calculations based on a discrete dipole approximation (DDA) [80]. It is also assumed that the size distribution of the particles follows a log normal distribution.

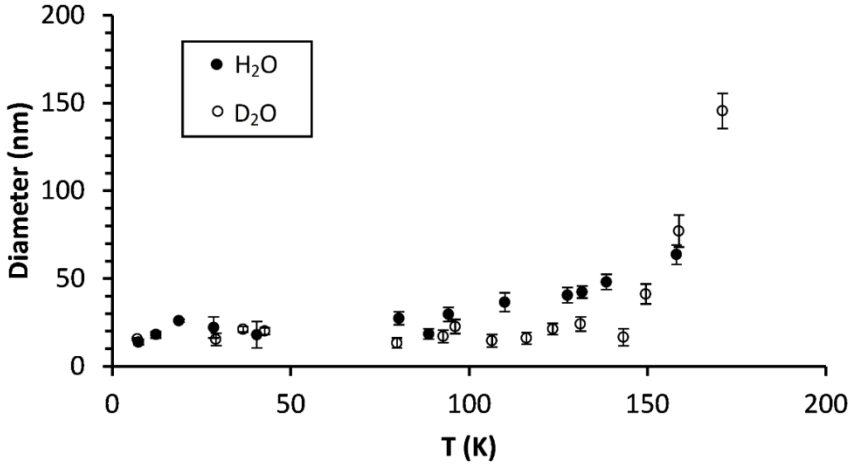

Figure 1: Average particle diameters for mostly pure H_2O (filled) and D_2O (open) nanoparticles. The larger error bars for particles below 60 K result in taking account N_2 adsorption.

Spectra and vibrational bands

A mid-IR survey spectrum of ice nanoparticles at 78 K between 550 - 4000 cm^{-1} is provided in **Figure 2**. The % OH and % OD values cited throughout refer to the molar percentage of all the hydrogen atoms that are protium and deuterium, respectively. They can be approximately evaluated using **Equations 3a, 3b** and **3c**.

$$\%\ \mathrm{OD} = \frac{\sqrt{2} f I_{OD}}{1+(\sqrt{2}-1) f I_{OD}} * 100 \qquad \textbf{(3a)}$$

$f I_{OD}$ is the fraction of total hydride stretch intensity in the OD region, given as

$$f I_{OD} = \frac{I_{OD}}{(I_{OH}+I_{OD})} \qquad \textbf{(3b)}$$

$$= \frac{\%OD}{\%OD+\sqrt{2}(100-\%OD)} \qquad \textbf{(3c)}$$

where I_{OD} and I_{OH} are the integrated intensities in the OD and OH stretch regions respectively.

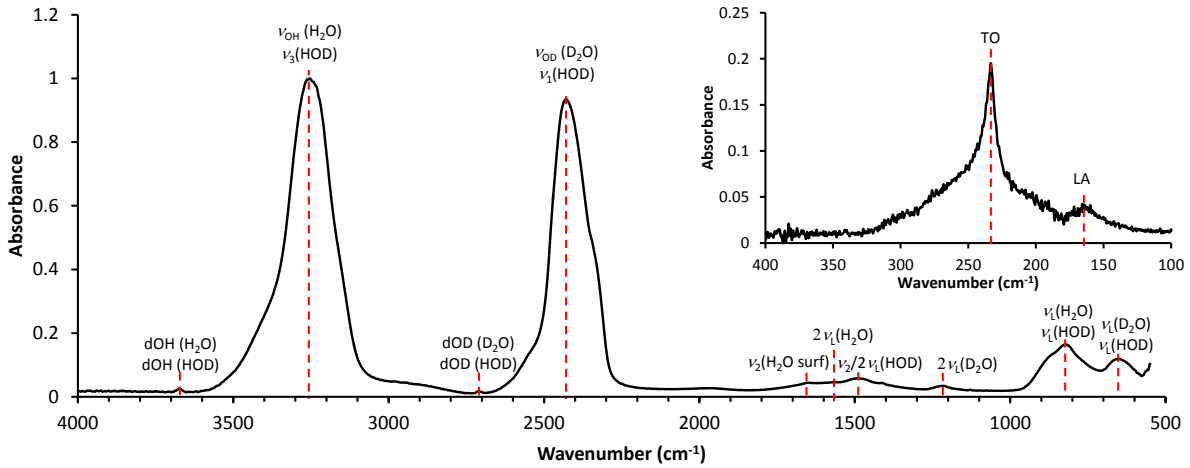

Figure 2: A normalised mid-IR survey spectrum between 500-4000 cm^{-1} of ice nanoparticles with *ca*. 51 % OD at 78 K. The inset shows the far-IR spectrum of pure H_2O ice nanoparticles at 80 K.

It is clear that many of the vibrational bands are still very broad even with isotopic dilution and **Figure 3** shows the evolution of the ν_L and $\nu_2/2\,\nu_L$ bands of each species as % OD is increased from ≈ 3 % starting at the top trace. Each isotopologue contributes its own set of intramolecular vibrations, but these along with the intermolecular modes may be affected by coupling to the surrounding molecules (see for example the ν_2 mode of HOD which differs slightly in D_2O and H_2O matrix). Estimations for the positions of the overtone bands of ν_2 and ν_L are given in **Table S2** of the supplementary data. Further broadening within the mid-IR region results from the addition of thermally excited hot bands. Given that the mid-IR spectra of I_h and I_c are identical, we assume that the nanoparticles in this study consist of the latter phase as it is kinetically favoured [81-83] and has a faster nucleation rate [84] at the temperatures employed in this study. The shapes of particles are also assumed to be spherical [46].

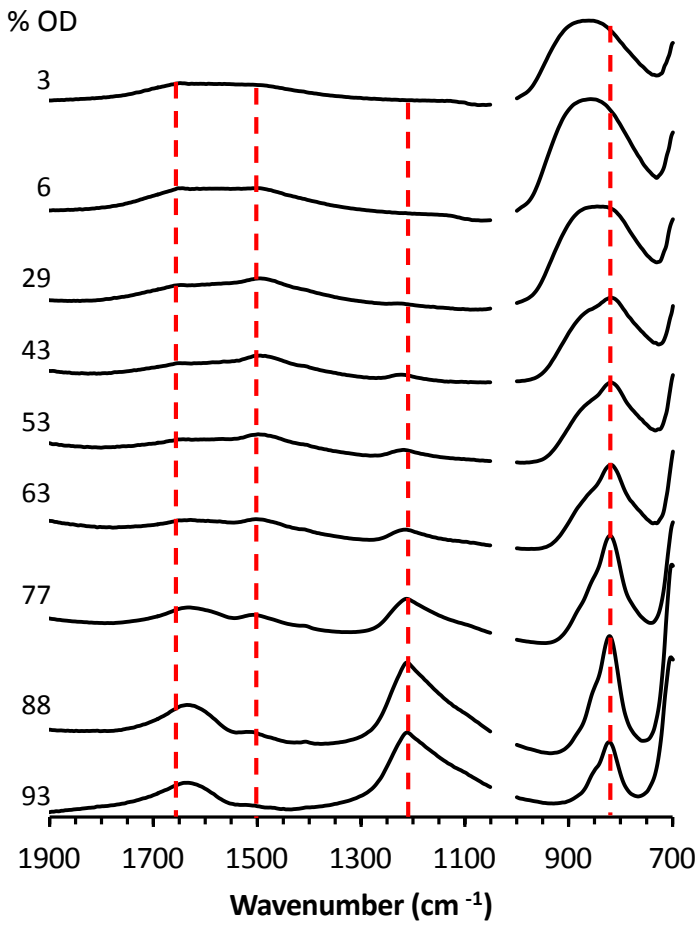

Figure 3: Changes in the mid-IR spectrum of ice particles between 700 - 2000 cm^{-1} as % OD increases. A small peak from residual isopropanol impurity between 1050 - 1000 cm^{-1} has been removed.

Libration (ν_L) vs temperature and isotopic concentration

The ν_L band of H_2O particles has a broad and flat top structure with a peak maximum near 867 cm^{-1} at 7.4 K. As the temperature is increased from 7.4 to 195 K, the ν_L band is red-shifted by only 15 cm^{-1}, corresponding to a modest, negative gradient of *ca*. - 0.08 cm^{-1} K^{-1}. These results are comparable to those previously reported by Severson *et al*. [14], where the ν_L band of crystalline H_2O clusters at 90 K (with diameters ≈ 12 nm) is located at approximately 868 cm^{-1}. In the context of aerosol particle spectra, the ν_L band is shifted much more with decreasing size (and greater surface contribution) [12, 14] than directly by temperature effects and hence the decrease in particle size below 50 K is probably the cause of the flatter curve at the coolest temperatures. There is a significant difference of *ca*. 30 cm^{-1} between crystalline aerosol and thin film data [13, 14], though the temperature gradient is similar. Even with particles sizes large enough to undergo scattering related red-shift in wavenumber value (*ca*. 0.6 μm in diameter) the ν_L band positions observed by Clapp *et al*. [85] are still higher than in the thin film, see **Figure 4**. The temperature trend and gradient for the libration band of D_2O

mirrors that in H_2O, although the wavenumber values of $\nu_L(D_2O)$ below 50 K are anomalous (**Figure S1** in the supplementary data) because of the increased noise levels near the detector low wavenumber cut-off.

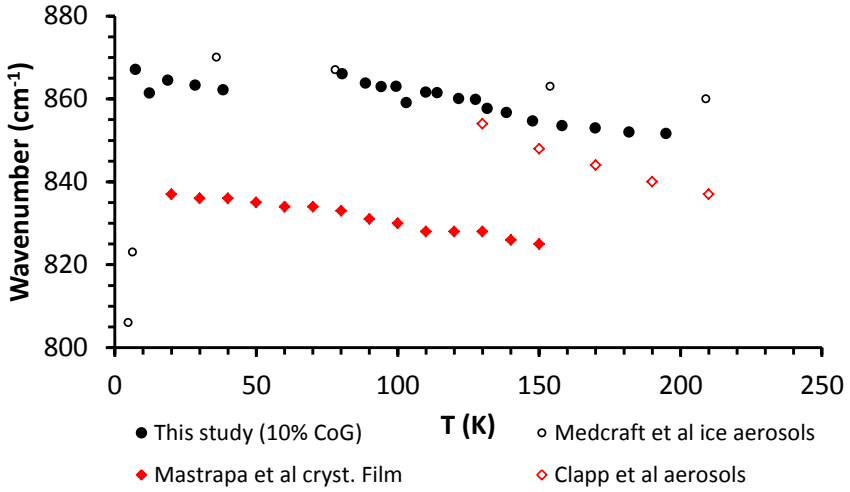

Figure 4: Peak position of the $\nu_L(H_2O)$ band showing the red-shift with increasing temperature. The present data is obtained by COG integration of only the top 10 % of the peak, corresponding to the integration limit $A(\bar{\omega}) = 0.9A_{max}$.

At 78 K, the relatively featureless ν_L bands for pure H_2O and D_2O are located near 866 and 655 cm^{-1} respectively. Both bands are fairly symmetrical with differing full-width half-max (FWHM): 160 ± 5 cm^{-1} for H_2O and 91 ± 5 cm^{-1} for D_2O. As % OD increases, the FWHM of the $\nu_L(H_2O)$ band is decreased linearly to *ca.* 50 cm^{-1}. Also, the band becomes more structured and is red-shifted to 827 cm^{-1} (see bottom trace in **Figure 3**). In this situation, the ν_L band is most likely emanating from HOD rather than H_2O as pointed out in Buch's study (827 cm^{-1} for isolated HOD in D_2O) [14], and is reassigned to ν_L(HOD). The $\nu_L(D_2O)$ band shift is not observed as it is below the 700 cm^{-1} cut-off of the MCTm detector, however it is expected that a similar trend occurs given that the wavenumber values of D_2O/HOD isolated in H_2O have previously been reported to be near 525 and 515 cm^{-1} respectively [14].

Bending (ν_2) vs temperature and isotopic concentration

H_2O

In the ν_2 bend region also, the profile of H_2O bands changes markedly with both temperature and size. For particles with "large" (i.e. greater than ≈ 40 nm) diameter at 78 K, the peak maximum is located around the centre of the very broad (FWHM ≈ 320 cm^{-1}) band at *ca.* 1580 cm^{-1} (**Figure S2** in the supplementary data). Around 140 K, the peak maximum shifts and a shoulder feature appears on the

high wavenumber side at 1649 cm^{-1}. The trend is consistent with the crystalline thin film data of Mastrapa *et al*. [13], with the band maximum position changing from 1564 cm^{-1} at 20 K to 1624 cm^{-1} at 150 K. This contradicts the expectation that the ν_2 band will be red-shifted as temperature is increased due to weakening of intermolecular hydrogen-bonds and reduction in the intramolecular H-O-H angle [52]. It also runs counter to the observation that increasing temperature shifts the peak position of every other band of crystalline ice towards the corresponding amorphous solid or liquid band.

The apparently anomalous trend only makes sense in the context of the overlapped and Fermi mixed $\nu_2/2\nu_L$ character of the band, as outlined by Devlin and co-workers [11, 86]. The $2\nu_L$ overtone in this region displays the same broad character as the ν_L fundamental band and has sufficient intensity that it can obscure the ν_2 contribution. In marked contrast to the OH stretch modes, IR intensity of the bending mode decreases with hydrogen-bonding and is particularly weak for low temperature crystalline ice. In their molecular dynamics study, Imoto *et al*. [52] attributed this to a strong anti-correlation between the permanent dipole moment and the induced dipole moment of its hydrogen-bond acceptor molecule, an effect that is diminished with hydrogen-bonding disorder. The ν_2 band intensity is much greater in the amorphous layer of aerosol particles than the crystalline core, giving rise to the distinctive peak around 1650 cm^{-1} that is clearly evident for particles of diameter up to 20 nm at 100 K [11]. Thus, the apparent blue-shift as the temperature increases is more a consequence of increasing disorder allowing an enhanced ν_2 contribution at the higher wavenumber end of the $2\nu_L$ envelope.

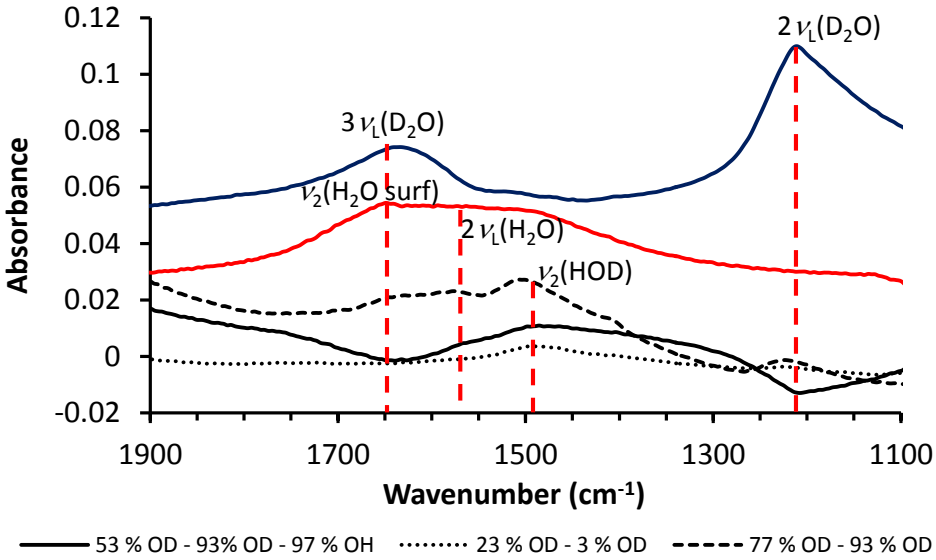

Figure 5: The $\nu_2/2\nu_L$ region of H_2O, HOD and D_2O nanoparticles at 78 K. The blue and red traces represent 93 and 97 % OD and OH respectively and are vertically offset for ease of comparison. The three black traces show the notional HOD ν_2 band by subtracting different combinations of spectra.

With isotopic dilution, there is little evidence of a shift in the amorphous 1649 cm^{-1} shoulder as shown in **Figure 3**. It is difficult to observe what occurs with the broad underlying $2\nu_L$ band because of overlap with both HOD and with the $3\nu_L$ band of D_2O at ≈ 1634 cm^{-1}.

D_2O

The corresponding $\nu_2/2\nu_L(D_2O)$ band evident in the blue trace of **Figure 5** has a distinctive asymmetric triangular shape with a long tail toward lower wavenumber values and a FWHM linewidth of *ca*. 145 cm^{-1} which is much reduced compared to H_2O. The peak maximum of 1211 cm^{-1} is barely shifted for temperatures ranging from 7 - 190 K and the band profile is not very sensitive to particle size. However, isotopic dilution does narrow the band and blue-shift it (e.g. at 80 K and % OD ≈ 43 %, the band peaks at 1223 cm^{-1} and has a FWHM of 50 cm^{-1}. The analysis of Hernandez *et al*. [86] assigns the bulk crystal ν_2 mode to around 1265 cm^{-1}, and hence the observed band to $2\nu_L$.

HOD

HOD is the most difficult isotopologue to characterise in our experiments because it is always present with at least one of the other isotopologues, and at a maximum concentration of ≈ 50 %. At intermediate D/H isotopic ratios, HOD has the highest concentration and a separate feature becomes visible at ≈ 1500 cm^{-1}, on the "red edge" of the $2\nu_L(H_2O)$ band (**Figures 2** and **3**). This band of HOD has an approximately Gaussian shape with a width of *ca*. 70 cm^{-1} depending on temperature and isotopic concentration. By subtraction of spectra with different isotopic ratios, we can derive notional spectra of this HOD band (black traces in **Figure 5**). The reduced linewidth compared to H_2O or D_2O bands tends to support the assertion by Devlin *et al*. [18] that this band is predominantly ν_2 in character. It undergoes only a modest red-shift with temperature (e.g. 1497 cm^{-1} at 78 K to 1494 cm^{-1} at 140 K). More interestingly, the position shifts depending on the isotopic concentration at 78 K to 1487 cm^{-1} in mostly H_2O to 1508 cm^{-1} in mostly D_2O. Observing similar shifts in thin film spectra, Hernandez *et al*. [86] attributes this to Fermi resonance coupling with the libration overtones of the surrounding host species. The cancellation of transition dipole contributions inferred for the ν_2 vibrations of H_2O [52], and by implication D_2O, is expected to occur to a lesser extent in HOD.

OH/OD stretching modes vs temperature

The hydrogen bonded hydride stretch bands of near pure crystalline H_2O and D_2O are shown in **Figure 6**. The sub-structure that is evident includes at least three clearly discernible peaks labelled 2 - 4 for consistency with Shi *et al*. [58] where peak 1 is seen in the Raman but not IR spectra. These features have been interpreted in many, but sometimes contradictory ways, based on different models [58]. In **Figure 6**, the labelling is from firstly, Buch & Devlin's work based on excitations in periodic systems comprised of four oscillating dipoles tetrahedrally arranged around each O-atom [87] and

secondly, in square brackets, the recent assignments of Shi *et al*. [58] where S and W refer to strong and weak intermolecular couplings, while H and L simply denote high and low wavenumber. Intramolecular couplings (W(I)) are also present in D_2O, however only W is used in this work for simplicity.

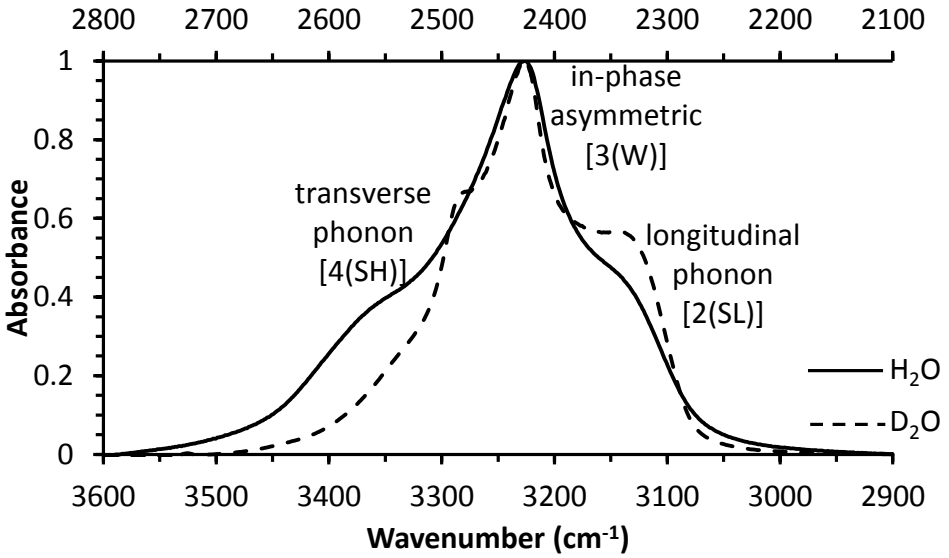

Figure 6: The OH and OD H-bonded bands of almost pure crystalline H_2O and D_2O particulate ices at 78 K. The three observed peaks are labelled using both the phonon mode description of [12, 76] and in square brackets the assignment by Shi *et al*. [48].

Figure 7 compares a series of experimental and MD simulated spectra vs temperature for the OH stretch. Throughout the temperature series, peak 3 (W) in the hydride stretch remains the most prominent feature and the intensity ratios between the three peaks remains fairly consistent. Individual peak components are broadened at higher temperatures but the overall width is little changed. More significantly, the band system is blue-shifted with increasing temperature in contrast to the ν_L, $2\nu_L$ and ν_2 bands. Thermal excitation of low energy intermolecular modes contributes to the weakened longer intermolecular H-bonds and correspondingly strengthened intramolecular O-H/D bonds. This matches the observation of a larger unit cell (and lower densities) at warmer temperatures as explained by Wagner [88], and the lattice mode band positions in the far-IR region do show the corresponding red-shift with temperature [3]. In a recent MD study based on hydrogen (O--H-O) bond co-operative relaxation, Sun *et al*. [49, 53] predicted a blue-shift in the OH stretch phonon of + 50 cm^{-1}, and a red-shift of smaller magnitude (- 15 cm^{-1}) for the lattice mode associated with intermolecular H-bonding over the range of 98 - 258 K. The simulations of **Figure 7** correctly predict the blue-shift with temperature, although the magnitude is somewhat greater than observed.

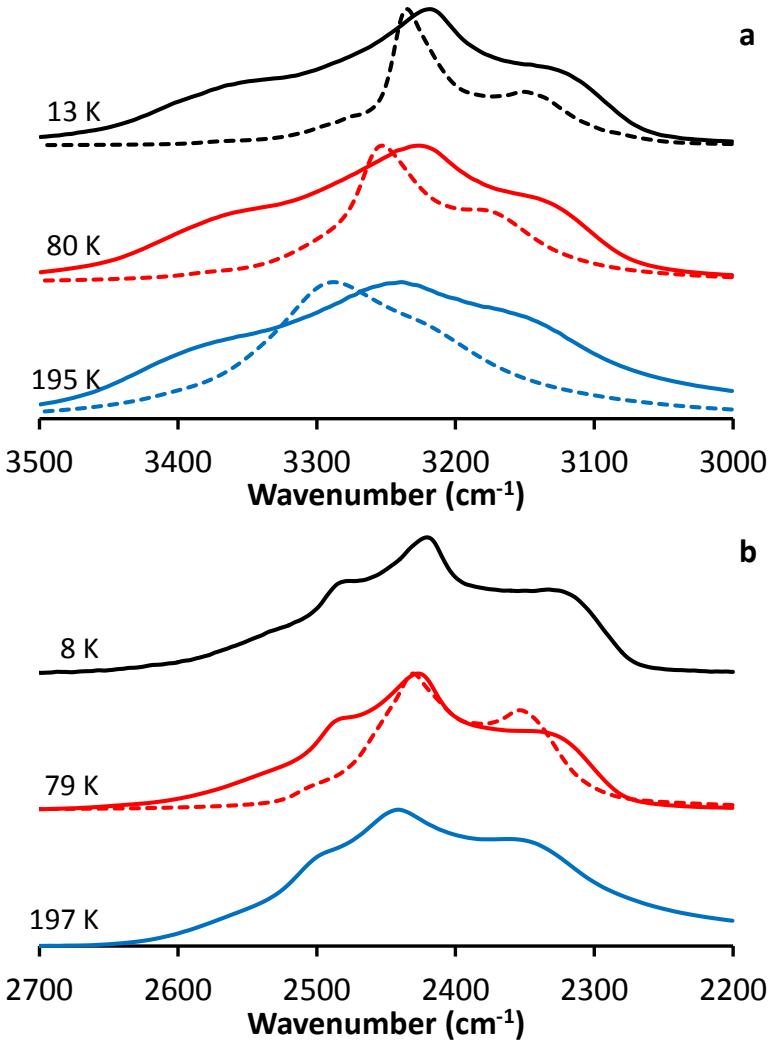

Figure 7: Comparison of the experimental (solid) and calculated (dotted) band shapes and wavenumber shifts for the OH H-bonded stretch for near pure crystalline H_2O in **panel a**. The simulations were performed at 10, 80 and 200 K. **Panel b** shows the same H-bonded stretch, but for near pure crystalline D_2O.

Gradients

Figure 8 plots the temperature dependence of H-bonded stretching peaks determined in three different ways to facilitate analysis of the trends. The peak maximum values of the band system, corresponding to the position of peak 3, follow a linear trend. The positions of peaks 2 and 4 for both near pure H_2O and D_2O were also determined, by using the second derivative function in OPUS and reducing the resolution of the spectra to 8 cm^{-1}. The positions of peaks 2, 3 and 4 are all blue-shifted at very similar rates, with gradients corresponding to 0.14, 0.12 and 0.12 cm^{-1} K^{-1} respectively. The gradient of the shift is slightly less than previously reported [12, 58] due to lower wavenumber values from spectra with T > 150 K. This may be accounted for by some larger particle sizes for the present set of experiments as discussed below.

In near pure D_2O, a similar trend is observed where peaks 2, 3 and 4 are all linearly blue-shifted with increasing temperatures. The differences in gradients for all three peaks are slightly larger for the H-bonded OD stretch, compared to OH, and their calculated gradients are 0.16, 0.11 and 0.10 cm^{-1} K^{-1} respectively. The larger gradient for peak 2 is due to the increased widths at higher temperatures, as seen in the blue trace of **panel b** in **Figure 7**, which has a strong influence on the second derivative position. Taking this into account, it is clear that the gradients for peaks 2, 3 and 4 are almost the same, both in H_2O and in D_2O.

The COG measurements, corresponding to the mean position of the entire band system, are blue-shifted at slightly smaller gradients of 0.09 cm^{-1} K^{-1} (for OH) and 0.05 cm^{-1} K^{-1} (for OD) and reflects the influence of the two SL and SH phonon bands. In particular, the SL band has a long tail that extends to lower wavenumber values on the red edge of the OH and OD stretching bands (**Figure 7**). Larger particles at warmer temperatures (e.g. > 130 K) also show increased intensities for the two phonon bands, which further red-shifts the COG band position, leading to a smaller gradient. We estimate the upper limit of particle sizes can be estimated by comparing observed short-wave scattering to predictions from simulations formed within our group using refractive index data [85]. At 130 K, the scattering profile in some spectra suggests large particles *ca*. 200 nm in diameter and this value increases to *ca*. 300 nm at 200 K. The diameters are still small compared to the wavelength of IR light but ($d \approx \lambda / 4\pi \approx 250$ nm) is a more realistic estimate of where effects begin to be significant and Mie scattering theory suggests this is sufficient to produce a slightly asymmetric band profile that skews the centre of gravity to a lower wavenumber while having less effect on the peak maximum position. The MD simulations do not suffer from the Mie scattering derived band shape asymmetry also show a linear blue-shift in COG band position.

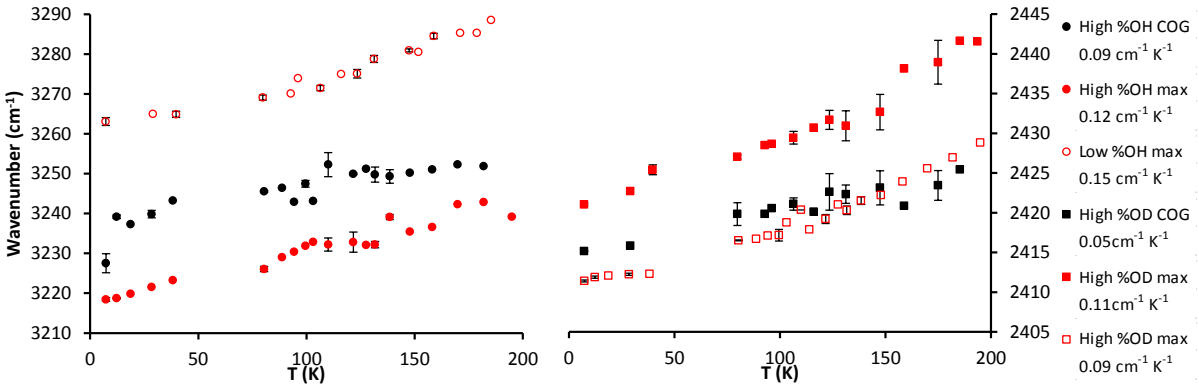

Figure 8: Comparison of the COG band position to the peak max position for the H_2O and D_2O stretching bands as a function of increasing temperature. Max and COG refer to the method used to calculate the peak position, whereas high OH (OD) refers to almost pure H_2O (D_2O) crystalline ice.

Dilute oscillator gradient

The OH stretch, **Figure 6**, is broad with a FWHM of 168 cm^{-1} in pure H_2O. As % OH decreases and the OH oscillators are diluted, the band structure collapses to a single peak with a FWHM of 50 cm^{-1}. At 8 % OH, very little H_2O is present and the OH oscillators that remain are predominantly found in the HOD species. Similarly, HOD is responsible for most of the OD oscillators at low OD concentrations. When HOD is diluted this way, the OH (or OD) oscillators in the absence of inter- and intramolecular coupling can be regarded as a "basis function" or local mode, the intrinsic starting point for building up the phonon modes. Their band positions represent in a straightforward manner the potential energy relation of the OH (or OD) group in the hydrogen bonded environment.

Figure 8 also incorporates the temperature dependence of the dilute OH/OD oscillator bands of HOD. The gradients for dilute OH and OD are 0.15 and 0.09 cm^{-1} K^{-1} respectively. It is significant that the gradients are similar to that of the peak maximum ($W(H_2O)$ or $W(D_2O)$) in the isotopically pure species and are consistent with previous thin film studies of dilute HOD in D_2O [69]. Slight differences between the isolated and H-bonded stretching gradients are mainly due to differences in the intensities of the bands. The dilute oscillator bands have intensities much weaker than their H-bonded counterparts and consequently the real refractive index values in that region of the spectrum are less affected, the scattering related band shape changes and shifts are greatly diminished. In turn this will give a slightly different gradient. From these results, it is possible to conclude and confirm that the blue-shift with increasing temperature observed in crystalline ice is almost entirely due to the intrinsic change in the local hydride potential energy as H-bonding is weakened, rather than to any consequent changes in intermolecular coupling between oscillators.

Dangling OH

The "free" or "dangling" OH band (dOH) around 3693 cm^{-1} does not shift over the temperature range from 80 - 170 K, as shown in **Figure S3** in the supplementary data. Between 40 - 70 K, the dOH band is red-shifted due to the onset of nitrogen adsorption onto the aerosol surface. The associated OH--N_2 vibrational mode is observed at a wavenumber value of 3670 cm^{-1} which is consistent with previous studies [12, 70].

The temperature range observed here is slightly higher than in the study by Hujo *et al*. [71], where the onset of N_2 adsorption began at 30 K for small clusters of 100 water molecules (1.8 nm diameter). This discrepancy in temperature is most likely due to the partial pressure of N_2 or to the dependence on cluster size. The relative proportion of N_2 molecules to available dOH sites has an appreciable influence on the temperature for N_2 adsorption. This is evidenced by the elevated temperature of 120 K found in experiments that used a substantial N_2 pressure of 0.4 bar [see **Figure 1** in [70]) in comparison to < 0.1 mbar in the study by Hujo *et al* [71]. The concentration of N_2 in this study is most

likely higher than that used in [71]. Particle size may also be a factor, as those measured by Hujo et al were at least two times smaller than the particles observed in this study even at the coldest temperatures. Cluster size influences the intrinsic position of the dOH band, which has a position of 3692 cm^{-1} for large particles in comparison to > 3700 cm^{-1} for small particles [46] and is indicative of more strongly H-bonded H_2O molecules and more polarised dOH bonds. This would lead to stronger OH--N_2 interactions for larger clusters, and hence adsorption could occur at a higher temperature.

OH/OD stretching modes vs concentration

The experimental results of isotopic variation in the OH and OD stretch regions are shown in **Figure 9**. The local OH oscillator band of dilute HOD in D_2O is narrow with a simple lineshape. This broadens initially with more HOD present and then as the H ratio increases still, the triple peak band contour associated with H_2O gradually emerges. It is much broader overall, and red-shifted. These trends are well reproduced in the corresponding simulations shown in **Figure 10**, though it is noticeable that the corresponding simulations have greater FWHM linewidths (e.g. 50 cm^{-1} for dilute OD and 75 cm^{-1} for dilute OH). From the 2nd derivative analysis, the absolute positions and the relative distance between the SH and W peaks in the OH stretching region remains consistent across the dilution range where they are observable (*ca*. 37 – 100 %), with a separation of *ca*. 140 cm^{-1}. In contrast to the SH band, the SL phonon band is red-shifted from its first observable position when OH < 50 % (3149 cm^{-1} at 47 %) to 3126 cm^{-1} at 97 % OH.

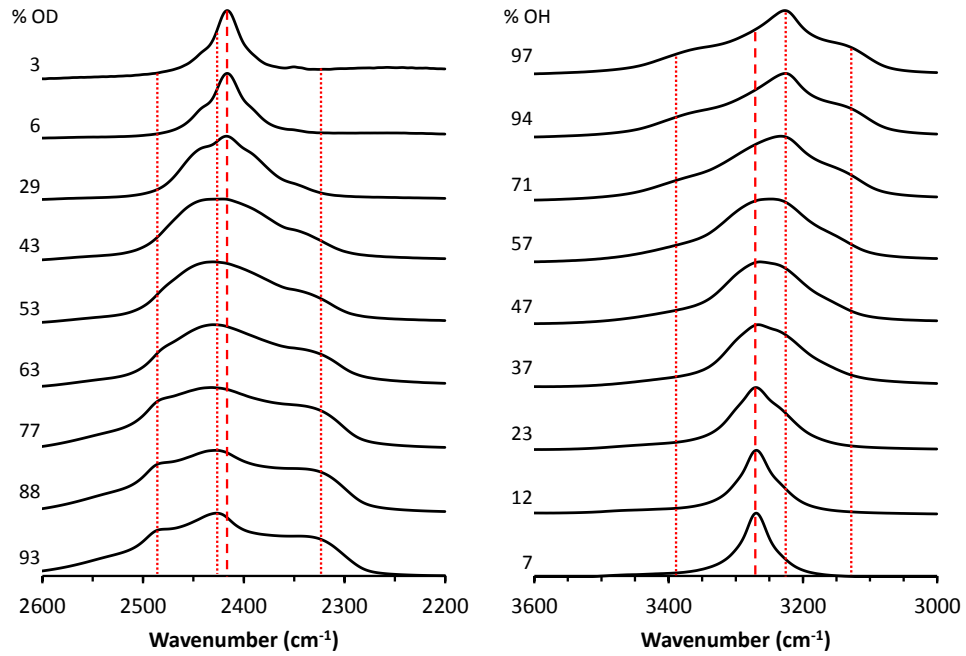

Figure 9: Changes in the OD (left) and OH(right) hydride bands as a function of % OD and % OH respectively. The dotted lines represent peaks 2, 3 and 4 of the H-bonded band, whereas the dashed lines show the position of the ν_1 (left) and ν_3 (right) bands of HOD respectively.

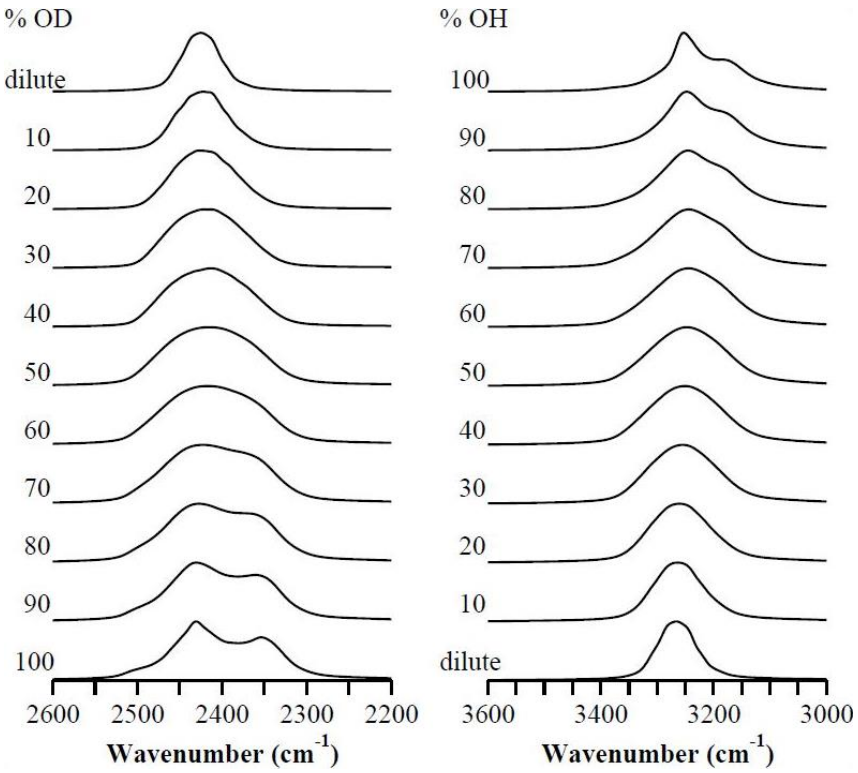

Figure 10: Calculated OD and OH stretching bands as a function of % OD (left) and % OH (right) respectively.

The band shifts that take place as OH (or OD) oscillator concentration increases are also instructive. In the OH stretch region, the COG wavenumber value is red-shifted in a linear manner from 3270 to 3240 cm^{-1} (**panel a** in **Figure 11**), while the corresponding peak maximum shifts from 3270 to 3226 cm^{-1}. The MD simulations provide a very similar result, with a linear reduction in COG band position (open circles in **Figure 11**) together with a red-shift in the peak 3 maximum of 15 cm^{-1}.

In the OD stretch region, even at OD concentrations as low as 6 %, shoulder bands are evident at *ca.* 2440 and 2380 cm^{-1} (see **Figure 9** in text and **Figure 3** in [15]). The D_2O concentration should still be negligible and the spectral features must arise entirely from OD oscillators in HOD molecules largely surrounded by H_2O. The intensity of the high wavenumber shoulder band gradually increases with increasing % OD, and its position exhibits a modest blue-shift when % OD is increased from 2.7 % to 30 % (2445 to 2450 cm^{-1}). Beyond this point, the proportion of OD is high enough that D_2O concentration becomes significant and the spectrum smears out before the phonon features associated with the D_2O profile evolve. The low wavenumber shoulder band position shows a similar trend. Similar early hints of sub-band structure are observed in the OH spectra with the appearance of a high wavenumber shoulder at 10 – 30 % OH. The appearance of phonon like band structure even with quite dilute OD (and OH) oscillators implies strong intermolecular coupling and a high degree of delocalisation, as shown in previous theoretical studies [58, 60]. Broadening of the W peak in both

H-bonded OH and OD scenarios, as % OH (% OD) is increased further, may be due to increased inter- and intramolecular coupling.

The OD stretch bands, surprisingly, show two different trends for the COG band position as shown in **panel b** in **Figure 11**. Firstly, as % OD increases toward 60 %, the COG average wavenumber value is red-shifted. Although the peak maximum broadens and shifts to higher wavenumber, a low wavenumber phonon band at *ca*. 2330 cm^{-1} becomes evident at 30 % OD. It shifts slightly to 2319 cm^{-1} and becomes prominent at 50 % OD where HOD is still the dominant species, but then does not shift any further with increasing % OD. This sub-band is also evident in the corresponding MD simulations (**Figure 10**). Its early evolution suggests highly delocalized vibrational eigenstates due to both strong intramolecular and intermolecular couplings that are in a sense "saturated" already at *ca*. 50 % (theoretically, this could be framed as a percolation threshold).

However, with further increases in OD concentration beyond 60 %, the overall band system is then blue-shifted to the extent that at 92 % OD the COG position of 2420 cm^{-1} is higher than in the low OD limit. This trend is opposite to that observed in the OH stretch region. The spectra in **Figure 9** reveal the growth of a shoulder band at *ca*. 2480 - 2490 cm^{-1}, along with an increasingly pronounced high wavenumber tail to the band profile. In the MD simulations, neither of these features is very well reproduced and even at higher % OD concentrations the COG average band position is increasingly red-shifted (**panel b** in **Figure 11**). These observations raise the question of whether the omission of Fermi resonance interactions with the $2\nu_2$ band overtone level in D_2O may be responsible for the discrepancy.

The expected position of the $2\nu_2$ band is affected by the difficulty in pinning down the ν_2 band fundamental for bulk crystalline ice. A value of 1735 cm^{-1} has been found for H_2O isolated in D_2O at 90 K [86], while *ab initio* results and extrapolation of bend vs stretch mode wavenumber values as H-bond strength changes suggest a value closer to 1708 cm^{-1} [11]. The ν_2 fundamental of D_2O isolated in H_2O has also been measured at 1225 cm^{-1} [18] but subsequently estimated to be closer to 1265 cm^{-1} [86]. HOD diluted in D_2O or H_2O is observed at 1510 or 1490 cm^{-1} respectively. Anharmonic constants $2X_{22}$ = - 38 cm^{-1} for H_2O, - 25 cm^{-1} for HOD and - 20 cm^{-1} for D_2O may be obtained from well determined gas phase monomer values for the ν_2 and $2\nu_2$ bands [29, 36, 87]. Using these values the $2\nu_2$ band positions in crystalline ice may be estimated as 3378 - 3432 cm^{-1} for H_2O, 2930 - 2970 cm^{-1} for HOD and 2430 - 2510 cm^{-1} for D_2O. This puts the $2\nu_2$ band of HOD quite some distance from the hydride stretches, while for the other two isotopologues, this same band is a little higher than the associated hydride stretch band centres. In D_2O the spacing is very close and therefore more likely to influence the underlying band structure on the high wavenumber side and is consistent with our observations. Rice *et al*. [90] included this Fermi resonance in modelling of the IR and Raman band profiles, concluding that it significantly improved the simulations in the D_2O case. Even

so, the IR simulations did not reproduce the shoulder and tail seen on the high wavenumber side of the experimental spectra. It is entirely possible that the value used for the ν_2 fundamental in that modelling (1220 cm^{-1}) is too low and that a value closer to 1265 cm^{-1} [86] might be required.

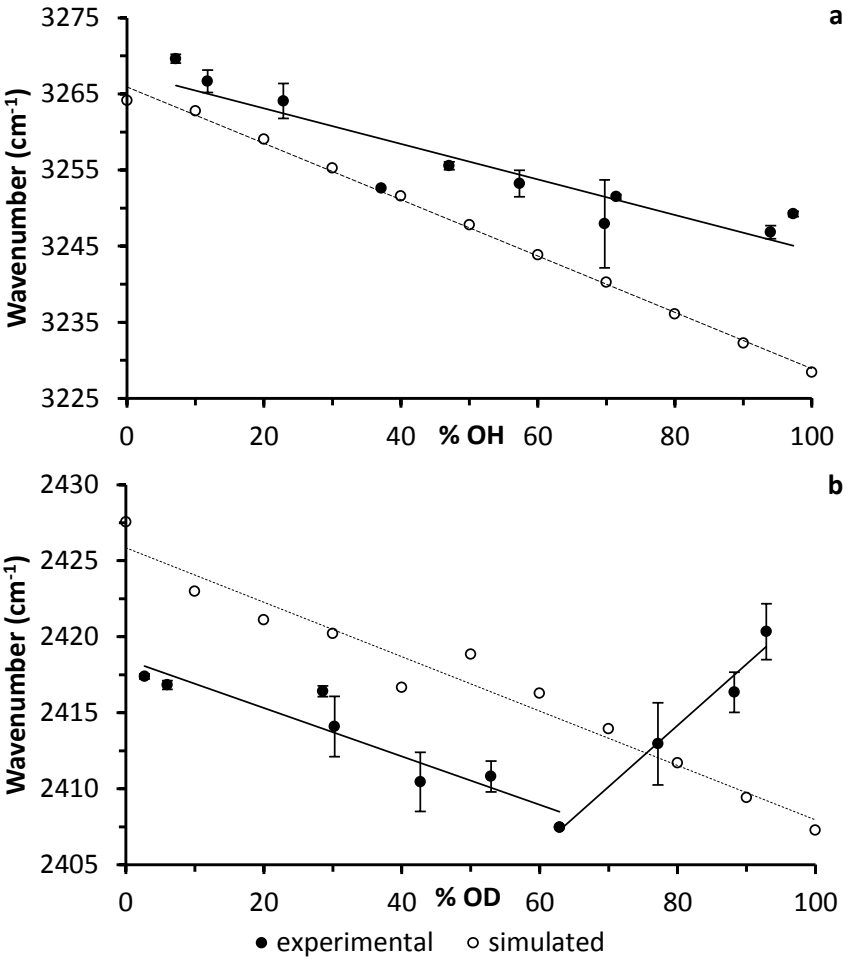

Figure 11: Wavenumber shifts for the H-bonded OH (**panel a**) and OD (**panel b**) stretching bands at 78 K as a function of increasing % OH respectively.

The FWHM of the band profiles in the OH and OD stretch regions are comparable across the entire dilution range (**Figure S4** in the supplementary data) and even the FWHM of the dilute (HOD) peaks are the same in the OH and OD regions. This is unexpected as crystalline D_2O produces more linear H-bonds, compared to H_2O [91], which should lead to narrower band widths for each sub-band. The reduced mass of the OD oscillators should also decrease the magnitude of the couplings and therefore reduce the distances between sub-bands. This narrowing is supported by the frequency distribution calculations performed by Shi *et al*. (**Figure 14** in [58]), where the frequency distributions for the weak intermolecular phonon modes in D_2O are calculated to be approximately 25 % less than H_2O. The decrease in FWHM for the OH stretch beyond 94 % OH is simply due to the increased height of narrow central peak 3.

Dangling OH/OD bands

The dangling OH and OD bands associated with the particle surface also show some changes with isotopic concentration, as seen in **Figure 12**. As the concentration of OD is increased, the dangling OH band for H_2O at 78 K is slightly blue-shifted from 3693 to 3696 cm^{-1}. The band is also broadened and appears as an unresolved doublet with a second, more intense peak becoming visible near 3688 cm^{-1} at 13 % OH (top trace in the left panel of **Figure 12**). A similar observation was made by Rowland *et al*. [70] for microporous amorphous ice particles, where the singlet dangling band changed to a broad, unresolved feature and the dangling bands for surface OH groups from H_2O and HOD were observed at 3692 and 3686 cm^{-1} respectively at 80 K. It is known that the surface layers of ice aerosols are quite disordered (e.g. amorphous H_2O bending feature near 1649 cm^{-1}) and so it is not surprising that the observed position for the dangling OH groups are similar to those of amorphous ice. These dangling bands are assigned to 3 co-ordinate water molecules (double H-bond acceptor, single donor). There is little evidence for 2 co-ordinate (single donor, single acceptor) molecules in our spectra, which exhibit signature bands around 3720 cm^{-1} in both microporous amorphous ice particles [70] and in small gas phase clusters [92].

In the case of the dangling OD groups, the two bands are more resolved and have larger splitting of *ca*. 14 cm^{-1}. The dangling OD group from HOD is observed at a lower wavenumber (2712 cm^{-1}) compared to D_2O (2726 cm^{-1}). Beyond 43 % OH, the intensity of the dangling OD bands was too weak to be observed, probably due to the preference for single donor HOD molecules on the surface to be deuterium bonded [28]. These assignments and shifts are supported by harmonic frequency calculations at the CCSD(T)/CBS level on isotopologues of the water dimer [93]. In the dimer, the dangling OH stretch of a HOD donor molecule is 8 cm^{-1} lower than a corresponding H_2O donor, while the dangling OD stretch of HOD is red-shifted 14 cm^{-1} compared to D_2O. The agreement with the aerosol data suggests that these shifts are due to intramolecular coupling that is greater in D_2O than in H_2O.

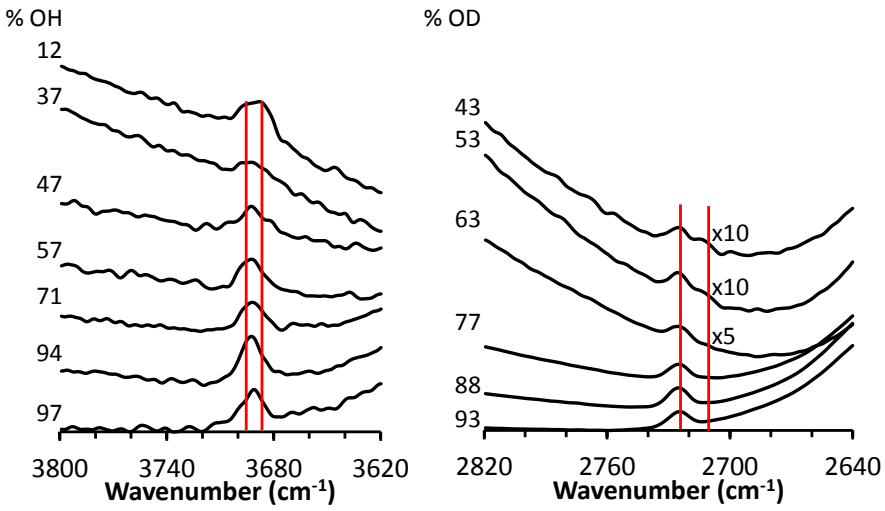

Figure 12: Changes in the dangling OH (left) and OD (right) bands at 78 K as the concentration of OH and OD are increased.

Conclusions

The mid-IR spectra of nanoparticle ices have been recorded over a range of temperatures as well as at different isotopic concentrations. Analysis of the spectra has allowed us to address how the effects of particle size, temperature and isotopic dilution influence the observed spectra, as well as the interplay between intermolecular and intramolecular coupling within the ice lattice.

Particle size affects the spectra of all three isotopologues, at the small size limit (diameters near *ca* 10 - 20 nm) due to substantial contribution from amorphous surface layers and at the large limit (300 nm) due to scattering. However, the degree of influence differs greatly depending on the vibrational band. For the ν_L libration bands, the observed red-shift with temperature is modest in magnitude, and the band position may be significantly red-shifted by either small or large particle effects. The significance of this is to confirm our recent findings that the ν_L libration band is not a useful for estimating temperature profiles in clouds [12]. The analyses suggest that the OH stretching band is a far better marker for estimating cloud temperature.

Within the bending region of H_2O, D_2O and HOD, all three exhibit quite different behaviours. We assign the dominant broad feature centred at 1580 cm^{-1} in spectra at 80 K to the $2\nu_L$ band following the results presented by Devlin and co-workers [11, 86]. The narrower band around 1650 cm^{-1}, enhanced at temperatures over 140 K, and most intense for small particles, is assigned to ν_2 vibrations of more amorphous, disordered molecules found on the surface layers or at high temperatures. The $2\nu_L$ band in near pure crystalline D_2O ice is asymmetrical in shape with a peak max at 1211 cm^{-1} at 78 K, and is insensitive to both temperature and particle size. A notional spectrum of the ν_2(HOD) band has also been derived by subtracting off spectral features emanating from both parent isotopologues. The width of this band, located near 1500 cm^{-1}, is relatively small (half-width half-max of *ca*. 70 cm^{-1} compared to *ca*. 320 cm^{-1} and 145 cm^{-1} for the $2\nu_L$ bands of H_2O and D_2O) suggesting that it may be primarily ν_2 in nature. The nature of the spectra in this region and the reasons for the significant isotopic differences remain unclear. The different libration motions and the likelihood of $\nu_2/2\nu_L$ Fermi resonance makes for a complex analysis and these bands are yet to benefit from the same level of scrutiny by theoretical methods as the hydride stretches have received.

As isotopic dilution is varied, the broad $\nu_L(H_2O)$ band decreases in width (and intensity) and is red-shifted to the corresponding value for dilute HOD in D_2O. The $2\nu_L(D_2O)$ band is barely blue-shifted as % OD is changed from near 0 to almost 100 %. A feature for the ν_2(HOD) band becomes prominent at approximately equal proportions of OH and OD, and is seen on the ”red shoulder” of the $2\nu_L(H_2O)$ band. The position of this band varies depending on the host matrix due to Fermi resonance (1487 cm^{-1} in mostly H_2O and to 1508 cm^{-1} in mostly D_2O at 78 K). The intensity of

the $2\nu_L(H_2O)$ band decreases with increasing % OD and is replaced with the $3\nu_L(D_2O)$ band around 1632 cm^{-1} at 93 % OD.

Several different trends are observed for the hydride stretching bands which are dependent on the method used to determine the band position. At least three sub-components are evident in the case of near pure H_2O and D_2O. The peak maximum for the overall band system, corresponding to the most intense central peak, when plotted against temperature shows a positive linear trend, and similar gradients are found for the high and low wavenumber shoulder peaks evaluated using second derivatives. At higher temperatures, the particles generated are large enough (*ca.* 300 nm) for scattering to begin to influence the central peak maxima to a small extent, but the COG position for the band system as a whole changes to a greater extent such that a net red-shift is observed. The band shapes of the dilute OH/OD oscillators for HOD in H_2O or D_2O are much less influenced by scattering due to their lack of intensity, since low values of the imaginary refractive indices (k) in that region correspond to only small local deviations of the real refractive indices (n). The blue-shift gradients for the isolated OH (or OD) oscillators are very similar (*ca*. 25 % more (for OH) and 20 % less (for OD)) than the corresponding peak maxima for near pure H_2O and D_2O ices. This supports the argument that the blue-shift in the hydride band position with temperature is predominantly due to the intrinsic change in the local OH (or OD) oscillator potential, and that weakening of intermolecular coupling of OH (or OD) oscillators has little influence.

Dramatic changes in the OH and OD stretch band profiles with increasing isotopic oscillator concentration clearly illustrate the high degree of delocalisation in the vibrations of neat ices. Furthermore, two different trends are observed for the COG peak position of the OH and OD stretches. The OH stretch band is linearly red-shifted as % OH changes from near 0 % (corresponding to dilute HOD in D_2O) and approaches 100 % (corresponding to pure H_2O). In contrast to the OH stretch, the OD stretch band shows a red-shift as % OD changes from near 0 % to 60 %. Beyond this point, the OD stretch band is blue-shifted such that the position of the OD stretch in near pure D_2O is at a higher wavenumber value than the OD stretch of dilute HOD in H_2O. This highlights the effect of Fermi resonance in this region, albeit its influence is much more significant in D_2O than H_2O due to closer proximity of the $2\nu_2$ level. Although the COG positions of both bands changes as a function of isotopic concentration, the positions of the intermolecular W peaks (in both OD and OD stretching bands) only change by a few wavenumbers with isotopic dilution and this is indicative of the delocalised nature of the stretching bands.

It is notable that the MD simulations which do not account for the Fermi resonance can reproduce well the triple peak structure of crystalline H_2O, its blue-shift with temperature and the red-shift in band position with increasing OH oscillator concentration. The same calculations do not perform so well in the OD region and the simulated contours at high D_2O concentration show a lack of intensity

in the high wavenumber shoulder and the overall red-shifted band position (as in the OH case) in contrast to experiment.

In the case of the dangling OH and OD groups, it has been possible to experimentally resolve the separate contributions that arise depending on whether the H-bonded atom is H or D, and the splitting is larger in the OD region (*ca*. 14 cm^{-1}) than in the OH region (*ca*. 8 cm^{-1}).

Being able to accurately determine the positions of the $\nu_2(H_2O)$ and $\nu_2(D_2O)$ bands remains a challenge as both are intrinsically weak in crystalline ices and there is large overlap with the $2\nu_L(H_2O)$ and $3\nu_L(D_2O)$ bands in the case of H_2O. This affects the estimation of the $2\nu_2$ band position which is important for determining the magnitude of Fermi resonance between ν_1 and $2\nu_2$ in D_2O, subsequently affecting the band shape of the simulated spectra as pointed out by Hernandez *et al*. [86]. Although some aspects of this research require further clarification, we have been able to identify the underlying causes for changes in band shapes (due to particle size and isotopic dilution) and band positions (due to Fermi resonance, isotopic dilution, temperature and changes in oscillator strength) that were observed in our experimental spectra.

Acknowledgements

We gratefully acknowledge the Australian Synchrotron and thank the staff for their assistance with experiments at the Far-IR beamline. AW thanks the Monash University Faculty of Science for a Dean's postgraduate scholarship, and RA is grateful for a La Trobe University Postgraduate Scholarship. We appreciate the insightful discussions with Prof. James. L. Skinner.

References

[1] A. Falenty, T. C. Hansen and W. F. Kuhs, *Nature*, **516**, 231 (2014).

[2] J. B. Hasted, S. K. Husain, F. A. M. Frescura and J. R. Birch, *Chem. Phys. Lett.*, **118**, 622 (1985).

[3] C. Medcraft, D. McNaughton, C. D. Thompson, D. Appadoo, S. Bauerecker and E. G. Robertson, *Astrophys. J.*, **758**, 17 (2012).

[4] J. E. Bertie, *Appl. Spectrosc.*, **22**, 634 (1968).

[5] J. E. Bertie and E. Whalley, *J. Chem. Phys.*, **46**, 1271 (1967).

[6] L. Shi, Y. Ni, S. E. P. Drews and J. L. Skinner, *J. Chem. Phys.*, **141**, 084508 (2014).

[7] V. Buch and J. P. Devlin, *J. Chem. Phys.*, **94**, 4091 (1991).

[8] F. Montmessin, F. Forget, P. Rannow, M. Cabane and R. M. Haberle, *J. Geophys. Res.*, **109**, E10004 (2004).

[9] D. C. B. Whittet, R. G. Smith, A. J. Adamson, D. K. Aitken, J. E. Chiar, T. H. Kerr, P. F. Roche, C. H. Smith and C. M. Wright, *Astrophys. J.*, **458**, 363 (1996).

[10] J. P. Devlin, *J. Chem. Phys.*, **91**, 5850 (1989).

[11] J. P. Devlin, J. Sadlej and V. Buch, *J. Phys. Chem. A*, **105**, 974 (2001).

[12] C. Medcraft, D. McNaughton, C. D. Thompson, D. R. T. Appadoo, S. Bauerecker and E. G. Robertson, *Phys. Chem. Chem. Phys.*, **15**, 3630 (2013).

[13] R. M. Mastrapa, S. A. Sandford, T. L. Roush, D. P. Cruikshank and C. M. D. Ore, *Astrophys. J.*, **701**, 1347 (2009).

[14] M. W. Severson, J. P. Devlin and V. Buch, *J. Chem Phys.*, **119**, 4449 (2003).

[15] C. Haas and D. F. Hornig, *J. Chem. Phys.*, **32**, 1763 (1960).

[16] J. E. Bertie and S. M. Jacobs, *J. Chem. Phys.*, **67**, 2445 (1977).

[17] P. A. Giguére and K. B. Harvey, *Can. J. Chem.*, **34**, 798 (1956).

[18] J. P. Devlin, P. J. Wooldridge and G. Ritzhaupt, *J. Chem. Phys.*, **84**, 6095 (1986).

[19] M. N. Afsar and J. B. Hasted, *J. Opt. Soc. Am.*, **67**, 902 (1977).

[20] J. –J. Max and C. Chapados, *J. Chem. Phys.*, **116**, 4626 (2002).

[21] Y. Maréchal, *J. Chem. Phys.*, **95**, 5565 (1991).

[22] G. Herzberg, *Molecular Spectra and Molecular Structure*, 281 (1945) Van Nostrand.

[23] J. P. Devlin, C. Joyce and V. Buch, *J. Phys. Chem. A*, **104**, 1974 (2000).

[24] M. S. Bergren, D. Schuh, M. G. Sceats and S. A. Rice, *J. Chem. Phys.*, **69**, 3477 (1978).

[25] J. E. Bertie and E. Whalley, *J. Chem. Phys.*, **40**, 1646 (1964).

[26] F. Perakis, S. Widmer and P. Hamm, *J. Chem. Phys.*, **134**, 204505 (2011).

[27] E. C. W. Clarke and D. N. Glew, *Can .J Chem.*, **50**, 1655 (1972).

[28] J. P. Devlin, *J. Chem. Phys.*, **112**, 5527 (2000).

[29] R. A. Toth, *J. Mol. Spectrosc.*, **195**, 73 (1999).

[30] B. Rowland, N. S. Kadagathur, J. P. Devlin, V. Buch, T. Feldman and M. J. Wojcik, *J. Chem. Phys.*, **102**, 8328 (1995).

[31] A. Shalit, F. Perakis and P. Hamm, *J. Phys. Chem. B*, **117**, 15512 (2013).

[32] A. B. Horn, M. A. Chesters, M. R. S. McCoustra and J. R. Sodeau, *J. Chem. Soc. Faraday Trans.*, **88**, 1077 (1992).

[33] M. A. Everest and C. J. Pursell, *J. Chem. Phys.*, **115**, 9843 (2001).

[34] A. Millo, Y. Raichlin and A. Katzir, *Appl. Spectrosc.*, **59**, 460 (2005).

[35] S. Y. Venyaminov and F. G. Prendergast, *Anal. Biochem.*, **248**, 234 (1997).

[36] R. A. Toth, *J. Mol. Spectrosc.*, **195**, 98 (1999).

[37] C. Medcraft, E. G. Robertson, C. D. Thompson, S. Bauerecker and D. McNaughton, *Phys. Chem. Chem. Phys.*, **11**, 7848 (2009).

[38] J. P. Devlin, C. A. Yinnon and V. Buch, *Phys. Chem. Chem. Phys.*, **11**, 7819 (2009).

[39] Ó. F. Sigurbjörnsson, G. Firanescu and R. Signorell, *Phys. Chem. Chem. Phys.*, **11**, 187 (2009).

[40] T. Häber, U. Schmitt and M. A. Suhm, *Phys. Chem. Chem. Phys.*, **1**, 5573 (1999).

[41] R. Signorell, M. K. Kunzmann and M. A. Suhm, *Chem. Phys. Lett.*, **329**, 52 (2000).

[42] M. Jetzki and R. Signorell, *J. Chem. Phys.*, **117**, 8063 (2002).

[43] R. Signorell and D. Luckhaus, *J. Phys. Chem. A*, **106**, 4855 (2002).

[44] M. Seaver, A. Galloway and T. J. Manuccia, *Rev. Sci. Instrum.*, **60**, 3452 (1989).

[45] E. J. Davis, *Aerosol Sci. Tech.*, **26**, 212 (1997).

[46] V. Buch, S. Bauerecker, J. P. Devlin, U. Buck and J. K. Kazimirski, *Int. Rev. Phys. Chem.*, **23**, 375 (2004).

[47] G. Firanescu, D. Hermsdorf, R. Ueberschaer and R. Signorell, *Phys. Chem. Chem. Phys.*, **8**, 4149 (2006).

[48] C. D. –Grau and D. Marx, *Phys. Rev. Lett.*, **112**, 148302 (2014).

[49] C. Q. Sun, X. Zhang, X. Fu, W. Zheng, J. –L. Juo, Y. Zhou, Z. Shen and J. Zhou, *J. Phys. Chem. Lett.*, **4**, 3238 (2013).

[50] M. Praprotnik, D. Janežič and J. Mavri, *J. Phys. Chem. A.*, **108**, 11056 (2004).

[51] M. J. Wójcik, K. Szczeponek and S. Ikeda, *J. Chem. Phys.*, **117**, 9850 (2002).

[52] S. Imoto, S. S. Xantheas and S. Saito, *J. Chem. Phys.*, **138**, 054506 (2013).

[53] Y. Huang, X. Zhang, Z. Ma, Y. Zhou, W. Zheng, J. Zhou and C. Q. Sun, *Coord. Chem. Rev.*, **285**, 109 (2015).

[54] Y. Huang, Z. Ma, X. Zhang, G. Zhou, Y. Zhou and C. Q. Sun, *J. Phys. Chem. B.*, **117**, 13639 (2013).

[55] B. Auer, R. Kumar, J. R. Schmidt and J. L. Skinner, *P. Natl. Acad. Sci. USA.* **104**, 14215 (2007).

[56] C. P. Lawrence and J. L. Skinner, *J. Chem. Phys.*, **118**, 264 (2003).

[57] S. A. Corcelli and J. L. Skinner, *J. Phys. Chem. A*, **109**, 6154 (2005).

[58] L. Shi, S. M. Gruenbaum and J. L. Skinner, *J. Phys. Chem. B*, **116**, 13821 (2012).

[59] F. Li and J. L. Skinner, *J. Chem. Phys.*, **132**, 204505 (2010).

[60] F. Li and J. L. Skinner, *J. Chem. Phys.*, **133**, 244504 (2010).

[61] L. Shi, F. Li and J. L. Skinner, *J. Chem. Phys.*, **140**, 244503 (2014).

[62] L. Shi and J. L. Skinner, *J. Chem. Phys.*, **143**, 014503 (2015).

[63] C. J. Tainter, L. Shi and J. L. Skinner, *J. Chem. Phys.*, **140**, 134503 (2014).

[64] J. Ceponkus and B. Nelander, *J. Phys. Chem. A*, **108**, 6499 (2004).

[65] M. E. Fajardo, S. Tam and M. E. DeRose, *J. Mol. Struct.*, **695-696**, 111 (2004).

[66] G. Ritzhaupt and J. P. Devlin, *J. Chem. Phys.*, **67**, 4779 (1977).

[67] E. A. Raymond, T. L. Tarbuck, M. G. Brown and G. L. Richmond, *J. Phys. Chem. B*, **107**, 546 (2003).

[68] Z. Wang, A. Pakoulev, Yonsoo Pang and D. D. Dlott, *J. Phys. Chem. A*, **108**, 9054 (2004).

[69] T. A. Ford and M. Falk, *Can. J. Chem.*, **46**, 3579 (1968).

[70] B. Rowland, M. Fisher and J. P. Devlin, *J. Chem. Phys.*, **95**, 1378 (1991).

[71] W. Hujo, M. Gaus, M. Schultze, T. Kobař, J. Grunenberg, M. Elstner and S. Bauerecker, *J. Phys. Chem. A*, **115**, 6218 (2011).

[72] S. Bauerecker, M. Taraschewski, C. Weitkamp, H. K. Cammenga, *Rev. Sci. Instrum.*, **72**, 3946 (2001).

[73] J. L. Skinner, B. M. Auer and Y. –S. Lin, *Advances in Chemical Physics, Volume 142* , edited by Stuart A. Rice Copyright © 2009 John Wiley & Sons, Inc.

[74] V. Buch, R. Martoňák and M. Parrinello, *J. Chem. Phys.*, **123**, 051108 (2005).

[75] L. G. Dowell and A. P. Rinfret, *Nature*, **188**, 1144 (1960).

[76] V. F. Petrenko and R. W. Whitworth, *Physics of Ice*, Oxford University Press, Oxford 1999.

[77] C. J. Tainter, P. A. Pieniazek, Y. –S. Lin and J. L. Skinner, *J. Chem. Phys.*, **134**, 184501 (2011).

[78] B. Hess, C. Kutzner, D. v. d. Spoel and E. Lindahl, *J. Chem. Theory Comput.*, **4**, 435 (2008).

[79] D. M. Hudgins, S. A. Sandford, L. J. Allamandola and A. G. G. M. Tielens, *Astrophys. J. Suppl. S.*, **86**, 713 (1993).

[80] S. Bauerecker, A. Wargenau, M. Schultze, T. Kessler, R. Tuckermann and J. Reichardt, *J. Chem. Phys.*, **126**, 134711 (2007).

[81] L. S. Bartell and J. Huang, *J. Phys. Chem.*, **98**, 7455 (1994).

[82] L. S. Bartell, *J. Phys. Chem.*, **100**, 8197 (1996).

[83] L. Delzeit and D. Blake, *J. Geophys. Res.*, **106**, 33371 (2001).

[84] G. P. Johari, *J. Chem. Phys.*, **122**, 194504 (2005).

[85] M. L. Clapp, R. E. Miller and D. R. Worsnop, *J. Phys. Chem.*, **99**, 6317 (1995).

[86] J. Hernandez, N. Uras and J. P. Devlin, *J. Chem. Phys.*, **108**, 4525 (1998).

[87] V. Buch and J. P. Devlin, *J. Chem. Phys.*, **110**, 3437 (1999).

[88] R. Feistel and W. Wagner, *J. Phys. Chem. Ref. Data*, **35**, 1021 (2006).

[89] T. Salmi, V. Hänninen, A. L. Garden, H. G. Kjaergaard, J. Tennyson and L. Halonen, *J. Phys. Chem. A*, **112**, 6305 (2008).

[90] S. A. Rice, M. S. Bergren, A. C. Belch and G. Nielson, *J. Phys. Chem.*, **87**, 4295 (1983).

[91] M. H. Brooker, G. Hancock, B. C. Rice and J. Shapter, *J. Raman Spectrosc.*, **20**, 683 (1989).

[92] E. G. Robertson, *Chem. Phys. Lett.*, **325**, 299 (2000).

[93] R. Kalescky, W. Zou, E. Kraka and D. Cremer, *Aust. J. Chem.*, **67**, 426 (2014).

Declaration for Thesis Chapter 3.2.2

Declaration by candidate

In the case of Chapter 3.2.2, the nature and extent of my contribution to the work was the following:

Nature of contribution	**Extent of contribution (%)**
Initiation, key ideas, development and writing up	80 %

The following co-authors contributed to the work. If co-authors are students at Monash University, the extent of their contribution in percentage terms must be stated:

Name	**Nature of contribution**	**Extent of contribution (%) for student co-authors only**
D. R. T. Appadoo	Experimental assistance	
D. McNaughton	Initiation and key ideas	
E. G. Robertson	Initiation and key ideas	

The undersigned hereby certify that the above declaration correctly reflects the nature and extent of the candidate's and co-authors' contributions to this work*.

Candidate's Signature		**Date**
Main Supervisor's Signature		**Date**

*Note: Where the responsible author is not the candidate's main supervisor, the main supervisor should consult with the responsible author to agree on the respective contributions of the authors.

Far and mid-IR spectroscopy of ethylene aerosols at astrophysical temepratures.

Authors

A. Wong[a], D. R. T. Appadoo[c], D. McNaughton[a] and E. G. Robertson[b]*

[a] School of Chemistry, Monash University, Wellington Road, Clayton, Victoria 3011, Australia.

[b] Department of Chemistry & Physics, La Trobe Institute for Molecular Science, La Trobe University, Victoria 3086, Australia.

[c] Australian Synchrotron, 800 Blackburn Road, Clayton, Victoria 3168, Australia

*Corresponding author email: [redacted]

Abstract

Ethylene aerosols have been synthesized at temperatures below 78 K using a 10 % mixture in helium. Spectra in both the mid-and far-IR regions have been recorded using a synchrotron source. A transition from the high temperature (53 - 78 K) $P2_1/n\ 1\ 1$ (C_{2h}^5) to the low temperature (< 53 K) $Pnnm$ (D_{2h}^{12}) structure was observed over the temperature series. No spectral features were present which made the $P1\ 2_1/n\ 1$ (C_{2h}^5) and $P2_1/n\ 1\ 1$ (C_{2h}^5) structures distinguishable from one another. Spectra corresponding to the high and low temperature structures have also been derived using multivariate statistical analysis.

Introduction

Titan is the largest moon that orbits Saturn and its chemistry has become a topic of interest due to its atmospheric composition being very similar to Earth's early reducing atmosphere. The temperature on Titan can become as cold as 78 K and the atmosphere is composed of mostly nitrogen (97 %) and methane (1.4 %). Small hydrocarbon species like ethane, ethylene and acetylene are formed as a result of the photo dissociation of methane [1]. Lakes [2] and oceans [3] of these small hydrocarbons have also been observed from passing satellites [4], with the Cassini spacecraft carrying the first unmanned (Huygens) robotic probe to land on Titan [5] and more fully explore the surface. Often, infrared emission and absorption spectra recorded by passing satellites can be very difficult to interpret due to a) contributions from multiple species and b) the different physical phases of each species depending on the atmospheric altitude. In order to accurately interpret spectra of these natural systems, it is important to be able to mimic such conditions on laboratory based benchtop instruments so that we are able to accurately characterise the species of interest. Of the major photoproducts formed in Titan's atmosphere, ethylene is the focus of this paper.

The crystal structure of solid ethylene, at 98 K, was first determined by Bunn to be *Pnnm* (D_{2h}^{12}) [6] with lattice dimensions of *a*, *b* and *c* equal to 4.87, 6.46 and 4.14 Å respectively. The unit cell is rectangular orthorhombic and has two ethylene molecules per cell; one located at the origin (0, 0, 0) and the other at ($\frac{1}{2}$, $\frac{1}{2}$, $\frac{1}{2}$). Both molecules are in-plane with the *c*-axis and are rotated 36° from the orthorhombic *a*-axis, as shown in **panel a** of **figure 1**, giving the unit cell two twofold screw axes (along the *a*- and *b*-axes); two glide planes (both perpendicular to the *a*- and *b*-axes) and a reflection plane perpendicular to the *c*-axis.

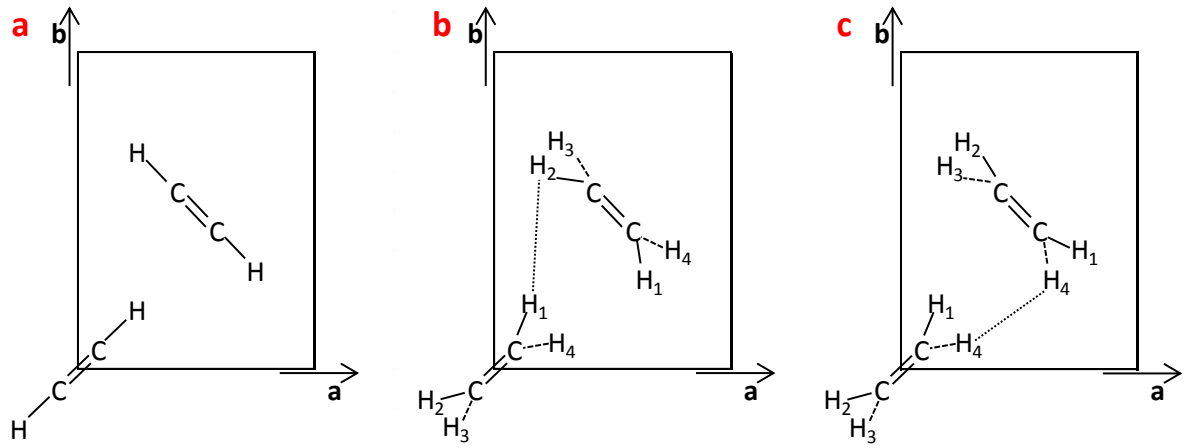

Figure 1: Illustrations of the structures for crystalline ethylene along the *ab* plane. (**a**) shows the *Pnnm* (D_{2h}^{12}) structure proposed by Bunn [6], (**b**) and (**c**) are for the $P2_1/n\ 1\ 1$ (C_{2h}^{5}) [7] and $P1\ 2_1/n\ 1$ (C_{2h}^{5}) [8] structures respectively.

Brecher & Halford [8] observed inconsistencies between the predicted and observed factor group splitting of the IR bands (**table 3** in [8]) and determined that Bunn's initial assignment [6] was incorrect. By rotating both ethylene molecules along their respective C=C axes, the space group of the unit cell is reduced to $P2_1/n\ 1\ 1$ (C_{2h}^5). As a consequence, one of the twofold screw axes, one reflection plane and the glide plane symmetry elements are removed (**panel c** in **figure 1**). This increased the number of predicted factor group splittings (band splittings) which subsequently matched the experimental spectra. The unit cell itself was reassigned to rectangular monoclinic.

In a later study by Dows [7], it was shown that there is a second possible C_{2h}^5 structure which differs only in the relative sense of the rotation of the ethylene molecule (**panel b** in **figure 1**), This minute change in the structure does not affect the factor group splitting, however does have a small influence on the C-H stretching bands due to different hydrogen atoms experiencing intermolecular H-repulsion. Dows concluded that the $P1\ 2_1/n\ 1$ (C_{2h}^5) structure is a more suitable assignment for crystalline ethylene, and therefore changed Brecher & Halford's [8] structure to $P1\ 2_1/n\ 1$ (C_{2h}^5).

Calculations of the factor group splitting were performed by Blumenfeld *et al* [9] based on Raman spectra of liquid and solid ethylene, further confirming the $P1\ 2_1/n\ 1$ (C_{2h}^5) structure. Splitting observed for the ν_{10} and ν_{12} bands using gas deposition at 4 K, lead Jacox to conclude that the *Pnnm* (D_{2h}^{12}) and $P1\ 2_1/n\ 1$ (C_{2h}^5) structures exist at low (< 53 K) and high (53-78 K) temperatures respectively [10].

Within the far-IR region, 12 bands (6 librations and 6 translations) are predicted for the low temperature structure, with only two are infrared active translational bands that were observed near 73 and 110 cm^{-1} by Brith & Ron using gas deposition [11]. Taddei & Giglio [12] predicted a third translational band to be infrared active for the high temperature structure, which has only 9 bands (6 librations and 3 translations) in total. The position of this band is estimated to appear somewhere between 16.9 and 31.4 cm^{-1} for the $P2_1/n\ 1\ 1$ (C_{2h}^5) structure, and between 29.7 and 47.6 cm^{-1} for the $P1\ 2_1/n\ 1$ (C_{2h}^5) structure. Matrix isolation experiments in xenon [13] have further complicated the thinking with features attributed to host-guest coupling as seen by the anomalous features of the ν_7 band (**figure 2a** within [13]). The first crystalline aerosol study was performed by Wang *et al*. [14] who observed a metastable intermediate phase before crystallisation was completed by 28 sec. The observed mid-IR spectra in their study corresponded to bulk phase high temperature (53 - 78 K) crystalline ethylene. Presented below are the mid- and far-IR spectra of ethylene aerosols synthesized at liquid helium temperatures using a similar technique to that employed by Wang *et al*., as well as results from a statistical analysis using multivariate curve resolution alternating least squares (MCR-ALS) [15] which has derived IR spectra for the *Pnnm* (D_{2h}^{12}) and $P1\ 2_1/n\ 1$ (C_{2h}^5) structures.

Experimental

The experiments were performed at the Australian Synchrotron far-IR beamline and spectra were recorded using the synchrotron source for both mid- and far-IR regions. A Bruker IFS125 spectrometer was used to record the spectra and aerosols were synthesized in a multipass White type cell designed for cold temperatures [16]. The combinations of optics used for the mid- and far-IR measurements are summarised in **table 1**.

Table 1: Windows and beamsplitters used for the mid- and far-IR regions

	Beamsplitter	Detector	Windows	no. of passes
Mid-IR	KBr	MCTm	KBr	4 (2.5 m)
Far-IR	6 μm Mylar	Si bolometer	Polyethylene	32 (20 m)

Ethylene gas was purchased from Sigma Aldrich (99 % purity) and used without further purification. Samples were prepared by filling an empty metal cylinder with either *ca*. 4 or 40 kPa ethylene gas, which was then pressurised to 400 kPa with helium to make mixtures containing 1 and 10 % ethylene in helium respectively. A 50 cm length of 6 mm nylon tubing was then pressurised between 69 - 345 kPa with the sample mixture before being pulsed into a cold enclosive flow cooling (EFC) cell for one second.

To reach temperatures of 6.7 K, the EFC cell was first pre-cooled to 78 K by filling the outer Dewar with liquid N_2. 50 kPa of He buffer gas was then introduced into the cell before removing the liquid N_2. The cell was then cooled to 6.7 K using liquid helium, and during these experiments, the cell was used in a static mode to avoid cryopumping. Spectra at intermediate temperatures were obtained by letting the EFC warm up slightly before stabilising the temperature with small additions of liquid helium or cold helium gas.

Spectra were recorded at a resolution of 1 cm^{-1} and treated with a Blackman-Harris 3-term apodization function and a zero fill factor of 2 during the Fourier transformation. A background spectrum was recorded prior to each experiment and used to calculate the absorbance spectrum using Bruker's OPUS software (version 6.0). Nanoparticle formation was monitored over the course of *ca*. 30 seconds (50 files with 2 scans per file) as particles quickly diffused through the optical beam. Spectra were then averaged together making sure to only include spectra that were recorded after the completion of particle formation. The shorter experimental time of 30 sec is due to a faster rate of crystallisation at the coldest temperatures.

Results and Discussion

Mid-IR

A survey spectrum for the mid-IR region of ethylene particles at 78 K between 600 - 3700 cm^{-1} is given in **figure 1** along with the assigned bands in **table 2**. The particles formed in these experiments correspond to crystalline ethylene as the spectra are comparable to those recorded by Wang *et al*. [14], who concluded that their particles were also crystalline in nature and because ethylene does not exhibit a phase transition to any other phase based on calorimetric data [17]. At low ethylene concentrations (i.e. 1 %), particles are small enough such that contributions from scattering are not observed. Vibrational bands from water become intense enough to be observed in the spectra (red trace in **figure 1**). Ethylene particles synthesized using a 10 % ethylene in helium mix show a lesser extent of water contamination, however scattering contributions from larger particles (seen as an increasing baseline in the black trace in **figure 1**) can influence the shape and position of vibrational bands. Serendipitously, short wave scattering can be used to estimate particle size through discrete dipole approximations (DDA) [18], or an empirical relationship between size and wavelength [19,20]. The wavenumber values for the mid-IR bands of ethylene aerosols are similar to those determined from thin films; and with the exception of the ν_{11} band, which is red-shifted by 7 cm^{-1}, all other bands of ethylene aerosols are within 3 cm^{-1} of their thin film counterpart. This suggests that the optical constants of crystalline ethylene are not greatly influenced by particle size or film thickness, which is in contrast to other molecular ices such as H_2O [19,21], where band positions are shifted by ten's of wavenumbers. In the case of ethylene, this greatly simplifies the analysis of spectra recorded of natural systems. The following spectra recorded at temperatures below 78 K used a 10 % ethylene in helium mix.

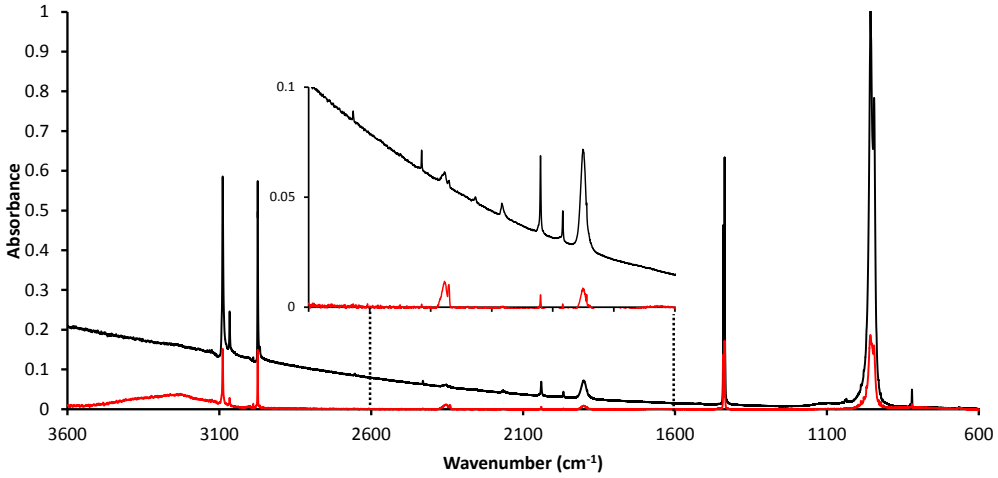

Figure 1: Normalised survey spectra of ethylene nanoparticles at 78 K using 69 kPa of 10 % ethylene:He mix in 5 kPa He buffer gas (black) and 276 kPa of 1 % ethylene:He mix in 5 kPa He buffer gas (red).

Table 2: Observed fundamental and combination bands.

Mode	position (cm^{-1})[a]	Thin film
ν_4	1035.9 1040.4	1036[c] 1042[c]
ν_7	943.7 952.7	942[c] 951[c]
ν_{11}	**2973.1** 2966.3 (^{13}C)	2980.1[b] 2978.5[b]
ν_9	3088.3	3095.6[b] 3087[b]
ν_{10}	819.9 822.7 --	820[c] 822.5[c] 825.5[c]
ν_{12}	1434.3 1436.8 1440.2	1432.8[b] 1433.7[b] --
ν_4=1, ν_8=1	1967.3	1967[d]
ν_6=1, ν_{10}=1	2040.2	2041[d]
ν_6=1, ν_7=1	2167.0	2166[d]
ν_4=1, ν_6=1	2253.8	2253[d]
ν_3=1, ν_4=1	2354.8	2357[d]
ν_2=1, ν_{10}=1	2429.7	2428[d]
ν_2=1, ν_4=1	2654.2	2652[d]
ν_2=1, ν_{12}=1	**3065.5**	--

Band positions in bold are linked by Fermi resonance [22]

[a]This work at 10.5 K, [b][13] at 12 K, [c][24] at 15 K, [d][23] at 60 K

Band position vs temperature

At 78 K, we assume the $P1\ 2_1/n\ 1$ (C_{2h}^5) high temperature structure is the dominant form (compared to $P2_1/n\ 1\ 1$ (C_{2h}^5)) where two of the four most intense fundamental bands appear as doublets (ν_7 and ν_{12}) and the other two as singlets (ν_9 and ν_{11}). The splittings of spectral bands are in agreement with the proposed structure [10] where ν_9 and ν_{11} are expected to appear as singlets. During these experiments, we were not able to observe the metastable phase that was reported by Wang *et al.* [14], in particular the resolved triplet structure for the ν_7 band (see **figure 1b** in [14]). This could be due to differences in particle size, given that the concentrations used in these experiments was 10 times greater than that

used by Wang *et al*. From their spectra, the ν_9 and ν_{11} bands also appear as singlets which are in agreement with the results reported here.

As the temperature is decreased to 6.3 K, splitting for the ν_7 band is reduced by approximately 2 cm^{-1} and additionally the peak at 952 cm^{-1} becomes narrower. A third peak becomes apparent near 1434 cm^{-1} for the ν_{12} band, which is the dominant peak at 6.3 K (**figure 2**). The shape of the ν_9 and ν_{11} bands remains unchanged throughout the temperature series and the bands are slightly red-shifted at the coldest temperatures.

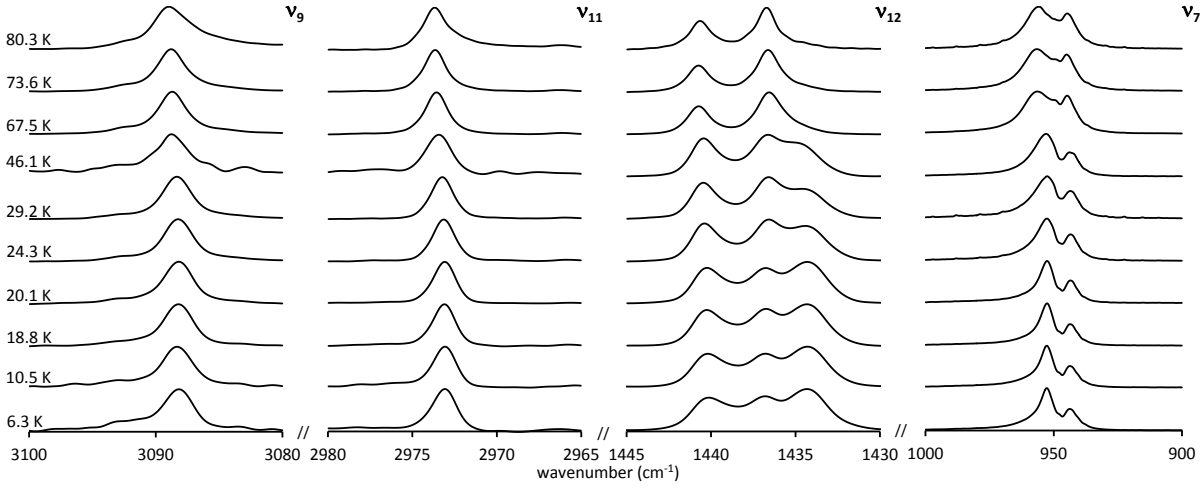

Figure 2: Evolution of the ethylene bands with decreasing temperature.

The ν_7 and ν_{12} bands are also red-shifted at very cold temperatures, with the exception of the central peak for the ν_{12} band, which is blue-shifted by *ca*. 0.1 cm^{-1} due to increasing contribution from the *Pnnm* (D_{2h}^{12}) structure, and are summarised in **table 3**.

Table 3: Peak shifts, in cm^{-1}, of the ν_7, ν_{12}, ν_9 and ν_{11} bands with decreasing temperature.

		ν_7		ν_{12}			ν_9	ν_{11}
		peak 1	peak 2	peak 1	peak 2	peak 3	peak 1	peak 1
T (K)	6.3	943.8	952.7	1434.3	1436.8	1440.1	2973.1	3088.2
	10.5	943.7	952.7	1434.3	1436.8	1440.2	2973.1	3088.3
	18.8	943.6	952.6	1434.3	1436.7	1440.3	2973.1	3088.2
	20.1	943.5	952.6	1434.3	1436.8	1440.2	2973.1	3088.2
	24.3	943.5	952.7	1434.4	1436.6	1440.4	2973.1	3088.2
	29.2	943.5	952.6	--	1436.6	1440.5	2973.2	3088.3
	46.1	943.8	953.0	--	1436.6	1440.4	2973.4	3088.7
	67.5	944.8	956.4	--	1436.6	1440.7	2973.6	3088.7
	73.5	945.0	956.5	--	1436.6	1440.7	2973.7	3088.8
	80	944.8	955.8	--	1436.7	1440.7	2973.7	3088.8

The very small red shift in wavenumber positions for the fundamentals indicates that a) in general, there is no significant change in the dimensions of the unit cell as a function of temperature and b) the structural transition from $P1\ 2_1/n\ 1$ (C_{2h}^5) to $Pnnm$ (D_{2h}^{12}) does not greatly affect the unit cell where the $r_{(H\text{-}H)}$ intermolecular distances are changed by ± 0.35 Å [8].

From **figure 2**, it is evident that there is a gradual change in the structure as it converts from the $P1\ 2_1/n\ 1$ (C_{2h}^5) to $Pnnm$ (D_{2h}^{12}) structure. Assuming that the spectral changes are simply due to different proportions of crystalline forms allows for the possibility of chemometric analysis in order to derive a spectrum for each structure, as well as calculating how the ratio of the components changes with temperature.

Because of the systems simplicity, chemometric analysis was performed using MCR-ALS [15] in MATLAB R2013b [24] as the program is fairly straightforward to use. Analysis by singular value decomposition (SVD) in MCR-ALS was able to extract two different components from the spectra. This is expected given that the structure transitions from $P1\ 2_1/n\ 1$ (C_{2h}^5) to $Pnnm$ (D_{2h}^{12}). From the ALS analysis, it was possible to derive spectra for the two crystal structures and the resultant ν_7 and ν_{12} bands are given in **figure 3**. The ν_7 and ν_{12} bands appear as multiplets due to factor group splitting where hydrogen-hydrogen repulsion is significant enough to cause the hydrogen atoms to become non-degenerate [6,23].

Results for the ν_9 and ν_{11} bands are not shown as their band shapes do not change with decreasing temperature, however, the MCR-ALS analysis was able to use the red-shift in their wavenumber

values to calculate the respective positions for the two structures. A small peak near 950 cm^{-1} is visible in the ν_7 band due to gas phase ethylene molecules at 80 K. Analysis using chemometrics was unable to differentiate between the two C_{2h}^5 structures ($P1\ 2_1/n\ 1$ and $P2_1/n\ 1\ 1$) due to a limited data set as well as the very subtle differences expected between the two structures.

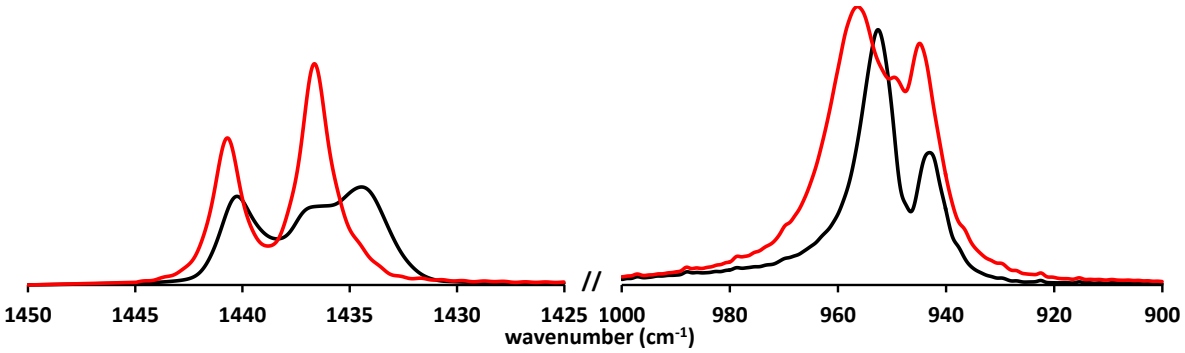

Figure 3: IR band shapes of the $P1\ 2_1/n\ 1$ (C_{2h}^5) structure (red) and *Pnnm* (D_{2h}^{12}) structure (black) for the ν_{12} (left) and ν_7 (right) bands.

From the MCR-ALS analysis, information for the change in concentration between the two structures was also extracted and is presented in **figure 4**. The model predicts that near 50 K, there is equal contribution from both the $P1\ 2_1/n\ 1$ (C_{2h}^5) and *Pnnm* (D_{2h}^{12}) structures.

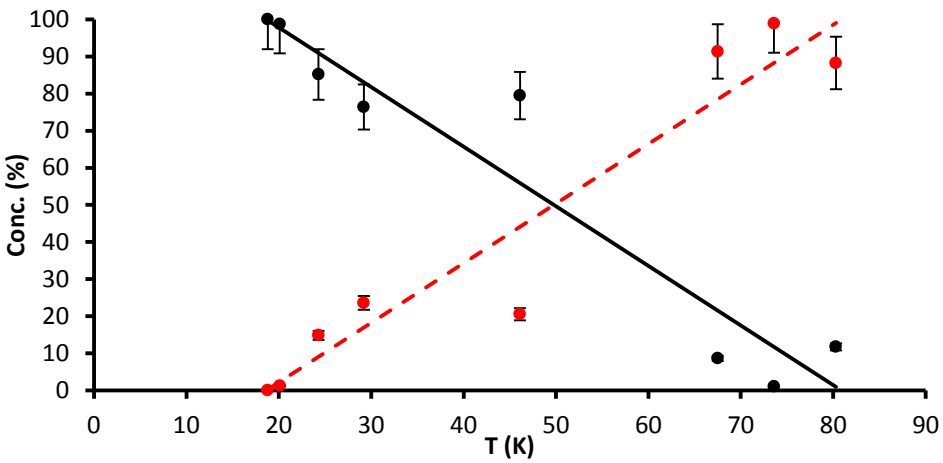

Figure 4: Changes in the concentration of the $P1\ 2_1/n\ 1$ (C_{2h}^5) structure (red) and *Pnnm* (D_{2h}^{12}) structure (black) as a function of temperature.

Far-IR

Spectra recorded in the far-IR region were limited to 78 K due to very weak absorptions from the lattice vibrations which are largely dependent on intermolecular interactions. In the case of ethylene, very weak hydrogen-hydrogen repulsions, bonding and van der Waals forces are the main interactions which hold the ethylene crystal together, giving rise to the weak lattice bands [23].

The two acoustic lattice bands were observed to be located at 67 and 106 cm^{-1}, which are red-shifted by 8 and 4 cm^{-1} respectively compared to thin film data at 50 K [11]. This shift is somewhat larger than what was observed for the bands in the mid-IR region and is attributed to the type of vibration as well as the composition of the crystal. Firstly, the wavenumber values of the lattice vibrations are very dependent on the extent of intermolecular coupling and it is not surprising that discrepancies between the two techniques are larger in the far-IR region compared to the mid-IR. Secondly, it is predicted that there is almost equal contribution to the IR spectrum from both structure at 50 K (**figure 4**) and the results reported by Brith & Ron [11] could be due to mixed $P1\ 2_1/n\ 1$ (C_{2h}^5) to $Pnnm$ (D_{2h}^{12}) crystalline ethylene.

Under the varying conditions tested at 78 K, no significant changes to the band shape or position were observed implying that particle size does not affect the lattice vibrations (**figure 5**). Taddei & Giglio [12] predicted a third translational lattice band to be infrared active between 16.9-31.4 cm^{-1} (for the $P2_1/n\ 1\ 1$ structure) and between 29.7-47.6 cm^{-1} for the $P1\ 2_1/n\ 1$ structure. The detector cut-off precludes observation below 35 cm^{-1} and thus it is not possible to observe the band for the $P2_1/n\ 1\ 1$ structure. If the structure was in fact $P1\ 2_1/n\ 1$, and the lattice band was above 35 cm^{-1}, it may have been too weak to be observed considering that a) the acoustic lattice band near 67 cm^{-1} has an absorbance of less than 0.08 in spectra **a** to **f** shown in **figure 5**, and b) the additional noise near the detector cut-off of 35 cm^{-1} makes it difficult to observed weak bands.

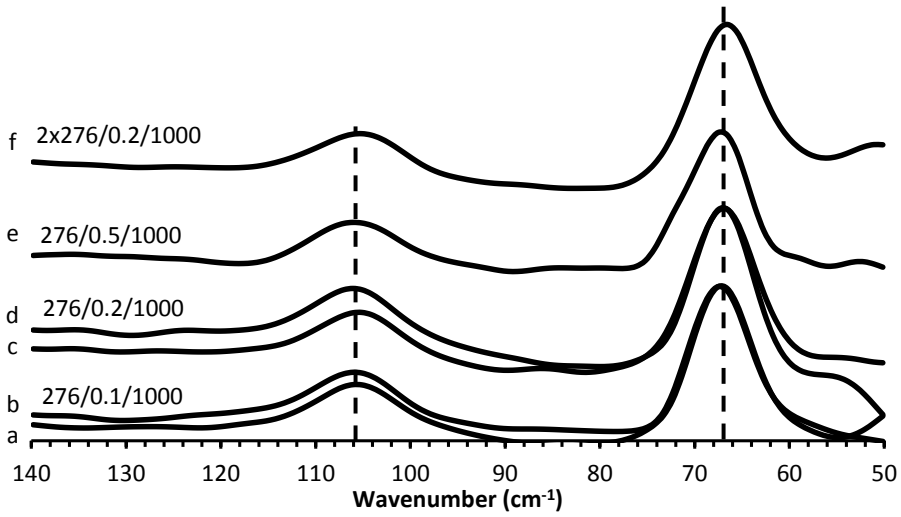

Figure 5: The far-IR lattice bands of ethylene at 79.7 ± 0.5 K, where the numbers given represent the experiment conditions for sample pressure, bath pressure and injection duration (kPa/kPa/ms) respectively.

Conclusion

The band positions for crystalline ethylene aerosols do not vary greatly compared to its thin film counterpart in the mid-IR region. The implications of this are that the method used to synthesize the crystals, as well as the differences in optical properties between thin films and aerosols are not very significant. This is in contrast to another molecular ice, H_2O [19], where the optical properties of the ice have strong influences on the band shape and position. Although data from thin films provides a good reference point, more often than not, the optical properties of aerosols are more applicable to infrared emission or absorption spectra from interstellar media.

Use of synchrotron radiation also provides the advantage of being able to measure intermolecular vibrations in the far-IR region (i.e. acoustic and translational lattice bands [21]) which have a higher signal to noise ratio compared to benchtop sources. Vibrational bands within the far-IR region can give information on the intermolecular interactions as well as the packing of molecules, which can be important for identifying the phase or structure of molecular ices.

For molecules that exhibit minor changes in band position, widths and shapes, multivariate statistical analysis can prove to be a useful tool for interpreting spectral features, and in the case of crystalline ethylene, analysis using MCR-ALS gave useful results.

References

[1] Y. L. Yung, M. Allen and J. P. Pinto, *Astrophys. J. Suppl. S.*, **55**, 465 (1984).

[2] E. R. Stofan, C. Elachi, J. I. Lunine, R. D. Lorenz, B. Stiles, K. L Mitchell, S. Ostro, L. Soderblom, C. Wood, H. Zebker, S. Wall, M. Janssen, R. Kirk, R. Lopes, F. Paganelli, J. Radebaugh, L. Wye, Y. Anderson, M. Allison, R. Boehmer, P. Callahan, P. Encrenaz, E. Flamini, G. Francescetti, Y. Gim, G. Hamilton, S. Hensley, W. T. K. Johnson, K. Kelleher, D. Muheleman, P. Paillow, G. Picardi, F. Posa, L. Roth, R. Seu, S. Shaffer, S. Vetrella and R. West, *Nature*, **445**, 61 (2007).

[3] J. I. Lunine, D. J. Stevenson and Y. L. Yungi, *Science*, **222**, 1229 (1983).

[4] voyager.jpl.nasa.gov

[5] Saturn.jpl.nasa.gov

[6] C. W. Bunn, *Trans. Faraday Soc*. **40**, 23 (1944).

[7] D. A. Dows, *J. Chem. Phys.*, **36**, 2836 (1962).

[8] C. Brecher and R. S. Halford, *J. Chem. Phys.*, **35**, 1109 (1961).

[9] S. M. Blumenfeld, S. P. Reddy and H. W. Welsh, *Can. J. Phys.*, **48**, 513 (1970).

[10] M. E. Jacox, *J. Chem. Phys.*, **34**, 140 (1962).

[11] M. Brith and A. Ron, *J. Chem. Phys.*, **50**, 5053 (1969).

[12] G. Taddei and E. Giglio, *J. Chem. Phys.*, **53**, 2768 (1970).

[13] S. T. Collins, P. A. Casey and G. C. Pimentel, *J. Chem. Phys.*, **88**, 7307 (1988).

[14] C. C. Wang, P. Zielke, Ó. F. Sigurbjörnsson, C. R. Viteri and R. Signorell, *J. Phys. Chem. A.*, **113**, 11129 (2009).

[15] J. Jaumot, A. d. Juan and R. Tauler, *Chemometr. Intell. Lab.*, **140**, 1 (2015).

[16] S. Bauerecker, M. Taraschewski, C. Weitkamp and H. K. Cammenga, *Rev. Sci. Instrum.*, **72**, 3946 (2001).

[17] C. J. Egan and J. D. Kemp, *J. Am. Chem. Soc.*, **50**, 1264 (1937).

[18] S. Bauerecker, A. Wargenau, M. Schultze, T. Kessler, R. Tuckermann and J. Reichardt, *J. Chem. Phys.*, **126**, 134711 (2007).

[19] C. Medcraft, D. McNaughton, C. D. Thompson, D. R. T. Appadoo, S. Bauerecker and E. G. Robertson, *Phys. Chem. Chem. Phys.*, **15**, 3630 (2013).

[20] D. M. Hudgins, S. A. Sandford, L. J. Allamandola and A. G. G. M. Tielens, *Astrophys. J. Suppls. Ser.*, **86**, 713 (1993).

[21] C. Medcraft, D. McNaughton, C. D. Thompson, D. Appadoo, S. Bauerecker and E. G. Robertson, *Astrophys. J.*, **758**, 1 (2012).

[22] J. L. Duncan, D. C. McKean and P. D. Mallinson, *J. Mol. Spec.*, **45**, 221 (1973).

[23] E. Rytter and D. M. Gruen, *Spectrochim. Acta*, **35A**, 199 (1979).

[24] MATLAB 2013b, The MathWorks Inc., Natick, Massachusetts, United States.

Chapter 4.0

Application of Chemometric Analysis to FTIR Gas Phase Spectra

4.1 Introduction

Chemometrics is the application of mathematical and statistical analysis in order to extract information from a given data set which may not be easily discernible via conventional methods. This technique is applicable to many chemical; biological; and physical problems, and is not limited to just laboratory scenarios. The ability to be able to analyse data with multiple components makes chemometric analysis a desirable method to aide in the understanding of spectra for techniques such as FTIR and Fourier transform microwave (FTMW) spectroscopy. The research detailed in this chapter is geared toward the application of chemometric analysis to spectra of gases recorded using high resolution FTIR and FTMW spectroscopy recorded under controlled laboratory conditions. This allows for the validation of applying chemometrics to gas phase spectroscopy and brings forth the possibility of applying this technique to real-world situations such as understanding the composition of planetary atmospheres, stars and interstellar gas clouds.

The vast range of possible applications has led to the development of many programs for use in chemometric analysis. Within the context of this thesis only two techniques will be considered: multivariate-curve resolution alternating least squares (MCR-ALS) [1] and band target entropy minimisation (BTEM) [2], however a broader review of the different chemometric techniques, methods and theory can be found within Massart *et al.* [3] and Keebe *et al.* [4].

The former technique (MCR-ALS) was used in **Chapter 3.2** as part of the analysis of FTIR spectra of ethylene nanoparticles and a description of this method is given here. The program utilises either a singular value decomposition (SVD) [5] or evolving factor analysis [6] routine in order to automatically, or manually, determine the number of components in a mixture and their corresponding spectra. The spectra of each component are then scaled using a concentration matrix (**C**) and fitted to the experimental spectra using a modified alternating least squares (ALS) regression model [1].

The latter technique (BTEM) will be the focus of this chapter as it involves the application of chemometrics to high resolution gas phase FTIR and FTMW spectra. BTEM also utilises the SVD method in order to determine the number of components in a mixture, however no *a priori* knowledge of the components is required as the vectors for each component are individually resolved using entropy minimisation theory [7]. The vectors for each component are then individually transformed in order to obtain their pure spectra before reconstructing mixed spectra using a concentration matrix (C).

BTEM [2] is a chemometric analysis method which was designed by the Garland group at the Institute of Chemical and Engineering Sciences (ICES) in A*STAR, Singapore. This method has been rigorously tested on a number of chemical situations ranging from: the analysis of UV-VIS spectra of organometallic reactions using rhodium complexes at ultra low concentrations (1 – 10ppm) [8, 9];

derivation of the X-ray powder diffraction patterns for five different lead complexes [10]; ^{1}H, ^{13}C, ^{19}F and ^{31}P NMR spectroscopy of a non-reactive mixture containing four components [11] and *in situ* FTIR spectroscopy [12, 13] of solutions to study the kinetics of aqueous reactions. BTEM presents certain advantages (in comparison to other techniques) which are desirable for the analysis of high resolution gas phase spectra. This manifests in the form of a) the ability to simulate spectra using the parameters which are extracted from the experimental data, b) being able to facilitate large data and c) no a priori knowledge, or initial estimation, of any of the properties of the components is required.

4.1.1 General theory

At the core of many modern chemometric analysis tools is a mathematical method known as singular value decomposition (SVD). In numerical algebra, SVD is used to describe the basic properties of matrices with a finite number of rows (m) and columns (n). A rigorous treatment of SVD can be found within [14 - 17] but essentially, if a complex matrix $\boldsymbol{A}$, has finite dimensions $m \times n$, then $\boldsymbol{A}$ can be expressed, in terms of SVD, using **equations 4.1 - 4.4**. ,

$$\boldsymbol{A = USV^T} \qquad \textbf{(4.1)}$$

where $\boldsymbol{S}$ is a diagonal matrix with dimensions $n \times n$ and are all real non-negative integers. $\boldsymbol{V}$ is a unitary matrix also with $n \times n$ dimensions and is defined as:

$$\boldsymbol{VV^T = V^TV = I_n} \qquad \textbf{(4.2)}$$

where $\boldsymbol{T}$ represents the transpose of $\boldsymbol{V}$ to give $\boldsymbol{V^T}$. $\boldsymbol{I_n}$ is the identity matrix with $n \times n$ dimensions and $\boldsymbol{U}$ is a matrix with $m \times n$ dimensions such that

$$\boldsymbol{U^TU = I_n} \qquad \textbf{(4.3)}$$

By taking the singular vectors within $\boldsymbol{U}$ and $\boldsymbol{V}$, the form of the complex matrix $\boldsymbol{A}$ can be re-expressed as

$$\boldsymbol{A = \sum_{i=1}^{n} s_i u_i v_i^*} \qquad \textbf{(4.4)}$$

where $\boldsymbol{u_i}$ and $\boldsymbol{v_i}$ represent the eigenvalues in matrices $\boldsymbol{U}$ and $\boldsymbol{V}$ respectively, summed across all values of i to achieve $\boldsymbol{A}$. With respect to chemometric analysis, SVD is often applied to a given dataset in order to ascertain the number of species present. From here, statistical methods such as alternating least squares (ALS) [18, 19], principal component analysis (PCA) [20], partial least squares (PLS) [21], and many others, can be applied depending on the type of information required.

One of the benefits of chemometrics is that, under the right conditions, it is very sensitive to the smallest changes in the composition of a chemical system. This is advantageous for FTIR spectroscopy because changes in the concentration, or number, of species may only result in subtle changes in the spectral bands.

4.1.2 Application to FTIR spectroscopy

If a chemical reaction uses/produces more than one reagent/product, then the infrared spectrum of the mixture, $S_{mixture}$, can be described using an expression similar to **equation 4.4**. That is:

$$S_{mixture} = \sum_{i=1}^{n}(\varepsilon_i s_i c_i) \qquad \textbf{(4.5)}$$

where s_i, c_i and ε_i represents the spectrum, concentration and molar absorption coefficient, respectively, for a given species, i, summed over all values of n to obtain $S_{mixture}$.

Furthermore, if all of the terms in **equation 4.5** are described as matrices, and an assumption that the spectra obey a linear Beer-Lambert law for a polychromatic source (**equation 4.6**) [22] is made, then chemometric analysis will be possible.

$$A_{molecule} = \log\frac{(I_0^{'}+I_0^{"})}{I_0^{'}10^{-\varepsilon^{'}lc}+I_0^{"}10^{-\varepsilon^{"}lc}} \qquad \textbf{(4.6)}$$

where $I_0^{'}$ and $I_0^{"}$ are the incident intensities for photons of wavelength $I^{'}$ and $I^{"}$ respectively, $\varepsilon^{'}$ and $\varepsilon^{"}$ are the molar absorptivities of a molecule at wavelengths $I^{'}$ and $I^{"}$.

However, like any technique, there will be limitations which will prevent chemometric analysis from being successful and need to be taken into consideration. These limitations will vary depending on the application and the most relevant ones to FTIR spectroscopy are introduced below.

First is co-linearity (**figure 4.1**). If two species, i and j, have concentrations c_i and c_j at time t_1, and increase (or decrease) at the same rate until t_2, then chemometric analysis will not be effective if spectra need to be normalised, as there will be no observable change in the spectrum between the two species

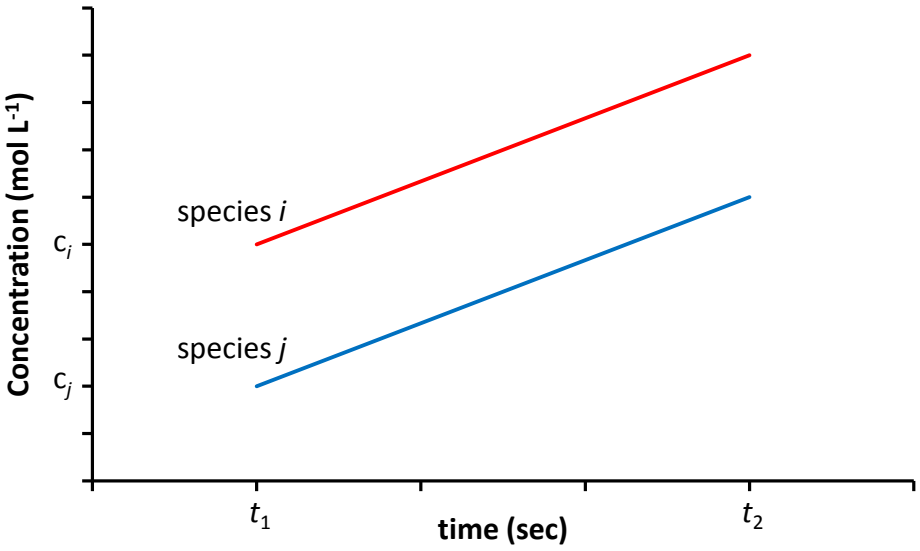

Figure 4.1: An illustration of co-linearity as a function of concentration.

Second is data size and computation. Although computational power is not a big issue, most chemometric programs are limited by the number of data points (i.e. the size of ***A***) that can be processed. The number of data points within a single high resolution file (0.00096 cm^{-1}) will be approximately four orders of magnitude larger than that of the same file recorded at 4 cm^{-1} resolution. Furthermore, the number of files required for chemometric analysis to be successful will also depend on the S/N levels in a FTIR spectrum. High resolution spectra have an intrinsically lower S/N ratio in comparison to low resolution spectra and therefore will require many more files to compensate for this. For example, only 10 may be needed at 4 cm^{-1} (see analysis using MCR-ALS in **Chapter 3.2**), whereas the FTIR study used 100 files.

Third is the error that is introduced into the simulation when performing the statistical analysis before and during the statistical analysis. Many of the available chemometric applications requires *a priori* (prior) knowledge of the number of species present in a mixture. In most cases, it is not possible to know the exact number and therefore an approximation is made. This then determines the number of vectors generated through the SVD process which can affect the quality of the fit. A further assumption about the molar extinction coefficients, band shapes, and unresolved components may be made when performing the regression model. These approximations can lead to small (or large) discrepancies between the simulated and experimental spectra.

4.2 Fourier transform microwave spectroscopy (FTMW)

Before applying the BTEM to high resolution FTIR spectra, the technique was benchmarked to data recorded from a FTMW spectrometer in order to ascertain its strengths and weaknesses. FTMW measures rotational lines from molecules in the gas phase and typically provides very short scan lengths of a few MHz and is not conducive to chemometric analysis. The measured rotational lines are typically very narrow (down to 3 kHz) and their complexity/splitting will depend on the resolution of the instrument and the structure of the molecule. Recently however, chirp pulsed microwave systems have been developed which allow for scan lengths of many GHz, providing both broadband spectra and reduced acquisition times.

4.2.1 Chirped pulse (CP) FTMW

Initially designed by Brown and co-workers [23, 24] and Grubbs *et al.* [25], CP-FTMW spectrometers utilise arbitrary waveform generators (AWGs) in order to provide a microwave pulse that sweeps over a large range of frequencies spanning several GHz. The bandwidth of the signal from the AWG is increased further to higher frequencies in the microwave region using a microwave conversion circuit. This allows for the observation of many more rotational lines, in comparison to conventional FTMW instruments, and makes broadband CP-FTMW spectroscopy amenable to chemometric analysis with long term applications aimed at separating out spectra of mixtures from pyrolysis or discharge experiments. Furthermore, by coupling a supersonic jet inlet system to a CP-FTMW spectrometer, it is possible to take advantage of the broadband nature of these instruments by increasing the populations of molecules being excited to low energy rotational states. Although some CP-FTWM systems span up to 8 GHz or more, the instrument that is used for these experiments is able to record between 3 - 26 GHz with a bandwidth of 1 GHz per spectrum by sweeping ± 500 MHz from the excitation frequency [26]. A brief outline of the processes involved in acquiring a spectrum using CP-FTMW spectroscopy is given below in **Chapter 4.1.3.1** and a more detailed description can be found within ref [27].

The selection rules for rotational transitions in the ground vibrational state of a molecular are similar to those outlined in **Chapter 2.1.3**, where the intensity of a rotational line will be predominantly dependent on the magnitude of the dipole moment and rotational temperature, rather than concentration and path length. Contributions from the translational temperature are expected to have very little influence as molecules are expanded in the same direction.

4.2.2 Experimental

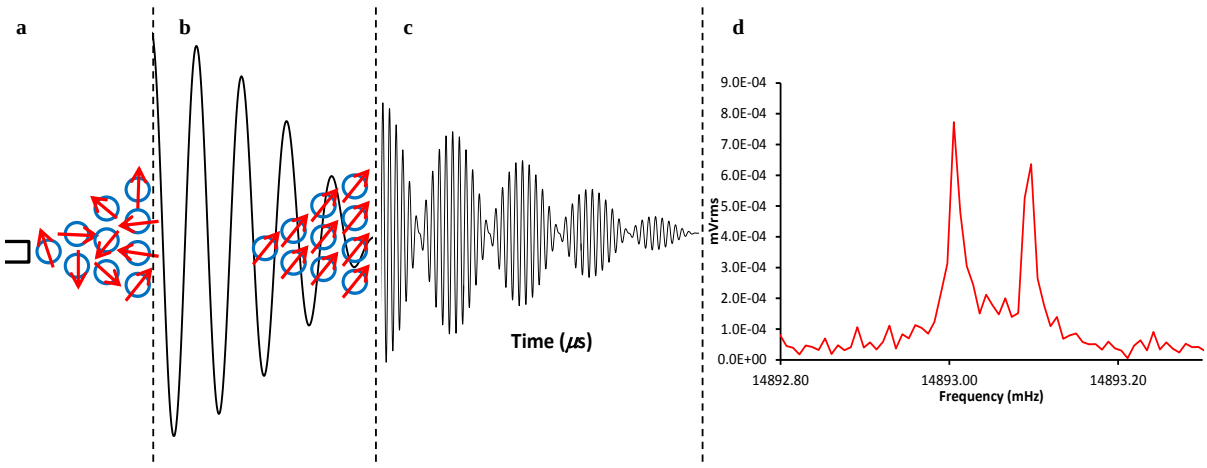

Figure 4.2: A general schematic of the processes involved with FTMW split into four panels: (**a**) (molecules are expanded), (**b**) microwaves pulsed to align dipoles, (**c**) decay of "macro" dipole and (**d**) Fourier transformation to calculate spectrum.

A simplified description of the processes involved in recording a FTMW spectrum is illustrated in **figure 4.2**. As molecules are expanded into the cavity, the individual dipole moments are aligned randomly and cancel out one another (**panel a** in **figure 4.2**). Microwaves are then pulsed into the chamber which rotationally excites the molecules and the individual dipoles become aligned such that they create a "macro" dipole (**panel b**), thus creating rotational lines which are intense enough to be observed. Overtime, the intensity of the aligned dipole will decay (**panel c**), allowing for a Fourier transform to be applied in order to calculate the line shape of a rotational line (**panel d**). This process will be repeated anywhere between 1×10^5 - 1×10^6 pulses in order to obtain a spectrum with intense rotational lines and high S/N levels which can take up to 8 hours to record a 1 GHz broadband spectrum.

Spectra of the individual gases, as well as their mixture spectra, were recorded by Mr. D. Dewald and Prof. D. McNaughton at the Institut für Physikalische Chemie und Elecktrochemie, Gottfried-Wilhelm-Leibniz Universität, Hannover, Germany, with a brief outline of the experimental given below.

Four sample gases: acetone, acrylonitrile, diethyl ether and trifluoroacetone, were used for this study which exhibit rotational lines between 18,250-19,250 MHz. The pure sample gases were prepared by making *ca*. 10 % sample-argon mixtures in a metal cylinder, whereas mixture gases (30 mixtures in total) consisted of varying the concentrations of each sample before being diluted with argon carrier gas. Each spectrum was measured over the duration of 100,000 scans and exported as (*x*, *y*) files before being sent to the Garland group for BTEM analysis.

4.2.3 Results

Figure 4.3 shows the pure experimental spectrum (left) of each species and their reconstructed spectra (right) after the BTEM analysis. Comparison of the simulated and experimental spectra indicates that the BTEM technique is successful in separating acetone and trifluoroacetone from the mixture in contrast to acrylonitrile and diethyl ether. This is most likely attributed to the low number of rotational lines present within this region for these two molecules as well as the large difference in the dipole moments between the two molecules: 3.68 D (acrylonitrile) [28] and 1.06 D (diethyl ether) [29].The dipole moments for trifluoroacetone (1.36 D) [30] and acetone (2.90 D) [31] are also given for reference. Large differences between dipole moments will also inhibit an accurate calculation of the concentration as seen by the intense rotational line of acrylonitrile in the simulated spectra for diethyl ether and trifluoroacetone near 19,000 MHz.

Aside from comparing the overall simulated spectra, it is also important to confirm that the rotational lineshapes are also accurately reproduced. Rotational lines for acetone and trifluoroacetone are compared as they have the most similarities between the pure experimental and simulated spectra. Although not shown here, almost all transitions were reproduced with a high degree of accuracy. The $4_{2,2} \leftarrow 4_{1,3}$ transition for acetone is shown below (**figure 4.4**) as an example.

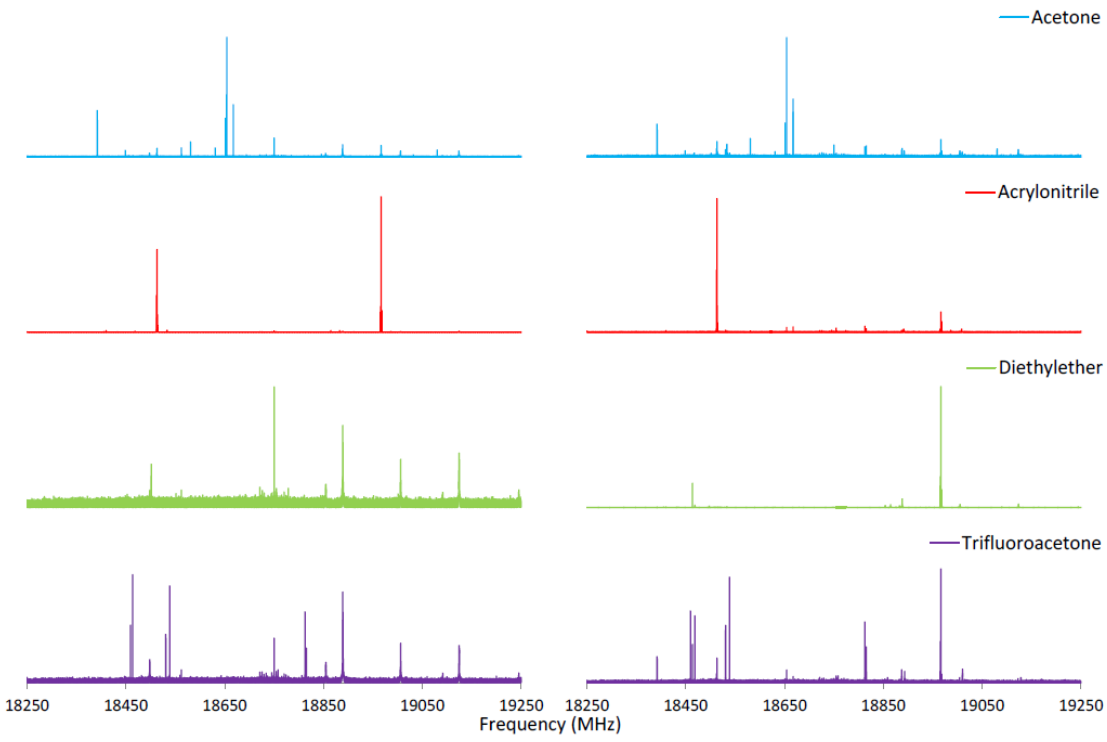

Figure 4.3: FTMW spectra of the four pure molecules (left) and their reconstructed spectra following BTEM (right).

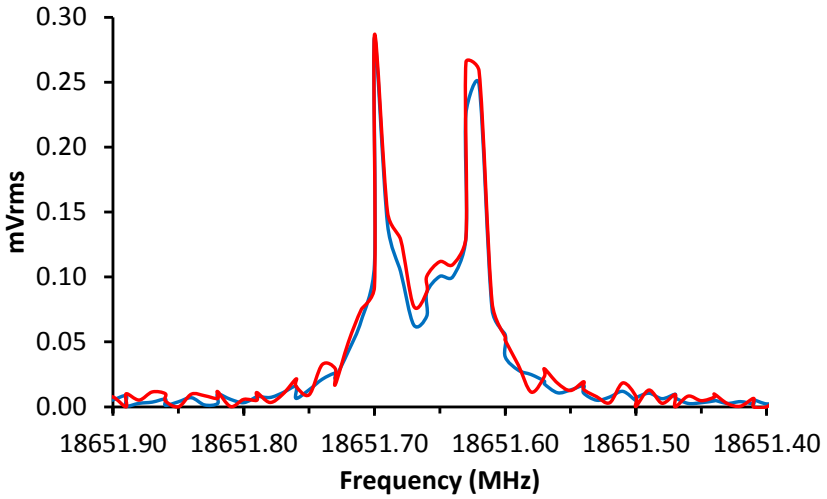

Figure 4.4: The $4_{2,2}$←$4_{1,3}$ rotational transition for acetone showing the experimental (blue) and simulated (red) line shapes.

4.2.4 Conclusions

The result from this benchmarking study indicates that the BTEM method is partially successful in analysing gas phase spectra, albeit with room for improvement given that only two of the four spectra were accurately reproduced, indicating that a larger sample size is required. This can be achieved by measuring as many different concentrations as possible to provide the BTEM method with many more variables which can be used during the SVD step of the analysis and then produce a more accurate simulation. There are also some instrumental factors which need to be taken into consideration, although some of these properties are not so easily treated.

The power scales (*y*-axis) of the spectra are not consistent when going from sample to sample due to the line intensities being predominantly influenced by the dipole moment of the molecule. Small variations in these intensities will give false positives in concentration change. Furthermore, changes in sample concentration will not guarantee that line intensities will change (i.e. decrease in intensity with decreasing concentration) and is again attributed to the dipole moment of a molecule. Although a species may have a small concentration, if it has a large dipole moment, then its rotational lines will dominate the spectrum. Conversely, a molecule with a small dipole moment, and high concentration, will have weak rotational lines as seen by the large differences in dipole moments between between diethyl ether (1.06) [29] and acrylonitrile (3.68) [28].

Despite these experimental and instrumental difficulties, application of chemometric analysis on gas phase FTMW spectra is still feasible if one is careful about the types of molecules being studied. The positive results achieved by BTEM shows potential application to sorting spectra from pyrolysis and discharge experiments.

4.3 C_3O

One of the long term objectives of applying chemometrics to gas phase spectra is its potential use for analysing spectra from interstellar media. Within the microwave region, there are numerous molecular signals originating from a range of different molecules and to date some 180 molecules have been detected. Furthermore, the number of observable molecular signals in current high sensitivity radio telescopes makes it difficult to assign a specific molecular structure to one, or multiple signals and chemometric analysis potentially could play a future role in separating molecular signatures from individual molecules.

High resolution FTIR spectroscopy also provides a test for the ability of techniques such as BTEM to sort spectra of pyrolysis or discharge experiments. C_3O is a transient molecule under laboratory conditions, has been found in interstellar media [32, 33] and has previously been shown to be generated through the pyrolysis of fumaroyl chloride [34]. This also yields several acetylenic by-products such as acetylene, mono- and di-chloro-acetylene, di-acetylene and mono- and di-chloro-di-acetylene. Secondary reactions can occur where the acetylenic species decompose to give HCl, CO and OC_4O. In the original study, McNaughton *et al*. [34] had also shown that the concentration of all of these species are dependent on the temperature of pyrolysis (see **figure 2** within [34]) and it is this characteristic that makes the pyrolysis of fumaroyl chloride a good model system for BTEM because a) multiple species are formed and b) there is no co-linearity amongst the different species.

4. 3.1 Experimental

Spectra were recorded at the Australian Synchrotron THz/far-IR beamline within the mid- and far-IR regions. KBr windows and beamsplitter, and MCTm detector were used for the mid-IR spectra, whereas the cell windows were changed to polyethylene with a Si-B boron-doped photodetector being used for the far-IR. An ambient temperature cell, housing White optics, was also used and set to 8 passes (*ca*. 4 m). All spectra (backgrounds and samples) were recorded at 0.002 cm^{-1} resolution between 720-4400 cm^{-1} and treated with a four point apodization function and zero fill factor of 2 during the Fourier transformation for consistency during the BTEM analysis.

Fumaryl (or fumaroyl) chloride (95 %), obtained from Sigma-Aldrich, was poured into a vacuum Schlenk tube (*ca*. 20 mL) and outgassed using a freeze-pump-thaw method by submerging the glass vial into liquid nitrogen. Frozen fumaryl chloride was then exposed to a pump to remove any dissolved gases as the sample thawed. This process was repeated until no more dissolved gasses were seen. 20 background spectra (10 files with 2 scans each) were recorded prior to introducing sample vapour with a furnace set to 740 °C. Fumaryl chloride vapour was then flowed through the furnace into the cell (operating in a flow through mode) at a rate to maintain a pressure of $3.33\pm0.06\times10^{-1}$ kPa

before recording 20 sample scans (10 files with 2 scans each). After 20 scans, the sample vial was isolated and the temperature of the furnace was increased to 760 °C whilst any residual molecules were removed. The process of recording 20 background spectra, followed by 20 sample spectra, was repeated as the furnace temperature was increased at 20 °C intervals up to 840 °C for both mid- and far-IR regions.

4.3.2 Preliminary results and analysis

A total of 176 sample and background spectra were exported as (*x*, *y*) data tables for BTEM analysis within the region of 2200 – 2280 where the ν_1 band of C_3O is situated. **Figure 4.5** shows a low resolution (1 cm^{-1}) survey spectrum encompassing the different species that are formed at a pyrolysis temperature of 760 °C, as well as a high resolution (0.002 cm^{-1}) inset of the ν_1 band for C_3O centred around 2250 cm^{-1}. The wavenumber region between 2000-2280 cm^{-1} was used for the BTEM analysis because it contains the ro-vibrational band from C_3O and other species such as carbon monoxide (2140 cm^{-1}) and chloro-acetylene (2114 cm^{-1}).

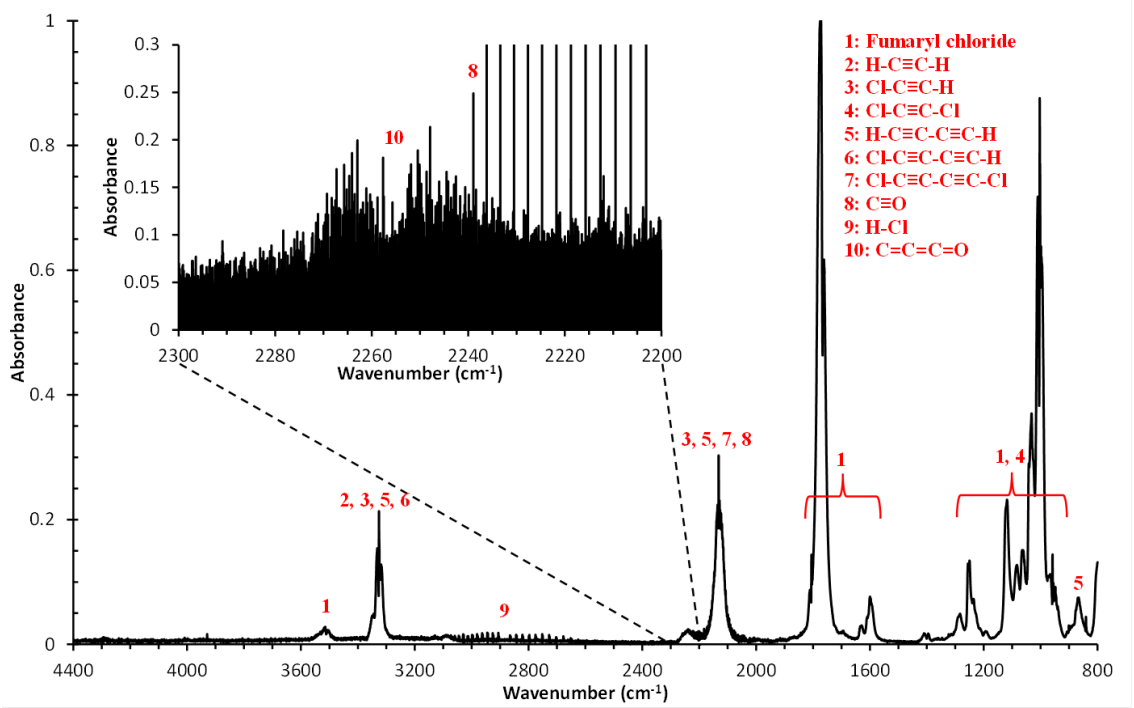

Figure 4.5: Mid-IR survey spectrum of pyrolysis products at a furnace temperature of 760 °C. Vibrational bands from each species are assigned from 1-10.

The result from the SVD analysis is illustrated in **figure 4.6** and indicates that this step of the BTEM analysis is successful. The first panel in **figure 4.6** is in essence the raw spectrum after combining all of the individual spectra together. BTEM then corrects the baseline (**panel b**) followed by the removal of each species from panel **c - e**. Each panel represents one vector from the SVD analysis which is in turn used for the spectral reconstruction.

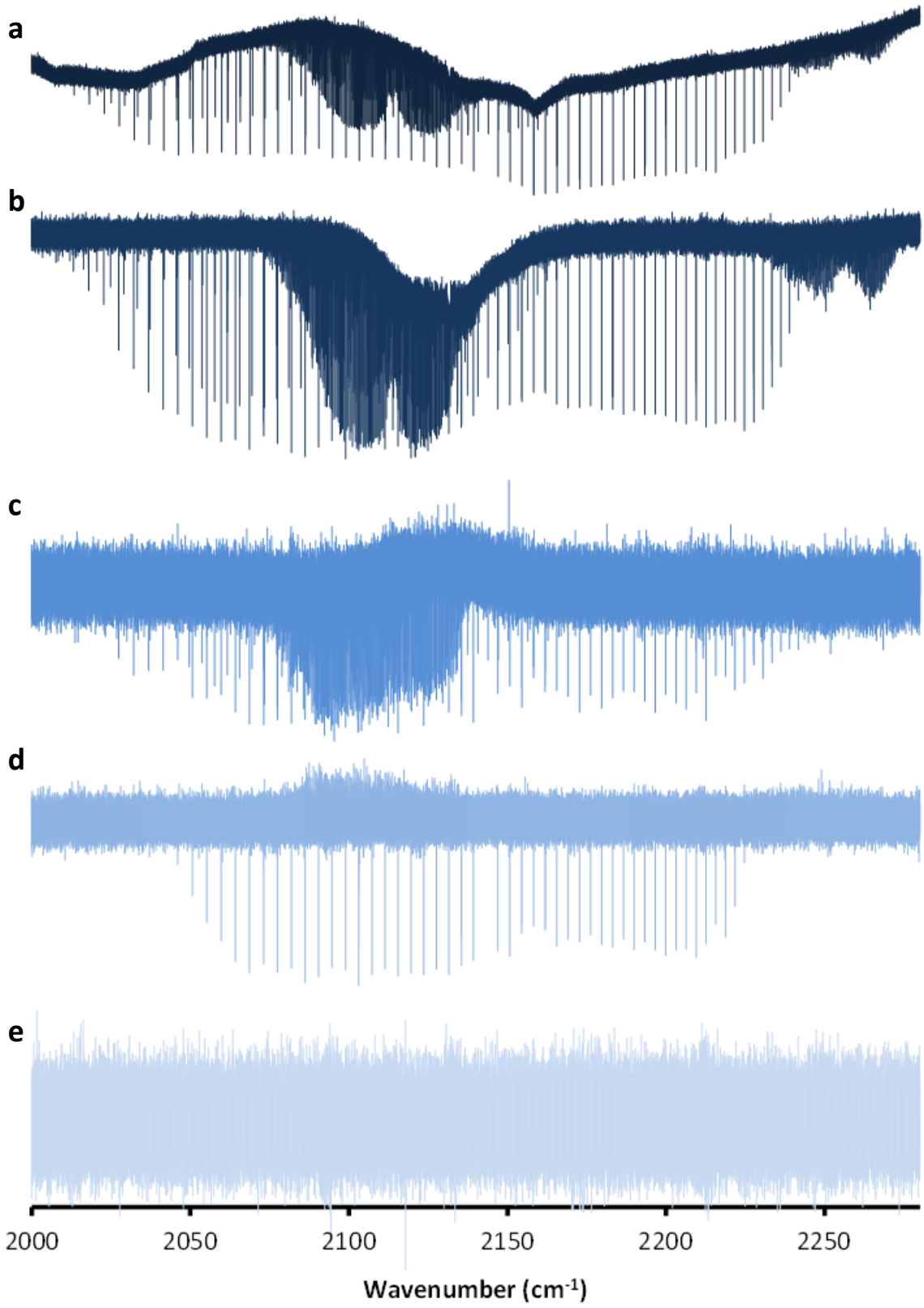

Figure 4.6: Illustration of the SVD analysis with the raw spectrum (**a**), followed by a baseline correction (**b**), then removal of C_3O (**c**), chloro-acetylene (**d**) and CO (**e**). The *y*-axes for each spectrum are on different scales, hence the differences in transmission intensity.

Ideally, the final step would be to use these vectors to reconstruct the experimental spectrum however there are some limitations which prevent this. First, the observed ro-vibrational lines for CO are saturated and do not follow a linear Beer-Lambert law (**equation 4.6**), preventing an accurate simulation of the concentration trends for all three molecules. Furthermore, the profiles of these lines do not follow a Gaussian-Lorentzian lineshape and are truncated by the OPUS 6.0 software. Although, this does not have a direct influence on ro-vibrational lines that are not saturated, the simulated lines are affected by the decreased S/N levels in high resolution spectra.

Second, the number of useful vectors is too small to perform an accurate spectral reconstruction and from **figure 4.6**, there are only 4 useful vectors which have been extracted (not including **panel e**). As a general rule of thumb, recommended by the Garland group, the minimum number of vectors required for the reconstruction should be equal to at least the number of species present during the reaction. For this experiment, at least 10 vectors would be required for successful reconstruction of the experimental spectra.

Third, the sampled spectral window is quite small as it consists of only three molecules. It was not possible to sample data over a larger spectral window, due to the BTEM algorithm reaching its limitations with 300,000 data points per file across 176 files. Given that high resolution spectra are intrinsically noisy, it was concluded that using more data files during the SVD would yield more reliable results than expanding the spectral window.

Finally, only a limited range of conditions were tested which would also influence the results, however it would also be necessary to reduce the spectral window of interest if the inclusion of spectra recorded at more temperatures were to be included into the analysis. From these results it is apparent that a careful experimental design is required to carry out a full study.

4.3.3 Conclusions

In order for the BTEM analysis to be successful, it is evident that several aspects of the experiment need to be improved. First, it is necessary to choose a pyrolysis pathway that does not produce molecules which gives saturated ro-vibrational lines so that concentration trends can be accurately calculated. Second, a larger sample size is required in terms of the different experimental conditions tested as well as the number of spectra per condition. This is the most difficult aspect to address as this will also introduce limitations to the BTEM technique itself. Due to the number of data points used in the BTEM analysis, the spectral region was limited to only a small window (2000-2280 cm^{-1}). If a larger sample size is recorded, this will further limit the region of interest and may also require spectra to be recorded at lower resolution.

Third, one must also consider the differences in applying chemometrics to laboratory systems; where experimental conditions can be manipulated, to natural systems such as interstellar media; where there are no artificial influences. This also highlights some of the intrinsic properties of these systems, such as varying temperatures with each star that lead to non-linear intensity changes that the present technique of BTEM cannot overcome. Furthermore, the temperature will affect the Boltzmann distribution of the molecular signals and will cause their intensities to change.

In light of these shortcomings, this does not mean that chemometric analysis is not a viable option. Rather, one must be quite meticulous about the experimental conditions when gathering spectra as well as the problem that it is being applied to.

References

[1] J. Jaumot, A. de Juan and R. Tauler, *Chemometr. Intell. Lab.*, **140**, 1 (2015).

[2] E. Widjaja, C. Li, W. Chew and M. Garland, *Anal. Chem.*, **75**, 4499 (2003).

[3] D. L. Massart, B. G. M. Vandeginste, S. N. Deming, Y. Michotte and L. Kaufman, *Chemometrics: a textbook*, **2**, Elsevier (1988).

[4] K. R. Keebe, R. J. Pell and M. B. Seasholtz, *Chemometrics: a practical guide*, **4**, Wiley-Interscience (1998).

[5] G. H. Colub and C. Reinsch, *Numer. Math.*, **14**, 403 (1970).

[6] W. Windig, D. A. Stephenson, *Anal. Chem.*, **64**, 2735 (1992).

[7] C. E. Shannon, *Bell Syst. Technol. J.*, **3**, 379 (1948).

[8] F. Gao, H. Zhang, L. Guo and Marc Garland, *Chemometr. Intell. Lab.*, **95**, 94 (2009).

[9] S. Cheng, F. Gao, K. I. Krummel and M. Garland, *Talanta*, **74**, 1132 (2008).

[10] L. Guo, F. Kooli and M. Garland, *Anal. Chim. Acta.*, **517**, 229 (2004).

[11] L. Guo, P. Sprenger and M. Garland, *Anal. Chim. Acta.*, **608**, 48 (2008).

[12] M. Tjahjono, C. Huiheng, E. Widjaja, K. Sa-ei and M. Garland, *Talana*, **79**, 856 (2009).

[13] C. Li, E. Widjaja and M. Garland, *J. Catal.*, **213**, 126 (2003).

[14] E. Biglieri and K. Yao, *Signal Process.*, **18**, 277 (1989)

[15] S. Palit and P. P. Kanjilal, *Signal Process.*, **40**, 269 (1994).

[16] K. Baker, *Singular Value Decomposition Tutorial* (2013).

[17] D. Kalman, *A Singularly Valuable Decomposition: The SVD of a Matrix* (2013).

[18] Y. Takane and F. W. Young, *Psychometrika*, **42**, 7 (1977).

[19] P. M. Kroonenberg and J. D. Leeuw, *Psychometrika*, **45**, 69 (1980).

[20] I. Joliffe, *Principal component analysis*, John Wiley & Sons, Ltd (2002).

[21] S. Wold, M. Sjöström and L. Eriksson, *Chemometr. Intell. Lab.*, **58**, 109 (2001).

[22] http://www.chem.uoa.gr/applets/appletbeerlaw/appl_beer2.html

[23] G. G. Brown, B. C. Dian, K. O. Douglas, S. M. Geyer, B. H. Pate, *J. Mol. Spectrosc.*, **238**, 200 (2006).

[24] G. G. Brown, B. C. Dian, K. O. Douglas, S. M. Geyer, S. T. Shipman and B. H. Pate, *Rev. Sci. Instrum.*, **79**, 053103 (2008).

[25] G. S. Grubbs II, C. T. Dewberry, K. C. Etchison, K. E. Kerr and S. A. Cooke, *Rev. Sci. Instrum.*, **78**, 096106 (2007).

[26] J. –U. Grabow, S. Mata, J. L. Alonso, I. Peña, S. Blanco, J. C. López and C. Cabezas, *Phys. Chem. Chem. Phys.*, **13**, 21063 (2011).

[27] M. K. Jahn, D. A. Dewald, D. Wachsmuth, J. –U. Grabow and S. C. Mehrota, *J. Mol. Spectrosc.*, **280**, 54 (2012).

[28] J. D. Swalen and C. C. Costain, *J. Chem. Phys.*, **31**, 1562 (1959).

[29] M. hayashi and K. Kuwada, *B. Chem. Soc. Jpn.*, **47**, 3006 (1974).

[30] L. Evangelisti, L. B. Favero, A. Maris, S. Melandri, A. V. –Toribio, A. Lesarri and W. Caminati, *J. Mol. Spectrosc.*, **259**, 65 (2010).

[31] M. C. L. Gerry, K. Yamada and G. Winnewisser, *J. Phys. Chem. Ref. Data*, **8**, 107 (1979).

[32] H. E. Matthews, W. M. Irvine, P. Frieberg, R. D. Brown and P. D. Godfrey, *Nature*, **310**, 125 (1984).

[33] R. D. Brown, P. D. Godfrey, D. M. Cragg, E. H. N. Rice, W. M. Irvine, P. Frieberg, H. Suzuki, M. Ohishi, N. Kaifu, and M. Morimoto, *Astrophys. J.*, **297**, 302 (1985).

[34] D. McNaughton, D. McGilvery and F. Shanks, *J. Mol. Spectrosc.*, **149**, 458 (1991).

Chapter 5.0

Application of the EFC Cell

to Transient FTIR Spectroscopy

5.1 Introduction

Many of the gaseous molecules that are observed in interstellar media are often unstable and have short lifetimes (< 5 sec) when synthesized under laboratory conditions using techniques like flash pyrolysis [1] or electric discharge [2]. Also referred to as transient species, these types of molecules can present experimental difficulties when attempting to record their IR spectra. In particular for high resolution spectroscopy, the long acquisition time needed to record at high resolution often results in the need for a large volume of precursor molecule. In order to address this issue, one way forward is to modify an experiment such that the lifetime of a transient species is increased, which in principle will decrease the amount of precursor molecule required and will allow for spectroscopy of species with otherwise too short lifetimes. One method of doing so is by replicating the physical conditions of the environments where these molecules are naturally found. That is: cold temperatures and low pressures. To reproduce both of these factors, one can use supersonic jet expansion or collisional cooling as they provide the coldest environments.

The former technique is widely used in FTMW and FTIR spectroscopy and produces molecules with low rotational temperatures. This ensures that molecules are rotationally cold which greatly reduces the spectral congestion in ro-vibrational spectra. Supersonic jet expansion also operates under high vacuum conditions which minimises any pressure induced line broadening. Unfortunately, for infrared studies this technique usually requires a large amount of sample, as carrier gas is either continuously flowed or pulsed through/over a sample. Furthermore, the limited number of molecules passing through the optical beam often results in vibrational bands which have low absorbance values.

The latter technique, collisional cooling, is a more viable option as it is able to address the issues which supersonic jet expansion cannot. Collisional cooling is achieved using an instrument similar to the EFC cell described in **Chapter 1.2.4.1** as it provides both a cold environment and high vacuum suitable for transient spectroscopy. The cell is also able to operate in a static mode which can greatly reduce the volume of precursor molecule required if the lifetime of a transient species is increased. This makes collisional cooling the ideal technique to see whether or not the lifetime of a transient species can be increased.

5.2 Propadienone

Propadienone (panel **a** in **figure 6.1**) is a molecule that is postulated to exist in interstellar media and is an unstable transient species under laboratory conditions. Its tricarbon backbone structure makes it the third member of the cumulenone family, following ketene and formaldehyde, and it can be generated via flash pyrolysis of acrylic anhydride [3] to give equal amounts of propadienone and acrylic acid. The microwave spectrum of propadienone was first recorded by Blackman *et al*. [3, 4], using a Meldrum's acid derivative and the structure of propadienone was initially thought to be

linear-planar (C_{2v} symmetry) based on *ab initio* results by Komornicki *et al*. using a low level of theory [5]. This however was corrected by Brown and co-workers [6 - 8] and shown to be bent-planar (C_s) from structural analyses of isotope substituted propadienones. Subsequent *ab initio* studies by Farnell & Radom [9], Brown & Dittman [10] and McNaughton & Ross [11] also confirmed the bent-planar structure. The non-linear structure of propadienone results in a double minimum potential well (panel **b** in **figure 6.1**) where all vibrational states (ν_i) (ground state included) are split into ν_i^- and ν_i^+ states with the possibility of intersystem transitions ($\nu_i^- \leftrightarrow \nu_i^+$).

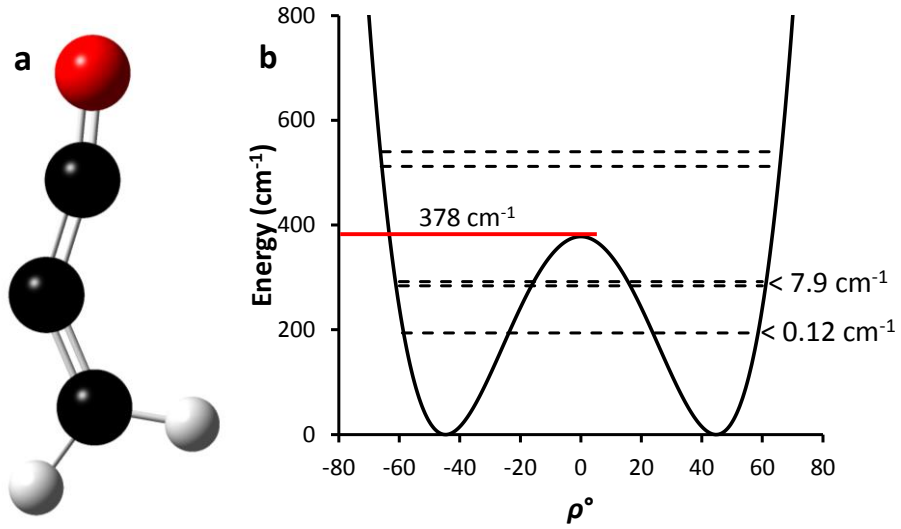

Figure 6.1: panel a) The structure of propadienone from MP2/cc-pVTZ calculations in Gaussian09 (Revision D.01) [12]. The oxygen atom is in red, carbons in black and hydrogens in white. **Panel b)** an illustration of the double minimum potential well for propadienone, where the dashed lines represent the energy levels for the three lowest vibrational states.

The first FTIR spectrum of propadienone was recorded using matrix isolation [13] without any attempt made at assigning the vibrational bands. Of the 12 fundamental vibrations, only two have been analysed thus far: ν_{12} [14] from microwave spectroscopy using transitions from vibrational satellites; and ν_2 [15] from laser diode absorption spectroscopy although the fit is far from complete. In a recent computational analysis [16], the energies of various isomers with the formula C_3H_2O were calculated using a minimum energy principle, where propadienone was determined to be the lowest energy isomer (0 kJ mol^{-1}) compared to propynal (22.7 kJ mol^{-1}) and cyclopropenone (45.0 kJ mol^{-1}). All three species are expected to be present in the interstellar medium and the results imply that thermodynamically, for a molecule with C_3H_2O atoms, propadienone should be the most abundant isomer.

5.2.1 Experimental

Spectra were recorded at the Australian Synchrotron THz/far-IR beamline using a Bruker IFS125 HR spectrometer with the listed experimental conditions in **table 5.1**.

Table 5.1: Summary of experimental conditions for recording spectra of propadienone

Optics		Acquisition	
Windows	KBr	Resolution	4 cm^{-1}
Source	MIR	Apodization	Blackman-Harris 3-Term
Beamsplitter	KBr	Zero fill/post zero fill	2/4
Detector	MCTm	Scans	1000 files of 2 scans

Acrylic anhydride (synthesis described in **Chapter 5.2.1.1**) vapour was flowed through a furnace set to 923 K into an ambient temperature White-type multipass cell set to 24 passes (*ca*. 14.4 m) operating in a flow through mode. The flow rate was fast enough such that the absorbance of the ν_2 band of propadienone at 2126 cm^{-1} was at its maximum.

A set of 2000 scans (1000 files with 2 scans per file) was initiated in OPUS 6.0 prior to introducing acrylic anhydride through the furnace. The cell was initially operated in a flow through mode to maintain a stable absorbance of the ν_2 band before closing the entry and exit values to switch to a static mode. Decay of the ν_2 band was monitored over the course of *ca*. 100 scans (38 sec) to ensure no more propadienone was present before exposing the cell to the pump in order to remove any lingering molecules. This process was repeated multiple times during the time it took to record the 2000 scans, enabling us to calculate the half-life of propadienone under room temperature for the very first time.

Survey spectra of the cell under flow through (red trace in **figure 5.2**) and static (blue trace in **figure 5.2**) conditions are shown in **figure 5.2**. Below 1900 cm^{-1}, there are very few differences between the two spectra, suggesting that these bands belong to a stable molecule such as acrylic acid. Under flow-through conditions, the ν_2 band of propadienone near 2100 cm^{-1} becomes visible and is overlapped with small amounts of CO. Shoulder features (*ca*. 2180 cm^{1}) in the flow-through spectrum have been assigned to ketene, as it is most likely generated from the pyrolysis of residual diethyl ether. CO_2 is also present in both spectra near 2350 cm^{-1}.

Comparison of the static spectrum (blue trace in **figure 5.2**) to that of the precursor (black trace in **figure 5.2**) shows little difference between the vibrational bands across range of the spectrum. This is expected as both acrylic acid and acrylic anhydride both have the same acrylic functional group which has vibrational bands that dominates the mid-IR spectrum.

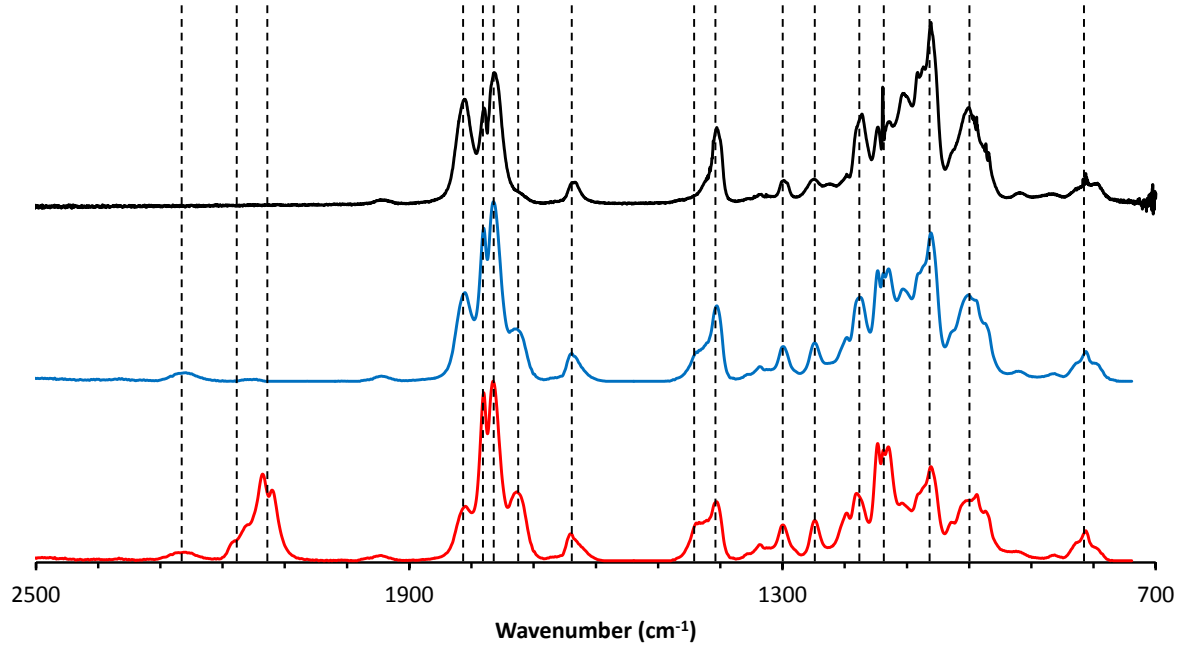

Figure 5.2: Normalised survey spectra of the pyrolysis products when the cell is operating in a flow-through (red trace) and static (blue trace) mode. The black trace is a spectrum of acrylic anhydride.

5.2.1.1 Acryloyl chloride

The method used to synthesize acryloyl chloride was adapted from [17] and is as follows. 140.57 g (0.93 mol) of benzoyl chloride (Benz. Cl.) was dissolved in 62.68 g (0.87 mol) of acrylic acid (Ac. Ac.) at ambient temperature. 0.05 g of hydroquinone (HQ) was added to the mixture and collection flask to act as a polymerisation inhibitor. This mixture was distilled at a rate such that the volatile material near the top of the fractionation column was maintained between 70 – 80 °C, before passing through a condenser tube into a round bottom flask that was immersed in an ice-water slurry. The crude product was re-distilled between 84 – 86 °C (31.86 g, 40.53 % yield) and confirmed to be acryloyl chloride (**figure 5.3**) through ^{1}H-NMR

^{1}H-NMR (400 MHz, 25 °C, $CDCl_3$): δ = 6.61 ppm (d, $^{2}J_{HH}$ = 16.8 Hz), 6.33 ppm (dd, $^{2}J_{HH}$ = 16.8 Hz, $^{2}J_{HH}$ = 16.8 Hz), 6.17 ppm (d, $^{2}J_{HH}$ = 10.4 Hz).

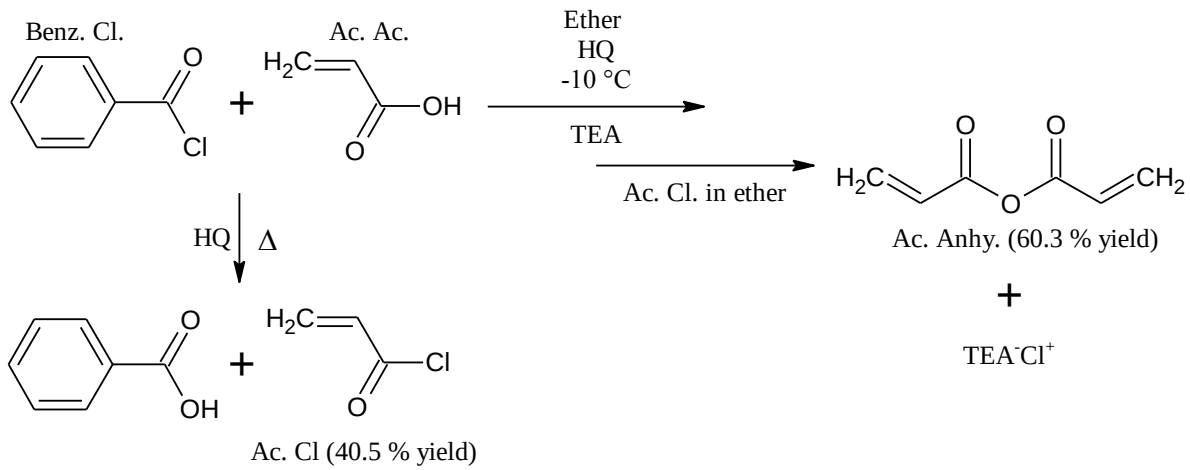

Figure 5.3: Synthesis steps used for the synthesis of acryloyl chloride (Ac. Cl) and acrylic anhydride (Ac. Anhy.)

5.2.1.2 Acrylic anhydride

Acrylic anhydride was synthesized using a method prescribed by [18]. 13.90 g (0.15 mol) of Ac. Ac. and 0.05 g of HQ were dissolved in 100 mL of diethyl ether and then cooled to -10 °C in an ice-water-salt slurry. This solution was treated with 15.30 g (0.15 mol) of triethylenamine (TEA) followed by drop wise additions of ethereal acryloyl chloride (Ac. Cl.) (13.68 g (0.15 mol) of Ac. Cl. dissolved in 100 mL of diethyl ether) so that the temperature of the reaction mixture was maintained below 0 °C. The solution was also constantly stirred with a magnetic stirrer during the addition of Ac. Cl. Triethylammonium chloride (TEA^-Cl^+) (white precipitate) was filtered from the mixture and rinsed with an additional 100 mL of diethyl ether, which was removed by rotary evaporation. The resulting liquid was vacuum distilled at - 84 kPa whilst maintaining the temperature of the volatile materials near the top of the fractionation column between 80 - °C. This method was repeated for another two batches before combining the crude products together to be re-distilled between 83 – 85 °C (38.15 g, 60.29 % averaged yield) into a round bottom flask with 0.05 g HQ immersed in an ice-water slurry. The product was confirmed to be acrylic anhydride (Ac. Anhy.) through ^{1}H-NMR and IR (black trace in **figure 5.2**).

^{1}H-NMR: (400 MHz, 25 °C, $CDCl_3$): δ = 6.58 ppm (dd, $^2J_{HH}$ = 0.8 Hz, $^3J_{HH}$ = 16.8 Hz), 6.16 ppm (dd, $^2J_{HH}$ = 2.4 Hz, $^3J_{HH}$ = 17.2 Hz), 6.06 ppm (dd, $^2J_{HH}$ = 1.2 Hz, $^3J_{HH}$ = 10.4 Hz).

5.2.1.3 New glassware and the EFC cell

Before the experiment could be performed in the EFC cell, it was necessary to design new glassware so that the distance travelled from the furnace to the optical path was as short as possible to maximise the number of molecules entering the cell (**figure 5.4**). With the current instrumental setup, it is only possible to reduce the distance to *ca*. 65 cm, starting from the end of the furnace to the bottom of the inlet tube. By using glass instead of stainless steel, the probability of molecules reacting with the tube wall is minimised and provides a more secure connection with the glass furnace tube.

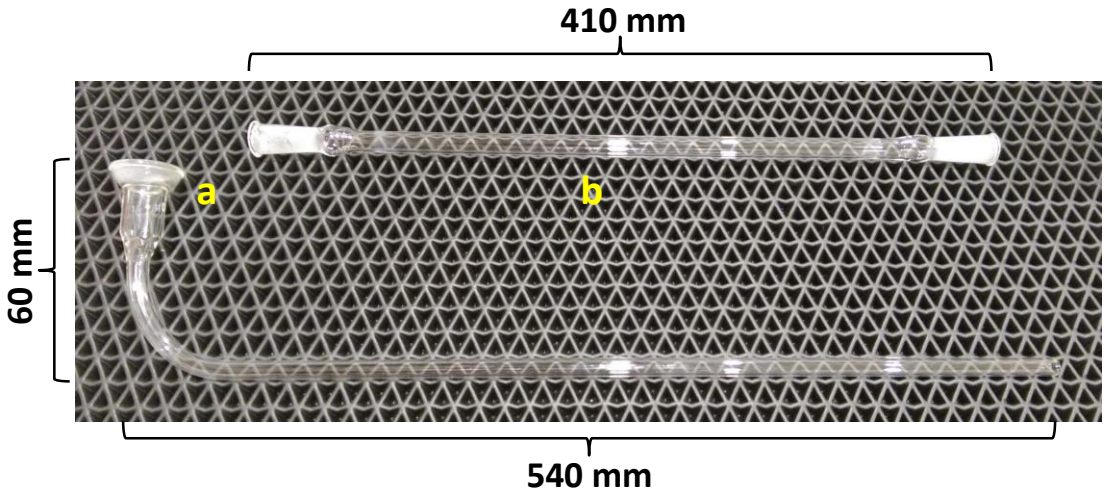

Figure 5.4: A picture of the glassware connecting the furnace to the EFC cell: **a**) inlet tube to the EFC cell outer diameter = 10 mm; **b**) furnace tube with an internal diameter = 10 mm.

The EFC cell was set to 32 passes (20 m) and cooled to 291, 264 and 258 K for the following experiments using cold nitrogen gas. In addition to cooling the cell, helium buffer gas was introduced into the cell to help constrain molecules within the optical path of the beam. The flow of buffer gas was controlled by a Whitey ¼ ″ needle valve such that the overall cell pressure was maintained between 2.0 - 2.3 × 10^{-2} kPa prior to introducing sample gas. The optics and acquisition conditions were unchanged from what was used in **Chapter 5.2.1**.

5.2.2 Preliminary results: Half-life

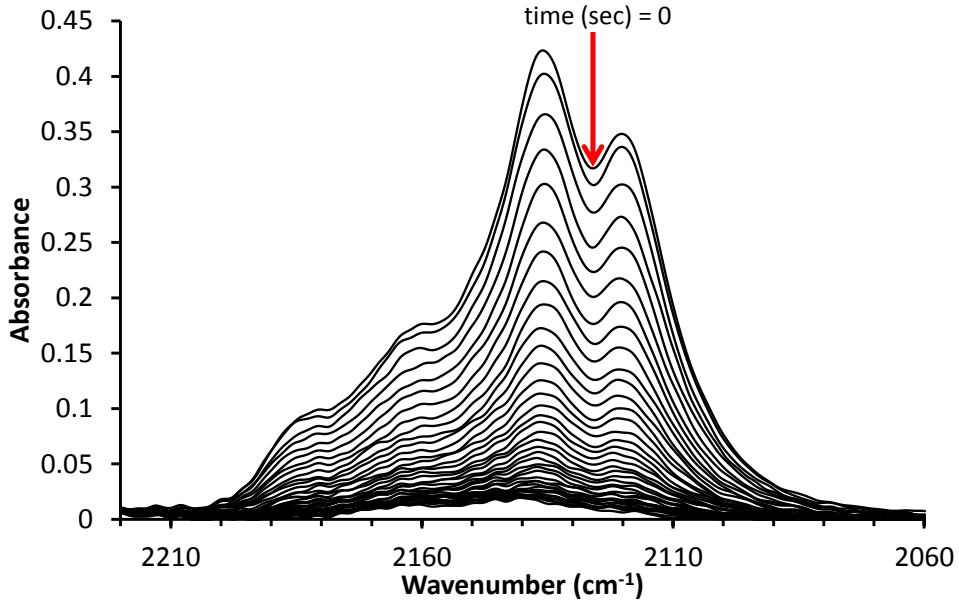

Figure 5.5: Decay of the ν_2 band of propadienone over the first 39 scans (14.7 seconds) at ambient temperature.

The absorbance of the ν_2 band is seen to decay over a time period of *ca.* 15 sec (**figure 5.5**) before it reaches a relatively constant absorbance value. When plotted as a function of time, the integrated area under the curve between 2060 – 2210 cm^{-1} decays at a rate similar to that of a 1st order logarithmic decay (panel **a** in **figure 5.6**), and from an initial estimate the half-life ($t_{1/2}$) of propadienone is estimated to be roughly 2.7 sec. By plotting the natural log of the integrated area versus time, it is possible to extract the rate constant *k* (panel **b** in **figure 5.6**) which can then be used to more accurately determine the half-life of propadienone using **equations 5.1 – 5.3**. Data points beyond 10 sec are not included in the plot shown in **figure 5.5b** due to increased contributions to the integrated area from the vibrational bands of by-products as well as lower S/N levels.

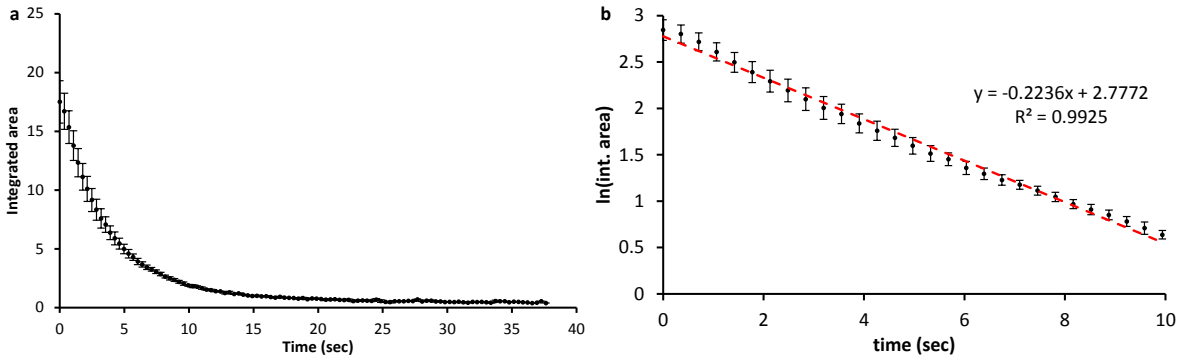

Figure 5.6: Panel a) Decay of the integrated intensity for the ν_2 band of propadienone over time. **Panel b**) Linear regression (red dashed line) used to calculate the rate constant *k*.

If we assume that the decay of propadienone follows a first order rate equation, then the rate of decay and half-life can be calculated using **equation 5.1**,

$$[A] = [A_0]e^{-kt} \qquad \textbf{(5.1)}$$

where [*A*] (mol L^{-1}) is the concentration at time *t* (sec), A_0 is the initial concentration and *k* is the rate coefficient (sec^{-1}), given as **equation 5.2**

$$-kt = \ln\left(\frac{A_t}{A_0}\right) \quad \textbf{(5.2)}$$

where $\frac{A_t}{A_0}$ is equivalent to the integrated area.

It is therefore possible to determine the half-life (**equation 5.3**) of propadienone to be 2.7 ± 0.2 sec which is consistent with the initial estimate based on the integrated area alone. Having established its half-life at ambient temperature, experiments were performed in the EFC cell to see if collisional cooling has any significant influence on its half-life.

$$t_{1/2} = \frac{ln2}{k} \qquad \textbf{(5.3)}$$

Figure 5.7 illustrates the increase in the calculated half-life of propadienone as temperature is decreased with the inclusion of helium buffer gas ($2.0 – 2.3 \times 10^{-2}$ kPa) as part of the experiment (red circles in **figure 5.7**). At 291 K, the half-life is increased by a factor of ≈ 2.5 to 6.6 ± 0.5 sec and is increased further to 20 ± 3 sec upon cooling to 264 K. The data can be fitted using a linear regression model (R^2 = 0.99) which indicates that there is a proportional increase in half-life as a function of decreasing temperature. The observed increase in half-life is most likely attributed to two factors. First, molecular collisions with the cell walls are reduced due to the presence of buffer gas molecules; and second, the thermodynamic and kinetic energies of the hot transient molecules are reduced as they collide with cold, inert buffer gas molecules.

In an attempt to de-correlate the effect of temperature and buffer gas pressure under the different experimental conditions, an experiment was performed near 280 K with no helium gas (blue square in **figure 5.7**). The calculated half-life at 280 K (3.2 ± 0.4 sec) is comparable to what was determined for the ambient temperature study (2.7 ± 0.2 sec). Their respective half-lives fall within one standard deviation of each other and implies that the conditions tested (i.e. cold cell with no buffer gas) provides conditions which are similar to the experiments performed at room temperature. Near 258 K, the half-life of propadienone deviates from the linear regression and has a calculated half-life of 8.8 ± 0.3 sec. The sudden decrease in half-life is most likely due to the reduced buffer gas pressure ($1.0 - 1.5 \times 10^{-2}$ kPa) which has a lower efficiency of heat transfer by molecular collisions. Extrapolation of the linear regression to the same temperature results in an expected half-life of *ca.*

23 sec, which is a factor of ≈ 3 longer than what was observed and may provide a very approximate guide to how buffer gas influences half-life. However, due to time constraints with the amount of allocated beamtime, it was not possible to validate this hypothesis and leaves room for more experimental data.

At the coldest temperature tested (227 K), no evidence of propadienone was observed in any of the experiments with and without the inclusion of buffer gas. The only plausible reason for this is that propadienone is freezing out on either the glass inlet tube or on the walls of the cell.

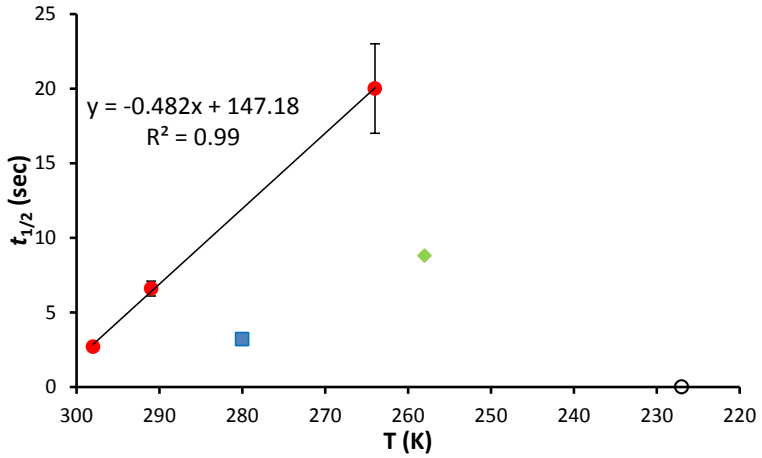

Figure 5.7: Comparison of the calculated half-lives for propadienone at different temperatures. Red circles are for experiments performed with a buffer gas pressure between 2.0 – 2.3 × 10^{-2} kPa; blue square used no buffer gas; green triangle used between 1.0 – 1.5 × 10^{-2} kPa helium. The hollow circle at 227 K shows the coldest temperature tested with no observable propadienone.

5.2.3 Conclusions

Although the current data set is far from complete, the result from this study makes it possible to address several key factors associated with transient spectroscopy. First, it is possible to extend the half-life of a transient species by exposing it to cold collisional cooling conditions and this highlights the potential application of an EFC cell to transient spectroscopy. The effect of collisional cooling will most likely depend on the molecule being studied and will help minimise the need for a large volume of precursor molecule when recording high resolution spectra.

Second, the IR bands of cold molecules will have a simplified ro-vibrational structure due to a decrease in the intensity of contributions from low energy vibrational states, allowing for a more amenable analysis of complex ro-vibrational bands. For very complex, and highly coupled vibrational states, it would be necessary to use supersonic jet expansion as the degree of spectral simplification afforded by collisional cooling is not as efficient as supersonic jet expansion; which provides the coldest rotational temperatures and thus simplest ro-vibrational structure.

Third, it is clear that there are some aspects of the instrumental setup (such as the path length from the furnace to the optical beam) that need to be improved. Although the current design has a distance of approximately 65 cm, this needs to be reduced further in order to increase the number of transient molecules which enter the cell before the onset of decomposition.

The range of experimental conditions tested also needs to be increased and will provide a more rigorous analysis of the resultant trends from changing both temperature and buffer gas pressure, as well as to verify these preliminary results.

References

[1] D. McNaughton, D. McGilvery and F. Shanks, *J. Mol. Spectrosc.*, **149**, 458 (1991).

[2] Y. P. Raizel and J. E. Allen, *Gas discharge physics*, Vol. 2 (1997).

[3] G. L. Blackman, R. D. Brown, R. F. C. Brown, F. W. Eastwood, G. L. McMullen and M. L. Robertson, *Aust. J. Chem*, **31**, 209 (1978).

[4] G. L. Blackman, R. D. Brown, R. F. C. Brown, F. W. Eastwood and G. L. McMullen, *J. Mol. Spectrosc.*, **68**, 499 (1977).

[5] A. Komornicki, C. E. Dykstra, M. A. Vincent and L. Radom, *J. Am. Chem. Soc.*, **103**, 1652 (1981).

[6] R. D. Brown, P. D. Godfrey, R. Champion and D. McNaughton, *J. Am. Chem. Soc.*, **103**, 5711 (1981).

[7] R. D. Brown, *J. Mol. Struct.*, **97**, 293 (1983).

[8] R. D. Brown, R. Champion, P. S. Elmes and P. D. Godfrey, *J. Am. Chem. Soc.*, **107**, 4109 (1985).

[9] L. Farnell and L. Radom, *Chem. Phys. Lett.*, **91**, 373 (1982).

[10] R. D. Brown and R. G. Dittman, *Chem. Phys.*, **83**, 77 (1984).

[11] D. McNaughton and S. C. Ross, *J. Mol. Struct.*, **348**, 221, (1995).

[12] Gaussian 09, Revision D.01, M. J. Frisch, G. W. Trucks, H. B. Schlegel, G. E. Scuseria, M. A. Robb, J. R. Cheeseman, G. Scalmani, V. Barone, B. Mennucci, G. A. Petersson, H. Nakatsuji, M. Caricato, X. Li, H. P. Hratchian, A. F. Izmaylov, J. Bloino, G. Zheng, J. L. Sonnenberg, M. Hada, M. Ehara, K. Toyota, R. Fukuda, J. Hasegawa, M. Ishida, T. Nakajima, Y. Honda, O. Kitao, H. Nakai, T. Vreven, J. A. Montgomery, Jr., J. E. Peralta, F. Ogliaro, M. Bearpark, J. J. Heyd, E. Brothers, K. N. Kudin, V. N. Staroverov, T. Keith, R. Kobayashi, J. Normand, K. Raghavachari, A. Rendell, J. C. Burant, S. S. Iyengar, J. Tomasi, M. Cossi, N. Rega, J. M. Millam, M. Klene, J. E. Knox, J. B. Cross, V. Bakken, C. Adamo, J. Jaramillo, R. Gomperts, R. E. Stratmann, O Yazyev, A. J. Austin, R. Cammi, C. Pomelli, J. W. Ochterski, R. L. Martin, K. Morokuma, V. G. Zakrzewski, G. A. Voth, P. Salvador, J. J. Dannenberg, S. Dapprich, A. D. Daniels, O Farkas, J. B. Foresman, J. V. Ortiz, J. Cioslowski and D. J. Fox, Gaussian, Inc., Wallingford CT, 2013.

[13] O. L. Chapman, M. D. Miller and S. M. Pitzenberger, *J. Am. Chem. Soc.*, **109**, 6867 (1987).

[14] R. D. Brown, P. D. Godfrey and R. Champion, *J. Mol. Spectrosc.*, **123**, 93 (1987).

[15] P. J. O'Sullivan, R. J. Livingstone, Z. Liu and P. B. Davies, *Mol. Phys.*, **105**, 727 (2007).

[16] R. A. Loomis, B. A. McGuire, C. Shingledecker, C. H. Johnson, S. Blair, A. Robertson and A. J. Remijan, *Astrophys. J.*, **34**, 799 (2015).

[17] D. McNaughton, Honours thesis. 1977.

[18] R. D. Brown, R. Champion, P. S. Elmes and P. D. Godfrey, *J. Am. Chem. Soc.*, **107**, 4109 (1985).

Chapter 6.0

Conclusions

High resolution spectroscopy

Since the installation of an EFC cell to Australian Synchrotron THz/far-IR beamline, it has been possible to record high resolution FTIR spectra of cold gases in the far-IR region, which has previously been a difficult region to access. Far-IR spectroscopy is becoming an increasingly important technique as it has many astrophysical and astrochemical applications.

By cooling down gaseous molecules, spectral complexity is reduced and is extremely beneficial for high resolution spectroscopy where ro-vibrational bands of highly asymmetric, or polyatomic molecules, can be severely congested at room temperature. The research presented in **Chapters 2.2.1 – 2.2.4** provides new understandings of some of the low energy vibrational modes belonging to atmospherically relevant molecules. This is important for atmospheric monitoring as many vibrational bands within the MIR region will have intensity contributions from hot bands emanating from low energy vibrational levels.

Particulate ices

Particulate ices consisting of isotopically mixed H_2O water ice aerosols, was the primary study in **Chapter 3** and provided insights to the nature of the intermolecular and intramolecular bonding within H_2O and D_2O. Molecular ices consisting of small hydrocarbons have also been generated in the EFC cell and these molecular ices are relevant to planetary atmospheres, by regulating the radiative forcing; as well as in interstellar media, where they can act as reaction sites. The majority of studies performed using the EFC cell have involved unimolecular ices, however there is potential application to investigate the chemistry of bimolecular, or multi-molecular ices.

Chemometrics

The application of BTEM to high resolution FTIR and FTMW spectra has shown that it is possible to separate multiple components from these gas phase systems. Although there are some aspects of BTEM (and chemometrics in general) that can be improved, the results from the preliminary studies in **Chapter 4** brings the technique one step closer to sorting out the different molecular lines that are observed in interstellar media.

BTEM also has potential application to pyrolysis and electric discharge experiments, where more than one species are often generated. Being able to separate their individual spectra, and quantify their concentrations, will simplify the analysis of high resolution spectra and will provide the possibility of determining reaction pathways with greater accuracy.

Transient spectroscopy

With the recent application of the EFC cell to transient spectroscopy, new avenues for experimental design have been discovered. The results from the preliminary study in **Chapter 5** were made possible as a result of modifying the inlet system for transient species. The lid of the EFC cell will require modifications to further minimise the distance travelled from the furnace to the optical beam. This will also allow for a laser to be steered into the EFC cell which can be used for laser photolysis spectroscopy.